
The Silicon Tracking System of the E16 experiment at J-PARC: Characterization, Beam commissioning, and implications for the CBM series production

Dissertation
zur Erlangung des Doktorgrades
der Naturwissenschaften

vorgelegt beim Fachbereich Physik
der Johann Wolfgang Goethe-Universität
in Frankfurt am Main

von
Dairon Rodríguez Garcés
aus La Habana, Kuba

Frankfurt am Main (2025)
(D30)

vom Fachbereich Physik der
Johann Wolfgang Goethe-Universität als Dissertation angenommen.

Dekan: Prof. Dr. Marc Wagner

Gutachter: Prof. Dr. Alberica Toia

Prof. Dr. Christoph Blume

Betreuer: Dr. Adrian Rodríguez Rodríguez

Datum der Disputation:

“To express science in everyday language: that is a great action that only few people do”

José Martí

To my family

Contents

Abstract	1
Kurzfassung	4
1 Introduction	7
1.1 Brief introduction to QCD	7
1.2 QCD phase diagram	8
1.3 High baryon density at low temperature	9
1.4 Heavy-ion collisions	10
1.5 FAIR facility	12
1.5.1 CBM physics program	13
1.6 J-PARC E16 experiment	16
1.6.1 Physics of the E16 experiment	16
1.6.2 Previous results	17
1.6.3 Upgrade from E325 to E16 experiment	18
1.6.4 Collaboration with J-PARC E16 experiment	19
1.7 Scope of this work	19
2 CBM and E16 experimental setups	21
2.1 The CBM experiment at FAIR	21
2.2 The E16 experiment at J-PARC	24
2.3 Silicon Tracking Detectors	25
2.3.1 Working principles of silicon detectors	26
2.3.2 The Silicon Tracking System (STS) detector module	28
2.3.3 STS at the CBM experiment	31
2.3.4 STS at the E16 experiment	34
3 Studies of the ADC and FAST discriminator response for enhanced calibration of the SMX ASIC	37
3.1 Introduction to the STS front-end electronics	37
3.2 Description of the analog measuring circuits and calibration functionalities of the SMX ASIC	39
3.2.1 The 5-bit flash Analog-to-Digital Converter (ADC)	39
3.2.2 The timing discriminator	41
3.3 The standard calibration procedure	41
3.4 Optimization of the calibration procedure	43
3.4.1 Implementation of the Successive Approximation Method (SAR)	43

3.4.2	Description of the experimental setups	44
3.5	Evaluation of the SAR method	45
3.5.1	Optimization of the SAR method parameters	49
3.5.2	Reproducibility of the calibration procedure	51
3.5.3	Implementation of the broadcasting as a method procedure	52
3.6	Transfer functions of the amplitude and timing circuits	53
3.7	Studies with the FAST discriminator	56
3.8	Quality control of the calibration settings	61
3.9	Summary towards series testing	63
4	STS pre-series modules for the E16 experiment	65
4.1	The E16-STs module	65
4.2	Basic considerations for a testing protocol for series production	67
4.3	Current-Voltage characteristic	67
4.3.1	Experimental setup	68
4.3.2	Results	69
4.4	Functional test and electrical performance	69
4.4.1	Experimental setup	71
4.4.2	Results	72
4.5	Response of E16 modules to $^{90}\text{Sr}/\text{Y}$ radioactive source	77
4.6	Module testing protocol	81
4.7	E16-STs upgrade for 2025 beam campaign	82
4.8	Towards E16 full acceptance coverage	83
4.9	Summary	84
5	In-Beam performance of E16-STs modules	85
5.1	Beam test at the Photon Factory Advanced Ring	86
5.1.1	Experimental setup and readout chain	86
5.2	Data analysis: from E16 to CBMROOT framework	88
5.2.1	Development of the data unpacker	89
5.2.2	Implementation of the geometry	92
5.3	Data analysis: results	92
5.3.1	Time resolution	92
5.3.2	Charge distribution and cluster size	95
5.3.3	Detection efficiency	99
5.3.4	Track reconstruction	101
5.4	Commissioning run at J-PARC	106
5.4.1	Results	107
5.5	Summary	109
6	Conclusions and Outlooks	111
A	The SAR method algorithm	114
A.1	The SAR method visual example	114
A.2	The SAR main method code	115
B	The prototype FEB-C	116

C	The SAR method quality parameters	117
C.1	Differential Non-Linearity	117
C.2	Integral Non-Linearity	119
C.3	Standard Deviation Linear Residual	120
D	Broadcasting commands and implementation in the SAR method	122
E	FAST discriminator trimming range	125
F	X- and Y-coordinate residuals under inclined tracks	126
G	Principal Component Analysis (PCA)	127
G.1	Intersection point line-plane	127
G.2	Coefficient of determination for a 3D line fit	128
	List of Acronyms	129
	Extended Abstract	134
	Zusammenfassung	139
	References	144
	Acknowledgements	149
	Curriculum Vitae	151

Abstract

The E16 experiment at the Japan Proton Accelerator Research Complex (J-PARC) aims to investigate the in-medium modifications of light vector mesons through their di-electron decay channels providing insight into the restoration of chiral symmetry in dense nuclear matter. To achieve the required mass resolution and precise vertex reconstruction, an upgrade of the innermost tracking detector was essential. This upgrade demanded a compact, low-mass, and radiation tolerant tracking system capable of operating at high interaction rates and within strong magnetic fields. After a detailed evaluation of available technologies, the silicon microstrip concept developed for the Silicon Tracking System (STS) of the Compressed Baryonic Matter (CBM) experiment at the Facility for Antiproton and Ion Research (FAIR), was selected for this proven performance, scalability, and suitability for the E16 experimental environment.

The CBM experiment at FAIR and E16 experiment at J-PARC share multiple synergies. Both aim to explore similar regions of the Quantum Chromodynamics (QCD) phase diagram and face comparable detector challenges, including very high interaction rates up to 10 MHz, tracker systems with 25 μm position resolution, and timing capabilities of around 5 ns. These common points help to build collaborative bridges between the two experiments.

Within the CBM-E16 collaboration, the construction, testing, characterization, and installation of 15 detector modules for the E16 setup were carried out, culminating in their commissioning during beam tests at Tsukuba with a 3 GeV/c electron beam. The modules were thoroughly calibrated and validated in preparation for the beamtime, during which three modules were successfully operated and illuminated in two planes. Within this collaborative framework, the present thesis focuses on the development, optimization, and validation of calibration and characterization procedures of the SMX Application-Specific Integrate Circuits (ASICs) used in the E16-STC modules. This work encompasses the entire module life cycle, from the algorithmic level of ASIC calibration to large-scale testing, qualification, systematic application of the procedures to the full series of E16 modules, commissioning support during the beam tests, and the subsequent analysis and experimental verification in the beamline.

The first part of this work addresses the optimization of the SMX ASIC calibration process. The STANDARD calibration procedure of the Analog-to-Digital Converter (ADC), although highly precise, was limited by the time-consuming coarse-scan stage, making it inefficient for series testing. To overcome this limitation, a different calibration approach based on a Successive Approximation Method (SAR) algorithm was developed. This method replaces the exhaustive threshold scanning of the standard technique with an iterative binary search, allowing for rapid convergence on the optimal discriminator threshold. The SAR procedure achieved equivalent precision to the STANDARD method,

with Differential Non-Linearity (DNL) and Integral Non-Linearity (INL) below 0.4 LSB, while reducing calibration time by approximately 30%. Subsequent optimization of algorithm parameters, such as number of iterations, search width, and fine-range was performed. The combination of ten iterations, a search width of 14 LSB, and a fine range of 12 LSB, achieved an extra time reduction of nearly 60% relative to the STANDARD method.

A further improvement was realized by implementing a broadcasting calibration mode, allowing the simultaneous calibration of all ASICs in one module. This parallelized scheme provided an additional 50% reduction in calibration time relative to the optimized SAR approach. Furthermore, the transfer functions of both the ADC and FAST discriminators were systematically analyzed, confirming a linear relationship between user register settings and effective thresholds. The extracted slopes were 822 e/LSB and 718 e/LSB for the n- and p-side of the ADC path, and 397 e/LSB and 361 e/LSB for the corresponding FAST paths. A global Digital-to-Analog Converter (DAC) setting for the FAST discriminator threshold was identified in the range between 22 LSB and 26 LSB, enabling the calibration of the totality of the channels in a module, excluding the so-called Z-strips.

As a large-scale validation, a total of 15 modules, including one prototype, ten pre-series, and four replacement units; were assembled, tested, characterized and then installed in the E16 detector setup. The modules (each comprising 8 ASICs per side) were fully calibrated using the optimized SAR algorithm. The resulting trim matrices demonstrated uniform correction behavior, with only a small fraction of uncalibrated discriminators ($\sim 0.03\%$ on the n-side and $\sim 0.08\%$ on the p-side). The p-side required smaller trimming adjustments, up to 20 LSB, to achieve 95% of calibrated channels, compared to 28 LSB for the n-side.

Furthermore, the functional assessment and validation of modules was performed. Fifteen modules that include one prototype, ten pre-series, and four replacement modules were tested following a standardized four-step procedure: Current-Voltage (IV) sensor characterization, ASIC calibration, Equivalent Noise Charge (ENC) evaluation, identification of broken channels, and readout from signals from a β -emitter $^{90}\text{Sr}/\text{Y}$ radioactive source. The IV measurements confirmed stable sensor operation up to 150 V. The calibration data revealed consistent ADC gains, threshold levels, and narrow threshold spreads across modules. The measured noise ranged between 700 e and 900 e, within 20% of analytical expectations. Broken channels were identified and cross-validated through source measurements, with all modules except one meeting the target production limit of 1.5% (31) defective channels.

Tests using the radioactive source enabled the evaluation of signal response at the channel level, providing additional confirmation of broken channels. Time correlation analyses between digital signals within clusters confirmed synchronization, with the correlation peak centered around $\Delta t = 0$ ns. Furthermore, a reconstructed hitmap showed agreement with the physical positioning of the source during measurements.

The knowledge and experience gained through these studies led to the definition of a comprehensive module testing and Quality Assurance (QA) protocol. This procedure is now implemented as part of the standardized QA workflow for the STS series production. The protocol has been successfully established for the large-scale CBM-STS production campaign comprising nearly 1000 modules, and has already been applied to the characterization and validation of more than 550 units.

The final part of the work presents the experimental validation of the E16-STs detector performance under beam conditions. A dedicated beam campaign was conducted at the Photon Factory Advanced Ring (PF-AR) facility in Japan using a 3 GeV/c electron beam. Three modules from the ten composing the E16-STs chamber were tested in different geometrical configurations to evaluate timing, charge collection, cluster size, detection efficiency, and spatial resolution. The measured time resolution reached 3.2 ns for large signals and approximately 5 ns for 2.7 fC signals, fulfilling the timing requirements of E16 and CBM experiments. The collected charges were approximately 22 ke and 20 ke for the n- and p-side, respectively, these values are up to 13% and 22%, for n- and p-side, below of the expected energy deposition of Minimum Ionizing Particle (MIP) in 320 μm of silicon, due to the large thresholds employed in the run. The corresponding Signal-to-Noise Ratio (SNR) were 27.8 ± 2.2 and 28.5 ± 1.5 for n- and p-side, respectively. At normal incidence, the detection efficiency reached $89.9\% \pm 0.1\%$. Spatial resolution, evaluated through a Principal Component Analysis (PCA)-based tracking algorithm, yielded $\sigma_x = 118 \mu\text{m}$ and $\sigma_y = 136 \mu\text{m}$ for single-strip clusters, improving to $\sigma_x = 20 \mu\text{m}$ and $\sigma_y = 33 \mu\text{m}$ for multi-strip clusters.

During the commissioning run (Run-0e), the first successful operation of CBM-STs modules under magnetic field conditions was achieved. The time synchronization, the tracking residuals, as well as the energy-loss measurements using one STs tracking layer revealed clear pion-proton separation up to 1 GeV/c. This result confirmed not only the tracking precision performance of the system but also its capability for particle identification.

These results mark a major milestone in validating the STs detector modules, confirming their suitability as the tracking device of E16 and providing a crucial performance benchmark for the full CBM-STs detector.

Kurzfassung

Das E16-Experiment am “Japan Proton Accelerator Research Complex (J-PARC)” zielt darauf ab, die Modifikationen leichter Vektormesonen in dichter Kernmaterie über deren Di-Elektronen-Zerfallskanäle zu untersuchen und damit Einblicke in die Wiederherstellung der chiralen Symmetrie zu gewinnen. Um die erforderliche Massenauflösung und eine präzise Vertexrekonstruktion zu erreichen, war eine Aufrüstung des innersten Spurdetektors notwendig. Diese Aufrüstung verlangte nach einem kompakten, massearmen und strahlungstoleranten Trackingsystem, das bei hohen Wechselwirkungsraten und in starken Magnetfeldern betrieben werden kann. Nach einer detaillierten Evaluierung verfügbarer Technologien wurde das für das “Compressed Baryonic Matter (CBM)”-“Silicon Tracking System (STS)” am “Facility for Antiproton and Ion Research (FAIR)” entwickelte Silizium-Mikrostreifenkonzept aufgrund seiner nachgewiesenen Leistungsfähigkeit, Skalierbarkeit und Eignung für die experimentellen Bedingungen von E16 ausgewählt.

Das CBM-Experiment bei FAIR und das E16-Experiment bei J-PARC weisen zahlreiche Synergien auf. Beide Experimente zielen darauf ab, ähnliche Regionen des “Quantum Chromodynamics (QCD)”-Phasendiagramms zu erforschen, und stehen vor vergleichbaren Detektorherausforderungen, einschließlich sehr hoher Interaktionsraten von bis zu 10 MHz und Spurrekonstruktion mit einer Ortsauflösung von 25 μm und Timing-Fähigkeiten von etwa 5 ns. Diese Gemeinsamkeiten fördern den Aufbau kollaborativer Brücken zwischen den beiden Experimenten.

Im Rahmen der CBM-E16-Kollaboration wurden 15 Detektormodule für das E16-Setup konstruiert, getestet, charakterisiert und installiert, was in ihrer Inbetriebnahme während der Bestrahlungstests in Tsukuba mit einem 3 GeV/c Elektronenstrahl mündete. Die Module wurden zur Vorbereitung auf die Strahlzeit eingehend kalibriert und validiert, wobei während der Messungen drei Module erfolgreich betrieben und in zwei Ebenen bestrahlt wurden. Innerhalb dieses kollaborativen Rahmens konzentriert sich die vorliegende Dissertation auf die Entwicklung, Optimierung und Validierung von Kalibrierungs- und Charakterisierungsverfahren für die in den E16-STs-Modulen eingesetzten SMX “Application-Specific Integrate Circuits (ASICs)”. Diese Arbeit umfasst den gesamten Lebenszyklus der Module, von der algorithmischen Kalibrierung der ASICs über detaillierte Tests und Qualifikationen, die systematische Anwendung der Verfahren auf die gesamte Serie der E16-Module, die Unterstützung der Inbetriebnahme während der Bestrahlungstests bis hin zur anschließenden Analyse und experimentellen Überprüfung im Strahl.

Der erste Teil dieser Arbeit befasst sich mit der Optimierung des SMX-ASIC Kalibrierungsprozesses. Das Standard Kalibrierungsverfahren des “Analog-to-Digital Converter (ADC)” ist zwar hochpräzise, war jedoch durch die zeitaufwändige Grobsuchphase begrenzt, wodurch es für die Serienprüfung ineffizient wurde. Um diese Einschränkung

zu überwinden, wurde ein alternatives Kalibrierungsverfahren auf Basis eines “Successive Approximation Method (SAR)” Algorithmus entwickelt. Diese Methode ersetzt das umfassende Threshold Scanning der Standardtechnik durch eine iterative binäre Suche, wodurch eine schnelle Konvergenz auf den optimalen Diskriminatorschwellenwert ermöglicht wird. Das SAR-Verfahren erzielte eine Präzision, die der des Standardverfahrens entspricht, mit “Differential Non-Linearity (DNL)” und “Integral Non-Linearity (INL)” unter 0.4 LSB, während die Kalibrierungsdauer um etwa 30% reduziert wurde. Anschließend wurden die Algorithmusparameter, wie die Anzahl der Iterationen, die Suchbreite und der Feinbereich, weiter optimiert. Die Kombination aus zehn Iterationen, einer Suchbreite von 14 LSB und einem Feinbereich von 12 LSB erzielte eine zusätzliche Zeitersparnis von nahezu 60% im Vergleich zum Standardverfahren.

Eine weitere Verbesserung wurde durch die Implementierung eines Broadcast Kalibriermodus erzielt, der die gleichzeitige Kalibrierung mehrerer ASICs innerhalb eines Moduls ermöglicht. Dieses parallelisierte Schema führte zu einer zusätzlichen 50%igen Reduktion der Kalibrierungszeit im Vergleich zum optimierten SAR-Ansatz. Darüber hinaus wurden die Transferfunktionen sowohl der ADC- als auch der schnellen Timing-Diskriminatoren systematisch analysiert, wodurch eine lineare Beziehung zwischen Kalibrier-“Digital-to-Analog Converter (DAC)”-Einstellungen und effektiven Schwellenwerten bestätigt wurde. Die extrahierten Steigungen betragen 822 e/LSB und 718 e/LSB für die n- bzw. p-Seite des ADC-Pfads sowie 397 e/LSB und 361 e/LSB für die entsprechenden FAST-Pfade. Eine globale DAC-Einstellung für die Schwellen der Timing-Diskriminatoren wurde im Bereich zwischen 22 LSB und 26 LSB identifiziert, wodurch die Kalibrierung der Gesamtheit der Kanäle eines Moduls ermöglicht wurde, ausgenommen die sogenannten Z-Strips.

Als großangelegte Validierung wurden insgesamt 15 Module – darunter ein Prototyp, zehn Vorserien- und vier Ersatzmodule – zusammengebaut, getestet, charakterisiert und anschließend im E16-Detektorsystem installiert. Die Module (jeweils bestehend aus 8 ASICs pro Seite) wurden vollständig mit dem optimierten SAR-Algorithmus kalibriert. Die resultierenden Trim-Matrizen zeigten ein gleichmäßiges Korrekturverhalten, wobei nur ein kleiner Bruchteil der Diskriminatoren unkalibriert blieb ($\sim 0.03\%$ auf der n-Seite und $\sim 0,08\%$ auf der p-Seite). Auf der p-Seite waren kleinere Trim-Anpassungen bis zu 20 LSB erforderlich, um 95% der Kanäle zu kalibrieren, verglichen mit 28 LSB auf der n-Seite.

Darüber hinaus wurde die funktionale Untersuchung und Validierung der Module durchgeführt. Fünfzehn Module – darunter ein Prototyp, zehn Vorserien und vier Ersatzmodule wurden nach einem standardisierten vierstufigen Verfahren getestet: “Current-Voltage (IV)”-Sensorcharakterisierung, ASIC Kalibrierung, “Equivalent Noise Charge (ENC)” Evaluierung, Identifizierung defekter Kanäle sowie Datennahme mit einer radioaktiven $^{90}\text{Sr}/\text{Y}$ Quelle. Die IV-Messungen bestätigten einen stabilen Sensorbetrieb bis zu 150 V. Die Kalibrierungsdaten zeigten konsistente ADC Verstärkungen, Schwellenwerte und geringe Schwellenwertstreuungen über alle Module hinweg. Die gemessenen ENC-Werte lagen zwischen 700 e und 900 e, innerhalb von 20% der analytischen Erwartungen. Defekte Kanäle wurden identifiziert und durch Quellenmessungen verifiziert, wobei alle Module bis auf eines das Produktionsziel von maximal 1.5% (31) an defekten Kanälen erreichten.

Messungen mit der radioaktiven Quelle ermöglichten die Bewertung der Signalantwort für jeden Kanal und lieferten zusätzliche Bestätigungen für defekte Kanäle. Zeitkorrela-

tionsanalysen zwischen digitalen Signalen innerhalb von Clustern bestätigten die Zeitsynchronisation, wobei das Korrelationsmaximum um $\Delta t = 0$ ns zentriert war. Darüber hinaus zeigte eine Rekonstruktion der Treffer auf der Sensorfläche Übereinstimmung mit der physikalischen Positionierung der Quelle während der Messungen.

Das durch diese Studien gewonnene Wissen und die gesammelten Erfahrungen führten zur Definition eines umfassenden Modultest- und “Quality Assurance (QA)”-Protokolls. Dieses Verfahren ist nun als Teil des standardisierten QA-Workflows für die Serienproduktion der STS-Module implementiert. Das Protokoll wurde erfolgreich für die großangelegte CBM-STS-Produktionskampagne von nahezu 1000 Modulen etabliert und wurde bereits auf die Charakterisierung und Validierung von mehr als 550 Einheiten angewendet.

Der letzte Teil der Arbeit präsentiert die experimentelle Validierung der Detektorleistung unter Strahlbedingungen. Eine spezielle Strahlkampagne wurde an der “Photon Factory Advanced Ring (PF-AR)” Anlage in Japan mit einem 3 GeV/c Elektronenstrahl durchgeführt. Drei der zehn Module, aus denen die E16-STS Kammer besteht, wurden in unterschiedlichen geometrischen Konfigurationen getestet, um Zeitauflösung, Ladungssammlung, Clustergröße, Detektionseffizienz und räumliche Auflösung zu bestimmen. Die gemessene Zeitauflösung erreichte 3.2 ns für große Signalamplituden und etwa 5 ns für 2.7 fC-Signale und erfüllte damit die Erfordernisse der E16- und CBM-Experimente. Die gesammelten Ladungen betragen 22 ke auf der n-Seite und 20 ke auf der p-Seite, diese Werte liegen für die n- und p-Seite um bis zu 13% bzw. 22% unter der erwarteten Energieabgabe von “Minimum Ionizing Particle (MIP)” in 320 μm Silizium, was auf die hohen Schwellenwerte zurückzuführen ist, die verwendet wurden. Die entsprechenden Signal-to-Noise Ratio (SNR)-Werte betragen 27.8 ± 2.2 und 28.5 ± 1.5 für die n- bzw. p-Seite. Bei senkrechtem Einfall erreichte die Detektionseffizienz $89.85\% \pm 0.11\%$. Die räumliche Auflösung, bestimmt mittels eines “Principal Component Analysis (PCA)”-basierten Tracking-Algorithmus, ergab $\sigma_x = 118 \mu\text{m}$ und $\sigma_y = 136 \mu\text{m}$ für Einzelstreifencluster, was sich verbessert auf $\sigma_x = 20 \mu\text{m}$ und $\sigma_y = 33 \mu\text{m}$ für Mehrstreifencluster.

Während des Inbetriebnahmelaufs (Run-0e) gelang der erste erfolgreiche Experimentbetrieb von CBM-STS-Modulen in einem Magnetfeld. Die Zeitsynchronisation, die Tracking Residualen sowie die Energieverlustmessungen zeigten eine klare Pion-Proton Trennung bis zu 1 GeV/c. Dieses Ergebnis bestätigte nicht nur die Präzision der Spurrekonstruktion des Systems, sondern auch seine Fähigkeit zur Teilchenidentifikation.

Diese Ergebnisse stellen einen wichtigen Meilenstein in der Validierung der STS-Detektormodule dar, bestätigen deren Eignung als Trackingsystem für E16 und liefern einen entscheidenden Leistungsbenchmark für den gesamten CBM-STS-Detektor.

Chapter 1

Introduction

For centuries, one of the most profound questions in science has been: How did the universe come to be and how does it work?

Over the past century, the development of advanced experimental tools, such as particle accelerators on Earth, powerful telescopes in space and on the Earth, has allowed exploration of both the smallest and largest scales in nature. Modern physics now ranges distances from a fraction of a femtometer ($\sim 10^{-15}$ m) to the scale of the observable universe ($\sim 10^{26}$ m), unified by our understanding of the four fundamental forces: gravity, electromagnetism, and the strong and weak nuclear interactions. At the heart of this progress is the Standard Model of particle physics. It describes how fundamental particles, quarks and leptons, interact via the strong, weak, and electromagnetic forces, all within a framework consistent with quantum mechanics and Einstein's theory of special relativity. Among them, the strong interaction, described by Quantum Chromodynamics (QCD), plays a crucial role in governing the behavior of nuclear matter.

1.1 Brief introduction to QCD

The QCD is the established theory of the strong interaction. It is formulated as a non-Abelian gauge theory based on the local symmetry group $SU(3)_{color}$. Its fundamental degrees of freedom are: the quarks (up, down, charm, strange, top, bottom), which are fermions with half-integer spin carrying electric and color charge; and the gluons, which are the gauge bosons of the theory and also carries color charge. Together, quarks and gluons account for the structure of hadrons, such as protons, neutrons and mesons; the properties of atomic nuclei and the generation of most of the visible mass in the universe.

A particular feature of the QCD is the called **asymptotic freedom**. This implies the decreases of the effective strong coupling constant when increasing the momentum transfer. At very short distances or high energies, the strong interaction becomes weak, and the quarks and gluons behave nearly as free particles. This characteristic underlies the success of the perturbative QCD, which accurately describes phenomena such as the Deep Inelastic Scattering (DIS) and jet production in high-energy collisions. In contrast, at large distances corresponding to low momentum transfer, the strong coupling becomes large, and the quarks and gluons can not exist as free. Instead, they are permanently confined within a color neutral bound states, the hadrons. This property is called **confinement**, and explains why only hadrons are observed in experiments, and never individual quarks

or gluons.

In the limit of massless quarks, the QCD possesses an approximate **chiral symmetry**, which distinguishes between left- and right-handed quark field. However, in the vacuum this symmetry is spontaneously broken, implying that the quarks acquire constituent masses much larger than their small current bare masses, especially for up and down quarks. The spontaneous breaking leads to the emergence of light pseudoscalar mesons, such as pions, which are interpreted as pseudo-Goldstone bosons of the broken symmetry. At sufficient high temperatures or baryon densities, conditions expected in the early universe, or in the interiors of neutron stars, or in neutron stars mergers or in relativistic heavy-ion collisions, the chiral condensate ($q\bar{q}$) is predicted to decrease. This signals an approximate restoration of chiral symmetry, typically associated with the formation of the quark-gluon plasma or dense baryonic matter.

Possible experimental signatures of chiral symmetry restoration include modifications of hadron properties in hot and/or dense media. In particular, vector mesons (ρ , ω , ϕ) are expected to exhibit in-medium modifications, including mass shifts and a broadening of their spectral functions. These effects are investigated through the measurement of dilepton spectra (e^-e^+ or $\mu^-\mu^+$), which provide a clean probe, because they interact only electromagnetically and thus escape the strongly interacting medium without significant distortion.

1.2 QCD phase diagram

Nuclear matter does not exist in just one state and it can undergo phase transitions depending on temperature and baryon density. Figure 1.1 illustrates the QCD phase diagram in the plane of temperature (T) and baryon chemical potential (μ_B).

Cold nuclear matter, present in the region of low temperatures and baryon chemical potential, is found in ordinary nuclei and exists in hadronic phase. Normal nuclear matter, such as nuclei, protons, neutrons, mesons, can be found in this phase. However, under extreme conditions of high temperature and/or high density, nuclear matter experiences transitions to states characterized by the deconfinement of quarks and gluons.

At high temperatures and low baryon densities, the Quark-Gluon Plasma (QGP) emerges, where quarks and gluons are no longer confined within hadrons. It is believed that the universe existed in the QGP phase during the extremely early stages (approximately 10^{-6} to 10^{-5} s) after the Big-Bang [1]. Understanding this state is crucial for exploring the early universe and the fundamental properties of QCD, and it has been well studied both experimentally and theoretically [2, 3]. In this region a smooth crossover from partonic to hadronic matter is expected. Experiments at the RHIC¹ and the LHC² have provided compelling evidence of the formation of a deconfined state of quarks and gluons for matter close to $\mu_B = 0$ and $T > 156$ MeV.

In the region of moderate temperatures and large baryon densities, a first-order phase transition has been predicted from hadronic to partonic matter [4]. These predictions, together with the existence of an end point or critical point at high μ_B have been proposed for several QCD-based models. However, the locations of the phase boundary, the

¹Relativistic Heavy Ion Collider (RHIC)

²Large Hadron Collider (LHC)

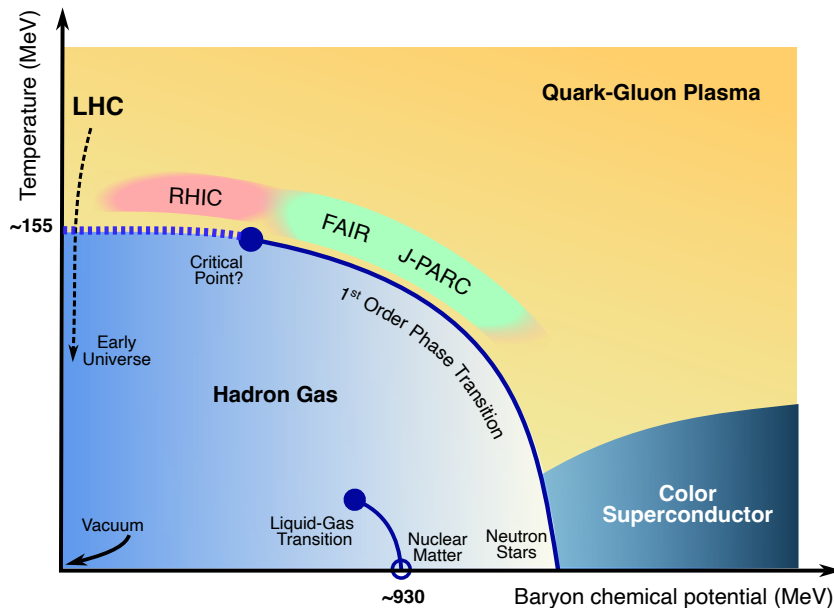


Figure 1.1: Schematic phase diagram for strongly-interacting matter in the baryon chemical potential (μ_B) and temperature (T) plane. The region of study for the different experiments is shown.

existence of a critical point and a first-order phase transition at higher μ_B remains to be confirmed experimentally. Their identification consist one of the major goals of heavy-ion collision experiments [5, 6].

At very high baryon net densities and low temperatures, the distance between nucleons becomes smaller, making these ones to crush into each other. At a sufficiently high density the matter should percolate, in the sense that their quark constituents are able to propagate throughout the system.

The deconfinement of nuclear matter with increasing density has many similarities to the way atomic gases, when compressed, become gases of itinerant electrons in a background of ions. This state of matter is possibly existing in the interior of the neutron stars. The phases of QCD are characterized by a variety of condensates in which a macroscopic number of particles (and antiparticles) are strongly correlated by the strong interaction. The emergence of condensates reduces the energy of the system, and in addition, condensates break symmetries in QCD, leading to states with lower symmetry than in the QCD Hamiltonian. The condensates, which depend on temperature and baryon density, play an important role in the structure of hadrons, as well as in neutron stars, since the condensation energies represent a large fraction of the energy density in a neutron star core.

1.3 High baryon density at low temperature

The largest known particle laboratory is cosmic space, where neutron stars serve as natural environments in which the phases of cold, dense, and strongly interacting nuclear matter are realized. Neutron stars are macroscopic objects ruled by the interplay of all fundamental forces in nature. Thereby, its internal structure is dominated by the strong

interaction, which counter balance the gravitational attraction. Typical masses are about 1.4 solar masses, while the radii are in the range of 10 to 14 km [7]. The density can reach values between 5 to 10 times nuclear saturation density ($\rho_{sat} \approx 0.16$ nucleons/fm³) and temperatures of 1 MeV. An exception occurs when a neutron star births in supernovae, where temperatures can reach tens of MeV, and during final gravitational mergers, where hot and dense matter may be produced with temperatures approaching 10² MeV [8].

A major breakthrough in the study of neutron stars came in August 2017, when the LIGO-Virgo Scientific Collaboration reported the first detection of gravitational waves (GWs) from a binary neutron star (BNS) coalescence, designated GW170817 [9]. In addition to the GW signal, which lasted approximately 100 s, multiple telescopes detected coincident electromagnetic emissions across a wide range of wavelengths, marked the beginning of GW multimessenger astronomy. The GW170817 event was the result of two neutrons stars colliding in a galaxy 130 million light-years from Earth. The combined LIGO-Virgo observations greatly improved the localization of the sources of the detected GWs. The collision also produced two notable observable phenomena: a short burst of X-rays and a transient optical near infrared powered by the synthesis of heavy elements via rapid neutron capture (r-process) [10]. One of the most important implications of GW170817 is the possibility of constraining the neutron star Equation of State (EoS) through the measurement of the tidal deformability of the binary components [11].

1.4 Heavy-ion collisions

While neutron stars offer a unique window into the cold and dense regime of QCD matter [12, 13], recreating such extreme densities in the laboratory is challenging. Instead, the access to other regions of the QCD phase diagram, in particular at high temperatures, is achieved through heavy-ion collisions at relativistic energies. These collisions momentarily generate extreme states of strongly interacting matter, enabling the investigation of its properties under controlled conditions.

In order to search for features such as the predicted first-order phase transition, the chiral phase transition, and the possible critical endpoint, it is necessary to reach moderate T and high μ_B that are experimentally accessible. High-energy heavy-ion collision facilities worldwide have been at the forefront of this effort. The RHIC at Brookhaven National Laboratory and LHC at the European Organization for Nuclear Research (CERN) have conducted extensive programs to investigate the QGP in the regime of low μ_B and high T [14, 15], where matter contains nearly equal numbers of particles and antiparticles [16]. Results from these collaborations provide evidence that partonic degrees of freedom dominate in the early stages of the fireball evolution.

Many experimental observables sensitive to the properties of dense nuclear matter require extremely high statistics, such as the flow of selected particle species, higher moments of event-by-event multiplicity distributions of conserved quantities, yields of multi-strange hyperons, and dilepton production. Consequently, one of the key requirements for future experiments is a high-rate capability, enabling these observables to be measured with high precision. Figure 1.2 shows the interaction rates of existing and planned heavy-ion experiments as a function of center-of-mass energy [17].

The QCD phase diagram at large μ_B has been explored through several heavy-ion experiments. However, the limitations of detector technology available at the time restricted

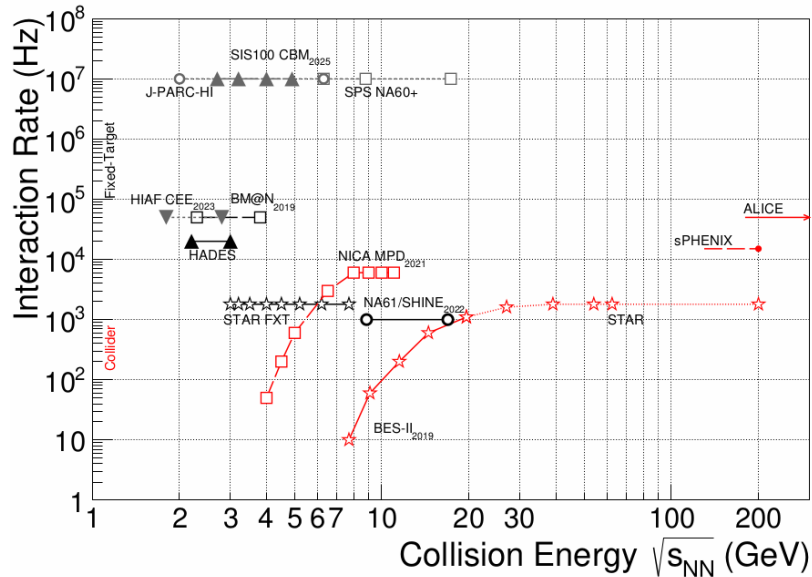


Figure 1.2: Comparison of the interaction rates of existing and planned heavy-ion experiments as a function of the center-of-mass energy [17]. Red markers represent collider mode, while black and gray indicate fixed-target mode. The solid curve corresponds to running facilities/experiments, the long-dashed line represents approved projects, and the short-dashed line indicates those in a conceptual design stage.

these measurements primarily to abundantly produced hadrons and di-electron spectra, often with limited statistics.

At the CERN-SPS³, the NA61/SHINE⁴ experiment continues the search for a first-order phase transition by measuring hadrons produced in collisions of light and medium heavy-ion beams. After a major upgrade during CERN LS2 its reaction rate has increased up to 1 kHz. At the SIS18⁵, the HADES⁶ experiment studies hadrons and electron pairs in heavy-ion collisions at rates of up to 20 kHz. At RHIC, the STAR⁷ collaboration has carried out a beam energy scan (BES-I and BES-II) down to $\sqrt{s_{NN}} = 3.3$ GeV by adapting the collider geometry to a fixed-target configuration. The reaction rates in STAR are limited to 800 Hz for $\sqrt{s_{NN}} > 20$ GeV due to the Time Projection Chamber (TPC) readout speed. At the Joint Institute for Nuclear Research (JINR) in Dubna, a Nuclotron-based Ion Collider fAcility (NICA) is planned with the goal to search for the coexistence phase of nuclear matter [18] at energies up to $\sqrt{s_{NN}} = 11$ GeV. Due to limitations in luminosity and detector capabilities, these experiments are restricted to study bulk observables, which are primarily sensitive to the late and dilute stages of the collision, when most particles freeze-out.

In contrast, the future research program of the Compressed Baryonic Matter (CBM) experiment [19] at the Facility for Antiproton and Ion Research (FAIR) in Darmstadt

³Super Proton Synchrotron (SPS)

⁴North Area 61 (NA61)

⁵Schwerionensynchrotron (SIS)

⁶High Acceptance Di-electron Spectrometer (HADES)

⁷Solenoidal Tracker at RHIC (STAR)

[20], is dedicated to measuring diagnostic probes that are sensitive to the early and dense phase of the fireball evolution with unprecedented rates.

1.5 FAIR facility

The international FAIR facility will provide unique research opportunities in the fields of nuclear, atomic and plasma physics, and applications in the fields of materials research and radiation biophysics, including novel medical treatments and space science [21]. The core of the FAIR facilities accelerator is the heavy-ion synchrotron SIS100, which has a circumference of 1084 m and a magnetic rigidity of 100 T m. The existing accelerators at GSI Helmholtzzentrum für Schwerionenforschung (GSI), namely UNiversal Linear ACcelerator (UNILAC) and SIS18, will serve as the first acceleration stage of SIS100. The SIS100 will provide proton beams with energies up to 30 GeV and Au ions beams up to 11 AGeV. The beam intensities will be 10^9 ions per second. Using a 1% target interaction probability, will provide 10^7 interactions per second.

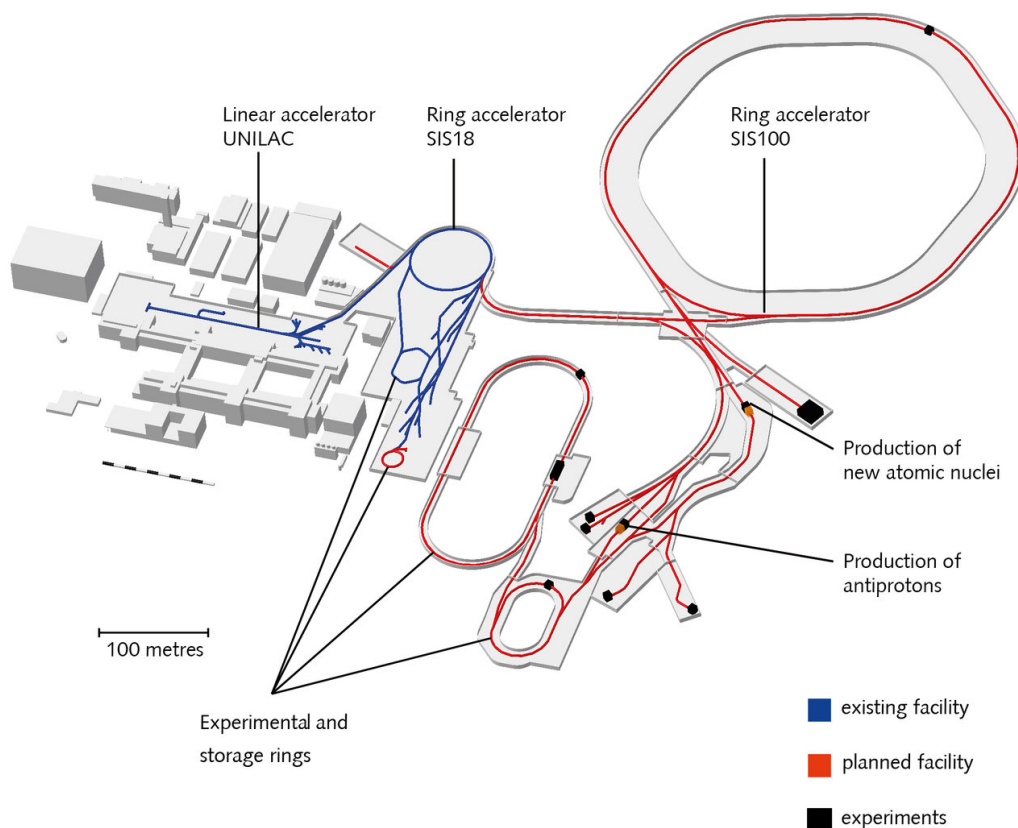


Figure 1.3: Schematic for the FAIR facility. The blue lines represent existing GSI facilities, while the red lines represent the ones in plan, also shown is the superconducting SIS100 accelerator that will provide ion beams for the CBM experiment [20].

FAIR will possess the unique capability to provide particle beams of all chemical elements and their ions, as well as antiprotons. Its research program is organized into four major experimental collaborations: Atomic, Plasma Physics and Applications (APPA),

CBM, NUClear STructure, Astrophysics and Reactions (NuSTAR), and antiProton ANnihilation at DArmstadt (PANDA). The APPA collaboration will perform tests of fundamental interactions and symmetries, as well as explore applications of nuclear physics in medicine. Its broad scientific scope encompasses atomic physics, plasma research, medical applications, and space radiation physics. The NuSTAR program will investigate the nuclear structure and processes relevant to nuclear astrophysics. PANDA will focus on antimatter studies, the interplay of weak and strong forces, exotic states of matter, and the structure of hadrons.

1.5.1 CBM physics program

The CBM experiment is a detector system under construction to be operated at FAIR, featuring one of the most ambitious research programs in contemporary heavy-ion physics. Its primary goal is to explore the QCD phase diagram at high baryon densities and moderate temperatures, employing high-energy nucleus-nucleus collisions. These studies, complementary to other heavy-ion experiments, have the intention of achieving a better understanding of the QCD EoS at densities similar to those present in the core of a neutron star. The program seeks evidence for a possible phase transition from hadronic to partonic matter, the existence of a critical point in the QCD phase diagram and signature of chiral symmetry restoration [22, 23].

The experiment will study collisions of heavy-ion and proton beams with fixed heavy element targets, at beam energies between 2 and 11 AGeV (up to 14 AGeV for light nuclei and 29 GeV for protons) [19]. In this energy range, heavy-ion collisions are particularly convenient to investigate the properties of dense baryonic matter. As illustrated in Figure 1.4, which shows the time-ending trajectories from several dynamical models at the excitation energy density in the fireball center as a function of net baryon density for central Au+Au collisions at beam energies of 5 and 10 AGeV [12, 24], as predicted by various transport models and a hydrodynamic calculation. According to these, at eight times saturation density the nucleons overlap, and theoretical models predict a transition to a mixed phase of baryons and quarks.

The following subsections briefly describe key observables that are particularly relevant for a comprehensive study of the QCD phase diagram.

Event by event fluctuations

Near the deconfinement phase transition, critical density fluctuations can cause non-statistical, event-by-event fluctuations of conserved quantities such as baryon number, strangeness, and electric charge. These fluctuations are linked to thermodynamic susceptibilities and can reveal properties of matter created in high-energy collisions [25]. Lattice QCD predicts that higher moments of these distributions are particularly sensitive to the phase structure, with a critical point expected to cause a non-monotonic dependence of these moments. While other experiments have searched for this effect, no higher-order event-by-event fluctuations have been measured at FAIR energies. CBM will perform precise measurements of these fluctuations at various beam energies in the high net-baryon density range $\sqrt{s_{NN}} = 2.7 - 4.9$ GeV, corresponding to $\mu_B \approx 800 - 500$ MeV [23].

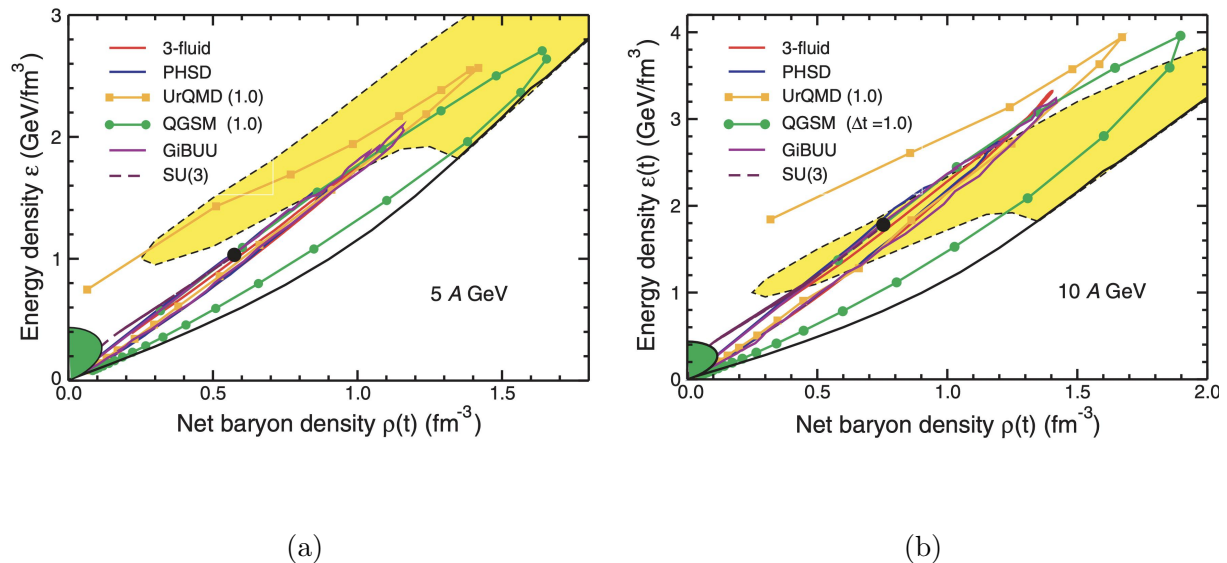


Figure 1.4: Excitation energy density (ε^*) as a function of the net baryon density $\rho(t)$ for central Au+Au collisions at beam energies of (a) 5 A GeV and (b) 10 A GeV, for different transport models.

Collective flow

The collective motion of hadrons from heavy-ion collisions reveals key aspects of the collision dynamics. The isotropic radial flow characterizes the system at kinetic freeze-out, when elastic interactions cease. Anisotropic flow arises from pressure gradients generated by initial density anisotropies, providing sensitivity to the EoS of dense nuclear matter [26].

It is quantified through the azimuthal distribution of the emitted particles in the plane transverse to the beam axis:

$$\frac{dN}{d\varphi} \propto 1 + 2 \sum_{n=1}^{\infty} v_n \cos[n(\varphi - \Psi_n)] \quad (1.1)$$

Where v_n are the flow coefficients [3]. The direct flow (v_1) is sensitive to the phase transition and EoS softening, while elliptic flow (v_2) reflects the early stage degrees of freedom. The flow of strange hadrons and antibaryons, influenced by their in-medium potentials, also probes chiral symmetry restoration.

CBM will measure flow for various hadron species at FAIR energies, including multi-strange hyperons and dileptons, providing critical input on the QCD matter EoS [23].

Strangeness and hypernuclei

High-precision measurements of yields, momentum, and angular distributions of multi-strange hyperons in nucleus-nucleus collisions at FAIR energies will allow to study the equilibrium state of the fireball. Strangeness production is a key observable potentially

linked to the deconfinement phase transition, and its systematic study as a function of collision energy is a promising approach [27]. In hadronic transport models without a partonic phase, multi-strange hyperons are produced through sequential collisions involving kaons (K) and lambdas (Λ), making them sensitive to the density of the fireball. Excited hyperon states can also be identified.

Replacing an up or down quark with a strange quark in a nucleon bound in a nucleus, forms hypernucleus, adding strangeness as a third axis to the nuclear chart. Measuring single and double hypernuclei enables studies of hyperon-nucleon and hyperon-hyperon interactions, important key for understanding neutron star structure [7]. Thermal model predictions place the peak of the hypernuclei excitation function at FAIR energies, due to increased light nuclei production with decreasing energies and increased hyperon production with increasing energies. Double-hypernuclei in heavy-ion collisions are produced via coalescence of Λ hyperons with nucleons or light nuclei in the final reaction stage [23]. CBM has unique opportunities for these measurements, as it contains excellent tracking with PID capabilities at unprecedented rates.

Open and hidden charm

The yields of charmed hadrons provide sensitive probes to the state in the fireball at early state, as $c\bar{c}$ pairs can only be produced in hard processes at the initial stage of nucleus-nucleus collisions. Their hadronization into D mesons, charmed baryons, or charmonium depends of the interactions with the medium.

At FAIR energies, hidden and open charm can be studied in proton-induced reactions near production threshold (up to 29 GeV) using various targets. Open charm measurements help clarify production mechanisms, properties at saturation density, and propagation in cold nuclear matter. In a deconfined medium, charmonium states are expected to dissociate due to color screening, been the first predicted signature for the QGP [28]. The CBM experiment will use very high interaction rates to investigate J/ψ production [23].

Lepton pairs

One of the main goals of heavy-ion collision experiments is to search for signatures of chiral symmetry restoration, which is expected at very high baryon densities and/or temperatures. A key observable is the modification of hadron properties in hot and dense matter. The degeneration of the spectral functions of chiral partners, such as the ρ - and a_1 -mesons, are signals of the restoration of the chiral symmetry. While the a_1 -meson is difficult to measure, the in-medium spectral function of the ρ -meson can be accessed via its decay into lepton pairs.

Short-lived vector mesons decay into dilepton pairs ($\rho, \phi, \omega \rightarrow e^+e^-, \mu^+\mu^-$), which interact only electromagnetically with the surrounding medium. As dileptons escape without further interaction, they provide a direct probe of the thermodynamical state of the medium at the time of their production.

The CBM experiment aims to perform multi-differential measurements of lepton pairs over the full invariant mass range emitted from a hot and dense fireball [23], in the electron and muon channel.

1.6 J-PARC E16 experiment

The E16 experiment aims to study the partial restoration of chiral symmetry in dense matter by examining changes in the properties of vector mesons. In particular, to investigate the in-medium spectral functions of vector mesons as a potential signature of chiral symmetry restoration. Specifically, it measures the dependence of the mass distribution of vector mesons on the relativistic factor $\beta\gamma$ through their decays into electron-positron pairs:

$$\rho, \omega, \phi \rightarrow e^+ + e^-$$

Electron pairs are ideal probes because they are minimally affected by final state interactions. The measurements will be performed in p+A collisions using a proton beam with an energy of 30 GeV.

1.6.1 Physics of the E16 experiment

Chiral symmetry is an intrinsic symmetry of the QCD Lagrangian in the limit of massless quarks, allowing left- and right-handed quarks to transform independently. Figure 1.5 illustrates the behavior of the quark condensate $\langle \bar{q}q \rangle_{T,\rho}$, which serves as the order parameter of the chiral symmetry, as a function of temperature (T) and baryon density (ρ). In the QCD vacuum, at $T = 0$ and $\rho = 0$, the condensate takes on a large value, signifying spontaneous breaking of the chiral symmetry. This breaking is responsible for generating large dynamical masses of order 300 MeV for light quarks, far above their small bare masses, and is the fundamental mechanism behind the generation of hadron mass.

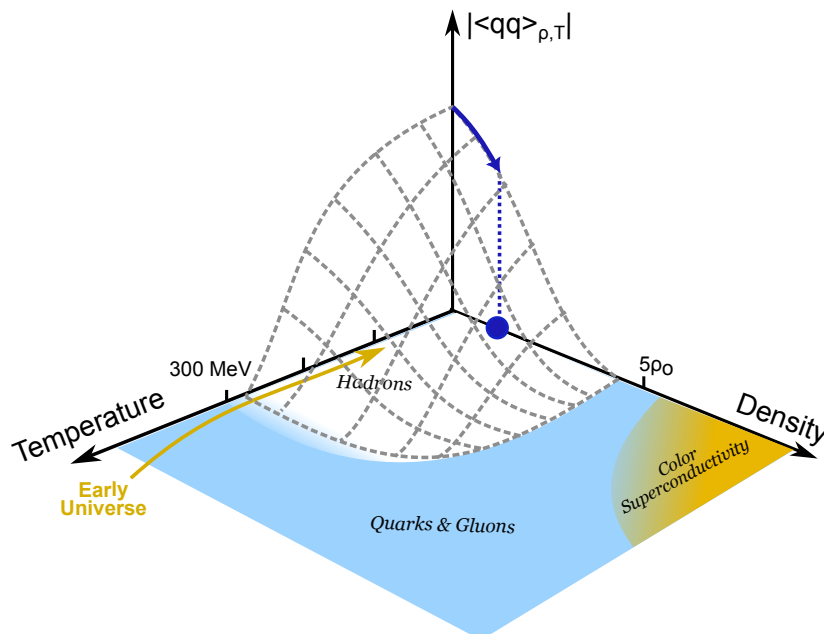


Figure 1.5: Schematic illustration of the condensate $\langle \bar{q}q \rangle$ as a function of density (ρ) and temperature (T). The density is given in units of nuclear matter density $\rho_0 \approx 0.16 \text{ fm}^{-3}$. Picture adapted from the lectures: “Strong interaction in the nuclear mediums: new trends” [29]

With increasing temperature, as realized in ultra-relativistic heavy-ion collisions where a hot and dense medium is created, the quark condensate decreases sharply near the critical temperature $T_c \sim 150 - 170$ MeV, signaling a phase transition-like behavior. This reduction indicates the partial restoration of chiral symmetry.

A similar reduction occurs at finite baryon density. At normal nuclear matter density $\rho_0 \approx 0.16 \text{ fm}^{-3}$, the quark condensate is already reduced by about 35%. At even higher densities, such as those expected in the interior of neutron stars or in compressed baryonic matter, the condensate decreases further and is predicted to approach zero at several times of ρ_0 , indicating partial restoration of chiral symmetry.

Different regions of the (T, ρ) plane correspond to different QCD phases. At low temperature and density, matter is in the hadronic phase where chiral symmetry is broken. At high temperature and/or density, matter transitions into new phases such as the QGP or, at extremely high density, possible color-superconducting phases. In the early universe, shortly after the Big Bang, QCD matter existed in the QGP state at high temperature but low density. In contrast, experiments such as Japan Proton Accelerator Research Complex (J-PARC) E16 probe the regime of high density and moderate temperature using p+A collisions, providing complementary access to chiral symmetry restoration.

The decrease of the quark condensate with temperature and density has direct physical consequences. As chiral symmetry is partially restored, the properties of hadrons embedded in the medium are modified: vector mesons such as ρ , ω , and ϕ may undergo mass shifts and broadening of their spectral functions. Experimentally confirming partial chiral symmetry restoration is essential to understand the dynamical generation of hadron masses and the structure of the QCD vacuum.

1.6.2 Previous results

In the past, other experiments have already investigated medium modifications of vector mesons. In hot and dense nuclear matter created in heavy-ion collisions, several experiments such as NA45/CERES and NA60 at the SPS, as well as PHENIX and STAR at RHIC, have reported strong modifications of the low-mass dilepton spectra, which can be interpreted as a broadening of the ρ meson spectral function. Complementary measurements in cold nuclear matter using p+A collisions have also been performed. The CEBAF Large Acceptance Spectrometer (CLAS) experiment at Jefferson Lab studied vector meson in various nuclear targets and reported hints of broadening effects, although with large systematic uncertainties which prevent conclusive evidence. In contrast, the High Energy Accelerator Research Organization (KEK)-PS E325 experiment observed an excess on the low-mass side of the ϕ meson peak in p+A reactions at 12 GeV, see Figure 1.6, suggesting a possible mass reduction of vector mesons inside nuclei.

While these measurements clearly indicate that vector mesons undergo modifications in a nuclear environment, the interpretation has remained inconclusive due to limited statistics and uncertainties in background subtraction. Therefore, a new generation of experiments with significantly higher precision and interaction rates, such as J-PARC E16, will provide definitive insight into the nature of in-medium modifications and their relation to chiral symmetry restoration.

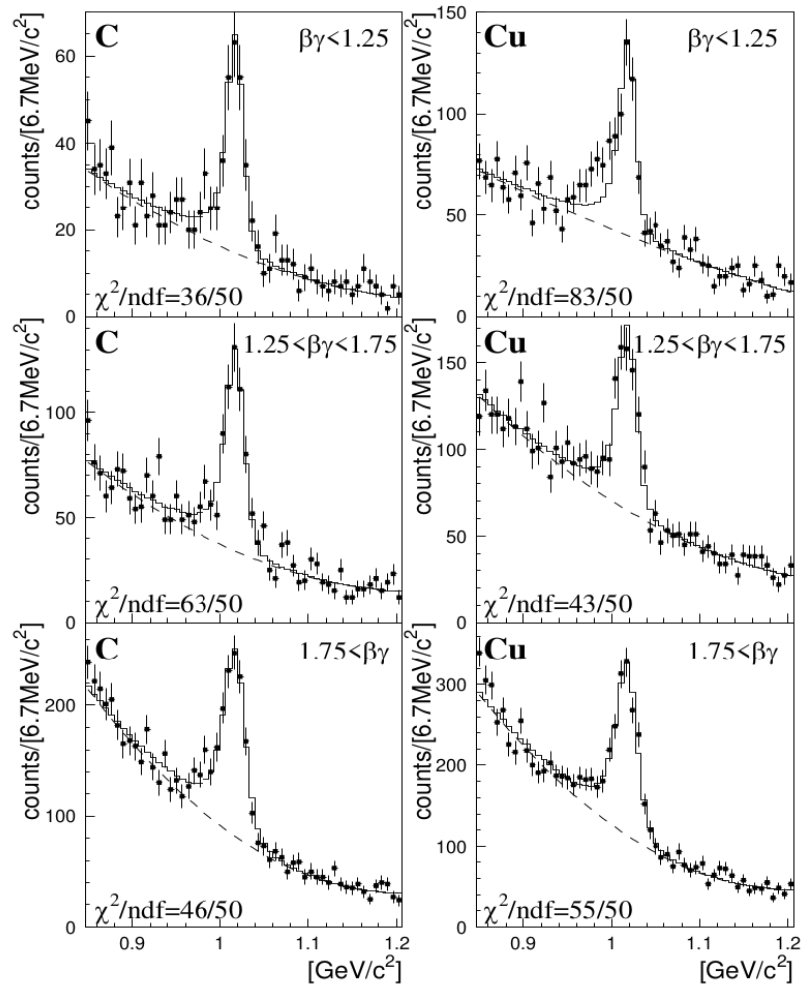


Figure 1.6: Invariant mass distribution of e^+e^- pairs near the ϕ meson mass [30]. The solid lines represent the fitting results, which include the $\phi \rightarrow e^+e^-$ peak and the combinatorial background. The left column shows the results for the C target, while the right column corresponds to the Cu target. Each one of them is divided into three regions based on the value of $\beta\gamma$ factor.

1.6.3 Upgrade from E325 to E16 experiment

Although many experiments have been carried out to study the mass distribution of vector mesons in nuclear matter, no clear conclusions have been reached so far. The main limitations of previous measurements were insufficient statistical precision and limited mass resolution. For example, in the KEK-PS E325 experiment, the interpretation of possible mass reductions of vector mesons depended strongly on theoretical models due to these experimental constraints.

To overcome these challenges, the J-PARC E16 experiment has been designed as a next-generation successor to E325. It aims to investigate the properties of the vector meson in nuclear matter by measuring e^+e^- decays from p+A reactions. However, E16 experimental setup introduces significant improvements:

- $10 \times$ higher beam intensity reaching (1×10^{10} protons/spill (2 sec));
- $5 \times$ larger spectrometer acceptance;
- $2 \times$ higher production cross section for ϕ mesons;
- an improved mass resolution of about $5 \text{ MeV}/c^2$.

Together, these improvements provide about 100 times higher statistical precision and roughly a factor of two better mass resolution compared to the E325 experiment. This enhanced capability will allow E16 to perform a decisive study of in-medium modifications of vector mesons with far greater reliability and reduced dependence on model assumptions.

1.6.4 Collaboration with J-PARC E16 experiment

The CBM experiment at FAIR and E16 experiment at J-PARC share multiple synergies. The similar physics goals along with comparable detector challenges, such as very high interaction rates up to 10 MHz, tracker systems with $25 \mu\text{m}$ position resolution, and around 5 ns time resolution, help to build collaborative bridges between the two experiments.

As part of this collaboration, the first tracking layer of the E16 experiment are equipped with detector modules from the Silicon Tracking System (STS) of the CBM experiment. In return, the STS modules are tested in a realistic scenario, including the presence of a magnetic field and high intensity beams, two conditions that are not feasible in the current status of prototype tests with CBM.

1.7 Scope of this work

This thesis brings together and highlights the synergies between the two Silicon Trackers of the CBM and E16 experiments. It was made possible through the collaboration and knowledge exchange between both projects. The work focuses on the development and characterization of detector modules built for the E16 experiment, during which a new approach to calibrate the front-end electronics was conceived. From this effort, a dedicated testing procedure was established and later adopted as the standard protocol for the production of CBM-STs modules. The thesis concludes with results from a beam test campaign carried out with the E16 STS setup at KEK, which served to validate the performance of the system and the methods developed throughout this work.

The thesis is structured in five chapters, the current one has an introductory character, in which some fundamental concepts of the heavy-ion collisions are summarized, also the physics program and main observables of CBM and E16 experiments are introduced. The second chapter details the description of the detectors, in particular STS in CBM and E16 experiments, its requirements and components design. The remaining chapters are organized as follows:

- Chapter 3 introduces the STS front-end electronics. Also, the implementation of a new method to calibrate the measuring circuits is performed, including studies related with the transfer functions of the measuring circuits.

- Chapter 4 focuses on the characterization of STS pre-series modules produced for the E16 experiment, where as result a testing protocol was developed. Parameters such as: noise and broken channels were evaluated, also the calibration values and the sensor voltage-current curve characteristic are presented.
- Chapter 5 reports results during the test experiment conducted using the electron beam at KEK. Principally focuses in the evaluation of time and spatial resolution, detection and charge collection efficiency, as well the signal-to-noise ratio.

Finally, a Chapter 6 provides a summary of the fundamental results presented and discussed in this thesis. Including also, an outlook of the work.

Chapter 2

CBM and E16 experimental setups

The CBM and E16 experiments have a wide and challenging physics program, where many of the key observables are rare diagnostic probes that carry crucial information about the dense stage of the fireball evolution [12].

The two experiments differ mainly in their detector concept and experimental environments. The CBM experiment is a large-scale, multipurpose detector system designed to investigate the properties of strongly interacting matter at high net baryon densities. In contrast, the J-PARC E16 experiment is a dedicated spectrometer specifically optimized for studying in-medium modifications of vector mesons via dilepton (e^+e^-) production. While CBM is capable of performing a wide range of measurements using various detector subsystems and heavy-ion beams, E16 focuses primarily high resolution tracking and precise di-electron identification using high intensity proton beams. To collect sufficient statistics, both experiments are designed to operate at extremely high interaction rates of up to 10 MHz, demanding very fast and radiation hard detectors.

In common, both experiments rely on precision tracking of charged particles as a central requirement. Both employ a silicon tracker based on the design of the CBM experiment as the core tracking detector, which provides high spatial resolution, fast response, radiation hardness, and the capability to reconstruct tracks and momenta in a high-rate environment.

The STS serves as a common technological backbone for both the CBM and E16 experiments. Understanding its performance, optimizing its operation, and exploring its potential applications are essential for achieving the physics objectives of both collaborations. This thesis contributes to the development, testing, and characterization of the STS, with the aim of ensuring its complete readiness for operation in future high-rate QCD experiments.

2.1 The CBM experiment at FAIR

CBM is a fixed-target experiment that will implement a free-streaming readout and a high performance computing farm for online event selection. The CBM detector has been designed capable to detect hadrons, electrons, and muons in p+p, p+A and A+A collisions, with an angular acceptance between 2.5° and 25° to cover the mid and forward rapidity hemisphere. Figure 2.1 shows the different subsystems that comprise the CBM experiment.

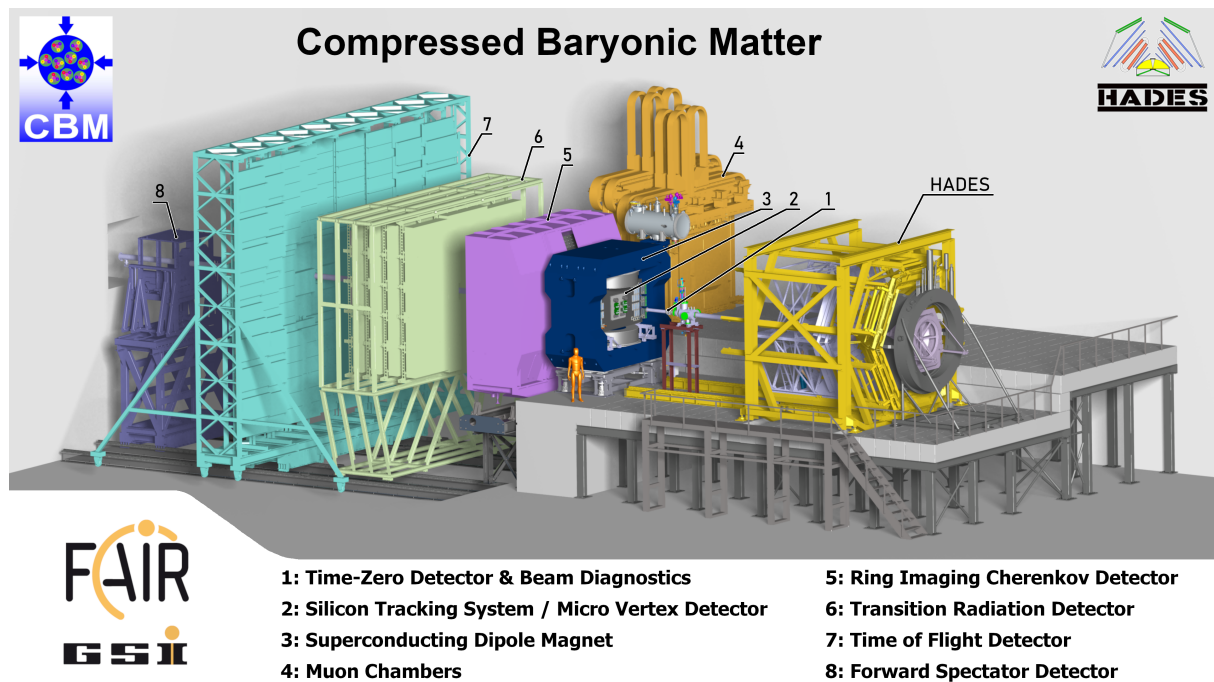


Figure 2.1: The CBM experimental setup at FAIR. The different detector subsystems that comprise the setup are marked [20]. In addition the HADES is shown upstream of the CBM detector experiment.

Superconducting dipole magnet: is a key component for determining the momenta of charged particles in the CBM experiment. Its function is to bend the trajectories of particles emerging from high-energy collisions. The curvature of a particle's path is inversely proportional to its momentum: particles with higher momentum are deflected less by the magnetic field, allowing momentum to be measured by tracking their trajectories. To minimize operational costs, the magnet is designed to be superconducting. It will generate a vertical magnetic field of 1 Tm from the interaction point to approximately 1 m downstream of the target [31].

Micro Vertex Detector (MVD): is also a tracking detector, complementary to STS. In addition, its function is to distinguish between primary and displaced vertices like those arising from decays of charmed hadrons, example D mesons or Λ_c baryons. To perform its task, it requires a high resolution along the position vector of approximately 70 μm , which turns to 5 μm spatial resolution and very low material budget. The MVD is placed in vacuum and directly behind the target inside the dipole magnet, allowing for analysis the reconstruction of low momentum tracks that also helps to reject background for di-electron [32]. The detector will use CMOS MAPS¹ with a pixel size of a few dozen of micrometers.

¹Monolithic Active Pixel Sensors (MAPS)

Silicon Tracking System (STS): is the main tracking detector of the CBM setup. Its task is to track charged particles and determine their momentum. More details of STS are presented in section 2.3.3.

Ring Imaging Cherenkov detector (RICH): is designed for particle identification via Cherenkov radiation [33]. It will allow to distinguish electrons from pions up to 8 GeV/c with a pion suppression factor above 300 and an electron identification efficiency above 85%. Its location will be 1.6 m downstream of the target. Its configuration consists of a CO₂ gas radiator, two arrays of mirrors constructed with a reflective Al+MgF₂ coating to direct the light to the photon detectors, and photo detector planes based on MAPMTs², providing high granularity, high geometrical acceptance, and high detection photon efficiency also near to the UV region.

Muon Chambers System (MUCH): will allow identifying muon pairs resulting from the decay of vector mesons like ρ , ω , ϕ and J/ψ [34]. The detector configuration consists of 5 hadrons absorber layers and tracking detector planes between them. The absorber layers comprise of a thick carbon plate and four iron plates of different thickness, while the tracking planes are based on GEM³ and RPC⁴ detectors.

Transition Radiation Detector (TRD): will help to identify electrons with momenta above 1 GeV/c and complement the electron identification capabilities of RICH for momenta above 5 GeV/c. The particle identification will be possible based on the transition radiation produced when an ultra-relativistic charged particle traverses the boundary of a medium with different dielectric constant. The detector will be located 5 m from the target and consists in a system composed of one station with four layers. The radiation will be detected employing MWPC⁵, filled with a mixture of Xe/CO₂ gases.

Time of Flight (TOF): is dedicated to identify charged hadrons like pions, kaons and protons. The identification will be possible based on time of flight measurements of the different particles, as particles with the same momentum but different masses traveled at different speed. The area covered by TOF will be 120 m², and it is built using MRPC⁶ detectors, providing high efficiency and excellent time resolution of 60 ps. The detector will be positioned at 6 m downstream from the target [35].

Forward Spectator Detector (FSD): is a dedicated subsystem designed to study the collective behaviour of nuclear matter, in particular anisotropic flow. It builds on the earlier development of the Projectile Spectator Detector (PSD) and operates at forward rapidity, where it measures spectator nucleons and fragments emerging from the remnants of the colliding nuclei. Its main function is to provide precise event-plane reconstruction and collision-centralty determination at interaction rates of up to 10 MHz. The detector is currently designed as a scintillator hodoscope composed of charge-sensitive tiles, with

²Multi-Anode Photo-Multipliers (MAPMTs)

³Gas Electron Multiplier (GEM)

⁴Resistive Plate Chambers (RPC)

⁵Multi-Wire Proportional Chamber (MWPC)

⁶Multi-gap Resistive Plate Chambers (MRPC)

segmentation optimized to match the particle flux-featuring finer granularity of $4 \times 4 \text{ cm}^2$ near the beam pipe and coarser segmentation towards larger radii. Simulation studies indicate that the FSD could achieve an event-plane resolution of about 70% for Au+Au collisions at 11 AGeV [36].

First Level Event Selector (FLES): is a dedicated computing farm for reconstructing and selecting online events, including short- and long-lived particles. For this purposes, CBM FLES will consists of nodes equipped with an important number of Central Processing Unit (CPU) and Graphics Processing Unit (GPU) [37]. They will perform online event selection based on fast and fully parallelized algorithms for reconstruction of hits, tracks and short-lived particles.

There are two operation modes that CBM detector system will use, one that include all the subsystems except MUCH detector, optimized for electron identification; and another that replace RICH with MUCH, dedicated to muon detection.

2.2 The E16 experiment at J-PARC

The E16 experiment consists in a fixed-target forward spectrometer. It comprises four types of detectors, divided in two main roles: momentum measurement and electron identification. The group tracking detectors are based on silicon strips and gas electron multiplier technology, while the particle identification are based on Cherenkov radiation and calorimetry. Figure 2.2 shows a top view of the E16 setup with its different detector subsystems. A set of detectors is referred as “one module”, covering $\pm 15^\circ$ vertically and 30° horizontally. For later runs, additional modules will be installed, making possible to cover $\pm 45^\circ$ vertically.

Magnet: the detector will use the so-called “FM magnet”, previously used by the KEK-PS E325 experiment. The magnet produces a central magnetic field of 1.77 T, and the yoke has 5.3 m wide, 4.9 m high, and 2.1 m deep, with a gap between the magnets of 400 mm [38].

STS: is the innermost tracking detector of E16 experiment. It is detailed in section 2.3.4.

GEM Tracker (GTR): features a layer structure composed by Mylar, a MESH, three GEMs, a readout foil, and an aluminum base frame [39]. All the components are mounted on square frames made of glass epoxy, except the aluminum frame. The chamber is filled with a mixed gas of ArCO₂ in a proportion 70 : 30. The readout foil strips are composed of X- and Y-strips orthogonally to each other achieving a position resolution of 100 μm , and the chip used is the APV25⁷. “One module” consists of three layers of GTR chambers with inner dimensions of 100 mm², 200 mm² and 300 mm², respectively.

⁷Developed by CMS and widely used in GEM detectors under the RD51 collaboration

Hadron Blind Detector (HBD): is a gas Cherenkov-type electron detector working in proximity-focus [40]. It is based on PHENIX⁸ design, and features CF_4 as radiator and amplification gas, GEMs as amplification component, and CsI photocathodes deposited on the GEM surface. Pions with a Cherenkov threshold of 4 GeV/c emits minimal Cherenkov light. This mechanism enable a pion rejection rate of 98% and an electron detection efficiency of 68%. The readout pads will be positioned 1400 mm from the center.

Lead Glass Calorimeter (LG): is an electromagnetic calorimeter for identifying di-electrons (e^+e^-) using the difference in the amount of light produced by electrons and pions in lead glass. The Cherenkov light produced is detected with a photomultiplier tube. The detector achieves 90% of electron detection efficiency and a pion rejection rate of 92% for momentum above 0.4 GeV/c [41].

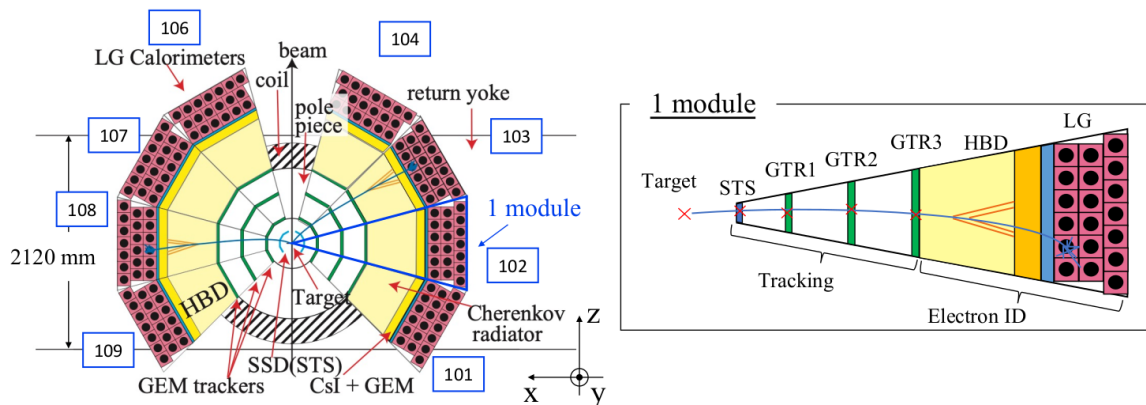


Figure 2.2: Schematic layout of the E16 experimental setup. On the left, a top view of the full spectrometer, showing the arrangement of the different subsystems. The beam direction and target position are indicated at the center. On the right, schematic view of a single detection module illustrating the sequence of detector components along the particle trajectory, from the target through the tracking detectors (STS, GTR1, GTR2 and GTR3) to the electron identification detectors (HBD and LG).

2.3 Silicon Tracking Detectors

In the world of high energy physics, trackers and vertex detectors based on silicon technology are very common, Figure 2.3. Among these, the most common types are silicon strip detectors and pixel detectors, which, in their various configurations, enable precise position measurements in both the X- and Y-coordinates. Examples include Single-Sided Silicon Strip Detector (SSSD) and Double-Sided Silicon Strip Detector (DSSD), as well as two-dimensional arrays of pixel sensors.

⁸Pionering High Energy Nuclear Interaction eXperiment (PHENIX)

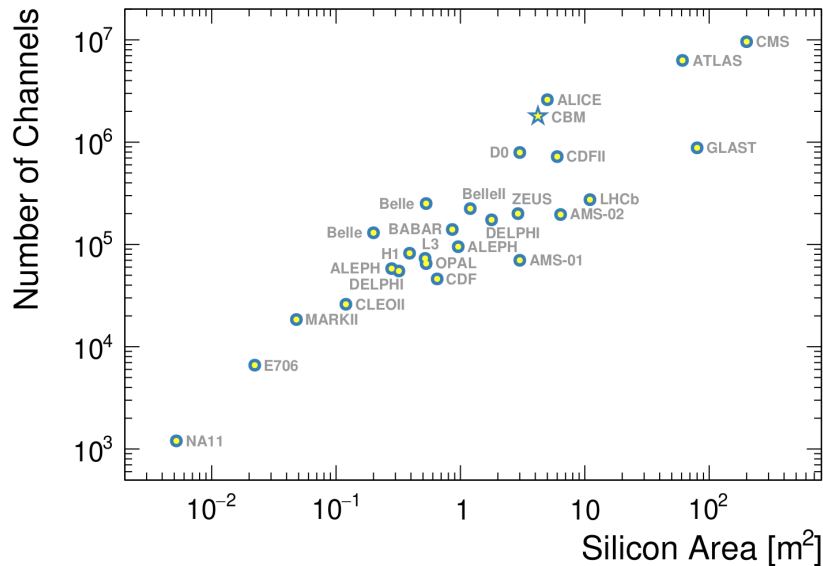


Figure 2.3: Illustration of the use of silicon technology in the different experiments. The number of readout channels versus the silicon area is shown. The figure is taken from the PhD thesis of I. Panasenکو [42].

2.3.1 Working principles of silicon detectors

Semiconductor detectors operate on the same basic principle as ionization chambers. Charged particles traversing the sensitive volume deposit energy, leading to the creation of electron-hole pairs. By applying an electric field across the semiconductor, these charge carriers are separated and collected at the electrodes, generating a measurable electrical signal proportional to the deposited energy.

To understand the operation of silicon microstrip detectors in detail, it is necessary to first review the fundamental principles of semiconductor materials. This includes a brief explanation of n- and p-type doping, the p-n junction, and finally the structure and function of silicon strip detectors.

P/N-type semiconductors

Silicon forms a crystalline structure with a regular atomic arrangement, and the energy states available to its electrons are organized into nearly continuous ranges known as energy bands. In this structure, the “valence band” is typically filled with electrons, while the higher-energy “conduction band” remains mostly empty. The region between these two bands, where no electron states exist, is referred to as the “forbidden band” or “bandgap”.

For silicon, the bandgap energy is approximately 1.12 eV at room temperature, which is much larger than the typical thermal energy of an electron ($k_B T \approx 0.025$ eV). Consequently, only a very small fraction of electrons can be thermally excited into the conduction band, resulting in a low electrical conductivity under normal conditions [43].

The electrical properties of silicon are determined by impurities in the crystal. The process of adding impurities is known as “doping”. For example, silicon has four valence electrons, when pentavalent elements such as phosphorus (P), arsenic (As), or antimony

(Sb) are added, one additional electron remains free after forming covalent bonds with neighboring silicon atoms. This loosely bound electron can easily move into the conduction band and participate in electrical conduction, resulting in an “n-type” semiconductor. In contrast, doping silicon with trivalent elements such as boron (B), aluminum (Al), or gallium (Ga) creates an electron vacancy or “holes”, that act as positive charge carriers. Such material is referred to as a “p-type” semiconductor.

The P-N semiconductor junction

The n- and p-type semiconductors are typically used together to form a p-n junction. Because of the difference in the concentration of electrons and holes between the two materials, electrons diffuse towards the p-region and a similar diffusion occurs with holes towards the n-region. This process causes the p-type region becomes negatively charged, and the n-type region becomes positively charged. As a result, an internal electric field is generated across the junction, which gradually counteracts and eventually halts further diffusion of charge carriers. The region that remains depleted of mobile electrons and holes, containing only immobile ionized donor and acceptor atoms, is known as the “depletion region” or “depletion layer” [43].

From an energy band perspective, the formation of the p-n junction causes the Fermi levels of the two regions to align, which brings them closer to the conduction and valence bands. The resulting potential difference is denoted as “diffusion potential” (V_D), and it is typically about 0.6 – 0.7 V in silicon, see Figure 2.4a.

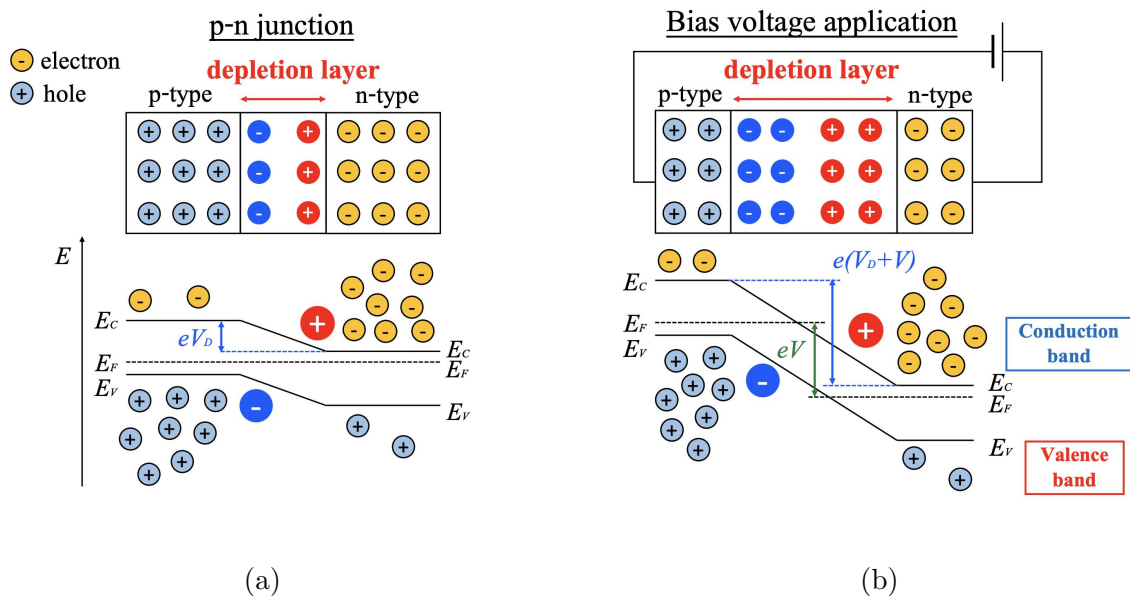


Figure 2.4: Comparison of a p-n junction at (a) thermal equilibrium and (b) under applied reverse bias voltage. The upper panels show the distributions of mobile carriers and fixed donor/acceptor ions, illustrating depletion-layer formation and its extension under bias. The lower panels depict the associated energy-band diagrams, including conduction band, valence band, Fermi level, and the built-in potential V_D , which increases to $V_D + V$ when an external voltage is applied.

Since the depletion layer is relatively thin under equilibrium, an external voltage can be applied to modify its width, see Figure 2.4b. When a positive voltage is applied to the n-type region and a negative voltage to the p-type region the depletion region widens, this configuration is known as the “reverse bias”.

The width of the depletion layer increases with the magnitude of the applied reverse bias, which enhances the active volume of the detector for charge collection. However, if the reverse bias exceeds a certain critical value, a sharp increase in the reverse current occurs, this phenomenon is known as “breakdown”.

Silicon strip detectors

In both CBM and E16 experiments, the STS modules used are of the DSSD type. In a DSSD, narrow p⁺-type semiconductor strips are implanted on one side of an n-type silicon wafer (bulk), while n⁺-type strips are patterned on the opposite side. Aluminum electrodes are connected to these strips to allow current read out. There are DC- and AC-coupled readout, the last one has the advantage that the dark current from each strip does not flow into the signal line.

When a charged particle passes through the depletion layer, it loses energy within the silicon bulk. This energy loss results in the creation of electron-hole pairs, with the number of pairs proportional to the energy deposited by the particle. Under the influence of the electric field, the electrons drift toward the n⁺ strips and the holes toward the p⁺ strips, where they are collected and read out as electrical signals via the aluminum electrodes.

Because the n⁺ strips are directly connected to the n-type bulk, electrons generated in the depletion region would, in principle, be detected by multiple adjacent strips simultaneously. To prevent this effect DSSDs incorporate the so-called “p-stop” regions, narrow p⁺-type implants placed between neighboring n⁺ strips. These p-stop regions form additional depletion zones with the n-type bulk, thereby electrically isolating adjacent n⁺ strips from each other.

In an orthogonal DSSD design, the p-side and n-side strips are arranged perpendicular to each other, providing high spatial resolution in both directions, but also generating $n^2 - n$ “ghosts” or fake hits that can only be eliminated with additional information. The STS modules utilize small stereo angle of 7.5°, where the strips subtend a small angle rather than 90°.

2.3.2 The STS detector module

The STS module is the functional building block of the CBM and E16 tracker. The module design as well as its components are determined by the challenging experimental conditions of both experiments. It consists of a double-sided double-metal silicon microstrip sensor interconnected to two Front-End Boards (FEBs) via a stack of low-mass aluminum polyimide microcables. Each FEB carries 8 custom Application-Specific Integrate Circuits (ASICs). Connected to the 128 readout channels of each ASIC, are bonded a pair of microcables to transfer the analog signals from the sensor to the Front-End Electronics (FEE). Figure 2.5 illustrates the STS module. A general description of the ASIC is presented in section 3.1.

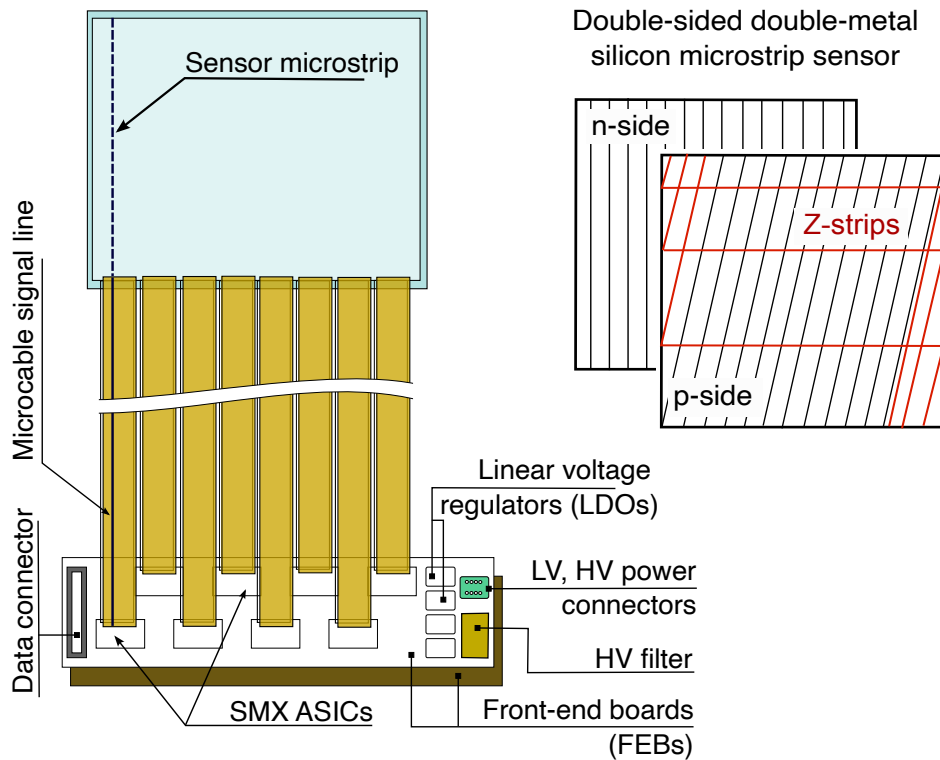


Figure 2.5: Schematic layout of the STS module. The different components that comprise the modules are labeled.

Silicon sensor

In STS, the sensors will have a configuration of a double-sided microstrip, chosen to optimize track reconstruction efficiency and fulfill the low-mass material constraint. The double-sided sensors are capable to provide 2D position in the same amount of material, while the sensors with an arrange of strips in only one side require twice the sensitive material. The strips angle respect to the edge of the sensors will be for n-side 0° , and for p-side an inclination of 7.5° . This strip configuration allows to reduce the number of ghost hits. This implies reduced resolution in Y-coordinate, which falls within the specifications for CBM since our magnetic bending is in X-coordinate. Also, it implies the presence of shorter strips for p-side at the edges of the sensor. These strips are interconnected via a second layer of metalization [44]. Due to their shape, they are referred as “Z-strips”, as illustrated in Figure 2.5.

The sensors are produced by Hamamatsu Photonics K.K in $320\ \mu\text{m}$ thickness n-type wafers. Each sensor side has 1024 strips with a pitch of $58\ \mu\text{m}$. The sensors feature an integrated AC-coupling, that avoid the implementation of a leakage current compensation circuitry in the FEE. STS will use four different sensors lengths (22, 42, 62 and 124 mm) and the same width of 62 mm for all sensors, see Figure 2.6, matching with the particle densities of the location where they will be deployed.

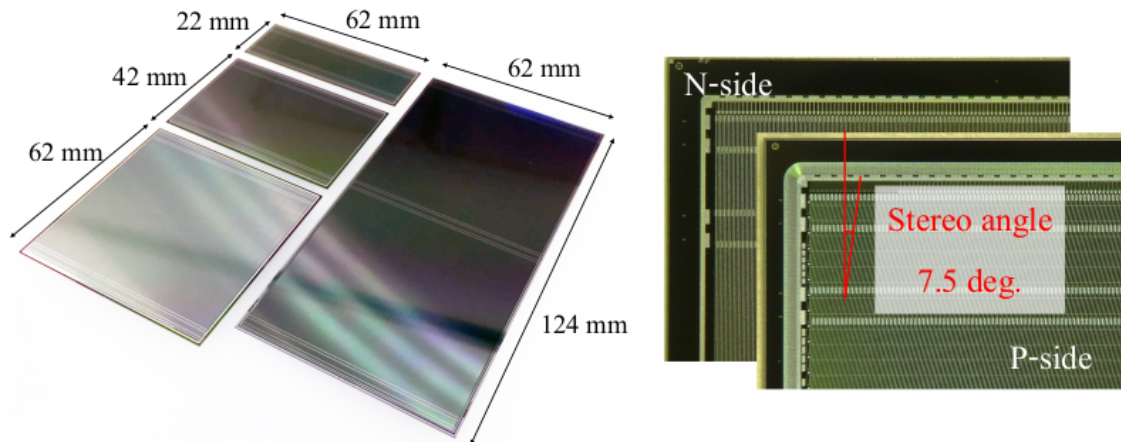


Figure 2.6: CBM-STs double-sided silicon microstrip sensors. On the left, overview of the different sensor geometries, with dimensions ranging from small to large lengths (22, 42, 62 and 124 mm). On the right, a close-up view of the sensor showing the strip layout on both sides. It also features the oriented stereo angle of 7.5° for the p-side strips.

Microcable

The analog signals from the sensor to the FEE are transferred via two layers of microcables with aluminum strips and $116 \mu\text{m}$ pitch, separated with a meshed spacer in order to reduce the parasitic inter-layer capacitance. They are covered with a shielding layer to reduce the electromagnetic interference and noise level. The supporting material for the aluminum strips is $20 \mu\text{m}$ polyimide.

Front-end board

The main function of the FEB is to provide power supply voltages to the SMX ASICs and a capacitive couple data interface, which establishes the connection of the Low Voltage Differential Signaling (LVDS) lines (clock, downlink and uplink) to the readout board. The board carries 8 custom-designed SMX ASICs for reading 1024 channels of one sensor side. To ensure adequate bandwidth allocation, each chip can be configured to provide 1, 2, or 5 readout links at 320 MHz each, depending on the expected local data load. This feature was considered in the design of the FEBs, resulting in two types of FEBs: FEB8-2 and FEB8-5. Each one of them comes in two flavors A and B, which are identical electrically, but mirrored in their geometrical design.

Figure 2.7 shows the final version of a FEB-8. Right next to the ASICs there are also four custom designed radiation hard (LDO) regulators developed at the Semiconductor Laboratory SCL Chandigarh in India [45]. The e-links between FEBs and Readout Boards (ROBs) are AC-coupled, in order to allow the connection of a single ROB to multiple FEBs operated at the different high voltage biasing potentials.

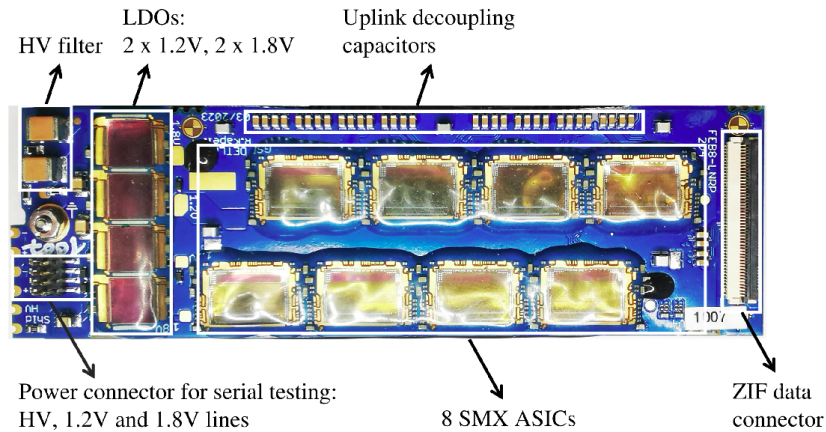


Figure 2.7: Image of a FEB8-2 used in the CBM-STC modules with its different elements: SMX ASICs, Low Drop-Out Voltage Regulators (LDOs), ZIF data connector, power connector and High Voltage (HV) filter circuit.

2.3.3 STS at the CBM experiment

STS is the key tracking detector of the CBM experiment. It has the capability to reconstruct tracks of charged particles with an efficiency of 95% and to measure momenta with resolution of 1.5% for $p \geq 1$ GeV/c. The 876 double-sided silicon microstrip sensors that STS comprise are arranged in 8 tracking stations, making possible to cover a physics aperture of $2.5^\circ \leq \Theta \leq 25^\circ$. STS has in terms of bandwidth and density the most demanding requirements of all CBM detectors, such as:

- the volume of the setup is approximately $1.4 \times 2.3 \times 1.3$ m³ inside the magnet. Placed between 30 cm and 100 cm downstream from the target [46];
- it must be capable to measure up to 1000 particles per central Au+Au collision at interaction rates up to 10 MHz without hardware trigger;
- low material budget, for this the front-end and readout and power electronics are placed on the periphery of the detector, out of the physics acceptance. In addition, the detector modules are mounted on low-mass carbon-fiber support structures;
- radiation hard silicon sensors, able to stand up to 10^{14} 1 MeV n_{eq} ;
- sensors will be read using fast and self-triggered FEE, which must have reliable performance under radiation environment up to 100 krad/yr. The signals from the sensors are transferred to the FEE via ultralight readout cables with up to 50 cm length;
- efficient cooling system, able to remove up to 50 kW of dissipated heat from inside the detector box. The FEE and readout electronics have the largest amount of heat contribution, around 40 kW. The rest is generated by the low voltage cables and sensors itself (6 mW/cm²). In order to maintain the operation temperature under control, the cooling system will use gas convection in the STS volume, also keeping the humidity low to avoid condensation.

Integration: ladder, half-unit, full detector

The CBM-STS detector is constructed through several complex levels of mechanical and electronic integration. Figure 2.8 illustrates the different integration levels of the CBM-STS detector, from ladders to half-units, half-units to tracking station, and finally the complete tracking system.

Starting from the basic building blocks, the first level consists of the STS modules. The next integration step is the assembly of “ladders”, each of which accommodates between two and ten modules mounted on a lightweight carbon-fiber support structure. In total, the complete STS detector comprises 106 ladders. Two ladder types are used: ladders with and without a “C-shaped cut-out”, the former (ie. the ones with cut-out) allowing placement of the ladders closer to the beam pipe.

At the subsequent integration level, ladders are mounted onto “half-units”. Each half-unit is a C-shaped aluminum frame that provides mechanical support for the ladders and incorporates cooling interfaces for the FEE, the ROBs and the Power Boards (POBs). In total, 20 mechanical half-units form the full STS detector.

The half-units are then assembled into eight tracking stations, divided as three upstream and five downstream of the beam pipe direction (commonly referred to as STS_u and STS_d). The complete tracking system is housed inside a thermal enclosure, forming the full STS detector. Within this enclosure, the sensors are maintained at approximately $+10^{\circ}\text{C}$ using gas cooling, while the electronics are cooled to about -20°C through a liquid-cooling system integrated into the thermal interfaces.

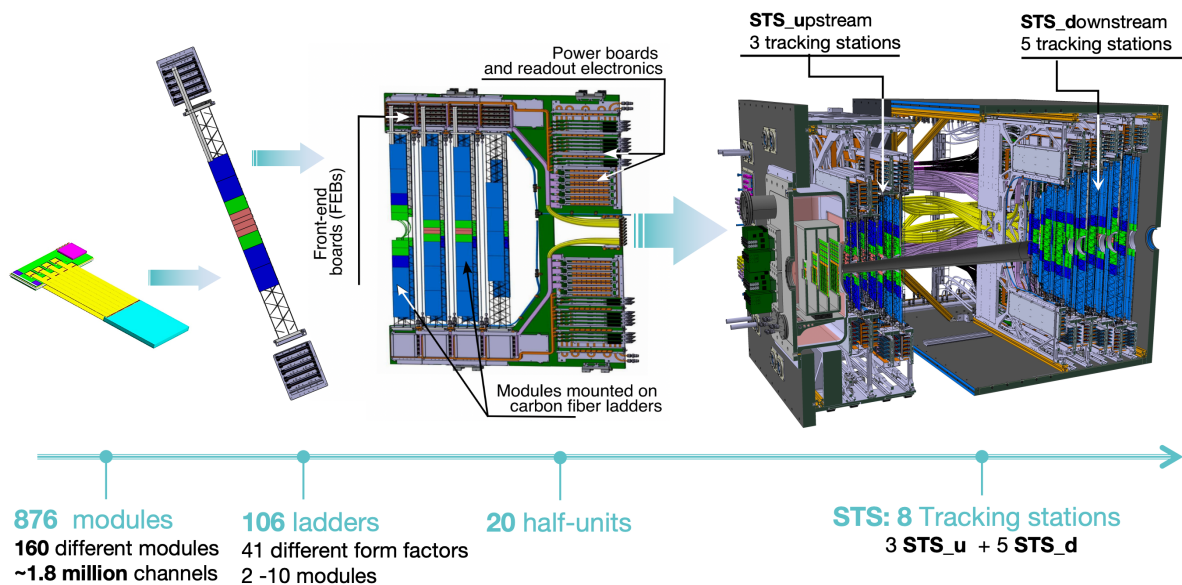


Figure 2.8: Conceptual layout of CBM-STS from the lower to the highest integration level: CBM-STS module, CBM-STS ladder, half-unit, and the eight tracking stations.

STS readout chain

The STS readout chain must ensure full control of all system functionalities while providing sufficient data throughput to store all relevant information. To achieve this,

the chain will integrate 14016 SMX ASICs, 1792 FEBs, 576 ROBs, and 2400 optical links between the Common Readout Interfaces (CRIs) and the ROBs. The STS will generate roughly 500 Gb/s of data, with signal rates reaching up to 300 kHz per channel. All of this data will be read out via high-speed optical links from the detector for subsequent processing and application of data reduction algorithms.

Figure 2.9 presents a schematic overview of the STS readout chain. In this setup, the digitized data from the FEBs are aggregated by the ROBs and transmitted out of the detector box through high-speed optical links. The CRIs, located in the experiment service building, will handle data pre-processing and the distribution of clock and control commands. A high-performance computing farm will then perform online event selection using highly parallelized algorithms.

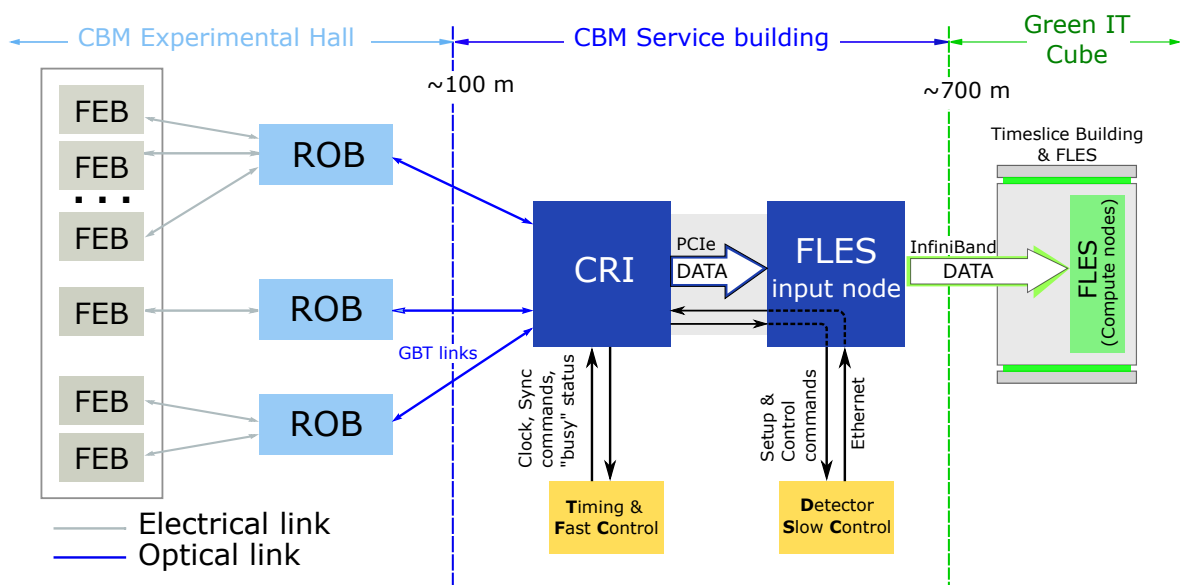


Figure 2.9: Block diagram of the STS readout chain concept. Its different elements are shown: FEB, ROB and CRI.

The main components of the STS readout chain are listed as follows:

FEB: is explained in section 2.3.2.

ROB: its purpose is the data aggregation from many electrical readout links and multiple FEBs, together with the electrical-to-optical interface to connect the experimental area to the CRIs. In addition, the ROB handles the distribution of the clock signal as well as slow and fast control commands to the FEE [47].

In the STS, the ROBs will be positioned outside the physics acceptance but inside the STS box, where they will be subject to a high radiation environment. For this reason, the ROBs are constructed from radiation-hard components. Additionally, they must operate in 1 T magnetic field conditions that fall well within the specifications of the Gigabit Transceiver (GBTx) and Versatile Link devices. Each ROB integrates three GBTx chips. One operates in transceiver mode, providing both uplinks and downlinks, while the remaining two function in transmitter mode, delivering only uplinks. A Gigabit

Transceiver-Slow Control Adapter (GBT-SCA) ASIC will be used for slow control of the GBTx in transmitter mode. These chips are paired with radiation tolerant optical transmitters (VTRx) and transceivers (VTTx). The ROB provides six phase-adjustable clocks and six downlinks at 160 MHz, allowing connect up to five FEBs. It supports 42 readout links at a maximum rate of 320 MHz, of which 40 are utilized in the STS system [48]. In the moment of this work, that final prototype was already under test, see Figure 2.10.

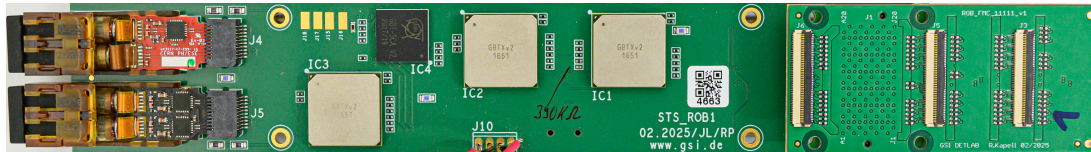


Figure 2.10: Photograph of the final prototype of the STS ROB. On the left, two optical transceiver modules provide high-speed data links to the Data Acquisition (DAQ) system. The central section hosts three GBTx ASICs responsible for slow-control, timing, and high-speed optical communication. Additional supporting electronics and power-management components surround them, including the GBT-SCA. On the right side, FPGA Mezzanine Card (FMC) connector interface the ROB with the FEBs.

CRI: is a unified FPGA-based hardware platform for CBM, equipped with system specific firmware. It implements the back-end of the optical interfaces to multiple readout boards, including adaptations of the Gigabit Transceiver-Field Programmable Gate Arrays (GBT-FPGA) core for communication with the GBTx devices as well as the back-end of the ASIC communication protocol. Pre-processing of the hit data, including address expansion, time alignment of data from multiple sources, and construction of microslices, in order to have data containers holding all the hit information generated within a given time interval. The CRI also provides the interface to the Detector Control System (DCS) via the back-end communication protocol for the front-end ASICs, and to the Timing and Fast Control System (TFC) [47].

2.3.4 STS at the E16 experiment

The STS in the E16 experiment serves as the vertexing detector and first tracking layer of the spectrometer. It fulfills the detector requirements for the innermost silicon strip tracking system, which are essential to achieve the target mass resolution of approximately $5 \text{ MeV}/c^2$. The main performance requirements are as follows:

- position resolution in the bending plane of $25 \text{ } \mu\text{m}$;
- time resolution of approximately 6 ns ;
- high detection efficiency of at least 95% .

The E16-STS will be positioned at a distance of approximately 120 mm from the center of the spectrometer. Figure 2.11a shows a 3D rendering of the E16-STS setup for Run-0d, Run-0e, and Run-1. In these configurations, a total of 10 CBM-STS modules

are integrated into the experiment. For subsequent runs, the system will be upgraded to include up to 26 STS modules. Figure 2.11b shows a top view of the J-PARC E16-STS chamber.

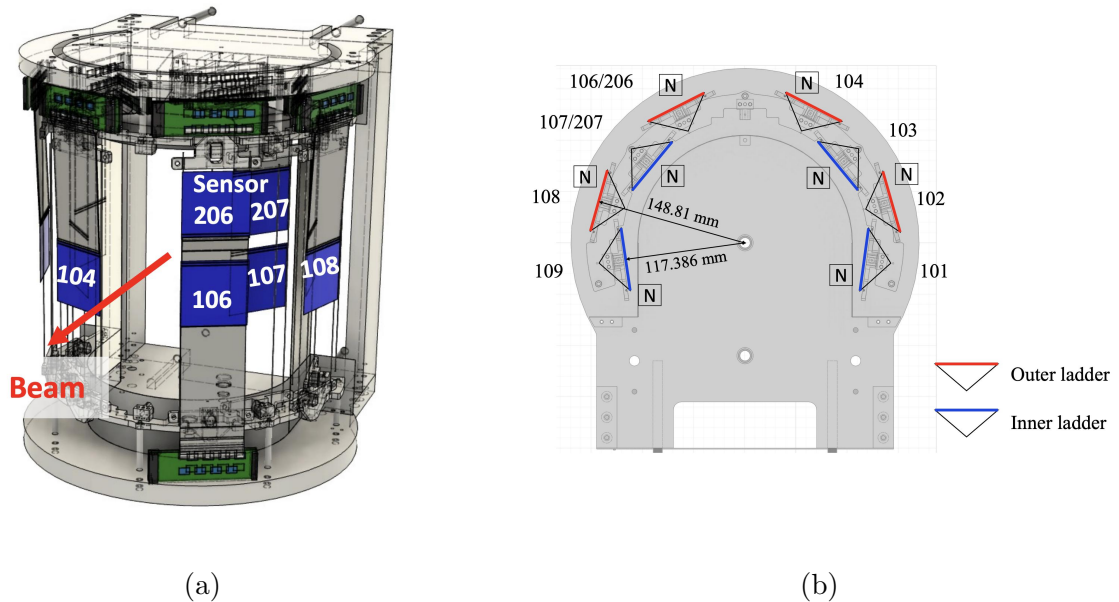


Figure 2.11: (a) 3D render of the E16-STS chamber for Run-0d, Run-0e and Run-1. The beam direction is indicated and six of the ten modules are visible, including the cooling pipe placed in the top plate. (b) Top view image of the J-PARC E16-STS chamber.

The setup has a cylinder shape equipped with eight ladders of 231 mm high that can accommodate up to three modules. In the current configuration eight modules are placed at the center positions of the ladders and two additional ones are placed above two of the central modules mentioned above. More information related to geometrical characteristics and naming convention of the modules is detailed in section 4.1. Inside the E16-STS chamber a target is installed.

The E16-STS chamber is designed with a top and a bottom plates supported by only two pillars located up- and downstream. Two copper pipes are installed inside the plates to provide water cooling to the electronics. Aluminized mylar sheets and black sheets are used to cover the outer and inner side of the structure, to prevent light intrusion and electronic noise.

By design, all modules have p-side glued to the ladder structures. This implies that modules naming with odd numbers have p-side oriented facing outward, while even numbers have n-side oriented facing outward. Odd numbered modules are mounted in the inner ladders at a distance of $117.38 \text{ mm} \pm 0.16 \text{ mm}$ from the center of the spectrometer, while even numbered modules are mounted in the outer ladders at a distance of $148.81 \text{ mm} \pm 0.16 \text{ mm}$ from the center of the spectrometer.

STS readout chain for the E16 experiment

The schematics of the STS readout chain implemented in the E16 experiment is illustrated in Figure 2.12, where each component (FEBs, LVDS repeaters, GBTx-EMULATOR (GBTx-EMU) boards, GERI boards, and the DAQ PC) is described in detail in section 5.1.1.

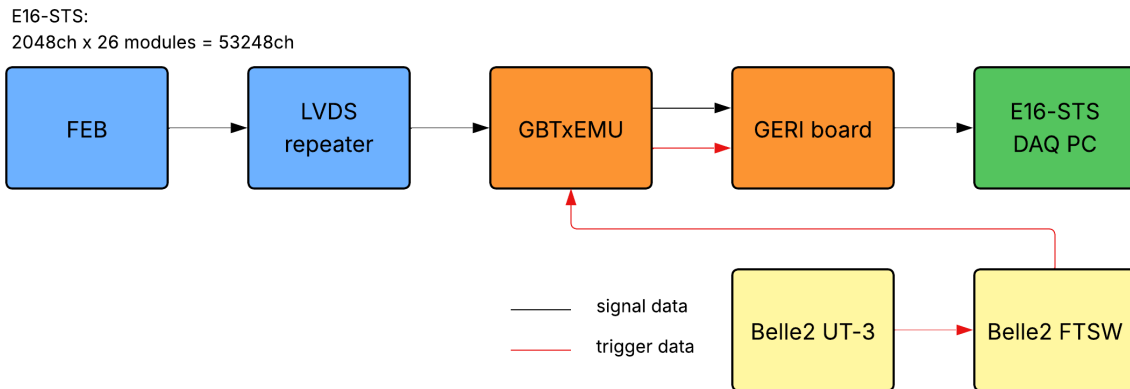


Figure 2.12: Schematic of the E16-STS readout chain. The signal data (black) from the FEBs are transmitted through the LVDS repeater to the GBTx-EMU and then to the GERI board, which interfaces with the E16-STS DAQ PC. The trigger data (red) are distributed via the Belle2 Universal Trigger Board 3 (UT-3) and Belle2 FTSW modules to the GBTx-EMU. The system handles a total of 53248 channels.

In total, the readout system integrates 416 SMX ASICs, providing 53258 readout channels, along with 52 FEBs, 52 LVDS repeaters, 26 GBTx-EMU boards, and 4 GERI boards. These elements collectively form the complete data acquisition chain, responsible for signal amplification, transmission, and readout of the E16-STS detector modules.

A distinctive feature of the E16-STS readout system in comparison to the CBM-STS readout is that, in addition to signal data, a trigger signal is also received by the GBTx-EMU board and forwarded to the GERI board. At this stage, event selection is performed based on coincidence signals and the information sent to the DAQ PC. The trigger signal is generated from the discriminator outputs of approximately 2620 channels, which include inputs from the third GTR layer (GTR300), the HBD, and the LG calorimeter. Timing coincidences and spatial correlations among these three detectors are used to identify events consistent with two electron tracks originating from the target region. The overall trigger decision and issuance are managed by the Belle2 UT-3, which processes the input signals from the different subsystems and distributes the generated trigger signals to the DAQ system.

Chapter 3

Studies of the ADC and FAST discriminator response for enhanced calibration of the SMX ASIC

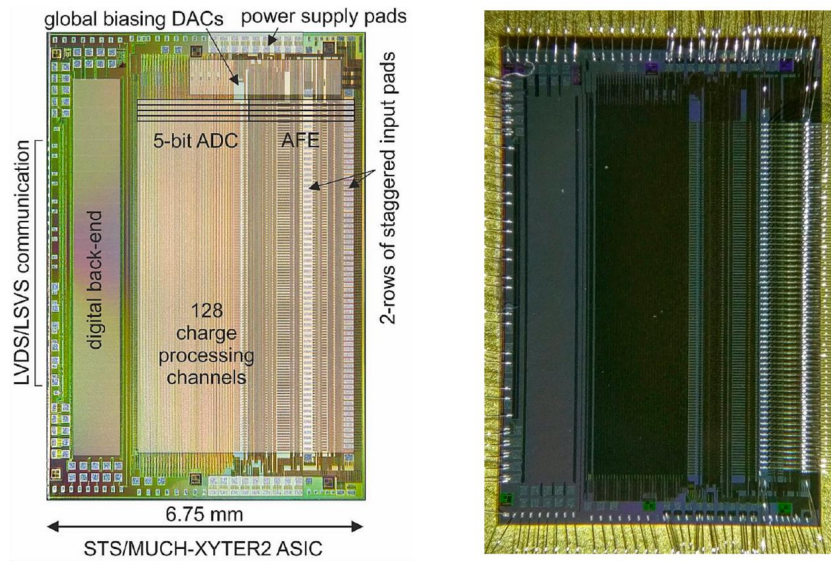
As the main goal of STS is to track charged particles, it is essential to achieve a high position resolution. To support this requirement, the SMX ASIC, the custom-designed FEE for reading out the STS modules, is built with a 5-bit flash Analog-to-Digital Converter (ADC). This circuit is designed to measure the registered signal amplitude and, hence, to support the hit reconstruction algorithm via the center of gravity method. In this context, the precise calibration of the ADC becomes a critical factor to ensure the hit position determination and tracking performance.

This chapter begins by describing the architecture of the ADC built into the SMX ASIC. Motivated by the need to improve speed without compromising precision, the development of an optimized calibration procedure for the ADC is presented. The results are evaluated through quality parameters, such as Differential Non-Linearity (DNL), Integral Non-Linearity (INL), and calibration time. Additionally, studies related to the FAST discriminator, and transfer functions of both the ADC and FAST discriminator are also discussed.

3.1 Introduction to the STS front-end electronics

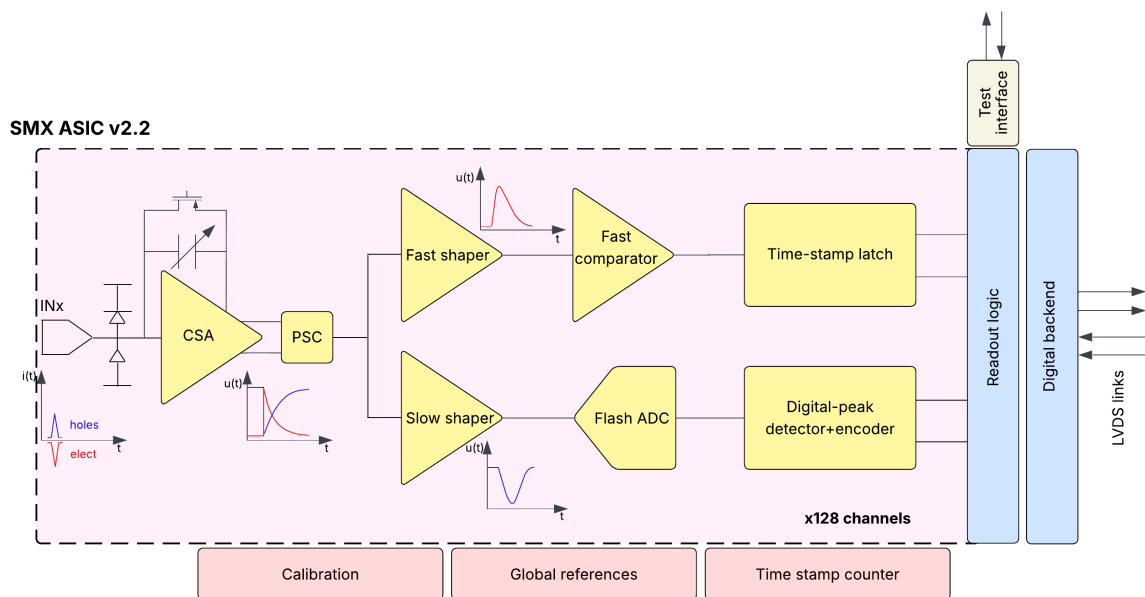
The SMX2.2 ASIC is the latest and final version of the STS FEE. The design had undergone multiple modifications compared to its predecessors, and it has been successfully tested in lab studies and beamlines [49]. The SMX ASIC, shown in Figure 3.1a, integrates 128 Analog Front-End (AFE) channels, each equipped with circuits for both time and amplitude measurement. In addition, two dedicated test channels are located at the periphery of the ASIC, featuring buffered outputs for monitoring internal signals. The design incorporates full-custom configuration registers, shared biasing blocks, and integrated calibration circuitry. The digital back-end operates at a clock frequency of 160 MHz, supporting access to configuration registers, free-streaming digital readout, and a range of diagnostic features [50].

In the Figure 3.1b is presented the block diagram of a single channel in the SMX ASIC. Each channel begins with a low noise Charge Sensitive Amplifier (CSA), which collects the



SMX2.2 ASIC

(a)



(b)

Figure 3.1: (a) SMX ASIC simplified diagram (left) and a view under the microscope after wire bonding (right). (b) A functional diagram of one channel of the SMX ASIC. After the first pre-amplification stage, the signal splits into two branches optimized for time and energy measurements, respectively.

charge generated in the active volume of the detector and converts it into a voltage step proportional to the amount of charge collected. The output of the CSA is routed through a Polarity Selection Circuit (PSC), which ensures uniform pulse polarity across the next processing stages. This feature supports the readout of double-sided silicon sensors.

The signal processing proceeds along two parallel paths:

- **Fast path:** designed for accurate determination of signal arrival time. It consists of a single-stage CR-RC shaper with a peaking time of 30 ns, followed by a comparator and a 14-bit timestamp counter operating at 320 MHz;
- **Slow path:** optimized for precise energy discrimination and measurement with low noise, it employs a two-stage amplifier with a CR-(RC)² followed by a 5-bit flash ADC. The slow shaper allows selection among four shaping times: 90, 150, 220, and 280 ns [51, 52]. The operation of the SMX ASICs in the STS detector is intended only for 90 ns.

The back-end logic is responsible for configuration register access and data readout. In addition, it includes several diagnostic features, such as an upset counter, a link error monitor, and multiple modes for generating test hits. To accommodate varying levels of detector occupancy, it also integrates five LVDS drivers, which can be selectively enabled [50, 53].

3.2 Description of the analog measuring circuits and calibration functionalities of the SMX ASIC

3.2.1 The 5-bit flash ADC

The SMX ASIC implements in each channel a 5-bit continuous type flash ADC with an integrated digital peak detector, already seen in Figure 3.1b. Other ASICs designed with similar requirements, namely ultra-high sampling speed, compact size, low noise, and relatively low power consumption, typically employ a SAR ADC or a pipelined ADC combined with peak detection over multiple samples. These alternative architectures often require a substantial amount of digital, clocked circuitry that remains active during signal processing. In self-triggered ASICs, such activity can degrade noise performance, as the switching noise generated may couple into the AFE.

The channel-ADCs in the SMX ASIC can digitize signals in a dynamic range of approximately 14 fC when used in STS mode. This is determined by two reference potentials, $VRef_P$ and $VRef_N$, controlled by 6-bit resolution registers. The common global threshold of each comparator, also called a discriminator, is generated by a resistor ladder stretched between these potentials, as shown in Figure 3.2.

The minimized area of each ADC introduces significant offset mismatches. To address this, trimming corrections are applied to equalize the ADC transfer characteristics across all comparators and channels. The converter employs $2^n - 1$ comparators. Each comparator is equipped with an 8-bit trimming DAC, allowing adjustment of its offset voltage over a correction range of ± 150 mV. These trimming settings not only compensate for offset and non-linearity in the amplitude measurement but can also be used to change the conversion characteristics of the ADC, i.e. to emphasize the amplitude range of interest for a particular experiment. The effective threshold of each discriminator is mathematically

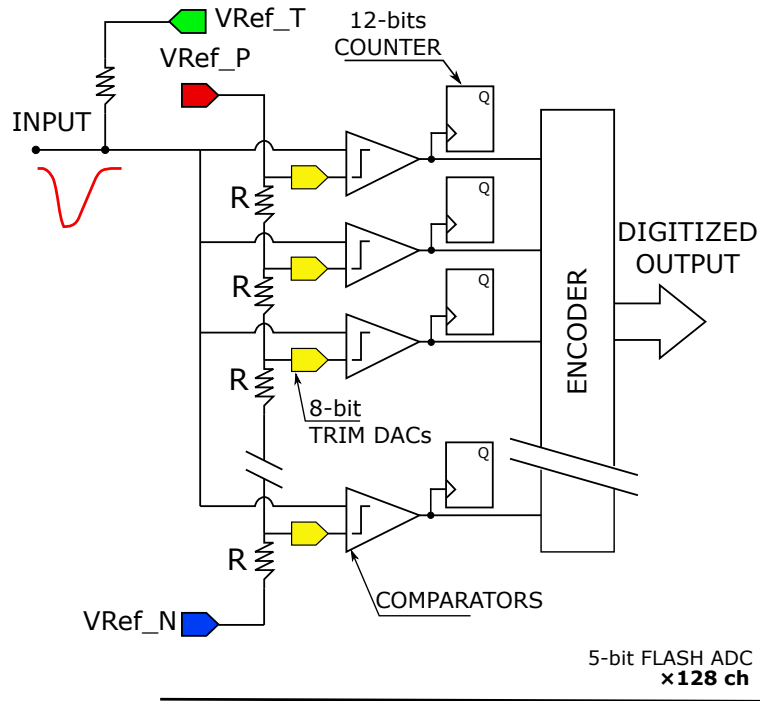


Figure 3.2: Block diagram of the SMX ASIC flash ADC architecture. Its main components, such as the resistor ladder, comparators, trim Digital-to-Analog Converter (DAC), counters, and encoder, are shown. The analog input signal is simultaneously compared against reference voltages in each discriminator generated via a resistor ladder stretched between two reference potentials ($VRef_P$ and $VRef_N$) and fine-tuned using trim DACs on each comparator. The absolute threshold of the ASIC is established via a common global reference DACs ($VRef_T$).

described in Equation 3.1.

$$V_i[\text{mV}] = \underbrace{\frac{VRef_P - VRef_N}{31}}_{\text{resolution}} \cdot d_i + \underbrace{\Delta v_i}_{\text{trim correction}} \quad (3.1)$$

Here, V_i , expressed in mV or units of charge, corresponds to the threshold of the i th comparator, and Δv_i represents the trim correction applied to the comparator voltage. The outputs of all comparators are connected to the peak detector logic, which provides thermometric encoding across the 31 comparator cells. To ensure unambiguous conversion to binary format, a priority encoder is used that selects the first active comparator output starting from the Most Significant Bit (MSB).

An additional reference potential, $VRef_T$, controls the position of the signal baseline relative to the ADC. As such, it serves as an effective system threshold. This simplifies both the calibration and operation of the ADC, since the calibration values remain valid regardless of baseline shifts. In scenarios with large amplitude noise, only $VRef_T$ requires adjustment.

3.2.2 The timing discriminator

Each channel includes a fast shaper that drives a leading-edge discriminator used for time-stamping data. This discriminator uses a global adjustable threshold, $Thr2_glb$, along with a 6-bit per channel offset trimming DAC to fine-tune its response, see Figure 3.3.

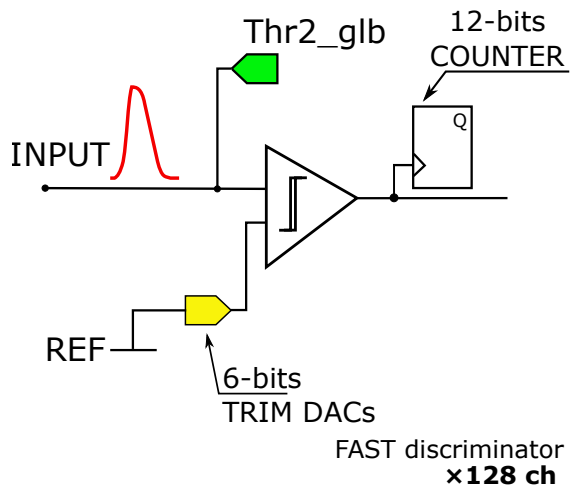


Figure 3.3: Simplified schematic of the FAST discriminator path. Each of the 128 channels includes a discriminator stage that compares the signal to a reference voltage, which can be adjusted by a 6-bit trim DACs. The $Thr2_glb$ DACs moves globally the position of the baseline for all channels, establishing the effective threshold. The comparator output latches a 14-bit timestamp value, and it also triggers a 12-bit dedicated counter.

3.3 The standard calibration procedure

At the beginning of this research, the ADC and FAST discriminator measuring circuits of the SMX ASIC were calibrated using a so-called “STANDARD” procedure, developed and described in [54]. The block diagram shown in Figure 3.4 describes the main steps of it, which consists of three main parts: an initial state where the user must define the signal polarity, reference potentials ($VRef_P$ and $VRef_N$), and the calibration range of the ADC, i.e, the threshold of the first and last discriminator. Since the procedure uses the ASIC internal pulse generator, the calibration range is expressed in units of it. This range is equally distributed in 31 steps, resulting in the corresponding threshold for each comparator. The threshold of the timing discriminator is adjusted to be the same as in the first ADC level.

The effective threshold of each channel’s discriminator is adjusted by scanning its trim DAC. The response function is read out using the 12-bit diagnostic counters. The trim scan is carried out in two steps:

- **coarse-scan:** the discriminator response referred to as $S - curve$ is evaluated in a wide range of trim values with a step of 5 LSB. A fast evaluation algorithm identifies

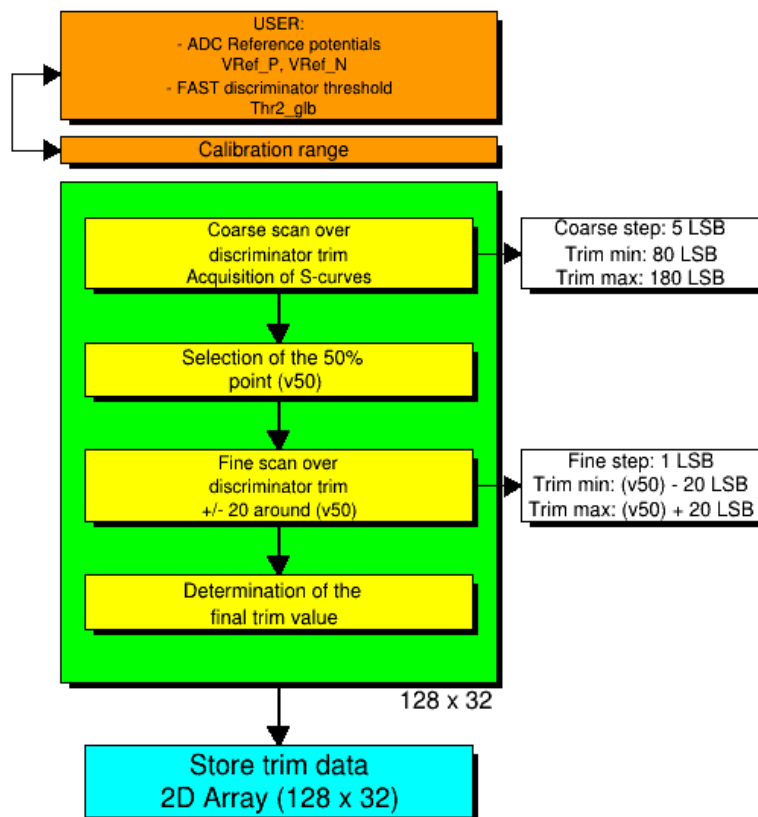


Figure 3.4: Flow diagram of the STANDARD calibration procedure, which is divided into three main parts: USER parameters input, CALIBRATION algorithm, and WRITING of the calibration matrix. The main calibration step includes a coarse-scan between a minimum and a maximum trim value with a defined step, selection of the V_{50} point, fine-scanning, and final determination of trim values across. The output of the procedure is an array of trim values corresponding to 128 channels and 32 discriminators of the SMX ASIC. Diagram adopted from PhD thesis of Adrian Rodriguez Rodriguez [54].

the trim value at which the hit occupancy reaches 50% of the total number of injected pulses. This value, referred as $primer_{v_{50}}$, is used as an input for the second step of the procedure;

- **fine-scan:** performed in a range of ± 20 LSB values around the $primer_{v_{50}}$, using a finer step of 1 LSB. This step allows for reducing the uncertainties in the procedure due to the local non-monotonic behavior of the trim DACs. Subsequently, a more refined algorithm is applied to the fine-scan data to determine the exact 50% ($v_{t_{50}}$) or switching point of the $S - curve$.

The output of the full procedure is a 128×32 elements matrix that stores the optimal trim values for every channel. These calibration parameters are specific to each ASIC and channel. Because of the channel-to-channel and ASIC-to-ASIC differences, the calibration matrix is unique of each ASIC and cannot be parametrized or applicable to others.

3.4 Optimization of the calibration procedure

The large deployment of SMX ASICs across the 876 modules of STS presents a significant challenge, particularly with respect to module characterization. Among the various steps of series testing, the calibration of the ADC is the most time-consuming. Although the procedure described in the previous section provides high accuracy, it requires considerable execution time, making the overall testing campaign impractically long if not optimized. This limitation becomes especially critical in large detector systems, where not only precision but also throughput is essential.

In this context, optimizing the ADC calibration procedure is essential to improve test throughput. In addition, a more time-efficient calibration would not only prove advantageous during series module testing, but it also allows recalibration in situ, in response to external factors such as noise.

3.4.1 Implementation of the Successive Approximation Method (SAR)

The Successive Approximation Method (SAR) was developed based on the principles described above, aiming to shorten the calibration runtime without compromising the precision of the previous algorithm. Both steps, followed by the STANDARD procedure during the main calibration step, are considered necessary to ensure accurate threshold determination. However, it is the coarse-scan that is the most time-consuming due to the wide range of trim values that must be evaluated to approximate the $S - curve$ response. In contrast, the fine-scan is relatively fast and must be performed regardless of the outcome of the coarse-scan to refine the v_{t50} value. Therefore, any attempt to optimize the overall calibration procedure should focus primarily on reducing the duration of the coarse-scan. Streamlining this step offers the potential to improve the efficiency of the STANDARD method without compromising the accuracy of the final trim values.

The SAR method was implemented as an alternative to the conventional coarse-scan approach, and it is shown in Figure 3.5. Both methods use the internal pulse generator and inject in all channels a fixed number of pulses with amplitude equal to the discriminator's calibration point. Instead of sampling the full $S - curve$, the SAR method performs a series of binary decisions that converge towards the switching point. This is achieved by iteratively adjusting the trim value around the estimated threshold using a binary search algorithm. At each iteration, the hit occupancy is evaluated and the search range is reduced, quickly converging to the correct trim. This targeted approach allows the determination of the effective threshold with significantly fewer measurements compared to the exhaustive coarse-scan. In other words, the SAR method pinpoints the trim value through successive approximation rather than exhaustive scanning, thus reducing the calibration time. An illustration of the SAR method is presented in Appendix A Figure A.1, where each iteration progressively narrows down the optimal trim value.

In Appendix A.2 is detailed the SAR method algorithm. It requires several input parameters: an initial matrix of trim values, a fixed number of injected pulses, the total number of approximation iterations n , and the initial search range, denoted as $width$. In each iteration, the adjustment step is calculated as $width/n$.

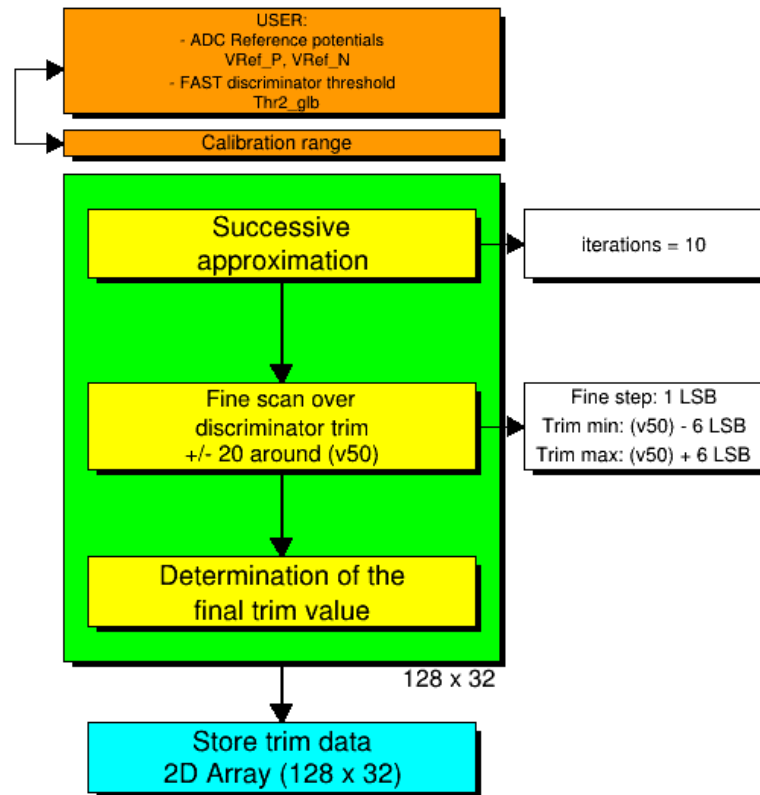


Figure 3.5: Flow diagram showing the optimized calibration algorithm, including a successive approximation step, fine-scanning, and final determination of the trim values for an array of 128 channels and 32 discriminators.

3.4.2 Description of the experimental setups

The implementation of the SAR based calibration procedure, along with other related activities such as optimization of the SAR method, were carried out across different testing setups in accordance with their availability. Initially, the SAR method was implemented in the STS laboratory in GSI, using the readout chain shown in Figure 3.6.

The main components of this readout are the following:

- a prototype FEB, called FEB-C, that contains one SMX ASIC;
- a Data Processing Board (DPB), FPGA-based board which implements the communication protocol back-end;
- a gDPB FMC, for interfacing the FEBs with the DPB.

The prototype FEB-C is a custom-designed front-end board developed for testing a single SMX chip, see the Appendix B. It features two ERNI connectors that support interfacing with 128 detector channels. A low voltage power supply provides 2.5 V for powering the 1.2 V for the AFE and the 1.8 V for the digital part. In the FEB-C design, several analog spy points are routed to external connectors. These probe points allow for monitoring multiple analog signals, and also for checking the reference biasing potentials.

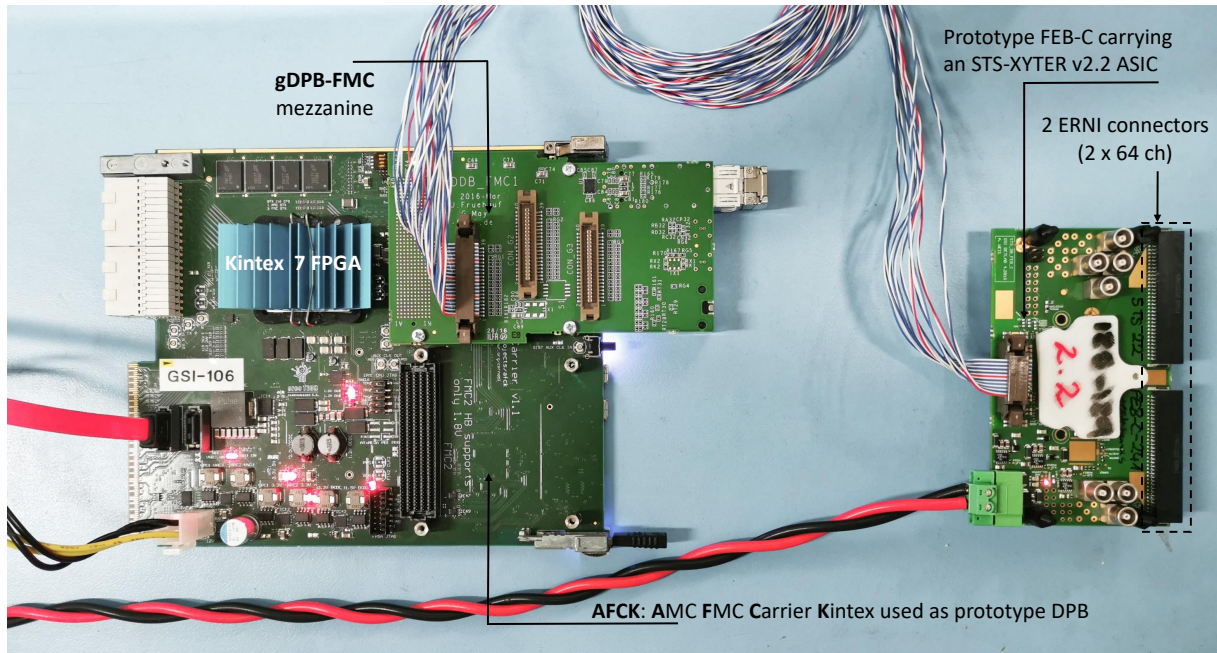


Figure 3.6: Prototype readout chain used for the implementation of the SAR method [49].

The hardware platform used to implement the readout back-end is based on the AFCK board [55], which has served as the prototyping platform for the CBM DPB boards. Communication with the controller back-end is established through the IPBus protocol [56].

For optimizing the SAR method, in addition to the DPB board, the readout chain included the following components:

- a FEB-8 as replacement of the prototype FEB-C;
- a Common Readout Board (C-ROB), which provides data aggregation and an electric-optical interface.

3.5 Evaluation of the SAR method

The reliability of the calibration values is influenced by statistical fluctuations in the acquisition of the $S - curve$. These fluctuations are directly related to the number of pulses injected in each channel, which, in turn, affects the required number of write/read operations. To assess the accuracy of the calibration procedure, the difference between the effective discriminator threshold and the set calibration value was measured. The standard deviation of the residual distribution across all channels serves as an indicator of the accuracy of the algorithm. This estimator helps to define decision criteria regarding the minimum number of pulses required and the corresponding calibration time. For reference, the results corresponding to the STANDARD method, evaluated under the same conditions, are also illustrated.

In the case of the ADC, additional reference parameters such as DNL and INL are used to cross-check the linearity performance. Their values are given in units of Least Sig-

nificant Bit (LSB). The DNL quantifies the deviation of the width of each ADC code bin from the ideal step size. It is calculated as the maximum difference between two consecutive bin centers and normalized to the expected voltage step, see Equation 3.2. A DNL value of 0 LSB corresponds to a perfectly uniform bin width, while a DNL greater than ± 1 LSB indicates missing or overlapping codes, which degrade the ADC performance.

$$DNL_{ch}[LSB] = \max \left(\frac{V_{i+1} - V_i}{\Delta V_{ideal}} - 1 \text{ LSB} \right) \quad (3.2)$$

In the case of the INL, it measures the accumulative deviation of the actual ADC transfer function from an ideal straight-line response. It is computed as the difference between the measured and the ideal centers of each code, normalized by the nominal step size. The INL reflects how well the ADC maintains a linear relationship between the input signal and the output code across the full dynamic range.

After applying the SAR calibration method with 90 injected pulses, the transfer functions of all 128 channels of an SMX ASIC were evaluated. The results, presented in Figure 3.7a, reveal an average ADC dynamic range of 75950 e, with an offset corresponding to 10500 e. The linearity parameters are illustrated in Figures 3.7c and 3.7e. For both DNL and INL, values remain below 1 LSB. A DNL below 1 LSB ensures a monotonic transfer function with no missing codes, while an INL below 0.3 LSB confirms good linearity of the system.

Figures 3.7b, 3.7d, and 3.7f show the corresponding distributions of the observables described above evaluated over the 31 discriminators in each of the 128 channels. The DNL and INL are used as performance parameters of the algorithm at a certain number of injected pulses, while the standard deviation of the residual is used as the third estimator. These metrics serve as observables to characterize the response of the system under different numbers of injected pulses, which, as mentioned previously, have a direct impact on the calibration time.

The performance of the calibration algorithm was evaluated for different numbers of injected pulses. Figures 3.8a, 3.8b, and 3.8c show, respectively, the average DNL, average INL, and the standard deviation of the residuals distribution as a function of the number of injected pulses. The plots compare the results obtained with the two calibration methods: the SAR method and the STANDARD method.

In general, both approaches yield comparable performances, with the SAR method showing slightly better results, particularly for more than 50 injected pulses. For both DNL and INL, the mean values remain below 0.4 LSB across the full range, confirming that the ADC linearity is properly achieved after calibration. In the three observables, a plateau is observed starting around 50 injected pulses, indicating that the calibration procedure reaches saturation in threshold precision beyond this point.

Additionally, the red bars in Figures 3.8a and 3.8b represent the percentage of channels with DNL or INL values exceeding 0.3 LSB, showing that this fraction rapidly decreases and stabilizes at low values as the number of injected pulses increases. Figure 3.8c shows how the standard deviation of the residuals distribution follows also a decreasing trend and stabilizes beyond 50 injected pulses, confirming the consistency and convergence of the calibration process. To confirm the quality, the red bars represent the percentage deviation w.r.t the result at 90 pulses obtained by the SAR method.

The results shown above confirm that the SAR method is an effective approach for

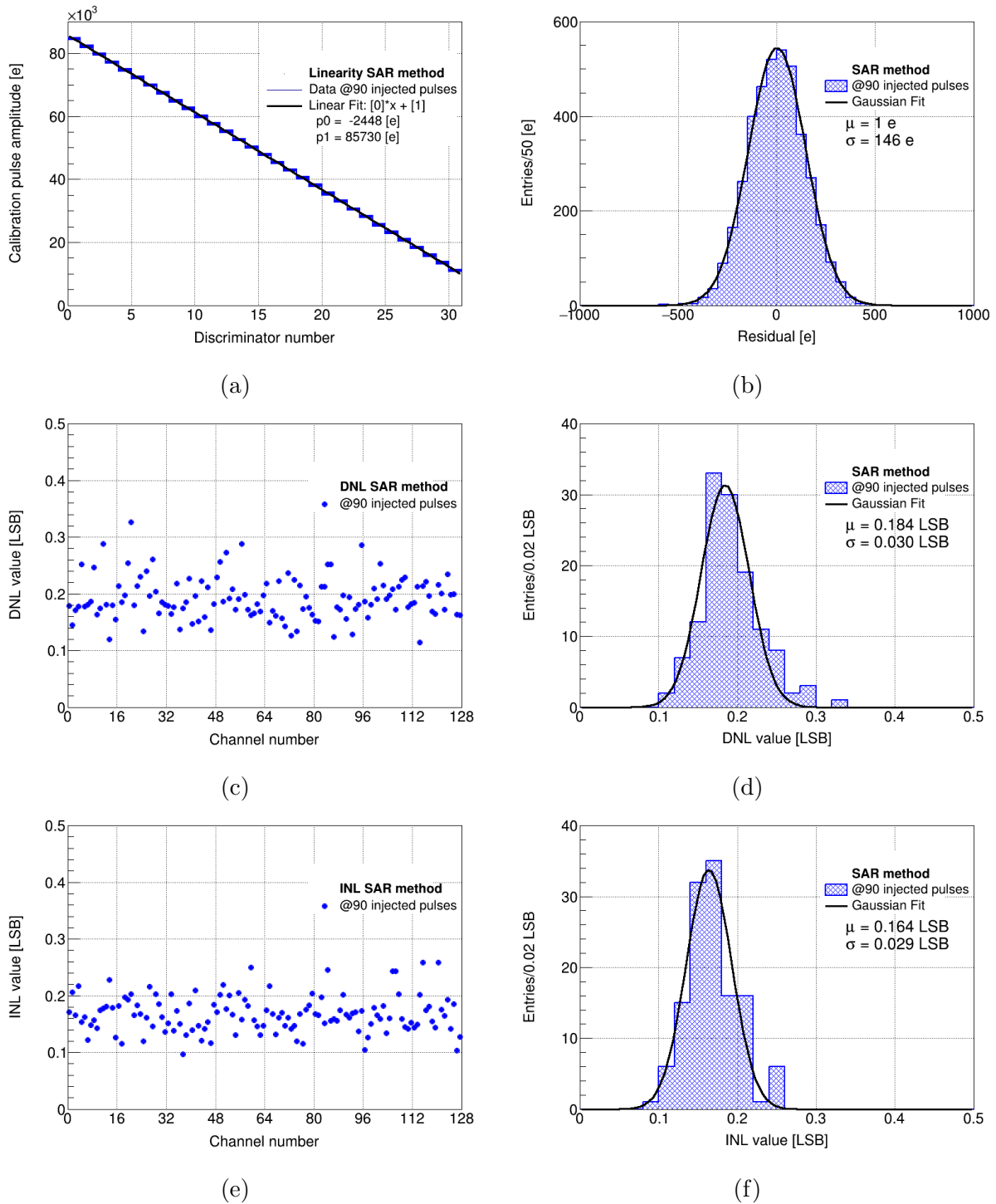


Figure 3.7: ADC transfer functions and linearity parameters after calibration for all 128 channels of a single SMX ASIC. The values represent the: (a) transfer function and (b) residual distribution, (c) DNL and (e) INL characteristics, (d) and (f) DNL and INL distributions, respectively, at 90 injected pulses.

calibrating the ADC of the SMX chip. However, the quality of the calibration alone is not sufficient, and optimizing the procedure in terms of processing time is also a criti-

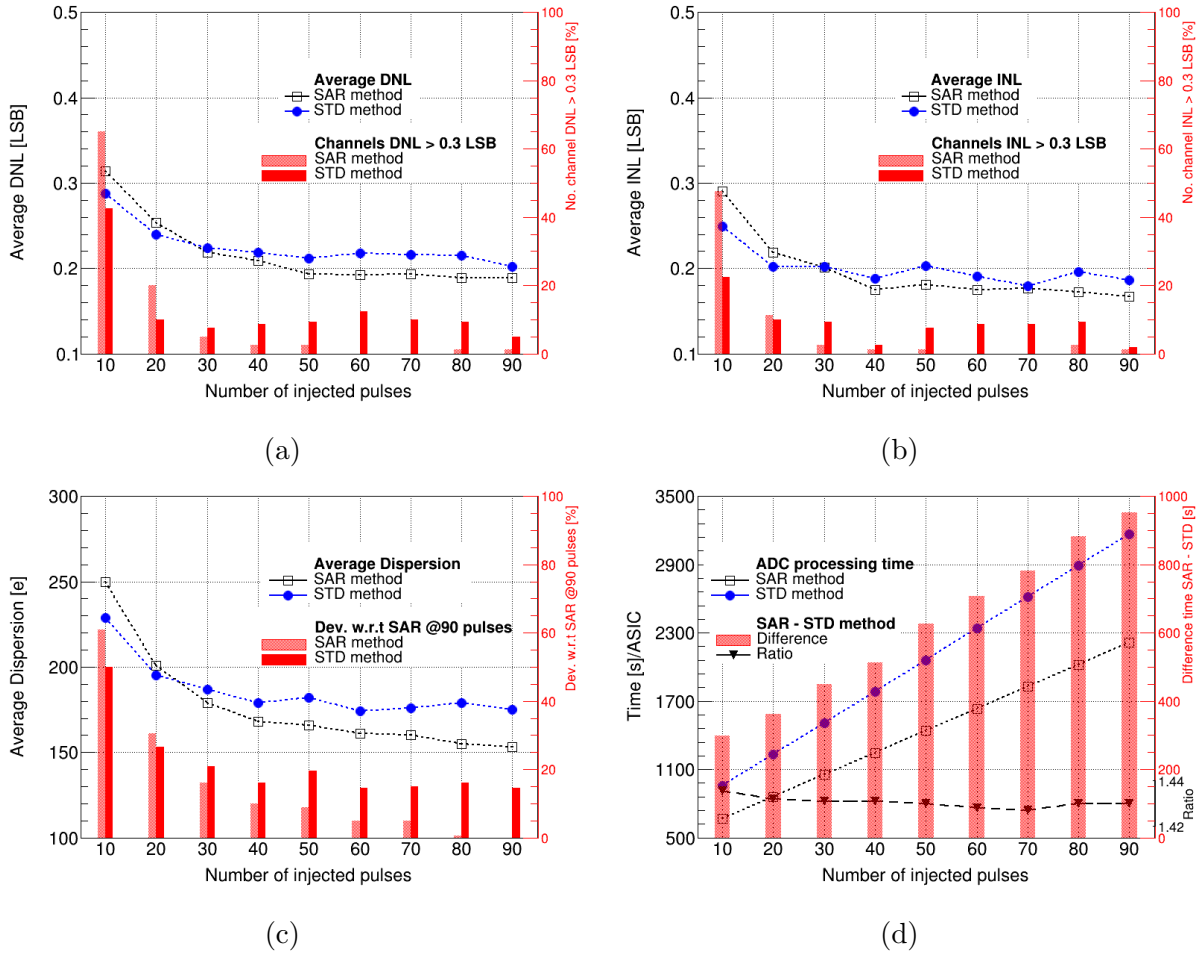


Figure 3.8: Comparison between the SAR and STANDARD methods as a function of the number of injected pulses. (a) Average DNL and percentage of channels with DNL > 0.3 LSB. (b) Average INL and percentage of channels with INL > 0.3 LSB. (c) Average dispersion and its deviation with respect to the corresponding method at 90 pulses. (d) ADC processing time per SMX ASIC for the two methods. In all panels, solid markers refer to the STANDARD method, and empty markers to the SAR method; red bars correspond to the percentage or ratio shown on the right axis.

cal requirement. Figure 3.8d presents the total calibration time for both methods as a function of the number of injected pulses. Although both methods exhibit processing times longer than ideal, primarily due to communication delay caused by the network, the measurements were performed under identical conditions. Therefore, the observed time improvement with the SAR method is a valid and significant advantage.

The linear increase in processing time with the number of injected pulses, combined with the observed saturation in calibration precision at 50 pulses, suggests that the use of 50 injected pulses provides the best compromise between calibration performance and processing time. In addition, the red bars in Figure 3.8d represent the difference in time between the two methods, while the black triangle markers show their corresponding time ratio.

3.5.1 Optimization of the SAR method parameters

Once the calibration using the SAR method demonstrated good performance and proved to be a valid alternative to replace the coarse step of the current STANDARD method, exploring possibilities to optimize the SAR approach became a necessary next step. As detailed in Section 3.4.1, the SAR method operates based on two main parameters: the number of iterations (n) and the initial search range ($width$). The goal is to optimize these parameters in order to reduce the overall processing time while maintaining the accuracy of the calibration. Using 50 injected pulses, identified as the optimal point that balances the calibration performance and time, a scan was performed to determine the best values for n and $width$. This optimization was carried out in combination with a fine-scan to optimize the full calibration sequence. As a result, the search range of the fine-scan was also refined. The parameters of the SAR method were scanned into the followed range:

- **n:** [3-11] with step of 1;
- **width:** [10-24] with step of 2 LSB;
- **fine-scan range:** [10-19] with step of 1 LSB.

After analyzing the measurements, it was concluded that the algorithm yields a poor performance for a number of iterations below 8. As an example, Figure 3.9 shows the DNL and INL of one ASIC for a number of iterations of 7, where a significant number of channels (17%) exhibit values greater than 1 LSB, indicating the presence of missing codes.

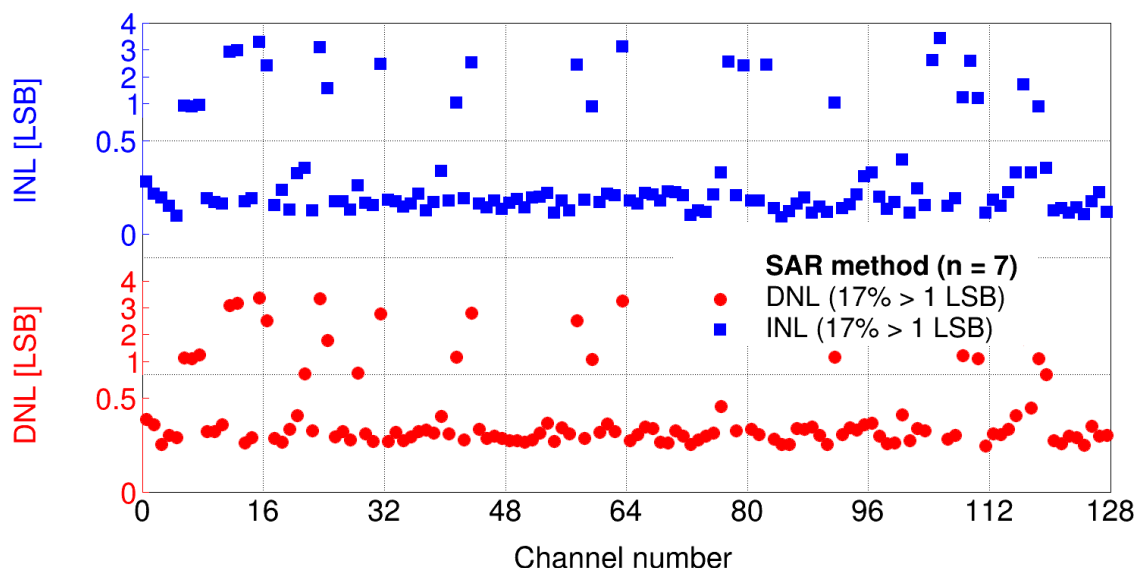


Figure 3.9: ADC linearity parameters of 128 channels of a single SMX ASIC. The values represent the DNL and INL for the SAR method using $n = 7$ iterations. The red vertical axis indicates DNL values, plotted as red circles. The blue vertical axis indicates INL values, plotted as blue squares. The results demonstrates that approximately 17% of the channels exhibit DNL or INL larger than 1 LSB.

From the various combinations of n and $width$, Figures 3.10a-c illustrate the resulting DNL, INL, and standard deviation of the residual values for the specific case of a fine-scan range equal to 12 LSB. Additional results for the others fine-scan range values can be found in Appendix C. Figure 3.10d illustrates the calibration times associated with the configurations explored above as a function of the fine-scan range of the calibration procedure. In Figures 3.10a, 3.10b, and 3.10c, a trend is observed: the values of DNL, INL, and standard deviation of the residual generally improve with increasing number of iterations and decreasing width values.

Although multiple parameter configurations yield acceptable performance in terms of our metrics, the combination of 10 iterations, a width of 14 LSB, and a fine-scan range of 12 LSB was ultimately selected. The decision to opt for a width of 14 LSB despite lower values of the width parameters that also yields good results, was made to ensure a broader calibration range. This, allow to target possible outliers discriminators.

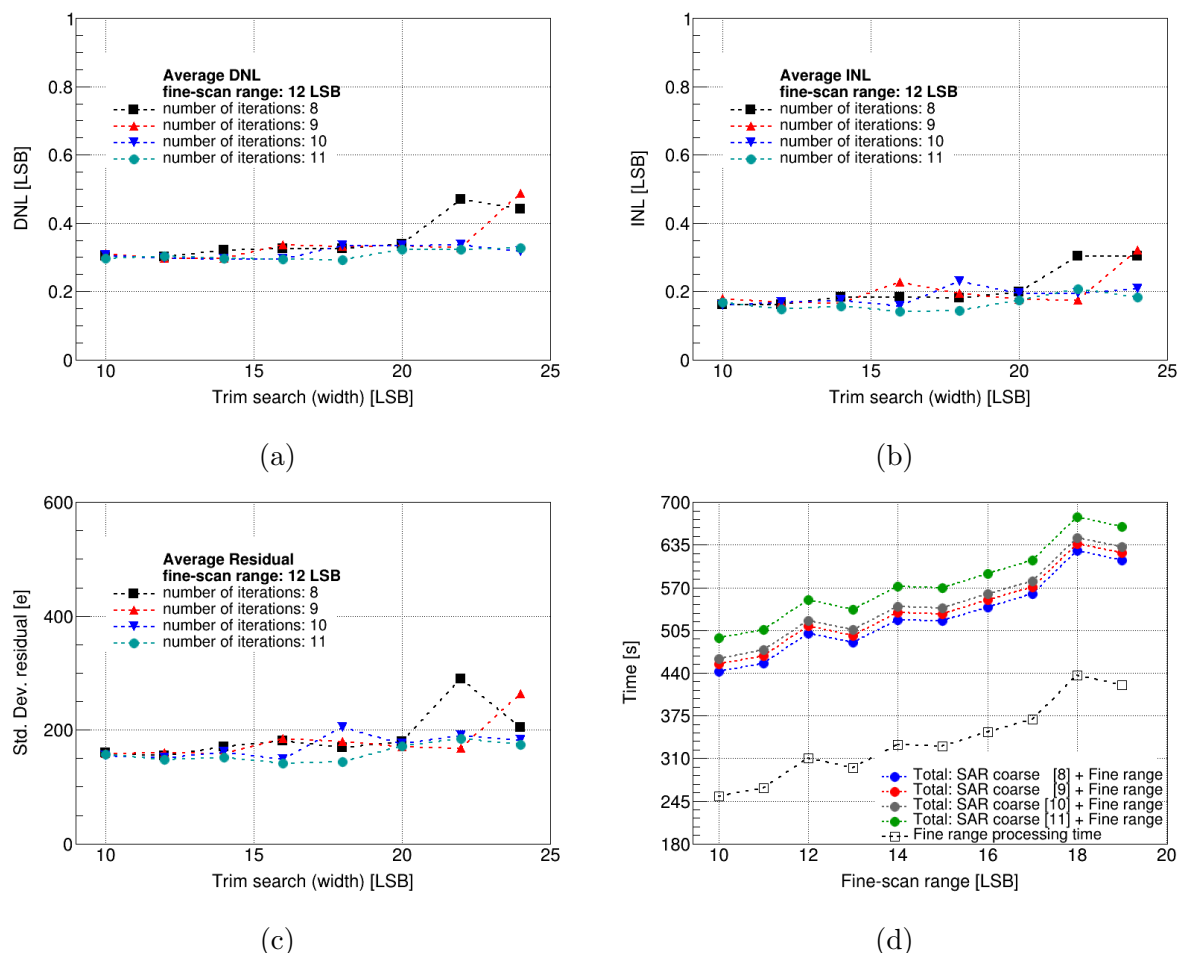


Figure 3.10: ADC linearity parameters of 128 channels of a single SMX ASIC. The values represent the: (a) DNL, (b) INL and (c) standard deviation of the residual performed at different number of iterations and $width$ range. The data correspond to an specific fine-scan range equal 12 LSB. (d) Calibration time processing for different values of the fine-scan range. Additionally the time processing of the SAR coarse and the combination of SAR coarse + fine-step is illustrated.

With respect to the calibration time, the primary parameters that influence the duration of the process are the number of iterations and the range of the fine-scan. Due to the fluctuations introduced by network performance, repeated measurements under the same parameter settings can yield significantly different processing times. To reduce the impact of these inconsistencies, the median of the measured values was used to represent the processing time.

Figure 3.10d illustrates the processing times under different configurations. The black dashed line and black empty squares represent the time required to perform the fine-scan across various fine-ranges. Additionally, the processing time associated with the SAR coarse-scan is indicated for each number of iterations. The total calibration time, combining both, the SAR coarse and fine-scan durations, is shown using solid circles and dashed lines of different colors. For the selected parameters: 10 iterations, a trim search width of 14 LSB, and a fine-scan range of 12 LSB, the total calibration time amounts to approximately 520 s/ASIC. This result, although large, represents an improvement of at least 60% in running time with respect to the STANDARD calibration, while yielding equal level of accuracy.

3.5.2 Reproducibility of the calibration procedure

Once the optimum calibration parameters were found, a reproducibility study was conducted to evaluate the long-term stability and reliability of the calibration method. The idea was to calibrate the ADC every hour for a period of 10 hours and assess the quality of the calibration using the same quality parameters defined previously. The relative deviation respect to the first measurement for DNL, INL, and the standard deviation of the residuals are shown in Figure 3.11.

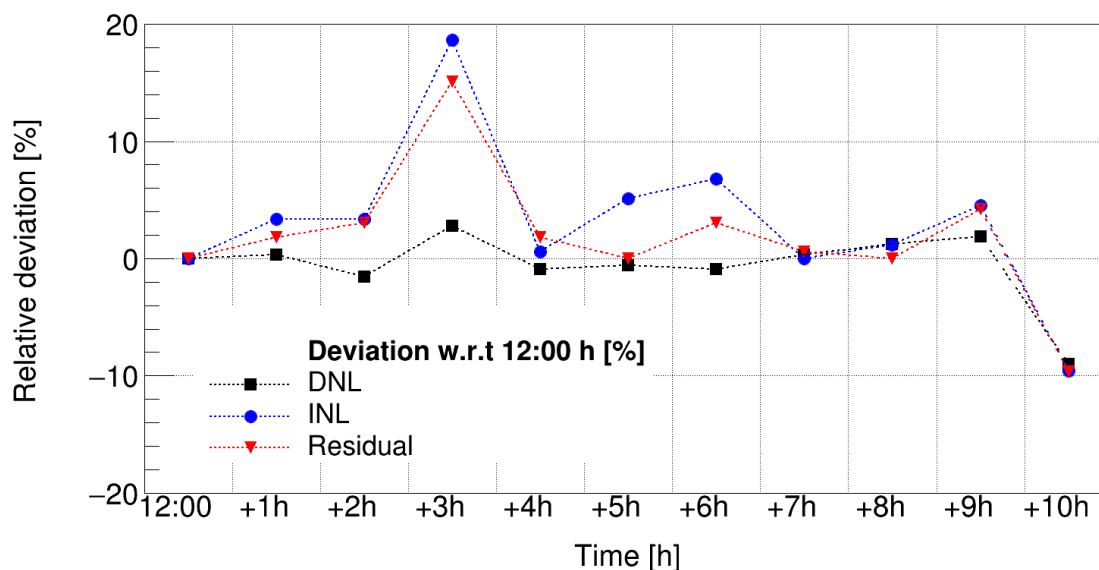


Figure 3.11: Calibration reproducibility over time using the SAR method. The relative deviation in percentage with respect to the first measurement (12:00).

In general, the measurements exhibit consistent behavior over time and confirm the reproducibility of the calibration using the SAR method. The relative deviation for the

three parameters remains steady close to 5% with minor fluctuations for the duration of the measurements. For the particular cases of measurements taken at +3 h and +10 hour, the results were in the order of 20% and 10% of relative deviation, respectively. Despite of this the values were very small between 0.16 LSB and 0.21 LSB in the case of DNL and INL, and around 140-150 e for the residuals. These values are considered very good, indicating that the calibration method is reliable.

3.5.3 Implementation of the broadcasting as a method procedure

The effort to optimize the calibration algorithm has resulted in a satisfactory level of accuracy while also reducing the calibration time. However, despite this improvement, the overall duration of the procedure remains relatively long. For a large-scale system such as the STS, time efficiency is a critical factor, particularly during the module Quality Assurance (QA) phase and in real operational conditions. The dedicated SMX ASIC communication protocol called HCTSP [53], includes a broadcasting function designed to transmit commands and configuration settings simultaneously to multiple ladders, modules, and ASICs within the system.

Most of the time consumed by the calibration algorithm when reaching convergence with sufficient precision is due to writing/reading operations on the ASICs. This limitation can be partially mitigated by exploiting the HCTSP broadcasting feature. The improvement is only partial because the writing operations to the calibration registers can be executed simultaneously on several ASICs, while the read out must still be performed sequentially.

Figure 3.12 shows the time consumed by the SAR method as a function of the number of calibrated ASICs. The calibration time (in seconds) is plotted on the Y-axis, while the number of ASICs ranges from 1 to 16 on the X-axis. Two different approaches of the SAR method are compared: the broadcasting approach (blue circles) and the sequential approach (red squares). As expected, the sequential approach exhibits a linear behavior because it calibrates each ASIC one after another, and all ASICs in a FEB on a module are equivalent. The calibration time for an entire module is approximately 2 h, this value corresponds to roughly 7 min per ASIC and it is extracted from the slope ($t_{cal}/1 \text{ ASIC}$) of the linear fit of the sequential approach.

For the broadcasting approach, the overall measured time (t_{bc}) also exhibits a linear increment, however, with a smaller slope. The t_{bc} includes a constant term corresponding to the writing actions in one ASIC (t_{write}), plus a reading time (t_{read}) that increases linearly with the number of calibrated ASICs, the expression resulted is $t_{bc} = t_{write} + N_{ASICs} \cdot t_{read}$. The reading time is estimated by the slope and equal to $t_{read} = 199 \text{ s}$. Therefore, the writing time can be calculated as $t_{write} = t_{cal}/1 \text{ ASIC} - t_{read}/1 \text{ ASIC}$, resulting in approximately 239 s.

In addition, Figure 3.12 also shows the calibration time using the broadcasting approach, but implementing the optimized parameters found for the SAR method (empty blue circle). A time for calibrating a full module becomes approximately 36 min.

Overall, the figure clearly demonstrates that the broadcasting approach reduces the total calibration time by approximately 50% compared to the sequential approach, making it far more suitable for systems containing a large number of ASICs. The implementation

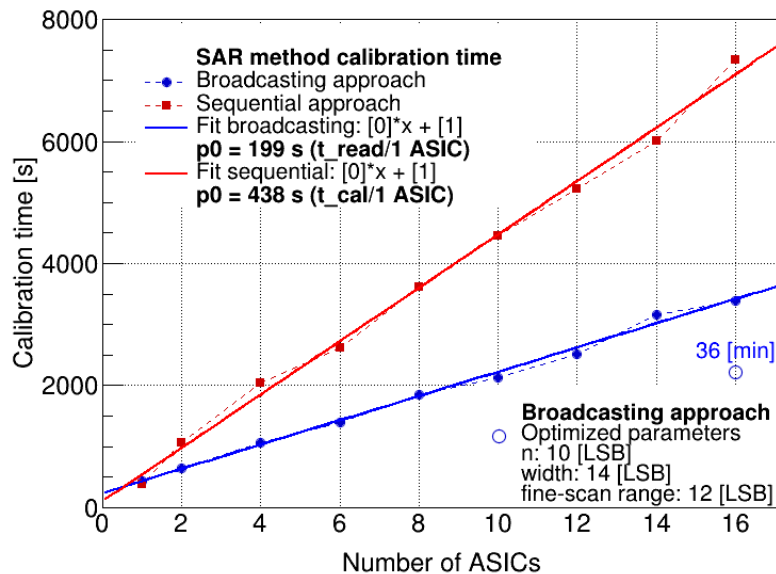


Figure 3.12: Comparison of the SAR method calibration time as a function of the number of ASIC for two different communication approaches: the broadcasting approach (blue circles) and the sequential approach (red squares).

of the broadcasting approach was done and tested for one module (i.e. 16 ASICs), however the method can be realistically scaled up with the existing version of the firmware to two modules (i.e. 32 ASICs) connected to the same readout board. The broadcasting commands and their implementation in the SAR calibration method are detailed in Appendix D.

3.6 Transfer functions of the amplitude and timing circuits

For operational purposes, setting the correct threshold for both paths of the SMX ASIC is crucial. This is due to how the hit generation mechanism of the SMX ASIC is implemented. The generation of a hit is triggered only when the signal crosses the first discriminator of the ADC. As a result, it is essential to establish a correlation between the timing and amplitude measurement thresholds, since it could result in sampled hits carrying inaccurate time information.

Figure 3.13 illustrates the hit generation mechanism under three different conditions. In Figure 3.13a, the ADC signal does not cross the ADC threshold; therefore, no hits are generated regardless of the FAST discriminator threshold being crossed. In Figure 3.13b and Figure 3.13c, the ADC signal crosses the ADC threshold, which means a hit is generated in both cases. However, in Figure 3.13b, the FAST discriminator threshold is set too high, causing an incorrect time assignment for the hit, i.e. the hit arrival time is not updated and the time of the previous crossing of the FAST discriminator threshold is used for the hit. Finally, Figure 3.13c illustrates the correct configuration, where the ADC and FAST discriminator thresholds are properly correlated, resulting in accurate hit timing.

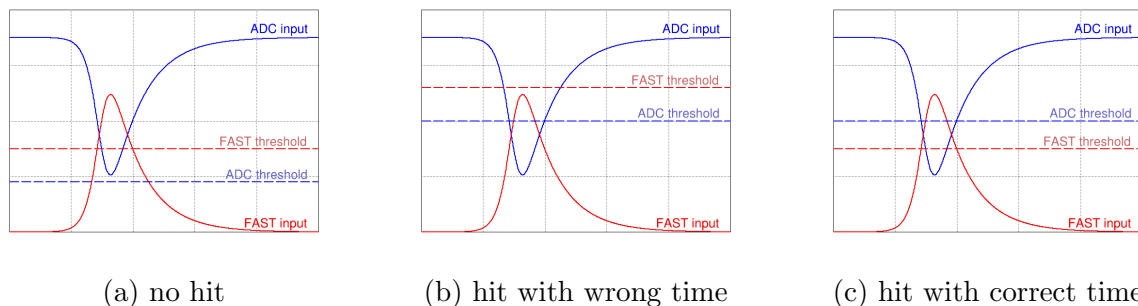


Figure 3.13: Illustration of the hit generation mechanism at the analog level: (a) The signal at the input of the ADC does not cross the corresponding threshold, so no hit is generated. (b) The ADC signal crosses the ADC threshold, but the signal does not cross the FAST discriminator threshold, resulting in a hit with incorrect timing. (c) Both signals in the ADC and FAST discriminator path cross their respective thresholds, producing a hit with the correct timing.

Variations from channel-to-channel and ASIC-to-ASIC are present within a FEB that reads the entire sensor side, these variances have the potential to induce the issues mentioned above. In addition, the intrinsic design of the slow and fast shaper with different bandwidths and therefore different noise susceptibilities, can lead to situations as described in Figure 3.13b. Therefore, comprehending and quantifying the threshold correlations is fundamental.

The study was carried out using one module, namely CRT-01-PB. This is a more complex object, due to it includes new elements to take in considerations such as, broken, noisy channels, and also the so-called Z-strips. They play a role in such channels-channels variations, in particular the last two ones.

The measurements are performed through a pulse amplitude scan, in which the response of each discriminator to a fixed number of pulses with varying amplitudes is recorded using the dedicated 12-bit counters in the ADC and FAST discriminator. The resulting response function, *S - curve*, is fitted with a gaussian error function¹ and the inflection point is extracted. This is interpreted as discriminator threshold and its spread as noise. The effective threshold for each path is then defined as the average threshold across all channels. The width of this distribution reflects the channel-to-channel variation and serves as a metric for the quality of the calibration. In the case of the ADC, only the response of the first discriminator, which defines the effective threshold is considered.

The effective threshold at the calibration point corresponds to the settings of $VRef_T$ and $Thr2_glb$ equal to 58 LSB and $\Delta_{Thr2_glb} = 0$ LSB, respectively. It is worth mentioning that for the $VRef_T$ DAC a common value can be established for all ASICs. On the other hand, the $Thr2_glb$ for every ASIC is different. Therefore, threshold values will be expressed in units of difference with respect to the calibration point. For each value of $VRef_T$ and $Thr2_glb$, the distribution of effective thresholds for p-side is shown in Figure 3.14. These distributions have a Gaussian shape. An increase in non-uniformity channel-to-channel is observed as the width of the distribution increases as it moves away

¹ $erfc\left(\frac{x-\mu}{\sqrt{2}\sigma}\right)$

from the calibration point. To reduce this, corrective actions can be taken during detector operation. For example, re-calibrate the system at the operational threshold using the existing calibration matrix as a starting point to reduce processing time.

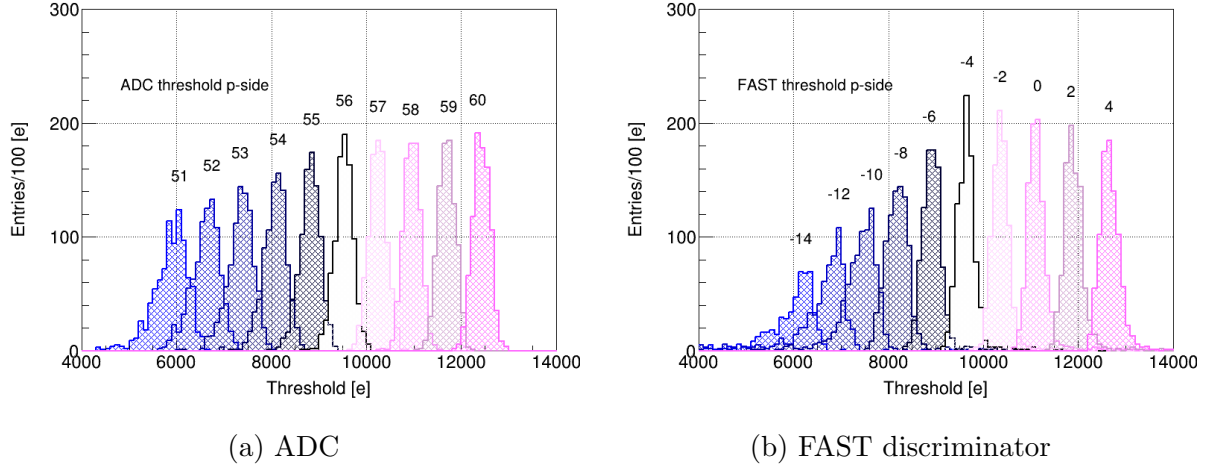


Figure 3.14: Evolution of threshold distribution for p-side of: (a) ADC for different values of $VRef_T$ and (b) FAST discriminator for different values of $Thr2_glb$.

The mean and sigma of each distribution in Figure 3.14, represent the effective threshold and channel-to-channel spread at a given setting of $VRef_T$ or $Thr2_glb$. They are extracted, plotted and fitted with a linear fit to determine the transfer function of the system. Figure 3.15 presents the resulting transfer functions for both the n- and p-side, separately shown for the ADC and FAST discriminator.

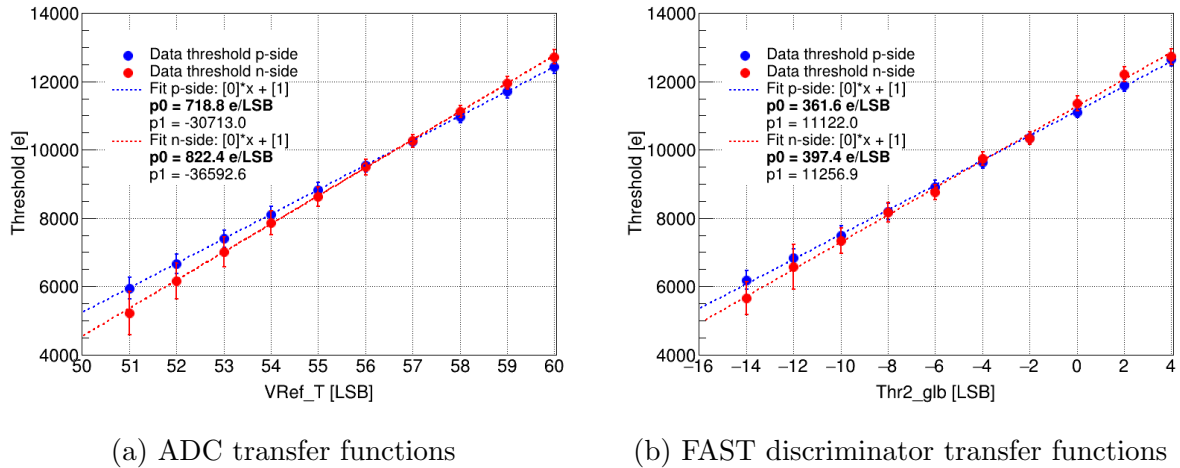


Figure 3.15: Transfer functions of ADC and FAST discriminator for n- and p-side. The mean represent the effective threshold among all channel and the errors bars the sigma of the distribution.

There are visible discrepancies in the slope of the transfer functions between n- and p-side. These differences are more pronounced for the $VRef_T$ DAC, and they are consistent with expectations. The ratio between the slopes of the ADC and the FAST discriminator is approximately a factor of two. These transfer functions allow to establish the operation

mode, by considering not only the relationship between the ADC and FAST discriminator threshold, but also the variations channel-to-channel. These results are valid for thresholds up to four-five times the noise of the corresponding discriminator, which represents a realistic operating scenario in STS. The results are summarized in Table 3.1, which illustrates the threshold dependencies and the corresponding channel spread, which are expressed as a percentage of the given value.

Table 3.1: Operational thresholds for the ADC and FAST discriminator. Marked in bold are the mean and spread at the calibration point.

VRef_T [LSB]	ADC		Thr2_glb [LSB]	FAST discriminator	
	n-side	Threshold [e] p-side		n-side	Threshold [e] p-side
51	5223 (12%)	5948 (5%)	-14	5653 (8%)	6181 (5%)
52	6156 (9%)	6657 (4%)	-12	6576 (10%)	6841 (4%)
53	7013 (6%)	7392 (3%)	-10	7332 (5%)	7489 (4%)
54	7862 (5%)	8103 (3%)	-8	8160 (4%)	8191 (3%)
55	8620 (3%)	8831 (2%)	-6	8760 (3%)	8911 (2%)
56	9494 (2%)	9540 (2%)	-4	9735 (2%)	9635 (2%)
57	10261 (2%)	10245 (2%)	-2	10335 (2%)	10359 (2%)
58	11120 (2%)	10964 (2%)	0	11354 (2%)	11100 (2%)
59	11954 (2%)	11698 (2%)	2	12204 (2%)	11882 (2%)
60	12716 (2%)	12428 (2%)	4	12727 (2%)	12641 (2%)

The way to interpret Table 3.1 for practical use is as follows. First, choose the target threshold from the ADC row. Next, select the FAST discriminator threshold such that there is no overlap between the ADC and FAST discriminator distributions. In other words, the sum of the ADC threshold and its spread must not overlap with the sum of the FAST discriminator threshold and its spread.

3.7 Studies with the FAST discriminator

One fundamental difference between the timing and amplitude circuits in the SMX ASIC is the way the signal baseline is positioned relative to the effective channel's threshold. As explained in the section 3.6, the effective threshold for the ADC and FAST discriminator are established via $VRef_T$ and $Thr2_glb$ registers.

During the calibration procedure, all ASICs in a module are set to a same $VRef_T$ value. This is possible because the $VRef_P$ potential, see Figure 3.2, is set for each ASIC such that the first discriminator of every channel is positioned at the same distance relative to the baseline. This can be understood as an additional degree of freedom with respect to the FAST discriminator. Moreover, within an ASIC, the trimming circuits can correct the offset mismatch among channels in a large amplitude range.

On the other hand, the FAST discriminator relies only on the $Thr2_glb$, see Figure 3.3. During calibration, all channels of a module are set to respond to an specific pulse ampli-

tude; however, fluctuations ASIC-to-ASIC, in addition to the reduced correction range of the FAST discriminator trim circuit, makes necessary to set different $Thr2_glb$ values for each ASIC.

As a precedent, during the study of the $Thr2_glb$ transfer function, a group of channels exhibited an incorrect calibration, as shown in Figure 3.16. The distribution of threshold values among the non-calibrated channels is an expected consequence of the calibration procedure. When a channel cannot be properly calibrated, the trim assignments to the channels result in similar threshold levels across those uncalibrated channels.

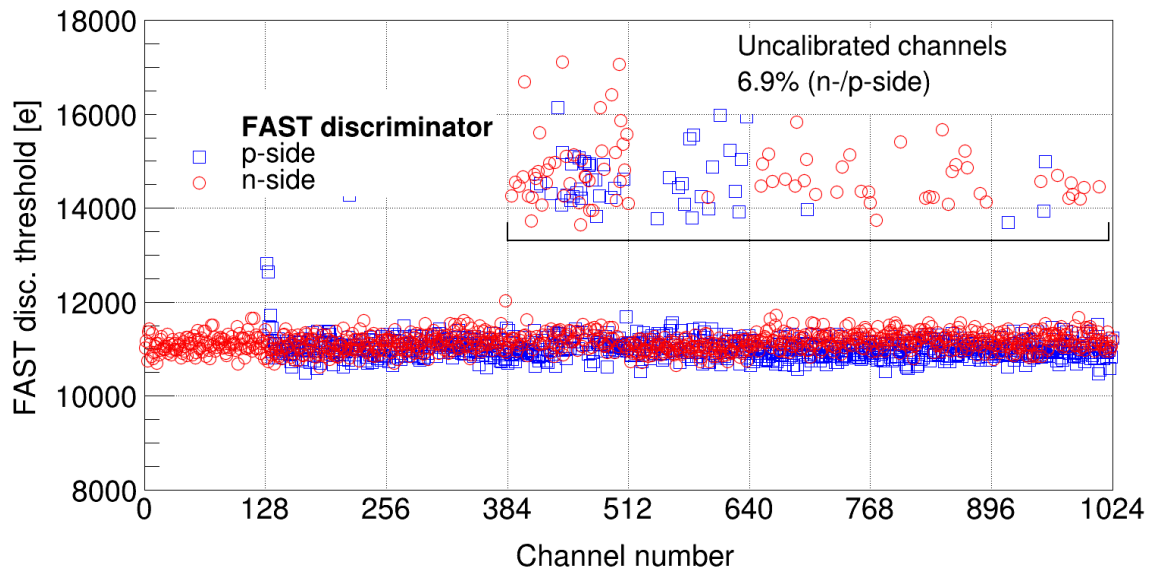


Figure 3.16: FAST discriminator threshold distribution for all channels across module CRT-01-PB during amplitude and timing transfer functions studies. A group of uncalibrated channels are also labeled.

In order to board the problem, a dedicated study was conducted for identifying $Thr2_glb$ settings that enables the calibration of the largest possible number of channels. For the study was used a prototype module, namely CRT-01-PB.

The study involves the scan of the FAST discriminator response as a function of the $Thr2_glb$ register. Injected pulse amplitude was kept fixed at 30 units of the internal pulse generator. The discriminator response was studied at three trim values (0, 36 and 63 LSB), which covers the default and the full correction range. This scan allow us to determine the correction range of the trim and to express it in units of the $Thr2_glb$.

Figure 3.17 shows a representative example based on one channel of one SMX ASIC of the CRT-01-PB module. The FAST discriminator response for the three trim configurations (0, 36 and 63 LSB) are shown at different colors (black, blue, red), respectively. The markers, given by the inflection point, represent the response express in units of $Thr2_glb$ and for further analysis used to define the full range correction. The width of the FAST discriminator response is given by the sigma value, that extend a bit the correction range defined by the $Thr2_glb$ and it is an element to have in consideration. The full correction range given by the inflection point and the sigma is represented by the shaded bar. As first approximation, the range is defined by the $Thr2_glb$ values in the configurations of 0 LSB and 63 LSB values of trim.



Figure 3.17: Threshold scan distributions for three trim configurations (0, 36, and 63 LSB) of based on one channels of one SMX ASIC. The curves show the FAST discriminator response as a function of the $Thr2_glb$ register. The extracted mean threshold values ($\mu_0, \mu_{36}, \mu_{63}$) and corresponding sigma ($\sigma_0, \sigma_{36}, \sigma_{63}$) are illustrate. The shaded band highlights the full correction range expressed in units of $Thr2_glb$ and sigma ($\mu_0 - \sigma_0, \mu_{63} + \sigma_{63}$).

Similar FAST discriminator response can be found for every channel of an entire module. Figure 3.18 shows for one SMX ASIC the correction range of every channel expressed in $Thr2_glb$ units, only $Thr2_glb$ values given by the inflection point are taken under consideration. In Figure 3.18a, the markers indicate the $Thr2_glb$ values under the default trim configuration, while the vertical bars span the range between the other trim configurations.

With the knowledge of the range of the FAST trimming it becomes possible to estimate the fraction of channels that can be correctly calibrated across an entire ASIC, for a given setting. In Appendix E the partial analysis code is presented. By scanning $Thr2_glb$ values, a profile of the calibrated channel ratio is performed and shows in Figure 3.18b. In it, a well defined window where all the channels can be calibrated is observed spanning from 19 LSB to 32 LSB of $Thr2_glb$. Outside of this optimal window the ratio decreases; however, it remains above 95% when the range is slightly extended from 18 LSB to 35 LSB. This indicates that most of channels can still be calibrated reliably within a moderately wider threshold range.

Analyzing the other ASICs, similar pictures are obtained. Figure 3.19 summarizes the $Thr2_glb$ window for each ASIC that allow the correction of $\geq 95\%$ of the channel on it. The Y-axis is labeled to distinguish between n-side (ASICs 0-7) and p-side (ASICs 0-7). The colored bars indicate the range of $Thr2_glb$ values for which a given ASIC achieves full (100%) or near full ($\geq 95\%$) of channels calibrated. The band colored in black highlights a common window for almost all ASICs, spanning from 22 LSB to 26 LSB of $Thr2_glb$. This range found as result of the study and without been looking for it was a pleasant surprise, and suggests the feasibility of using a single global $Thr2_glb$ setting for the entire

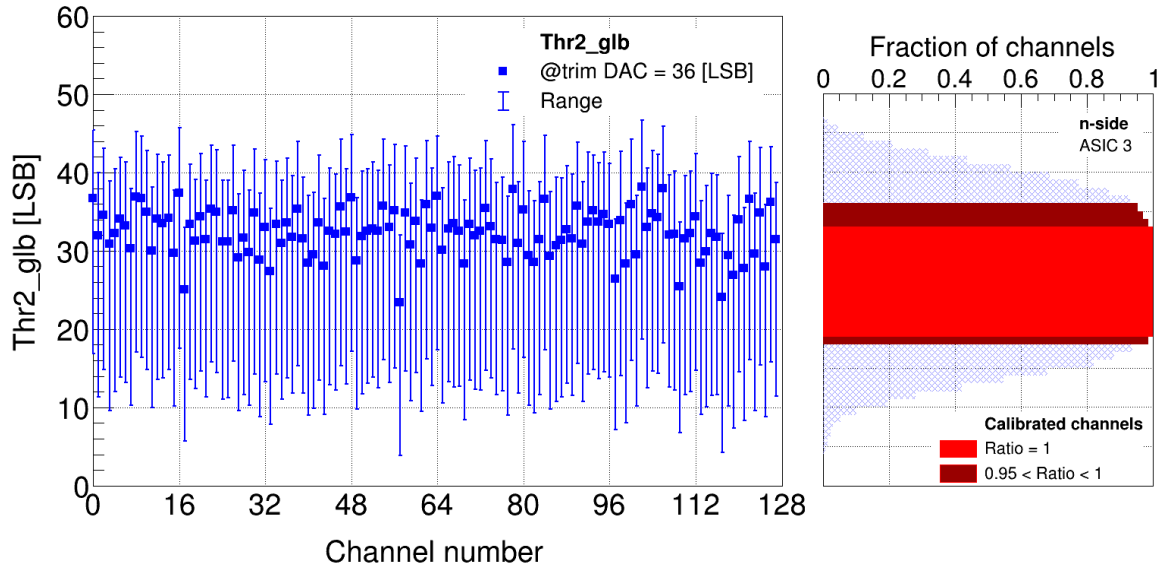


Figure 3.18: $Thr2_glb$ range for ASIC 3 of module CRT-01-PB. The markers represent the $Thr2_glb$ for a trim value of 36 LSB, while the whiskers represent the maximum $Thr2_glb$ that allow to calibrate each individual channel. Fraction of calibrated channels versus $Thr2_glb$ for ASIC 3. A plateau is observed for 19-32 LSB, indicating a window where all channels can be calibrated.

module. For the case of ASIC 0 in p-side, this contains the group of channels called Z-strip, which exhibit significantly higher noise compared to the rest of the channels. As a result, these channels typically require higher $Thr2_glb$ values.

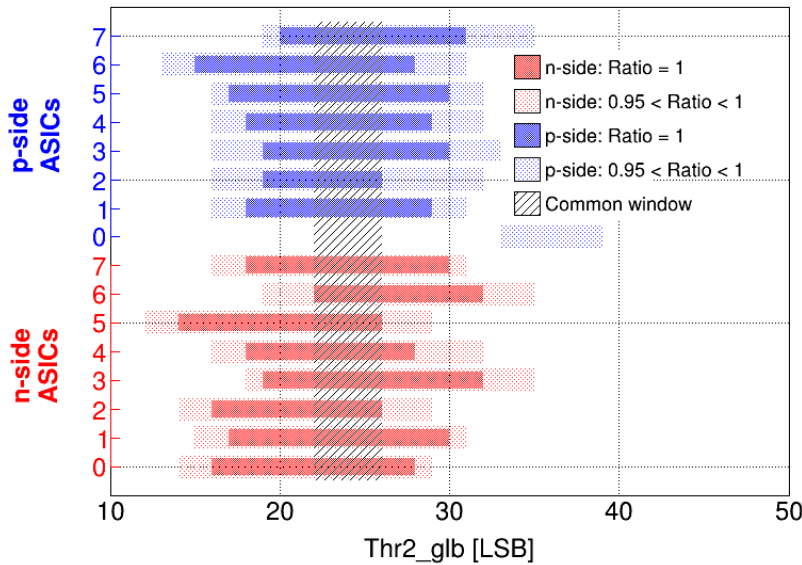


Figure 3.19: $Thr2_glb$ window for the FAST discriminator for each ASIC of the module CRT-01-PB. The bars represent $Thr2_glb$ range with ratio > 0.95 of channels calibrated.

Another evaluation is presented in Figure 3.20, where the uncalibrated channels are shown for both experimental measurements and predicted data. The open squares represent experimental data, while filled black squares indicate predicted results. The analysis compares the $Thr2_glb$ value applied during the FAST discriminator calibration versus the individual range identified for each channel. If the set $Thr2_glb$ value is found outside the valid range for a given channel, that channel is predicted to be uncalibrated.

In Figure 3.20, it can be seen that five ASICs are consistent in zero uncalibrated channels for both experimental and predicted data. Additionally, two ASICs display consistency with only two uncalibrated channels in both cases. In other cases, the number of uncalibrated channels predicted exceeds the number observed experimentally. This can be partially explained due to the correction range used for the analysis are limited to the $Thr2_glb$ setting given by the trim values (0 LSB and 63 LSB); however, the correction range can be spanned by the sigma of each as shown in Figure 3.17. Despite of that, the simulation still correctly identifies those uncalibrated channels, such as in ASICs 3, 5, 6 and 7. There are also channels that were not predicted to be not calibrated, but they did. In general, the level of agreement between the predicted and the experiment is considerably good.

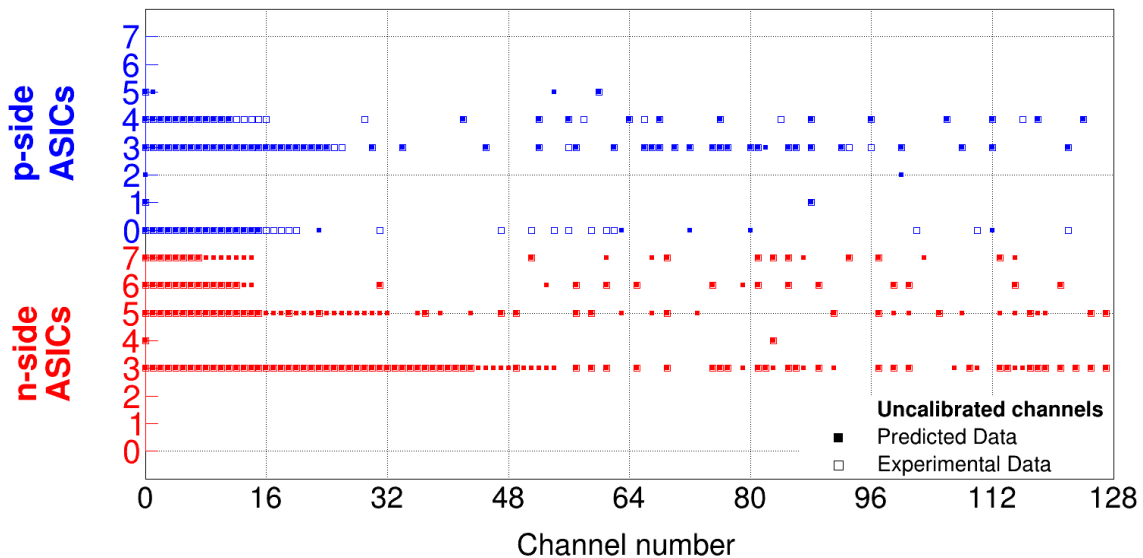


Figure 3.20: FAST discriminator uncalibrated channels predicted and identified from measured data distributed for each ASIC of the CRT-01-PB module.

Following this study, the CRT-01-PB module was recalibrated using $Thr2_glb$ values selected within the identified valid range. The results are shown in Figure 3.21. While a few channels remain uncalibrated and also, appear a different ones, their number has been significantly reduced, demonstrating the effectiveness of the refined threshold selection. In addition, a valid proof of the possibility to use a single global $Thr2_glb$ register.

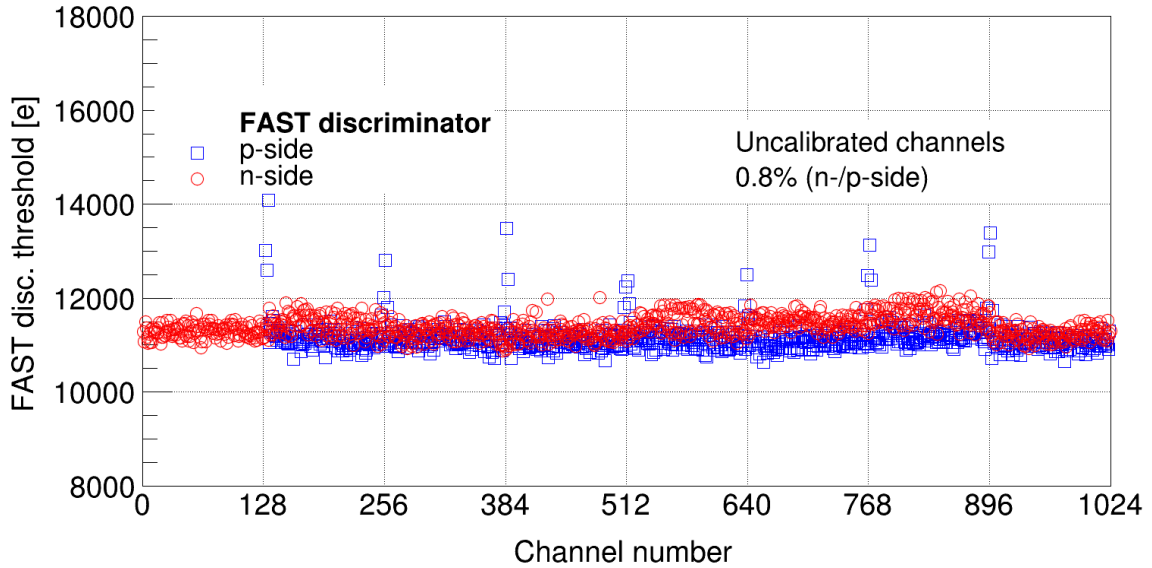


Figure 3.21: FAST discriminator threshold distribution for all channels across module CRT-01-PB after implement a common *Thr2_glb* setting. A total of 0.8% of channels remain uncalibrated (excluding the Z-strips).

3.8 Quality control of the calibration settings

As a final evaluation of the ADC calibration using the SAR method, 10 modules of the pre-series production were calibrated. The features and performance of these modules will be discussed in more detail in chapter 4.

This section does not intend to analyze calibration parameters such as the ADC gain or threshold. Those topics are covered comprehensively in the next chapter. Instead, the focus of this section lies on specific aspects related to the ADC trim calibration matrix. Examples include the number of uncalibrated discriminators and the average difference between the default trim matrix (all discriminators trim value equal to 128 LSB) and the one obtained after applying the SAR calibration method.

Figure 3.22a shows the percentage of discriminators that required correction from the default trim value, which is established at the beginning of the calibration procedure. The data corresponding to 10 modules are displayed as a function of the channel number (0-127) in the ASICs, for both the n- and p-side, respectively. With the same aim, it can be observed in 3.22b how the correction are distributed among discriminators. Overall, the results indicate homogeneous behavior in the correction process between channels and discriminators on both sides.

Figure 3.23a presents the cumulative distribution of the corrected trim normalized to the total number of discriminators per channel per ASIC. It is shown as a function of the difference in correction with respect to the default value, and it also considers the corresponding signal polarity. It can be observed that 95% of all discriminators on the n-side are calibrated with a trim difference below 28 LSB, while for the p-side, a similar percentage is achieved with 20 LSB. In the figure, it can be seen that all discriminators were calibrated; however, the saturation for the n- and p-side was found in 99.97% and 99.92%, the missing percentage corresponds to 81 and 258 discriminators, respectively.

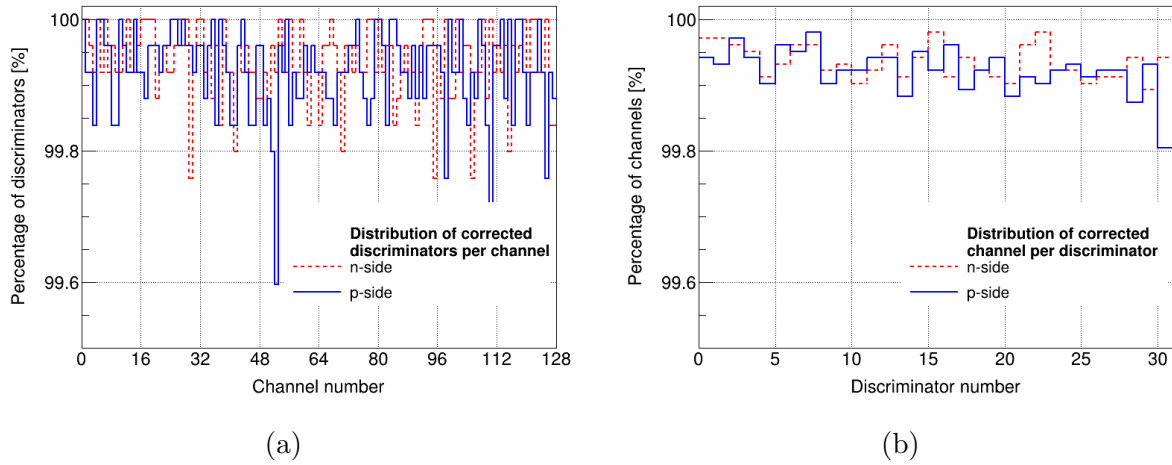


Figure 3.22: (a) Number of discriminators that required correction from the initial calibration matrix, distributed per channel. (b) Number of channel corrected distributed per discriminator.

These discriminators are considered outliers. It means that the adjusted trim differs from the default value by more than 60 LSB, or that they could not be calibrated at all.

The number and distribution of outliers for each channel were analyzed for both signal polarities. In either case, the number of them is counted on each channel and displayed in Figure 3.23b. For the p-side, the outliers are highly concentrated in just a few channels, in contrast to the n-side, which shows a broader distribution. Some specific channels, especially visible for p-side, show a large number of outliers. These are mostly related to very noisy channels or broken one. However, most of the channels are calibrated according to expectations.

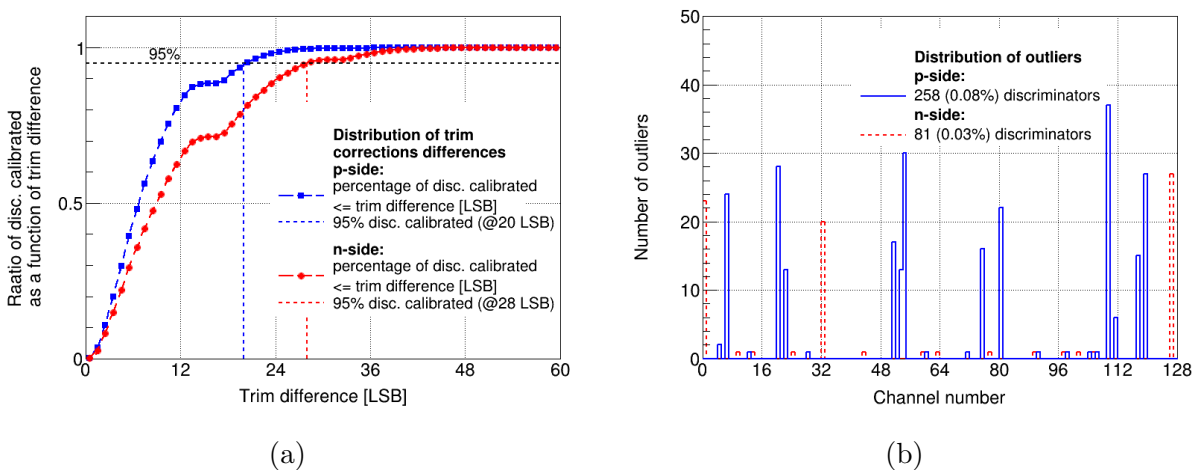


Figure 3.23: (a) Cumulative distribution of trim correction differences for all discriminators, channels, and ASICs of the 10 tested modules. Each point represents the fraction of discriminators whose trim correction differs from the default value by less than or equal to the given amount in LSB. (b) Distribution of outliers across channels, with red and blue representing the n- and p-side, respectively.

Figure 3.24 shows the average trim difference between the default ADC trim matrix and the one obtained using the SAR calibration method. The data is reported for each ASIC in every module, and it also illustrates the clear difference between odd and even channels for each polarity. In this representation, outliers are not included. In both cases, the error bars reflect the standard deviation of the distribution within each group. The black dashed line indicates the average between the odd and even channels.

On the n-side, larger odd-even deviations are observed, particularly in the module E16-108-PB, where all eight ASICs exhibit consistently elevated differences with respect to the default trim. This behavior is attributed to the non-optimal selection of the $VRef_P$ and $VRef_N$ potentials at the beginning of the calibration procedure, requiring larger trim adjustments to achieve a proper outcome. In contrast, the p-side shows relatively small and consistent deviations between odd and even channels across most modules. A notable exception is module E16-107-PA, where one ASIC displays a significant deviation, This effect is similar to the one explained above for the n-side.

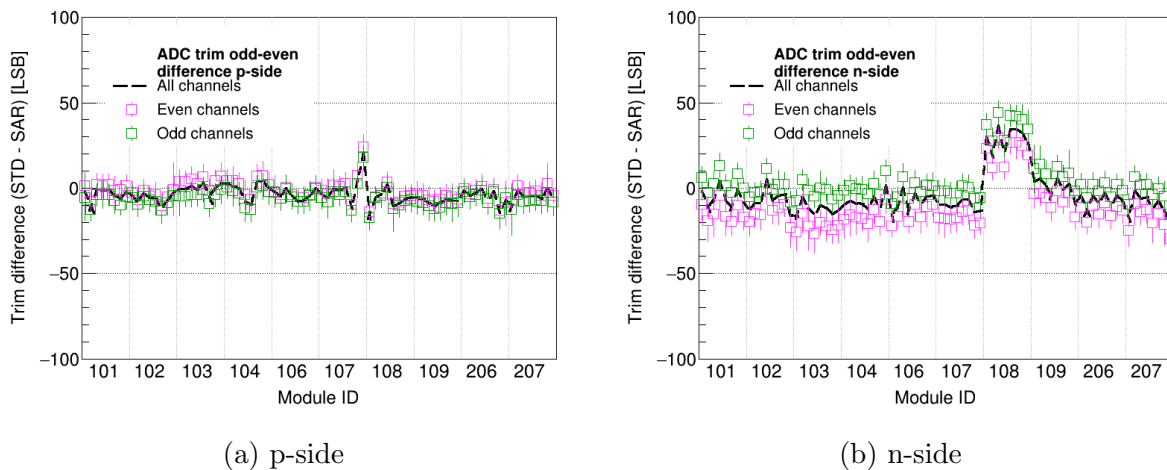


Figure 3.24: Average trim difference between initial trim matrix and the calibration matrix using SAR method for odd and even channels across ten modules: (a) p-side and (b) n-side.

3.9 Summary towards series testing

This chapter presents the development, optimization, and validation of the calibration procedure for the SMX ASIC, with the aim of improving both precision and efficiency for large-scale module characterization in the STS detector system. The standard ADC calibration method, although accurate, was limited by the time-consuming coarse-scan stage. To address this issue, a SAR algorithm was implemented as an alternative, replacing the exhaustive scan with an iterative binary search that rapidly converges on the threshold value. A Comparative analysis demonstrated that the SAR method achieves the same level of accuracy as the STANDARD approach, with DNL and INL performance indicators remaining below 0.4 LSB, while reducing the calibration time significantly. Furthermore, 50 injected pulses were identified as the optimal configuration to balance precision and processing time.

The optimization of the parameters of the algorithm SAR such as number of iterations, search width, and fine-scan range was also performed. The combination of 10 iterations, a width of 14 LSB, and a fine-scan range of 12 LSB yielded a reduction of approximately 60% in total calibration time compared to the STANDARD method while maintaining equivalent accuracy.

A broadcasting approach was successfully implemented based on the SAR calibration method. With this method, it was possible to reduce the calibration time by approximately 50% compared to the sequential implementation.

A detailed study of the transfer functions for the ADC and FAST discriminators was carried out. The results confirmed a well-defined linear relationship between DAC settings and the corresponding effective thresholds. The extracted transfer functions exhibited a slope ratio of approximately two between the ADC and FAST discriminator threshold settings, consistent across n- and p-side. This relationship establishes the proper correlation between the amplitude and timing thresholds.

A further study investigated the feasibility of applying a single global FAST discriminator threshold (*Thr2_glb*) for an entire module. Scans of *Thr2_glb* across multiple trim configurations identified an optimal range between 22 LSB and 26 LSB where 100% of the channels could be calibrated, excluding the so-called Z-strips.

Finally, as a large-scale validation, ten pre-series modules were calibrated using the optimized SAR method. The analysis of the achieved quality was focused on the trim calibration matrix, including the number of corrected and uncalibrated discriminators, as well as deviations from the default trim configuration. The results showed a uniform correction behavior across channels and discriminators, with outliers being limited to a small fraction of discriminators, below 0.1% for both polarities. On average, the p-side required smaller trimming adjustments, a maximum of 20 LSB, to calibrate 95% of all discriminators, while for n-side, a maximum of 28 LSB. In the context of odd-even channels trim difference, both sides showed a consistent separation, particularly small for the p-side.

Chapter 4

STS pre-series modules for the E16 experiment

This chapter presents the testing of prototypes/pre-series modules that have been specifically designed for installation in the E16 experiment at the J-PARC. A standardized testing protocol was developed with a focus on quality control, to ensure the reliable performance of the modules as a tracking layer of the E16 experiment, but also in the final STS detector. Observables such as noise levels, charge calibration, signal readout, and missing channels are shown as a part of the testing.

4.1 The E16-STS module

The STS project during its pre-series production prepared a total of one prototype and ten modules conceived for participation in the E16 experiment. Each group involved in the project, participated as a training for the upcoming STS series modules production.

Due to geometric constraints of the E16 experiment [57], the modules were assembled using a sensor with a size of 62×62 mm² and microcables of length between 12-20 cm (45 cm in case of the first prototype module). The design features of every E16 module are summarized in Table 4.1. The FEB-8, used for the objects corresponds to the third version (FEB-8v3) which are part of the pre-series modules towards series production of the STS. The v3 of the FEB-8 has unique features seen for the first time in pre-series modules: it uses a new data cable connector and include the HV filtering (2 stages RC-filter) on board. In addition, the signal return path was implemented between the boards of n- and p-side using a small multiwire cable. For the case of the prototype module 02-T1-6-PB, the version of the ASICs was v2.1 and the FEB-8 used the old configuration of 1.8 V LDO and diode to provide the expected 1.2 V.

A unique naming convention was used for the modules, specifically for their use in the E16 experiment. For instance, “E16-102-PB” encodes essential information: “E16” denotes the experiment, “102” specifies the module’s geometrical position: where “02” indicates the ladder position inside the E16-STS chamber, “1” the sensor’s placement within the ladder, and “PB” the type of FEB-8 assigned to the p-side of the sensor. As a consequence, this determines the orientation of the data connector after the modules are mounted on the ladder. Figure 4.1a shows one of the modules assembled for E16 experiment, and two of them mounted on each corresponding ladder. The Figure 4.1b

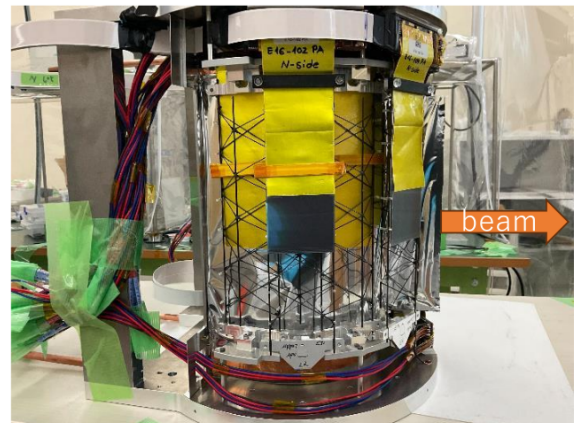
Table 4.1: Description of the geometrical features of sensor sizes and microcable length, FEB-8 type assigned to p-side and corresponding ladder for E16-STS modules.

Ladder No.	Module ID	Microcable length [mm]		FEB-8 type [p-side]	Sensor size [mm ²]
		n	p		
-	02Tl-6-PB	459	449	PB	62×62
L1	E16-101-PB	142	131	PB	62×62
L2	E16-102-PA	121	121	PA	62×62
L3	E16-103-PB	172	163	PB	62×62
L4	E16-104-PA	121	121	PA	62×62
L6	E16-106-PB	207	207	PB	62×62
	E16-206-PA	121	121	PA	62×62
L7	E16-107-PA	121	110	PA	62×62
	E16-207-PA	172	163	PA	62×62
L8	E16-108-PB	121	121	PB	62×62
L9	E16-109-PA	142	131	PA	62×62

shows a lateral view of the E16-STS chamber with the modules installed on it. For the particular case of the prototype 02Tl-6-PB, “02” refers to the middle position in the ladder, the letter “T” signifies a testing designation, while letter “l” determine the orientation of the data connector once the module is mounted on the ladder. The final digit serves as a mere assembly serial number or counter.



(a) E16-STS module



(b) E16-STS chamber

Figure 4.1: (a) Illustrate a module before and after be mounted on a ladder. (b) A lateral view of the E16-STS chamber, several ladders with their modules are visibles.

4.2 Basic considerations for a testing protocol for series production

The STS module could be considered as a monolithic and complex object, built through a series of multiple steps. During the assembly process, various components, such as the ASIC, sensors, LDOs and FEBs are rigorously tested. To ensure the correct operation of the CBM experiment, particularly the STS detector with its 876 modules, it becomes necessary to develop a testing protocol where a comprehensive characterization procedure is performed for every assembled module. This procedure should take into consideration all modules functionalities and their performance under stress conditions.

Once the modules are fully assembled, a careful characterization of each of them is the next step. To carry out this task, a testing protocol inherited from [49] was optimized and used to characterize modules produced for E16. The first control step is a visual inspection searching for possible damages that could occur during the handling and transportation. The decision in case of finding a critical damage, such as a mechanically broken sensor or damaged microcable is ruled out as a failure module.

After the modules have been visually inspected and have met the requirements, they are mounted on carriers [58], where the functional characterization is carried out, illustrated in Figure 4.2a. The carriers provide a safe and stable platform for handling this fragile objects, ensuring that no components are compromised during the characterization process. The carriers are low-budget objects made with two frames of aluminum, one of them which features holes for securing the FEB-8, and spacers to maintain structural integrity. An essential component of the carrier is the “sensor holder”, fabricated from plastic using laboratory 3D printer. The sensor holder consists of two Y-shaped legs that can slide along the aluminum frames, allowing to accommodate different microcables length. Sensor holders are mainly fabricated in two sizes, which allow accommodating all STS sensor sizes. To ensure the sensor’s light tightness, the carrier is enclosed within a protective covering called as “black sleeve”. For interfacing with power systems, the carrier is equipped with a plastic back panel that integrates two LEMO connectors of 8 and 4-pins for Low Voltage (LV) and HV inputs, see Figure 4.2b.

Once the modules have been installed on the carriers, the functional tests are followed. They consist of two main steps: the measurement of the current-voltage characteristic of the sensor (IV measurement), and a full performance characterization of the module. The latter include evaluating key parameters of the ASICs in the FEB, calibrating the module and study the detector response to radioactive sources.

4.3 Current-Voltage characteristic

The first step in the testing protocol is the measurement of the Current-Voltage (IV) of the sensors. Silicon sensors operate after reaching the region of full depletion in a reverse bias voltage mode. It is important to identify the full depletion value, as it dictates the minimum operational voltage of the sensor. In addition, the overall Equivalent Noise Charge (ENC) decreases after full depletion [59]. The magnitude of the sensor current is one element that is important to keep an eye on, since it is related with shot noise, equation $e_{in}^2 = 2eI_s$. Large leakage current values can be connected with a non-desirable significant

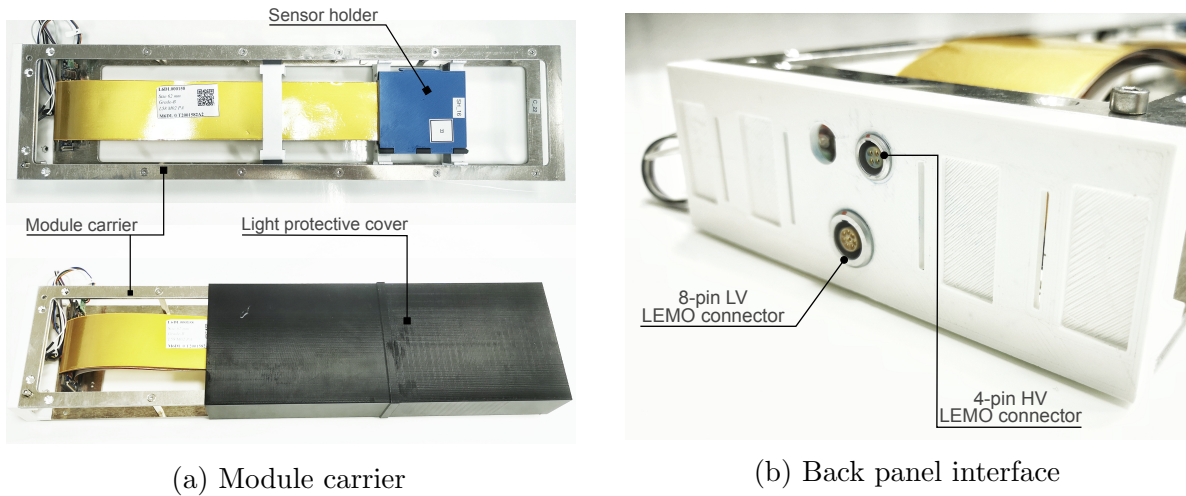


Figure 4.2: (a) Photograph of a module carrier, where an E16-STC module have been installed. The most important structures of the module carrier are labelled. (b) Back panel interface with the integrate LV and HV LEMO connector.

noise. Another element that is needed to check during this test is the maximum reachable bias voltage. During the modules operation, it is expected to suffer radiation damage to a greater or lesser extent in the E16 or CBM detectors, with a negative impact in the charge collection efficiency and the overall noise [60]. In the specific case of the sensors to be used in the construction of the STS detector, four quality grades were assigned during the quality assurance. The grades, based on the IV measurements result, were also according to radiation damage specification and charge collection efficiency study. They are specified as following: up to, A = 500 V, B = 350 V, C = 250 V and D = 200 V. Despite the modules will be exposed to a certain level of irradiation in the E16 experiment, it is not comparable to the final STS environment and as a consequence their sensors were tested to a maximum of 150 V bias voltage.

It can happen that a module presents issues in at least one of the elements mentioned before. The decision in that case is to declare the module as failed and subsequently discarded.

4.3.1 Experimental setup

The test station where the IV measurements were made, comprises two Keithley 2400 power supplies, each one of them connected to a side of the module (n- and p-side). The voltage was applied to the sensors symmetrically, until they reached the maximum of 150 V. For controlling the hardware and setting the desirable configuration, an application based on LabVIEW from National Instruments was implemented [61]. This tool serves also as a monitor of the current-voltage characteristic in live-time. The Figure 4.3 shows a picture of the IV testing setup.



Figure 4.3: Test station for the IV measurements. The two Keithley 2400 power supplies and the computer station with the LabVIEW application for controlling and monitoring are shown.

4.3.2 Results

The satisfactory results of the current-voltage characteristic test for the ten E16-STs modules, as a part of pre-series production, are shown in Figure 4.4. It is possible to observe that for the modules the depletion voltage is reachable at the level of around 60 V, after which a long operational plateau is visible. In addition, at 150 V the leakage current of each module is below 3 μA . The IV measurements have not been corrected by temperature, which is one of the reasons that causes different levels of leakage current between sensor of the same size. The other reason is related to the intrinsic properties of each sensor that determine the absolute current values. In addition, as main observable difference is seen between module E16-103-PB and the others, where a linear behavior beyond reaching the full depletion voltage is appreciated. This is a consequence of the configuration used for measuring the current-voltage curve for the E16-103-PB module and can be explained as follows: as the LV power supply was connected and it is not entirely floating, its protection circuit provides a resistive leakage path to the biasing circuit. This result in a linear ohmic behavior proportional to the resistance of the protection circuit.

4.4 Functional test and electrical performance

After completing the IV test, the modules are brought into operation to evaluate its performance. They are connected to the LV supplies to check the power consumption of each FEB. Even if the consumption is partially distributed randomly due to the fact that there is not configuration yet of the electronics, values above 1.2 A and 1.5 A are expected for the 1.2 V and the 1.8 V LV domain, respectively. In addition, it is possible to check if there is any short-circuit between the FEBs.

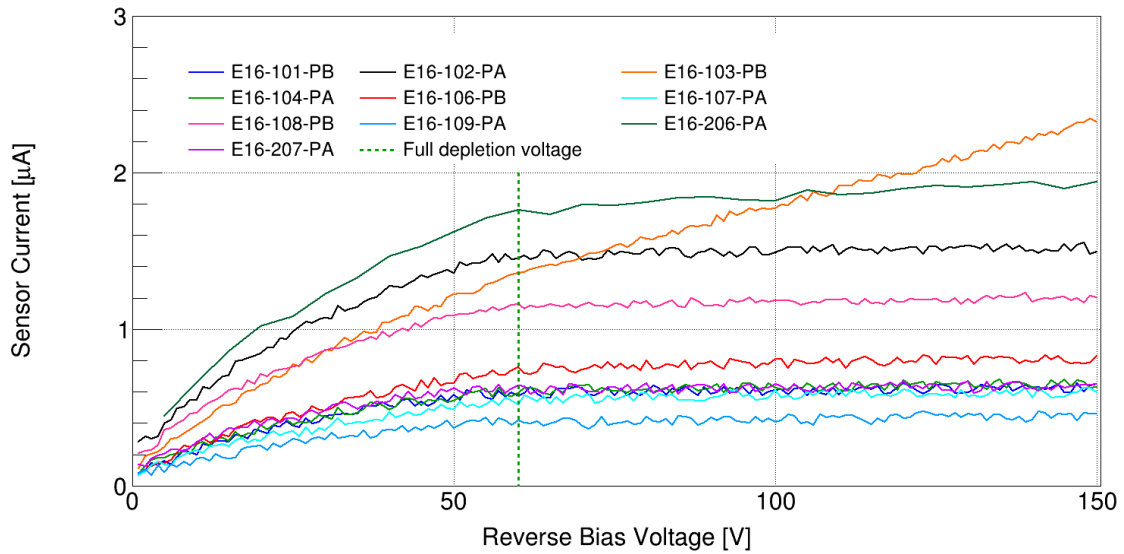


Figure 4.4: Current-voltage sensor measurement for the ten E16-STs modules. The full depletion voltage at 60 V is shown with a vertical dashed line.

Once no issues are found, the data link initialization and synchronization are launched, allowing the user to communicate with each ASIC on the module. A not responding ASIC automatically situates the module as a failed one. In the case of the E16-STs module, each ASIC has two uplinks connected, however, our testing readout chain admits only one. During the detector commissioning in Japan, all uplinks were cross-checked. The situation is different for the final STS, where according to the data rates, sensor size and station, the number of uplinks is going to have different configuration such as one, two or five. Although this is not a disqualifying criteria, it is important to note for the final operation of STS. At the same time, the unique ASIC e-fused identification number is read out.

The procedure continues with the setting of the registers configuration parameters, and multiple write/readback actions. The power consumption after configuration, temperature and VDDM (ASIC potential to evaluate the analog response of the CSA) values are verified. The consumption expected after ASIC configuration for the 1.2 V and 1.8 V is around, 2.5 A and 2.2 A, respectively. For VDDM values between 1.1 V and 1.3 V are considered as good. If VDDM values are found out of the range, additional actions are needed.

Finally, the sensors are biased at the operational value of 150 V, and the calibration of the AFE circuits is conducted. This step is essential for understanding and analyzing the measuring data, and it aims to determine channel-to-channel threshold corrections. The result of the calibration procedure should mostly remain stable over the operation lifetime of the detector, with the calibration parameters stored for future usage. The calibration procedure is explained in more detail in section 3.4.1.

An important parameter for evaluating the performance of the module is the ENC. This step involves the estimation of the noise and its comparison with the analytical expectation. It also allows identifying noisy and broken channels. The noise level is extracted from a pulse amplitude scan or $S - curve$ scan.

The last stage of the testing procedure involves to check the detector performance in terms of signal readout. The homogeneity of sensor performance over its entire area is performed by checking the sensor response with a source. Subsequent analysis includes source reconstruction, distribution of the cluster position and confirmation of noisy and broken channels measurement. Moreover, the time synchronization is verified through the time correlation of digitized hits and clusters.

4.4.1 Experimental setup

To evaluate the functional performance of the modules, a combination of specialized equipment and software was employed. Power supplies were used to provide both LV and HV. Specifically, the WIENER MPOD OMPV.8016 of an 8-channel module was used as the LV power supply [62], while the HV was supplied by an ISEG device version EHS 203 05x-K01 Customized [63]. These power supplies are the same to be used for the operation of the STS detector.

The FEB-8 temperature was maintained under control with a simple, but efficient cooling system composed of three basic elements: a cooling block, connecting pipes, and a LAUDA chiller [64].

The readout chain used in the module test consists of three main elements, and it can be seen in Figure 4.5:

- the FEB-8 in the module, which interfaces the silicon detector, processes analog signals and provide the digitized information;
- the C-ROB, which provides data aggregation and an electric-optical interface;
- the DPB, responsible for implementing the readout and control protocol.

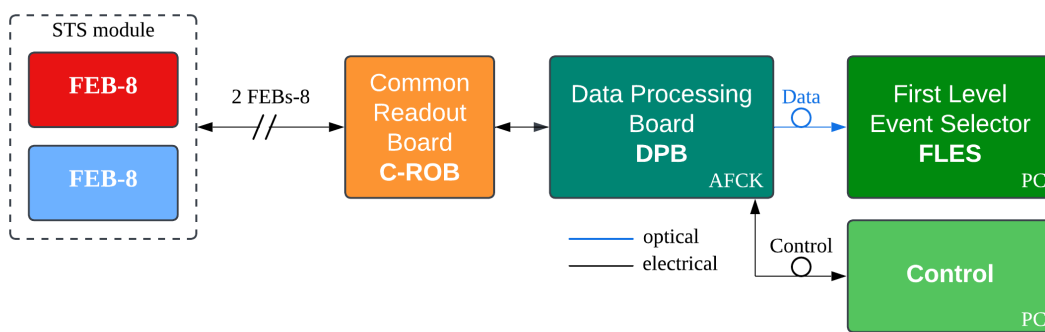


Figure 4.5: Schematic representation of the E16-STS modules testing readout chain. The E16-STS module connected to a C-ROB. The C-ROB transmits data to the DPB via electrical connections. Processed data are sent optically to the FLES, while control signals are exchanged electrically between the Control PC and the DPB over the IPBus protocol.

A Python-based code was developed to manage the control and full readout functionalities of the modules, such as: synchronization, configuration, calibration, and data readout.

4.4.2 Results

In this section, the overall results for the 10 E16-STS modules subjected to a comprehensive characterization are presented. These modules, comprising a total of 160 ASICs, demonstrated reliable performance throughout the testing process, with all ASICs and data links responding as expected. Detailed measurements were performed to evaluate the modules' operational stability, including assessments of the temperature and VDDM potentials. Both parameters were measured for each ASIC using the built-in diagnostic circuit, as described in [65], with calibrated transfer functions of each of those [66, 67].

Figure 4.6 summarizes these measurements, highlighting the consistency between modules. Additionally, this analysis provides valuable insights into the behavior of the modules under nominal conditions, forming a solid foundation for their use in future experimental setups. In the plots, the markers identify the average value per module. The error bars indicate the minimum and maximum values. In general the modules show similar behavior both for temperature and VDDM. The module's average temperature was measured to be 56 °C, with individual module temperatures ranging approximately between 50 °C and 70 °C. Additionally, extreme cases, such as the minimum and maximum temperatures, indicate that most values are close to the average. However, module E16-103-PB exhibits a concerning trend with its maximum temperature. This is likely explained by variations in the transfer function of each ASIC. Due to each ASIC has its own transfer function and the one used is the average of all of them, a degree of uncertainty in the measurement is introduced.

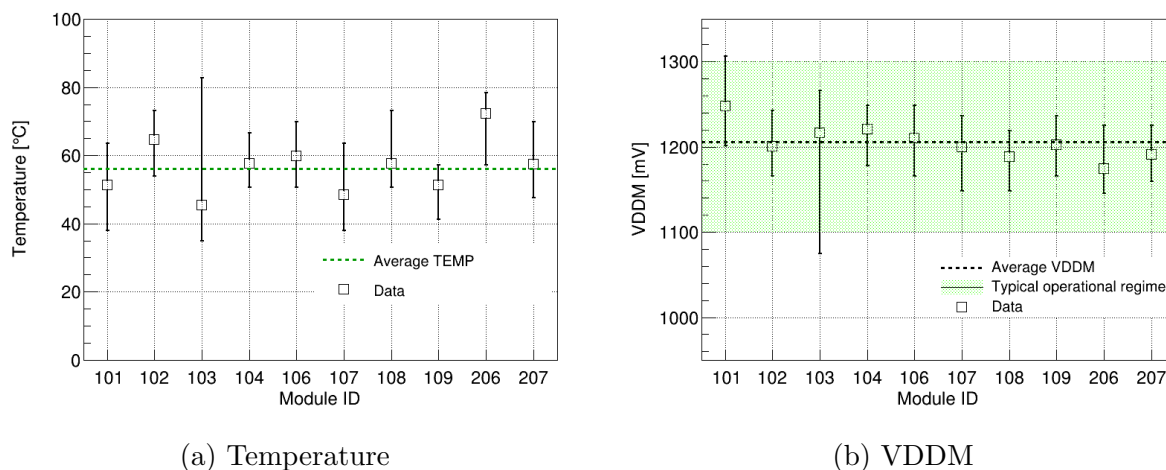


Figure 4.6: Temperature and VDDM potentials for each module measured with the built-in diagnostic circuit. Every point is the average among 16 ASICs and error bars represent the minimum and maximum measured values.

The average VDDM value was 1206 mV, which is close to the expected 1200 mV. However, one ASIC in modules E16-101-PB and E16-103-PB shown VDDM values out of the typical operational regime, implying for future operation adjustments in their configuration parameters to bring it into the operational limits.

Calibration of the ADC

The Figure 4.7a shows for an exemplary module, E16-106-PB, the distribution of the ADC gain among all the channels for the 16 ASICs. The average gain values for each side corresponds to 2098 e/LSB and 2101 e/LSB, for n- and p-side respectively, and they are shown in Figure 4.7b. Similarly, the threshold distributions for each side of the same module are displayed in Figure 4.8a and Figure 4.8b. The average thresholds values are 9205 e and 9130 e for n- or p-side, respectively, and their threshold spread of 180 e and 228 e. This is a remarkable good result if we consider that the amplitude of 1 LSB of the pulse generator is 350 e.

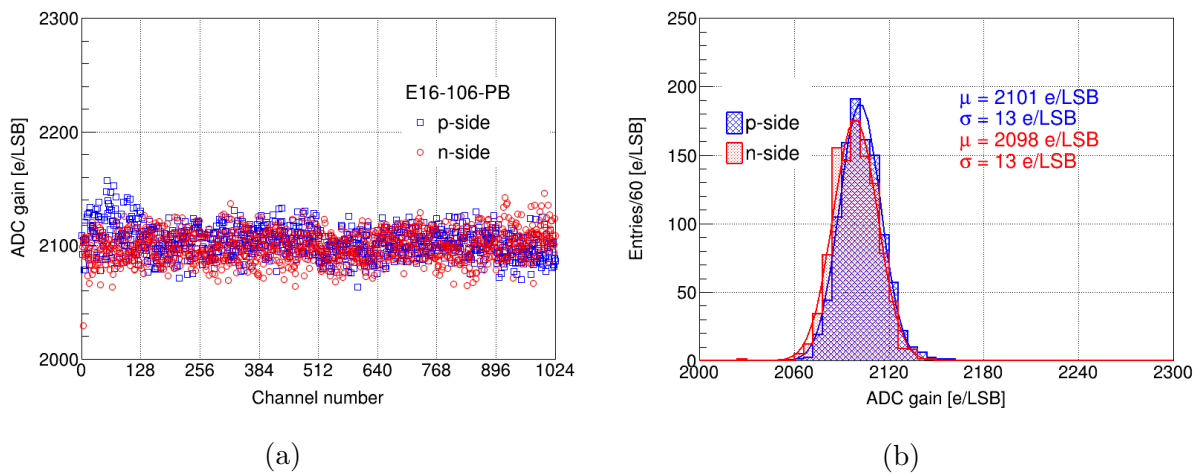


Figure 4.7: (a) ADC gain distribution for all channels across module E16-106-PB. (b) ADC gain corresponding histograms, with mean and sigma values determined for each side through a Gaussian fit.

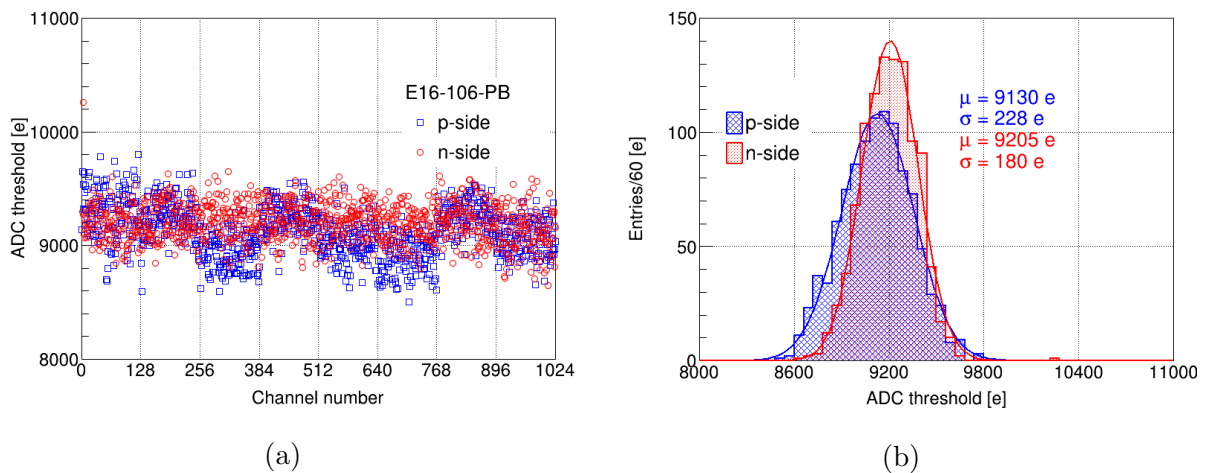


Figure 4.8: (a) ADC threshold distribution for all channels across module E16-106-PB. (b) ADC threshold corresponding histograms, with mean and sigma values determined for each side through a Gaussian fit.

Initially, the thresholds were set to high values to ensure better performance of the calibration procedure, due to its dependence with the noise level. It is important to note that not all modules were calibrated at the same threshold. As part of the pre-series production we aimed to explore the feasibility of calibrating and operating them at lower thresholds too. This adjustment was made with the intention of evaluating the potential to achieve enhanced performance in the upcoming series production, and also during STS operation. Nevertheless, the ADC gain remained the same for the entire set of modules. To bring all modules to the same threshold during the final operation, threshold adjustments could be later on applied using the $VRef_T$ reference potential shown in the previous chapter.

The gain and threshold spread, within approximately 1% and 2% for each module side, are considered sufficient to demonstrate a proper calibration of the channels, and indicate that the calibration procedure works effectively, minimizing deviations and ensuring uniformity across the channels. Such performance guarantees the correct module operation of the E16 experiment and in the future STS detector.

ENC study for E16-STC modules

The ENC across all channels for the exemplary module E16-102-PA is shown in Figure 4.9. The measured noise levels, 776 e and 781 e for n- and p-side, are in accordance within 20% with the analytical expected value estimated based on the total capacitance of the module [42]. This value equivalent to 631 e, is calculated from Eq. 4.1 and it takes into account the contribution of each element of the module to the total capacitance, where L_{sensor} and L_{cable} represent the dimensions of the sensor and microcable. The values 1.17 pF/cm and 0.38 pF/cm correspond to the measured overall capacitance per unit of length for sensor and microcable respectively [42]. In this particular module, $L_{sensor} = 6.2$ cm and $L_{cable} = 12.1$ cm, respectively; the value of 350 e noise is the intrinsic noise of the ASIC and it is also displayed together with the expected one, using dashed lines in Figure 4.9.

$$ENC[e] = \left[\underbrace{L_{sensor} \cdot 1.17 \frac{\text{pF}}{\text{cm}}}_{\text{sensor}} + \underbrace{L_{cable} \cdot 0.38 \frac{\text{pF}}{\text{cm}}}_{\text{microcable}} \right] \cdot 25 \frac{e}{\text{pF}} + \underbrace{350 e}_{\text{ASIC}} \quad (4.1)$$

In Figure 4.9, the distribution of ENC for each side of the module allows us to distinguish different features. Odd-even channel discrepancies in terms of noise, are visible in more detail at the ENC distributions plot in Figure 4.10a. The difference is typically related to the topology of the signal lines and the position adopted by the microcables. In each ASIC, the signals for odd and even channels are routed on different microcables. The variation in space between them and the shielding layers impacts the overall effective capacitance of each signal line in the cables. As a result, the noise level for the odd and even channels is slightly different. Another characteristic observable in Figure 4.9 constitutes the larger noise for the first channels of the p-side. These strips, referred as Z-strips, are connected via a second layer of metalization. As a result, they present a larger routing and in consequence, a larger capacitance, increasing the noise for this group of channels. For Hamamatsu silicon sensors, this capacitance has been measured to be around 17 pF [42]. However, after the test of the 10 modules, the recommendation for

more accurately estimating the ENC for the Z-strips is to use a value closer to 20 pF, see Figure 4.10b. The estimation is made by calculating the difference between the average noise for the so-called Z-strips ($ENC_{Z-strip}$) and the average noise for all other channels of p-side (ENC_{p-side}). The error bars represent the contribution of the sigma of the noise distributions and the 10% error level considered for the factor 25 e/pF. This factor relates the ENC_{CSA} for different input capacitance.

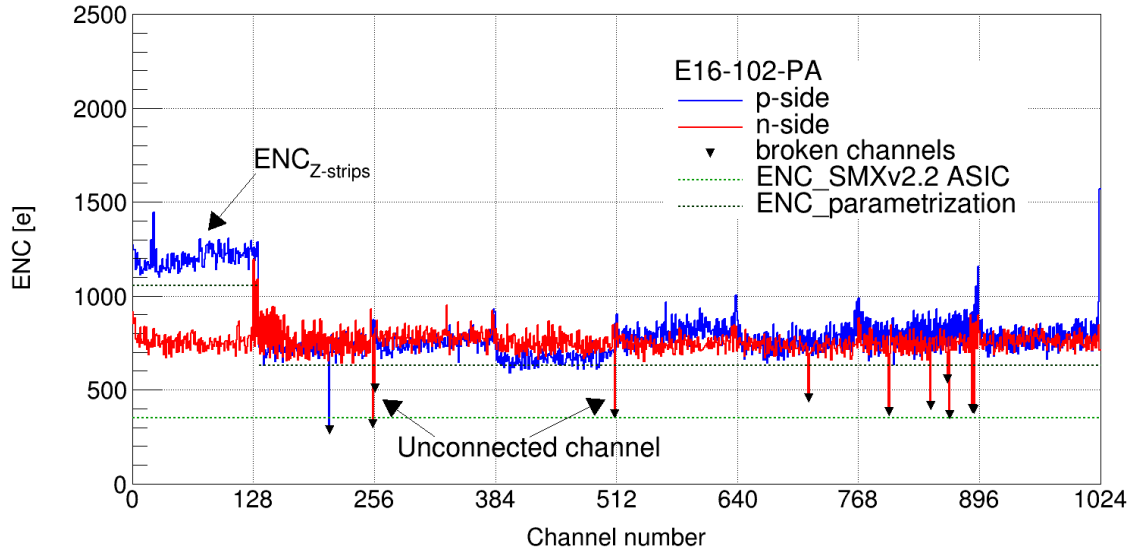


Figure 4.9: Noise across all channels for the E16-102-PA module. The red and blue lines represent the n- and p-side channels, respectively. The green dashed lines indicate the expected ENC from the SMXv2.2 ASIC and the ENC parametrization. Unconnected channels are marked with black triangles. The higher ENC observed for the Z-strips is also labeled.

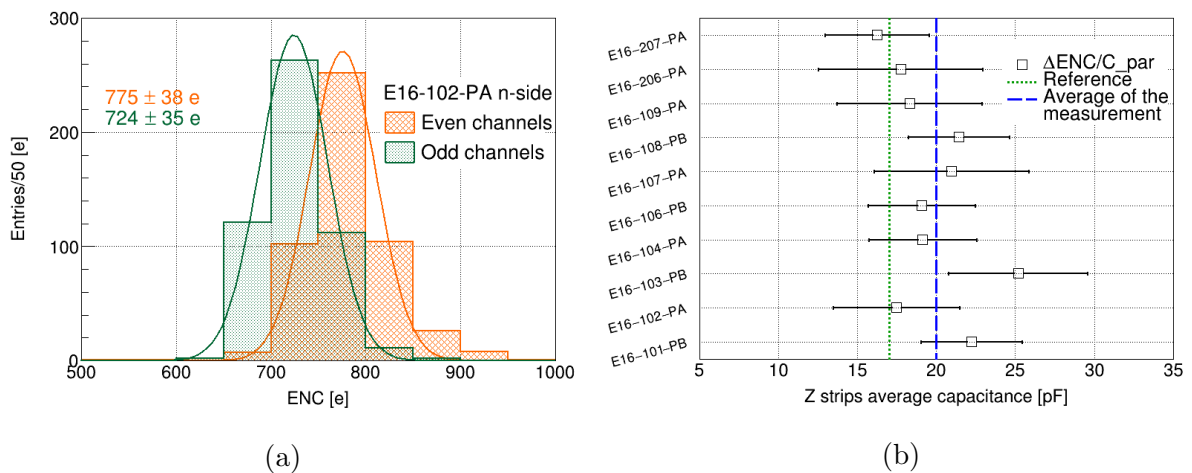


Figure 4.10: (a) Difference between odd and even channels on module E16-102-PA. (b) Z-strips average capacitance calculation based on the ENC measurement.

Figure 4.11 presents a summary of the ENC for the 10 tested modules. The markers indicate the average noise for n- and p-side, with error bars representing the standard deviation across channels. The solid line represents the analytical estimation of the noise for each module. Additionally, the bottom panel illustrates the percentage difference between the measured ENC and the analytical estimation for both sides of each module, relative to the first one.

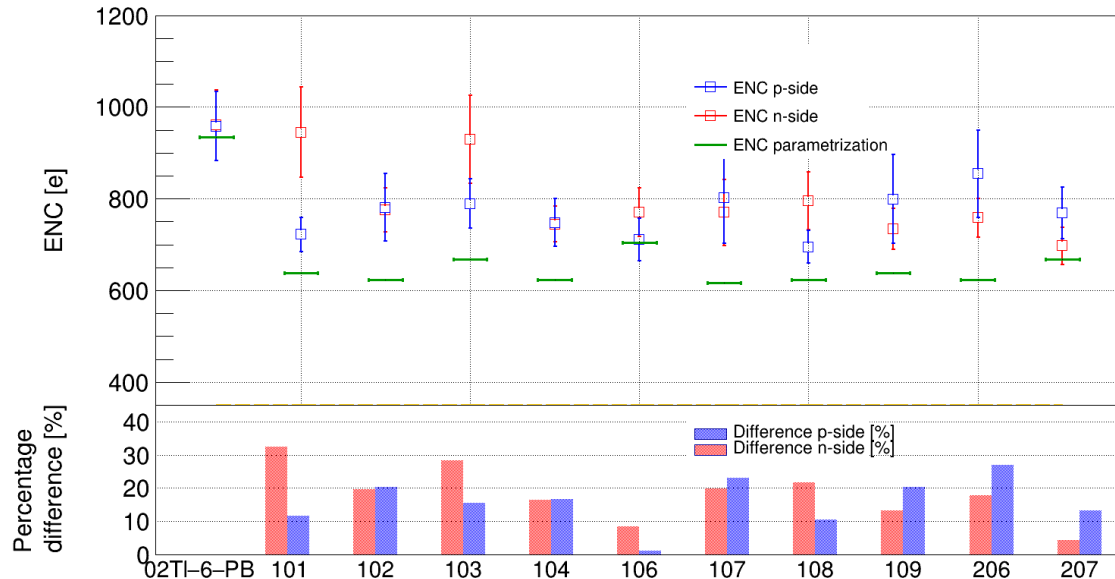


Figure 4.11: Summary of the noise measurements for the modules (prototype + E16-STs modules). The top panel displays the average ENC for the n- and p-side, with error bars representing the standard deviation across channels. The bottom panel presents the percentage deviation of the measured ENC from the analytically estimated values, see Equation 4.1.

Unconnected or broken channels can be recognized by their reduced noise compared to the connected ones, and they are also visible in Figure 4.9. The broken channels can be separated into three categories depending on their level of noise:

- No Analog Response (NAR), when the $ENC = 0$ and the channel is permanently damaged and no charge collection or amplification is done;
- broken Tape-Automated Bonds (TAB) bond at the ASIC (ASIC), when there is a faulty connection between ASIC and microcable. The typical noise is approximately 350 e intrinsic from the ASIC;
- broken TAB bond at the sensor (SENSOR), where there is a faulty connection between microcable and sensor or in the signal line of the microcable. For this case, there is not a fixed noise value and depends of the average ENC of the module and the neighboring strips.

Figure 4.12 presents the distribution of broken channels in their various modes across the 10 E16-STs modules. The production target, indicated by a dashed line at 1.5% or 31 channels, ensures the 97% efficiency required for primary track reconstruction by the

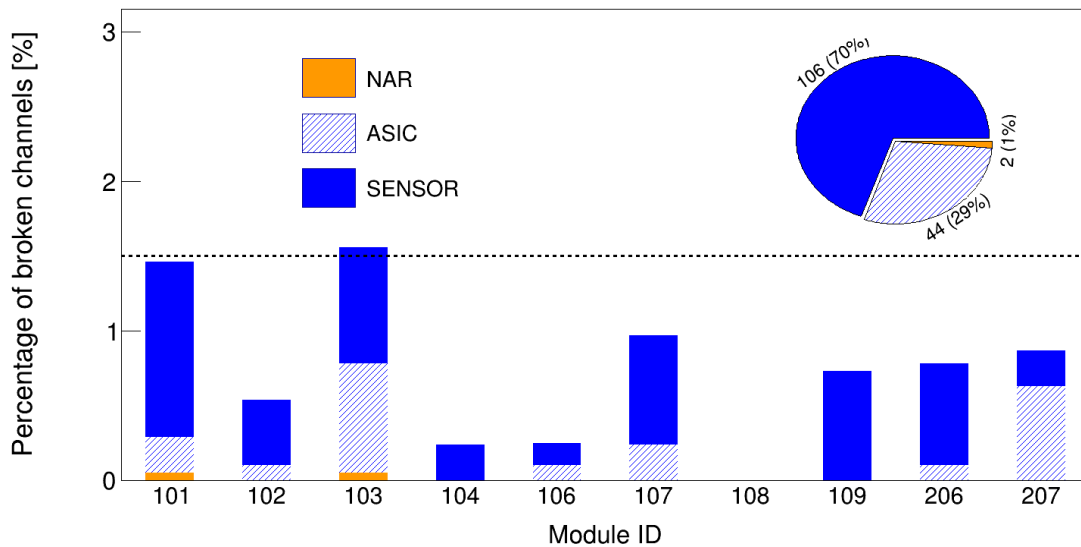


Figure 4.12: Distributions of broken channels of the tested E16-STS modules. It is possible to identify the location where the channel is disconnected based on the ENC level. In the pie chart, its percentages are also specified.

STS detector. Among the tested modules, 9 met the specified limit for broken channels. The remaining module, E16-103-PB, slightly exceeded the limit by one broken channel. However, this minor deviation does not compromise the overall performance of the module.

Table 4.2 provides a summary of some important electrical parameters measured for each tested module (1 prototype + 10 E16-STS modules). These parameters include the ADC gain, threshold values, and the total number of broken channels. It can be seen that there is a consistency in the ADC gain values. In addition, the particular threshold values and their spread are also illustrated. Moreover, the total number of broken channels before and after the module testing is indicated. In cases where the number of broken channels identified before module assembly was higher than after, this is due to the sensitivity of the individual components during their testing, which may lead to misidentification of broken channels. Different situation for the case of the module testing, which provides a more reliable identification of broken channels.

To conclude, in overall these results are very encouraging, demonstrating a high standard of quality and reliability for the modules and the assembly process. The outcome places the STS team favorably for progressing to series production.

4.5 Response of E16 modules to $^{90}\text{Sr}/\text{Y}$ radioactive source

The final stage of the testing procedure, is to evaluate the signal readout capabilities of the modules. For that purpose, the responses of six E16-STS modules and the prototype were studied using a β -emitting radioactive source, specifically $^{90}\text{Sr}/\text{Y}$. This source emits electrons with a spectrum up to 2.2 MeV. The collimated $^{90}\text{Sr}/\text{Y}$ source was placed at different distances from the center of the sensors (at 0 cm and 5 cm). The data collected

Table 4.2: Test results for the 11 modules produced for the E16-STS detector (1 prototype + 10 E16-STS). Every parameter is given as the mean value of the corresponding distribution, with the exception of the total of broken channels. The errors denote the standard deviation of the given values.

Module ID		ADC gain [e/LSB]	Threshold [e]	Broken channels (before) after
02Tl-6-PB	n	2109 ± 15	14740 ± 220	(7) 15
	p	2109 ± 20	11550 ± 270	(14) 27
E16-101-PB	n	2095 ± 12	14464 ± 186	(17) 26
	p	2098 ± 11	15011 ± 242	(4) 4
E16-102-PA	n	2098 ± 12	8944 ± 172	(3) 10
	p	2097 ± 13	9311 ± 169	(4) 1
E16-103-PB	n	2094 ± 13	14548 ± 177	(4) 7
	p	2096 ± 11	14530 ± 165	(8) 25
E16-104-PA	n	2103 ± 12	14533 ± 224	(1) 1
	p	2095 ± 11	14383 ± 167	(0) 4
E16-106-PB	n	2098 ± 13	9205 ± 180	(5) 3
	p	2101 ± 13	9130 ± 228	(2) 2
E16-107-PA	n	2088 ± 14	9254 ± 193	(1) 1
	p	2099 ± 12	9314 ± 212	(18) 19
E16-108-PB	n	2100 ± 11	14823 ± 168	(1) 0
	p	2096 ± 13	14611 ± 238	(2) 0
E16-109-PA	n	2094 ± 17	9615 ± 200	(8) 7
	p	2098 ± 12	9253 ± 181	(6) 8
E16-206-PA	n	2093 ± 12	9339 ± 159	(6) 7
	p	2095 ± 14	9266 ± 200	(4) 9
E16-207-PA	n	2092 ± 10	9306 ± 141	(1) 1
	p	2096 ± 11	9290 ± 175	(19) 17

were reconstructed using the CBMROOT framework, the software package for simulation, reconstruction, and data analysis for the CBM experiment [68, 69].

The first evaluation of the detector response corresponds with checking the channels distribution, see Figure 4.13. This reveals similar patterns to those observed in the ENC distribution regarding broken and noisy channels. It serves as a complementary method to identify broken channels, and it provides confirmation that the procedures implemented for detecting malfunctioning channels during testing are effective and accurate. The broken channels identified by the ENC evaluation are illustrated on the bottom plot. The appearance of noisy channels closer to broken ones is related to the process of evacuating the collected charge. Since the channel is broken, the charge couples capacitively to

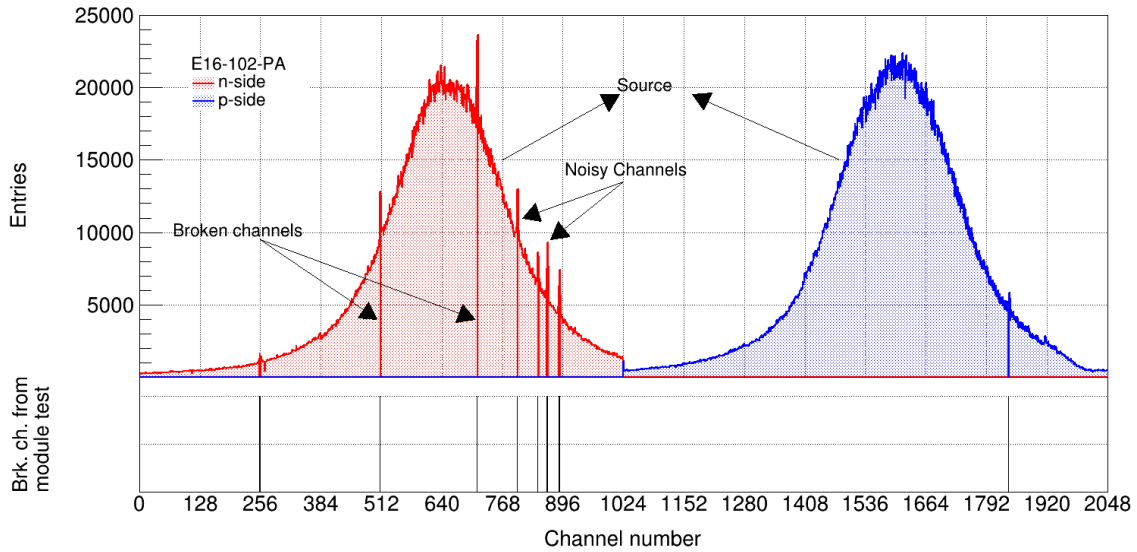


Figure 4.13: Channel distribution of the module E16-102-PA resulted of the irradiation of the sensor with $^{90}\text{Sr}/\text{Y}$. The broken channels identified through ENC measurement are also displayed for cross-checking.

neighboring strips, producing as result channels with higher levels of noise. In practice, noisy channels need to be masked via software to avoid saturating the bandwidth of the DAQ and therefore they also appears as broken channels.

In Figure 4.13, two prominent peaks are clearly visible in the distribution of channels: one on each side. They correspond to the group of channels located at the center of the sensor, precisely where the source was placed.

Another aspect worth exploring is the time correlation between “Digis”, which refers to the digitized signals from individual strips within the same cluster. Clusters are reconstructed by grouping signals from neighboring strips within a defined time window of 20 ns. During data collection in the laboratory with E16-STS modules, an improper synchronization of the electronics made it impossible to assign the correct time to each hit event. As a result, further analysis using the collected data of E16-STS modules was not feasible. However, it was still possible to reconstruct the channel distribution and perform a comparison of the broken channels.

For the rest of the analysis, the prototype module 02T1-6-PB will be used to illustrate other key aspects. Figure 4.14a demonstrates a good time correlation between “Digis” in a cluster. The maximum correlation peak is well-centered around $\Delta t = 0$, indicating that the signals within a single cluster are temporally close, which ensures proper reconstruction of localized energy deposition events.

Figure 4.14b illustrates the typical cluster size distributions for n- and p-side, respectively. In both cases, the predominant cluster size is 1. This result is consistent with the use of a collimated β source positioned close to the sensor, which primarily produces perpendicular tracks.

Another characteristic of the module concerns the signal amplitude distribution. In the case of $^{90}\text{Sr}/\text{Y}$, where no energy cuts were applied using an attenuator, the charge spectra appear as a continuum for both the n-side and p-side clusters, as shown in Figure 4.15a.

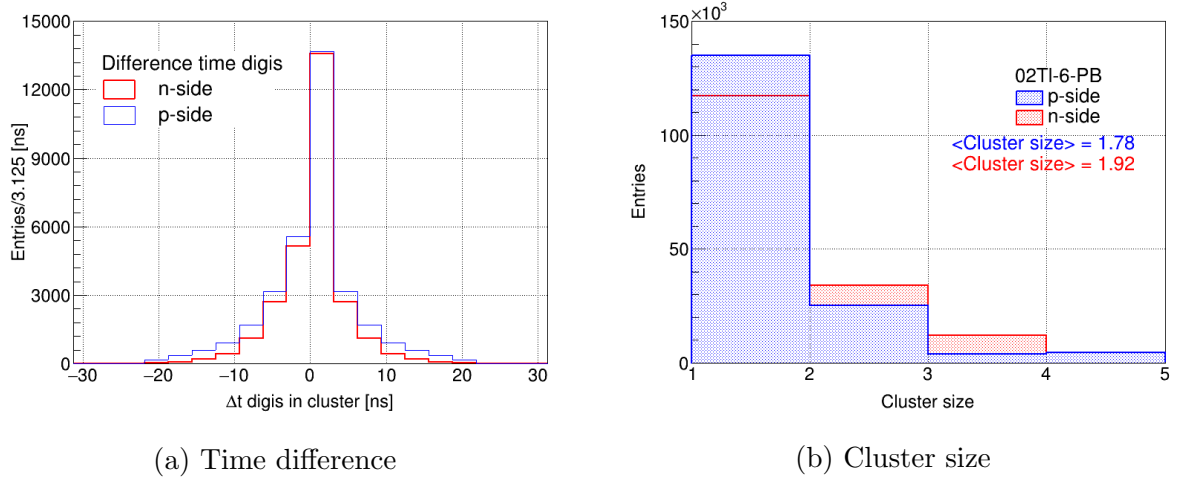


Figure 4.14: Performance of module 02-Tl-6-PB measured with a collimated $^{90}\text{Sr}/\text{Y}$ source. a) Time difference for Digis inside the cluster. b) Clusters size distribution.

For the analysis, a cut was applied to remove charges below 3 ADC to eliminate large noise contributions. However, even with this cut, a significant noise contribution is still observed at lower charges ($\text{ADC} = 4$) for the n-side. Figure 4.15b illustrates the charge correlation between the n-side and p-side clusters that form hits. It can be seen that there is a clear symmetric correlation for n- and p-side, indicating consistent signal collection across both sides of the detector. The intense red color at low charge primarily corresponds to noise events.

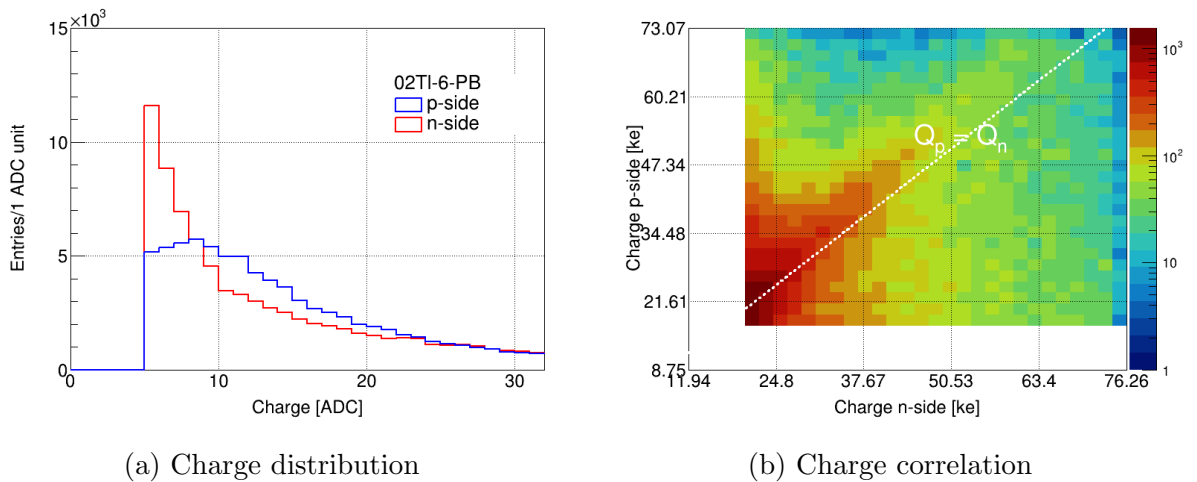


Figure 4.15: Signal amplitude and charge correlation for n- and p-side clusters that form hits, shown for the prototype module 02Tl-6-PB.

As a final step in the analysis, the reconstruction algorithm correlates the clusters and computes the hit position on the sensor plane, as shown in Figure 4.16. The 2D spatial distribution of reconstructed hits reveals a well-defined and concentrated area around $x = 0.2$ cm and $y = -1.0$ cm. This spot corresponds to the expected location of the

radioactive source in the experimental setup, perfectly aligning with its known placement during the lab test. The coherence between the reconstructed hitmap and the actual source location validates the proper response of the module, and it proves the reliability of the reconstruction software.

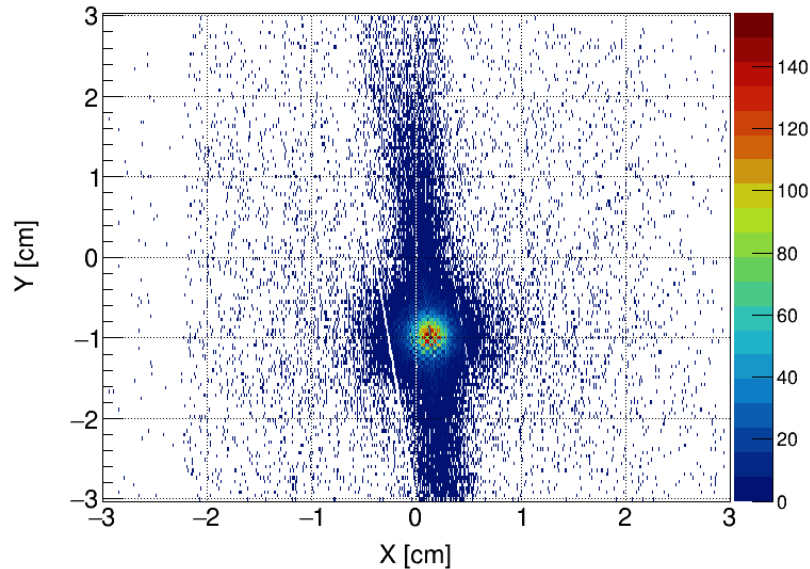


Figure 4.16: XY hitmap reconstruction of collimated radioactive $^{90}\text{Sr}/\text{Y}$ source illuminating the prototype module 02Tl-6-PB. The source was placed at 5 cm from the module.

4.6 Module testing protocol

After characterizing 10 pre-series modules produced at GSI Detector Laboratory for the E16 experiment, valuable insights were gained. These allowed us to develop a standardized module testing protocol. This protocol incorporates a range of important criteria to ensure confidence in the quality and performance of the tested modules. A comprehensive summary of the testing protocol is shown in Figure 4.17 as a flow diagram.

The protocol outlines three primary classifications for evaluating modules. Firstly, it identifies the criteria that result in immediate rejection of a module due to major issues or irreparable faults, labeled as “fail”. Secondly, it highlights conditions where a module may exhibit minor errors, but is still considered acceptable for use, labeled as “pass with error”. Thirdly, it describes actions that can be undertaken for modules with malfunctions to avoid rejection. These actions are aimed at resolving or mitigating issues to bring the module within acceptable performance standards, and require that the modules undergoes a second round of testing. And finally, when the module does not present any kind of issues, is declared as “pass”.

The structured testing protocol ensures consistency and reliability in the evaluation process. It integrates lessons learned during the module characterization phase and addresses potential ones that may occur. The protocol not only supports decision-making

damage. In preparation for the 2025 beam campaign, it was required that four new E16-STs modules were assembled, characterized, and integrated on ladders. They are meant to be used as a replacement for those damaged in previous campaigns.

The characterization of these modules followed the testing protocol described previously in this chapter. The IV measurements of the four new modules exhibited similar behavior to those of the previous ten tested modules. The leakage current remained below $3 \mu\text{A}$ at 150 V and the full depletion voltage was reached at the level of around 60 V . In addition, all sensors were successfully biased up to 150 V , the maximum require voltage for E16-STs. The modules were calibrated with an ADC gain around 2100 e/LSB and a high threshold of 14000 e . The average ENC was measured at around 720 e , and the number of broken channels in each module remained below 10 channels. Table 4.3 provides a summary of the parameters evaluated.

Table 4.3: Test results of four new E16-STs modules designated for the 2025 beam campaign. Every parameter is given as the mean value of the corresponding distribution, with the exception of the total of broken channels. The errors denote the standard deviation of the given values.

Module ID		ENC [e]	ADC gain [e/LSB]	Threshold [e]	Number of broken channels
E16-101-PBv2	n	770 ± 39	2104 ± 11	14192 ± 157	3
	p	726 ± 43	2105 ± 14	14186 ± 147	8
E16-103-PBv2	n	799 ± 42	2105 ± 15	14205 ± 180	1
	p	699 ± 39	2104 ± 15	14168 ± 157	0
E16-104-PAv2	n	741 ± 45	2095 ± 12	14165 ± 162	1
	p	706 ± 44	2104 ± 14	14161 ± 155	0
E16-106-PBv2	n	735 ± 36	2092 ± 18	14191 ± 180	0
	p	693 ± 39	2099 ± 14	14140 ± 228	0

The test of the module response using a radioactive source could not be performed due to time constraints. However, this test is planned to be conducted at J-PARC before the installation of the modules inside the E16-STs chamber.

4.8 Towards E16 full acceptance coverage

The full acceptance coverage for the E16 experiment is planned as part of Run 2 in 2028. This phase involves the deployment of a total of 26 sensor modules, arranged in a well-structured configuration to optimize performance and coverage. Specifically, the setup consists of eight ladders that accommodate three modules and two ladders with two modules. The assembly and characterization of these modules will be carried out by the STS team at GSI. A key upgrade in this phase is the implementation of the newest FEB-8 design, featuring two uplinks and their respective data readout cables. Furthermore, the sensor size will remain at $62 \times 62 \text{ mm}^2$, preserving compatibility with the existing design.

In addition, an important aspect of the setup is the thermal management. Given the increasing number of modules, various improvement strategies for the cooling system are currently being explored to ensure stable operation of all modules during the full-scale beam campaign.

4.9 Summary

The functional evaluation of modules for the E16-STS experiment was performed as part of the pre-series production phase of the STS construction. During the past two years, 15 modules were assembled and tested, on request: one prototype, ten pre-series modules intended for the E16-STS tracker, and four replacement units. The assessment followed four main steps: sensor IV characterization, calibration, functional testing of the front-end electronics, and data readout using a radioactive source.

The current-voltage characteristics of the sensors were measured up to 150 V to verify their operational performance. The calibration of the ASICs was carried out successfully, with parameters such as ADC gain, ADC threshold, and threshold spread demonstrating a well-established and consistent calibration procedure. The ENC for the modules was determined, showing results that aligned within approximately 20% of the expected analytical values. Furthermore, an identification of broken channels was performed, with almost all modules meeting the target production goal (1.5%). The signal response of the modules was also evaluated using a radioactive $^{90}\text{Sr}/\text{Y}$ source. Through the individual channel response, it was possible to identify and cross-check those that were broken or malfunctioning. Additionally, a time correlation analysis was performed between Digis and clusters, resulting in a reconstructed XY hitmap that agreed with the source's position during the measurements.

Based on these assessments, a comprehensive testing protocol was developed to standardize the evaluation process. This protocol is currently in use for testing the final STS modules, ensuring consistent quality and performance as the project progresses into full-scale series production.

Chapter 5

In-Beam performance of E16-STS modules

In November 2023, as part of the commissioning of the innermost tracking layer of the E16 experiment, the E16-STS chamber was operated in one of the test beamlines of the Photon Factory Advanced Ring (PF-AR), see Figure 5.1. These test intended to have the purpose to validate the performance of the E16-STS modules and elements of the readout under conditions similar to those expected in actual experiment. The E16-STS chamber was irradiated with an electron beam of 3 GeV/c. The beamline setup allowed to research important parameters such as position and timing resolution, efficiency when exposed to high-energy electrons, track reconstruction, and also to monitor the noise levels of the detector, as well as the calibration of the measurement circuits. The results indicate that the system performed within the expected specifications, which represents a significant milestone for the project.

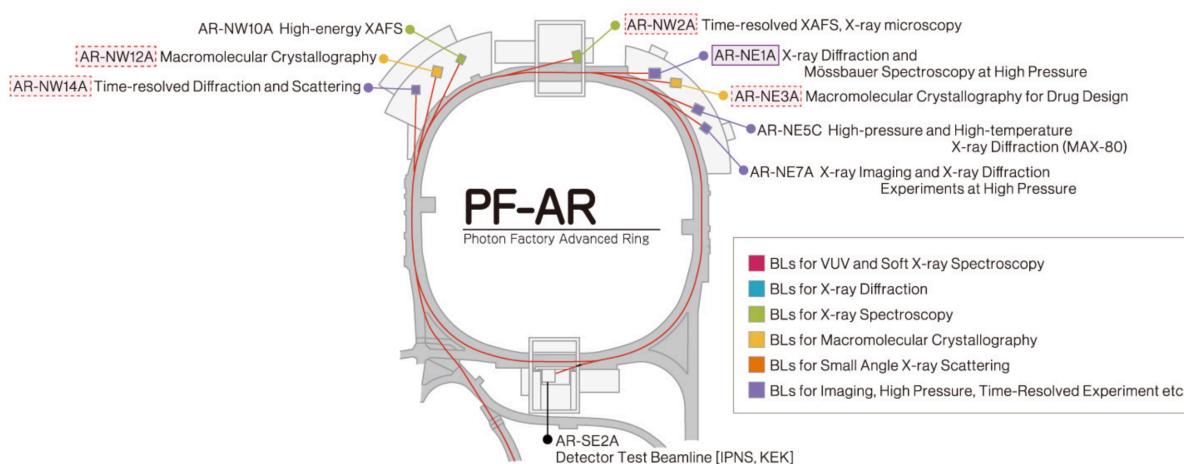


Figure 5.1: Top view of the PF-AR facility with all experimental lines and experiments. The test beamline for the detector test is shown at the bottom, labeled as “AR-SE2A”.

5.1 Beam test at the Photon Factory Advanced Ring

The Photon Factory (PF) is an accelerator-based light source facility and is part of the KEK of Japan. The PF comprises two storage rings, the PF Ring and the PF-AR. They are capable of storing beam energy up to 2.5 GeV and 6.5 GeV respectively, producing photons in the wavelengths from Vacuum-Ultraviolet (VUV) light to hard X-rays. In total, 47 experimental stations for research and medical applications are operated at PF [70].

The PF-AR operates with a single bunch electron beam with a revolution period of 1.25 μs and intensity of 50 mA. The photons are produced by inserting a wire target into the beam halo and converted to electrons with a cooper converter for producing electron-positron pair. The electrons are extracted and directed to the experimental areas using a combination of dipole and quadrupole electromagnets [71].

5.1.1 Experimental setup and readout chain

The experimental setup operated at the PF-AR beamline includes the J-PARC E16-STC chamber, where three out of ten modules, that are planned to be part in the first physics run (Run1) of the E16 experiment, were commissioned.

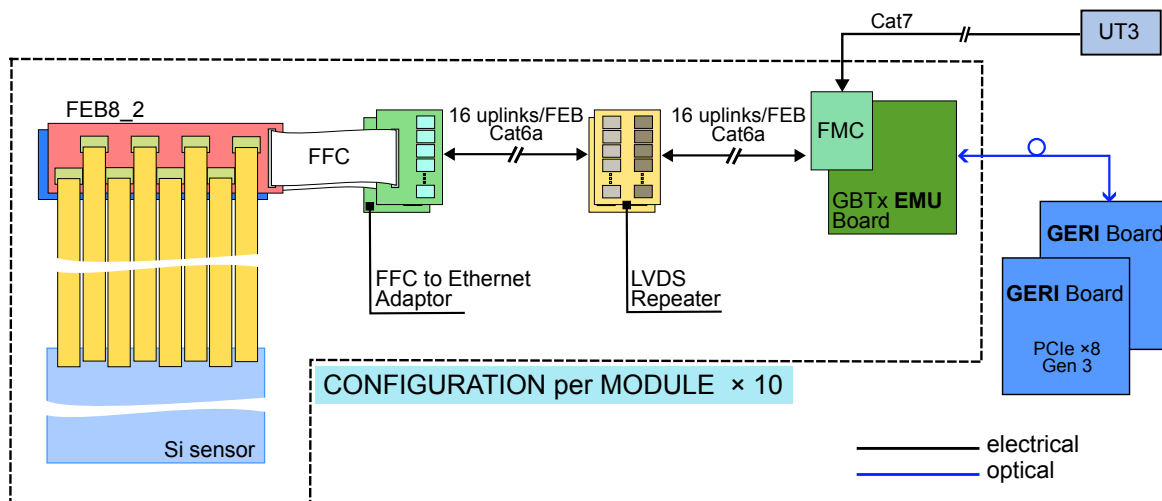


Figure 5.2: Schematic readout of the E16-STC detector. The raw signal is sent from the sensor to GERI board through the Flat Flexible Cable (FCC)-Ethernet adaptor, LVDS repeater and GBTx-EMU board

Several components of the schematic readout, shown in Figure 5.2, were included as part of the commissioning step. The descriptions below corresponds to the different elements of the readout chain, right after the signal is sent from the sensors and digitized in the FEB-8:

- $3\times$ repeater devices, for extending the LVDS signal range beyond its standard 10 m limit, ensuring reliable data transmission, due to the placement of the J-PARC E16-STC tracker within a magnetic field. This was necessary to position the GBTx-EMU boards at a safe distance to avoid potential magnetic interference

and single event effects, as these boards are particularly sensitive to such fields and radiation;

- 7× custom made FMC, which not only receive the data from the LVDS repeater, but also allow the GBTx-EMU boards to accept E16 trigger signal and clock information through CAT7 cables sent by UT-3 [72];
- 7× GBTx-EMU boards as a data concentrators. The data is received, serialized and sent to a GERI board through optical cables;
- 1× GERI board: this is a PCI-Gen3x8 board. The data is read out in Direct Memory Access (DMA) mode, which means that the data is transferred directly from the GERI board to the computer's memory without involving the CPU for each byte;
- 6× adapters from FCC to Ethernet cable;
- 10× Ethernet cables of 10 m.

Two read out data configurations were used:

- trigger-less mode, where all the data are recorded in HDD. This mode was part of the beam-line commissioning phase;
- trigger mode, where an online selection of the hits is made by the GERI according to the E16 timing trigger used in Run0e and Run1 [73].

For powering the systems 3 × LV modules serie MPOD OMPV.8016 with 8-channel manufactured by WIENER Company and 1 × HV module serie EHS F4 05x manufactured by ISEG were used. The temperature of the setup was kept under control using a cooling base with circular geometry, connecting pipes, and a LAUDA chiller operated with a bath temperature of 16°C.

Detector testing configurations

The E16-STC chamber was operated and several of its modules tested at the PF-AR facility. Two detector configurations were used and they are presented in Figure 5.3, where Figure 5.3a and 5.3b correspond to direct beam incidence on module E16-108-PB at different angles. The data recorded and analyzed correspond to Run91 and Run82 for angles of 0° and 16°, respectively. The other configuration is shown in Figure 5.3c, where three modules took data simultaneously. Each of them at different incidence angles. The data recorded and analyzed correspond to Run113.

Located around the E16-STC chamber, four scintillators were positioned upstream and downstream, as illustrated in Figure 5.4. Each pair of scintillators defined an active area with dimensions of 10 × 10 mm², arranged to form a detection sandwich surrounding the chamber. The coincidence signals from the scintillators was processed using a NIM coincidence module, which then routed the signal into the calibration port of a standalone FEB-8 for recording the scintillator timing [57]. Figure 5.5 shows the coincidence logic used during the data taking.

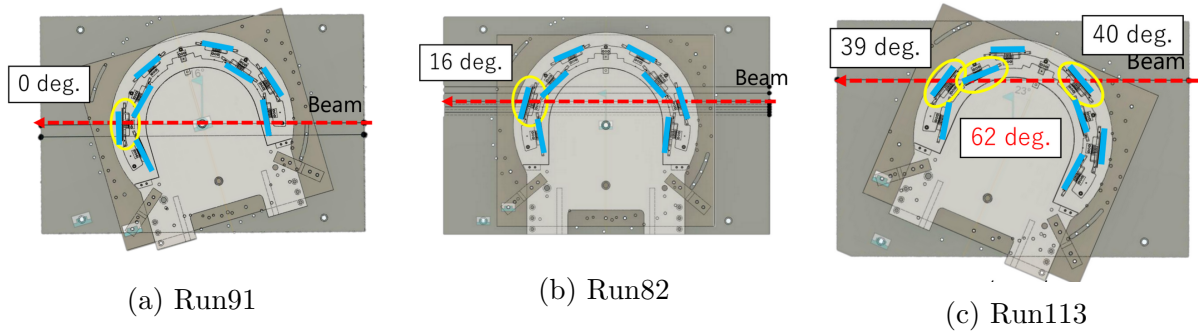


Figure 5.3: Two different testing configurations. Module E16-108-PA being hit with: an incident angles of: a) 0° and b) 16° . c) The three modules: E16-102-PA, E16-107-PB, E16-108-PA being hit with different angles of incidence.

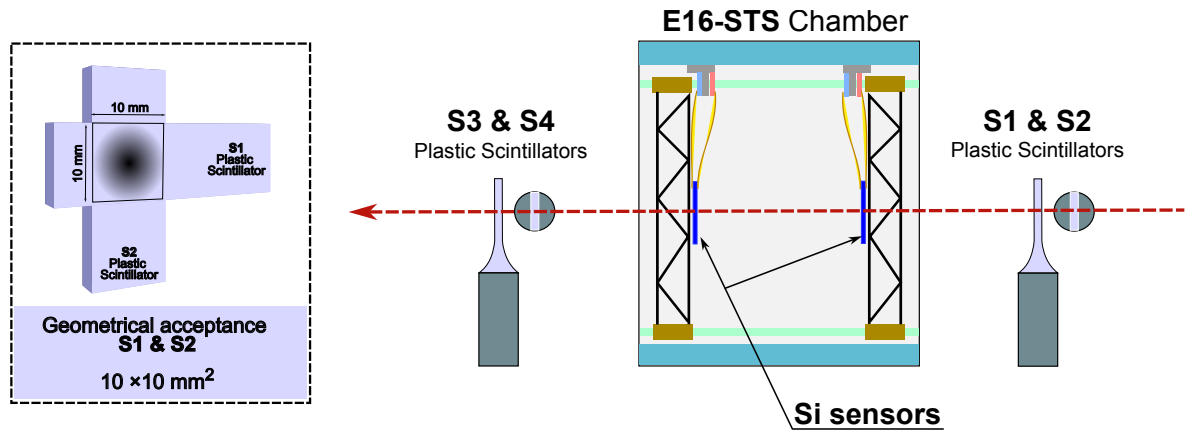


Figure 5.4: Schematic view of the E16-STS chamber and the four scintillators. The electron beam passes through two arrays of two scintillators (S1&S2 and S3&S4), defining a geometrical acceptance of $10 \times 10 \text{ mm}^2$.

5.2 Data analysis: from E16 to CBMROOT framework

Once the data is recorded, the next step is its analysis. However, due to fundamental differences in the readout chain between STS and the one implemented for the E16 experiment, direct usage of the CBMROOT framework as a package for the analysis was not feasible. This section describes the development of a data unpacker, which facilitates the merging of E16 data with the tools already available for processing the CBM data, in particular the one from STS.

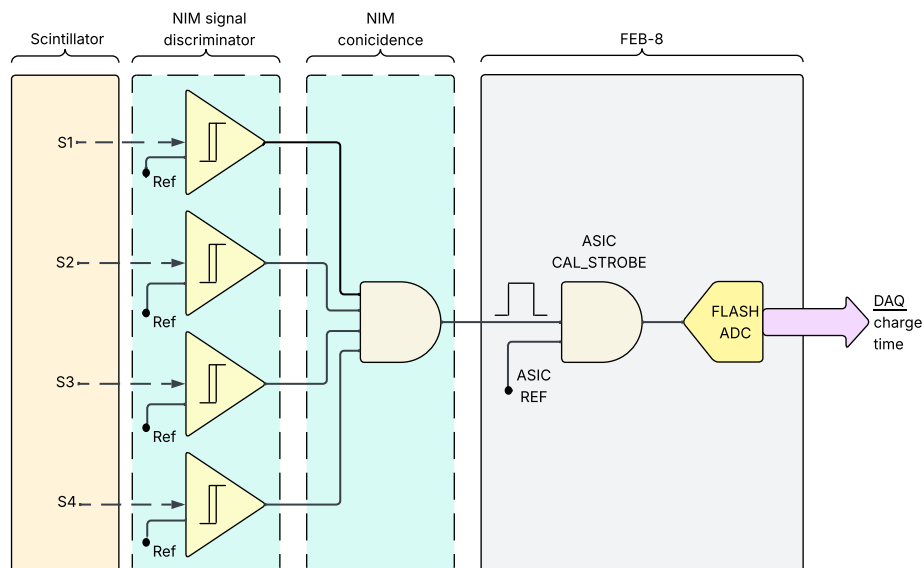


Figure 5.5: Block diagram of the coincidence detection logic. The signal flow from scintillator detectors (S1-S4) through discriminators and NIM coincidence modules to the SMX ASIC, which provide the time coincidence.

5.2.1 Development of the data unpacker

Data format

The first step in understanding how the development of a data unpacker should be oriented is to analyze and explain the format of the recorded data. The data is compacted into a series of 8×32 -bit words by the GERI board, as shown in Listing 5.1.

Listing 5.1: Data Format

1	TRAILER:	ed9acce7	0021a55d	f5e4bba3	0000059e	00000000	00000000	00000000
2	HEADER:	579acce7	0021a55e	4c7cd273	0000059f	00000000	00000000	00000000
3	DATA:	f5e44307	205a1a92	f5e4430a	20592290	4c7cfacf	24e79e7c	4c7cfad3

The TRAILER, leftover from older run, and the HEADER can be identified by their respective keywords, ed9acce7 and 579acce7. Both TRAILER as HEADER do not represent actual data and can be safely ignored.

If a words is neither a TRAILER nor a HEADER, it represents DATA. In such cases, the 32-bit words with an even index contain the time information from the GERI board, while the odd-ones 32-bit words contain the frames from the ASIC. The key structure of the uplink frames is illustrated in Table 5.1. In the frame two type of data, HIT and TS_MSB can be distinguished.

The HIT type contains information about the channel address, charge, and the 10 least significant bits of the Time-to-Digital Converter (TDC) from the ASIC, referred to as tdcL10b. This type can be identified by the value 0 in bit <23>.

The TS_MSB type, recognized by the value 1 in bit <23> is a data compression frame transmitted every time the hit timestamp bits <13:8> change. It contains information

Table 5.1: Structured uplink frames of the SMX ASIC.

Structure of the uplink frames (before 8b/10b encoding)																								
BYTE 0							BYTE 1						BYTE 2											
frame bits 23:16							frame bits 15:8						frame bits 7:0											
Type	23	22	21	20	19	18	17	16	15	14	13	12	11	10	9	8	7	6	5	4	3	2	1	0
Hit	0		7-bit channel address					5-bit ADC charge					TS 9:8		Timestamp 7:0				EM					
TS MSB	1	1	Timestamp 13:8					Timestamp 13:8					Timestamp 13:8				...							

regarding the 6 most significant bits of the the TDC from the ASIC. The remaining bits in the 32-bit DATA contain information related to the GBTx-EMU, which is connected to each side of the modules, and the e-links for transferring data.

Data unpacker

As shown in the flow diagram of Figure 5.6, the unpacker has the task to combine the data to the stage where it is possible to use it by CbmStsDigi. The CbmStsDigi class is a component of the CBMROOT framework and it is responsible for processing and analyzing the data recorded by the STS modules. This class handles the raw data, which have already been digitized into an object referred to as a Digi. The experiment runtime is divided into discrete intervals, known as TimeSlices.

The Digi object contains crucial information such as module address, channel number, charge, and time associated with each signal event. To interpret the data, the unpacker relies on a mapping system. The mapping contains the direct correspondence between the GBTx-EMU and the specific STS module connected to it.

The address and charge information are directly decoded from the DATA. In case of the channel number, it requires additional processing due to is unique only within the context of the specific ASIC to which it pertains. To construct a global channel number, which is equivalent to the strip on the detector sensor, the e-link information is also needed because it is related with one specific ASIC.

Regarding, the 14-bit TDC, means that the full TDC time is constructed by merging the tdcL10b and TS_MSB. The overlapping TS bits in tdcL10b and TS_MSB ensure that the correct TS_MSB is matched to the corresponding hit time. However, the TDC is periodically reset, which introduces a challenge: to ensure that the reconstructed time info maintain a consistent linear and growing progression. To address this, a reference time is required. This reference time, hereafter geritimestamp, allows the alignment of the reset TDC counts with the global experiment time.

In Figure 5.7, events 1 and 2 have their times determined by the TDC of the ASIC. However, based on this logic, it seems that event 2 occurred earlier than event 1. To resolve this issue, the geritimestamp is used to identify the specific reset of the TDC in which the event occurred.

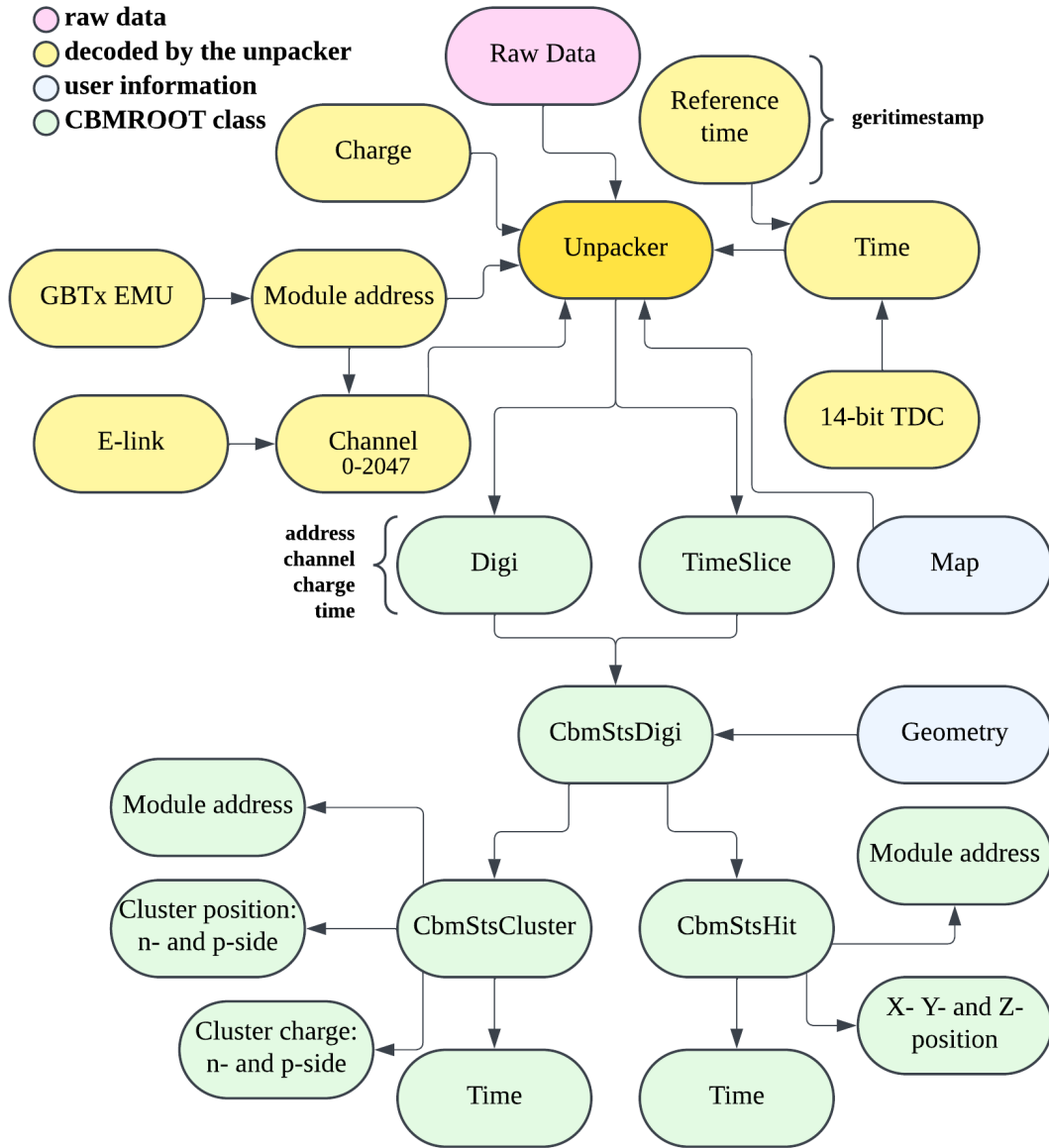


Figure 5.6: Flow diagram of the E16 data Unpacker from Raw data. The decoded data is handled by CbmStsDigi, CbmStsCluster and CbmStsHit classes.

The expression given by Equation 5.1, allows the calculation of the time for any event. In this calculation, the clock period for the TDC of the ASIC is 3.125 ns, and $\Delta t = 51.2 \mu\text{s}$ represents the full range of the 14-bit TDC, which is the maximum measurable time interval before a reset occurs. The duration of the TimeSlices is defined by a fixed number of reset counts.

$$time[\text{ns}] = CLK_{ASIC}[\text{ns}] \cdot (TDC + \Delta t \cdot N_{resets}) \quad (5.1)$$

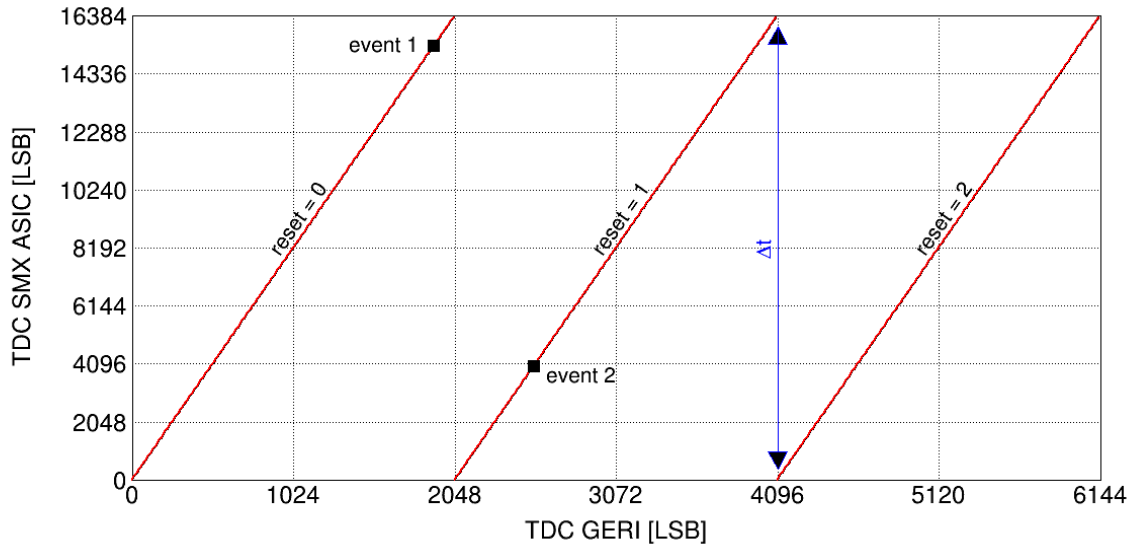


Figure 5.7: Correlation between TDC GERI and TDC SMX ASIC measurements across multiple ramp resets. The red lines represent successive TDC ramp periods (reset = 0, 1, 2). The blue arrow indicates the full time of one reset.

5.2.2 Implementation of the geometry

Once the unpacker decodes the DATA, the Digits and TimeSlice are stored on the CbmStsDigi class, completing the integration of E16 and STS data formats. Afterwards, the CBMROOT framework can be used for further data analysis.

In another level of complexity, objects such as clusters and hits can be reconstructed from the CbmStsDigi. A cluster is an arrange of neighboring strips grouped within a time window (usually 20 ns), while a hit is formed by correlating clusters from each side of the sensor within a time window (approximately 50 ns).

The reconstruction of clusters and hits requires not only the CbmStsDigi but also a dedicated code for reconstruction and the detector geometry. The code is responsible for executing the reconstruction algorithms, while the geometry provides the necessary mapping between local coordinates, such as the channel number, and global coordinates, such as the XY position on the sensor.

Figure 5.8 illustrates the detector geometry used for testing configuration 2 (Run113), when the chamber was positioned such that 3 sensors could be hit simultaneously. For earlier runs, such as Run91 and Run82, the geometry is constructed differently, featuring a single sensor along with the corresponding rotation angle of the module.

5.3 Data analysis: results

5.3.1 Time resolution

Accurate timing information of the hits is essential for establishing accurate time correlations within a single module and between multiple detectors. These correlations ensure that events registered on different detectors can be reliably associated with the

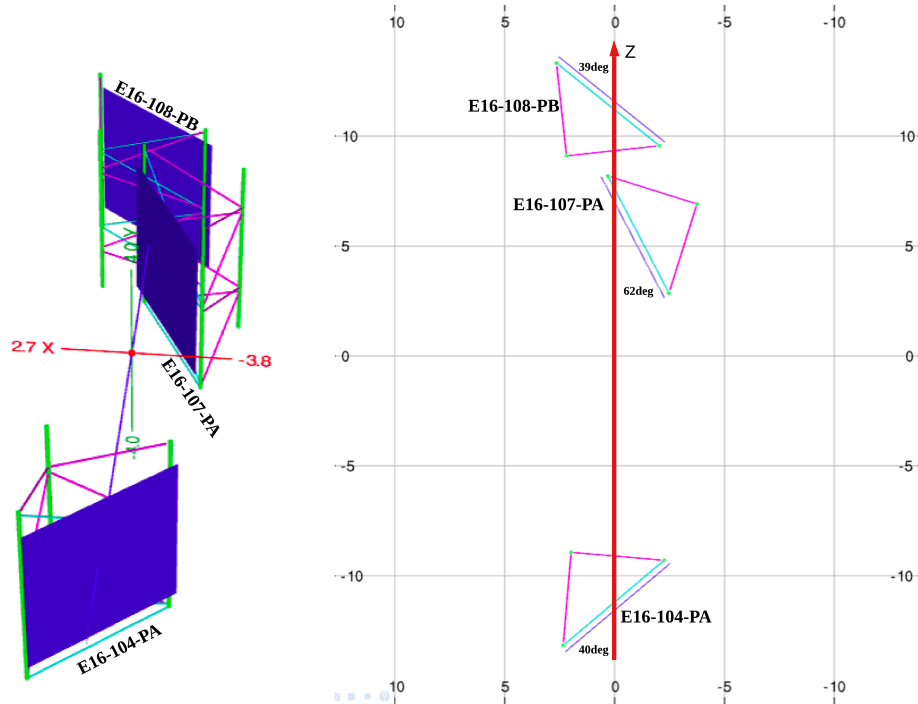


Figure 5.8: 3D and 2D visualization of the detector geometry used in Run113. The left panel shows a view of the setup, highlighting the tilted labeled E16-104-PA, E16-107-PA, and E16-108-PB. The right panel presents a projection onto the XZ -plane, showing the relative positions and alignments of the sensors along the beam axis (Z).

same physical occurrence. To prevent the reconstruction of hits from non-correlated clusters, it is essential to individually adjust the offsets of the ASICs. A precise time tuning requires a reference detector with very good time resolution. For this purpose, the scintillators were used, serving as a reference during the measurements and hereafter called as Bmon, see Figure 5.4 of the experiment setup.

One of the most significant factors affecting timing precision is the time walk effect, as illustrated in Figure 5.9a. This electronic effect introduces a time delay for signals with lower amplitudes when a fixed threshold is applied in combination with a finite signal rise time. In the case of the SMX ASIC, this correction is carried out in the offline data.

The time resolution was studied by correlating the signal measured by the module E16-108-PB in the three different inclination angles configuration, with the one measured by Bmon. Figure 5.9b, shows the time difference between the signals of Bmon and the E16-STC module as a function of the amplitude of the module signal. The first visible feature is the average time difference around 160 ns, which shows a time delay between Bmon and the module. This effect is related to the intrinsic propagation time induced by the readout chain. A second aspect is the presence of the time walk effect, highly visible at lower values of charge ($ADC < 6$). At these low amplitudes the delay reaches up to 40 ns, in correspondence with the single ASIC measurements in laboratory studies [54]. Figure 5.10a, shows the time calibration offset before and after performing the time walk correction at the Digi level, and after the propagation correction has been applied. The error bars represent the time resolution.

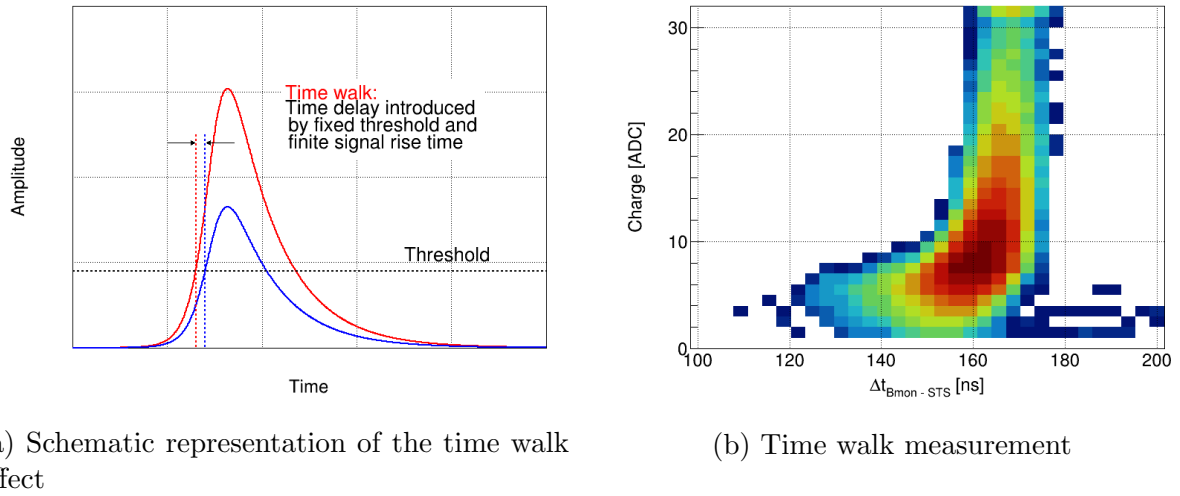


Figure 5.9: Time walk effect in the measured data for module E16-108-PB. Data correspond to the operation of the module at 0° of incident angle. See Figure 5.3

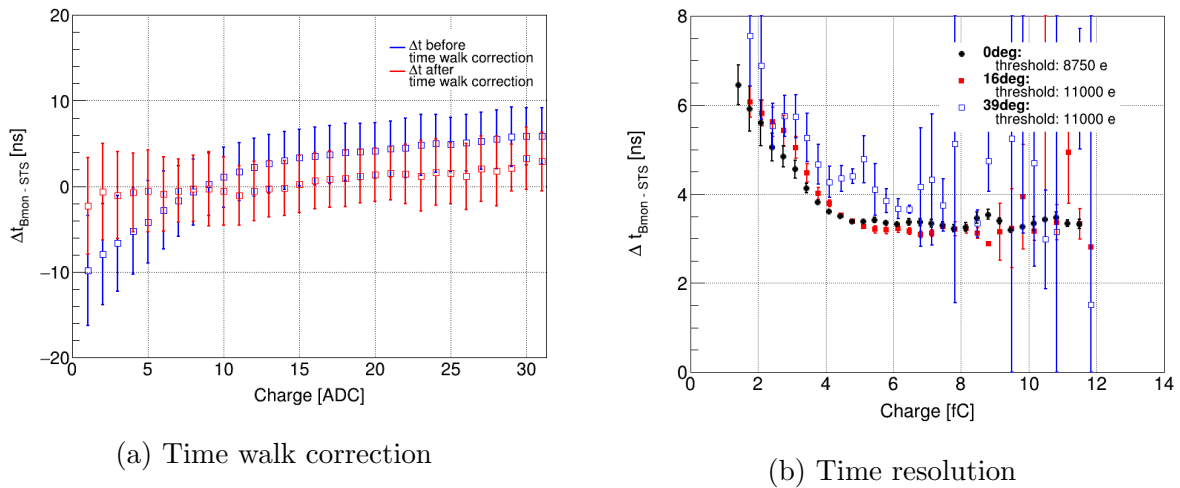


Figure 5.10: (a) Time difference between the measured signal and the reference signal. Time before and after the time calibration as a function of its charge in units of ADC. (b) Time resolution as a function of the signal charge after correction, illustrating improved timing precision with increasing charge.

Figure 5.10b shows the time resolution at the different signal amplitude. At low signal amplitudes, the combinatorial background and noise levels are significant and dominates the overall time resolution. It grows up to 7 ns in the case of 0° configuration. For 16° and 39° configurations, there is a degradation in time resolution with increasing angle, due to the increment of charge sharing resulting in a reduction of the signal amplitude, and as a consequence a more significant time walk effect. At large signal amplitudes, a good time resolution of 3.2 ns was achieved. In the cases of 16° and 39° , the large error bars are due to low statistics. For signal amplitudes in the order of ~ 2.7 fC, the measured time resolution is approximately 5 ns, as required for the E16 and CBM experiments.

Since the time resolution of the scintillators is in the order of ps, the overall resolution is dominated by the contribution of the E16-ST5 module. The error bars represent the fit uncertainty.

5.3.2 Charge distribution and cluster size

The total signal amplitude and the Signal-to-Noise Ratio (SNR) are some of the most important performance parameters of the detector. They provide a reference of the health of the detector on day-0 operation and at the end-of-life. In order to have a better picture of the energy deposited for an electron beam with momentum of 3 GeV/c in 320 μm of silicon material, a simple Monte Carlo simulation was performed using GEANT4. The simulated energy deposited spectrum is shown in Figure 5.11, in which is observable a Most Probable Value (MPV) of 0.092 MeV corresponding with a charge value of approximately 25500 e.

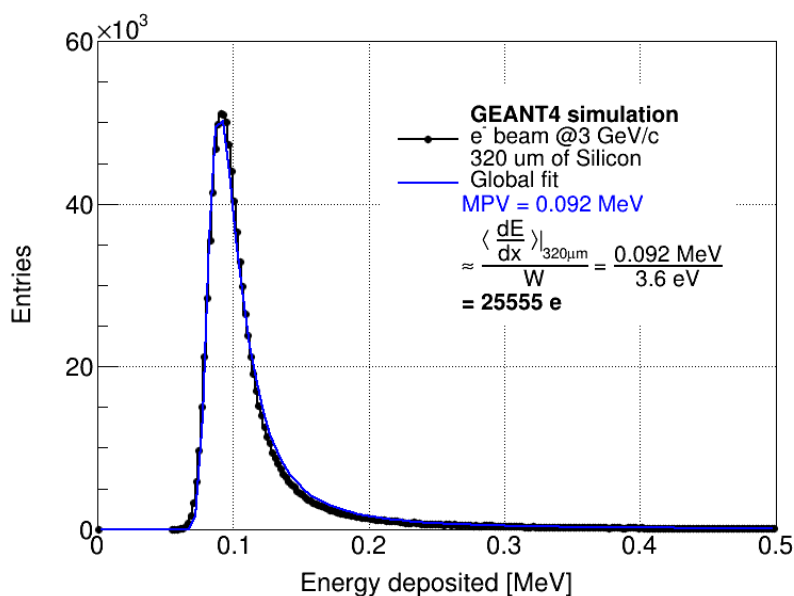


Figure 5.11: Spectrum of the energy deposited by a 3 GeV/c electrons simulated in GEANT4 for a 320 μm silicon detector. The black points represent the simulated data, and the blue curve shows the global Landau-fit. The MPV of the deposited energy is found to be 0.092 MeV. Using the average silicon ionization energy of 3.6 eV per electron-hole pair, the collected charge can be estimated to corresponds to approximately 25500 e.

Figure 5.12 shows the MPV equal to 7.4 ADC and 5.2 ADC of the deposited energy spectrum measured with the n- and p-side, respectively. For the analysis of the measured data, a cut in charge ADC = 1 was applied. This contributes to reduce the noise influence. To extract the peak centroid, the measured energy spectra were fitted using a composite function consisting of a Landau distribution convoluted with a Gaussian function around the expected position. The MPVs deposited charge can be calculated according to the ADC transfer function shown in Equation 5.2, resulting in $22212 e \pm 182 e$ for the n-side and $19803 e \pm 243 e$ for p-side, with threshold values of approximately 8750 e and 11000 e, respectively. For the estimation of the errors, the ADC gain and threshold

spread as well as the systematic error of the fitting were taken into account, see Table 4.2. The statistical error of the fitting was considered negligible with respect to the systematic error. The measured values are up to 13% and 22% below the expected charge deposited by Minimum Ionizing Particles (MIPs) for the n- and p-side, respectively. These values can be slightly different because of three main reasons: the high thresholds applied that cause the loss of some low-amplitude signals; inefficiencies during the charge collection in the sensor volume, due to parasitic capacitances; and the capacitive signal sharing between the sensor and the FEE. The last one can be understood because of the finite magnitude of the input capacitance of the CSA compared to the detector capacitance.

$$Q_{meas}[e] = (ADC_{fit} - 1) \cdot ADC_{gain}[e/LSB] + ADC_{thr}[e] \quad (5.2)$$

Using the corresponding noise measurements, Figure 4.11 with average values of 795 e and 695 e of ENC, excluding Z-strips, an average SNR of 27.9 ± 2.2 and 28.5 ± 1.5 was determined for the n- and p-side, respectively. Therefore, the measured SNR can be considered sufficient to ensure a successful operation of the STS modules in the E16 and CBM experiments, where for the second one, the different module configurations imply an increase in module noise, as a consequence a reduction in the SNR.

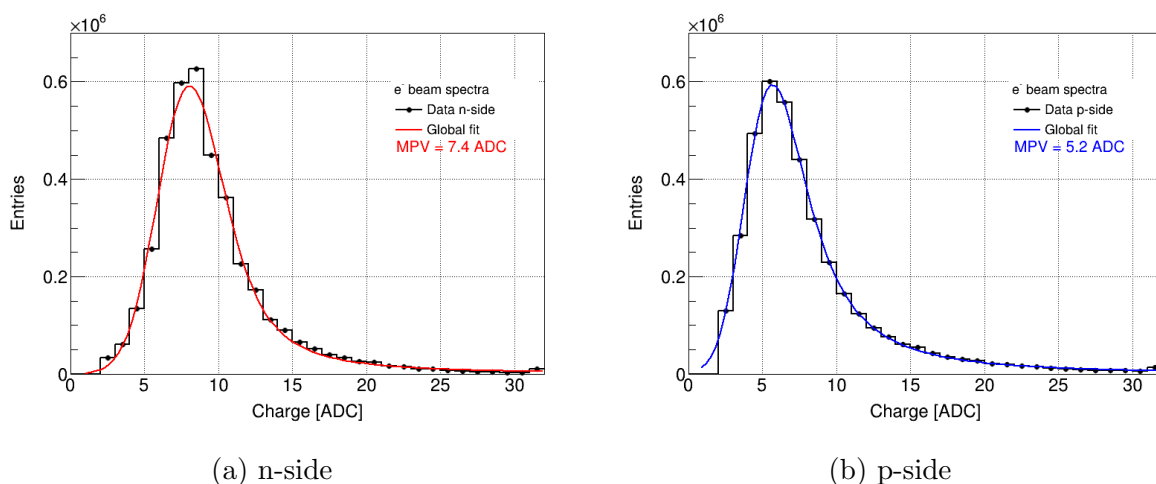


Figure 5.12: The signal amplitude spectra measured with module E16-108-PB for n- and p-side at an effective thresholds of approximately 8750 e and 11000 e, respectively. The data correspond to hits with clusters of size 1. The MPV was found to be about $ADC_{fit} = 7.4 \text{ LSB}$ for n-side and $ADC_{fit} = 5.2 \text{ LSB}$ for p-side.

Figure 5.13 shows the charge distribution for inclined tracks across the detector. As the incident angle of the tracks increases, a more pronounced charge sharing effect between adjacent strips is observed. This behavior is attributed to the longer path length of the particle through the sensor material, which causes the deposited charge to be distributed over a larger number of strips. Consequently, the charge collected by a single strip decreases, leading to an observable shift of the distribution peaks toward lower ADC values.

Figure 5.14 illustrates the correlation in collected charge between the n- and p-side for the different configurations. The white reference line in each plot represents the ideal case of maximum correlation, where the charge collected on both sides is equal ($Q_p = Q_n$).

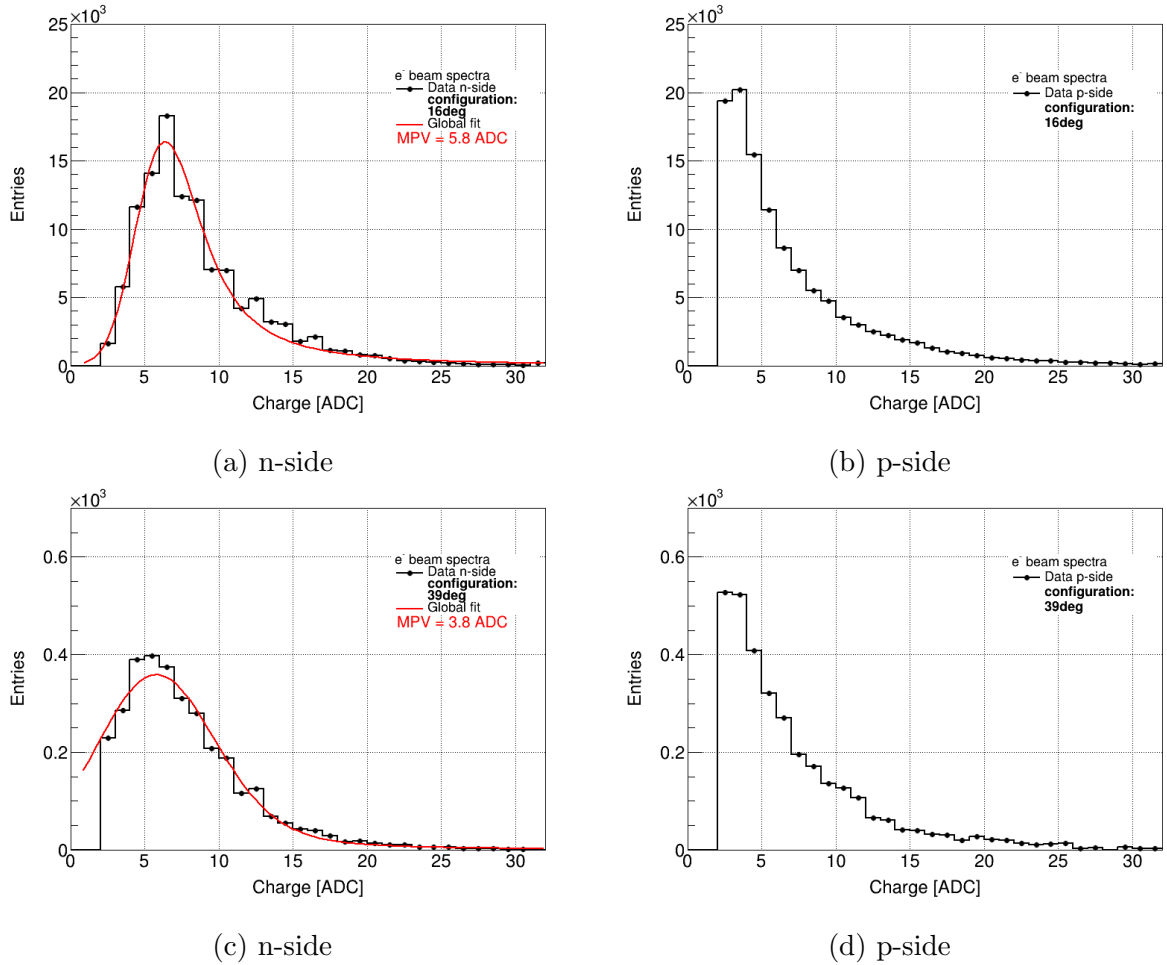


Figure 5.13: Charge spectra measured with module E16-108-PB for n- and p-side for inclined tracks (16° and 39°). The data correspond to hits with clusters of single-strip size.

In Figure 5.14a, a very strong correlation is observed. This is indicated by the intense red cluster around 23 ke, which corresponds to the MPV of the charge distribution and it is very close to the deposited charge by MIPs. The difference in the axis scales between the n- and p-side are due to differences in threshold settings applied during the measurement. The corresponding charge in electron was obtained by applying the specific charge calibration.

In the other configurations shown in Figures 5.14b and 5.14c, the correlation between the n- and p-side remains clearly visible, though the MPV shifts to lower charge values. This shift can be attributed to increased charge sharing between strips and the very large threshold. Additionally, the structures outside the correlation line and visible in all configurations are mostly caused by “ghost” hits, fake hits induced by the hit reconstruction algorithm.

Another important consequence of the different incidence angles is the physical size of the clusters that can be formed. Figure 5.15 illustrates the mechanism of how the size of the clusters changes relative to the incidence angle, and the main reason why the collected signal amplitude is reduced. In relation to this reduction in signal amplitude for

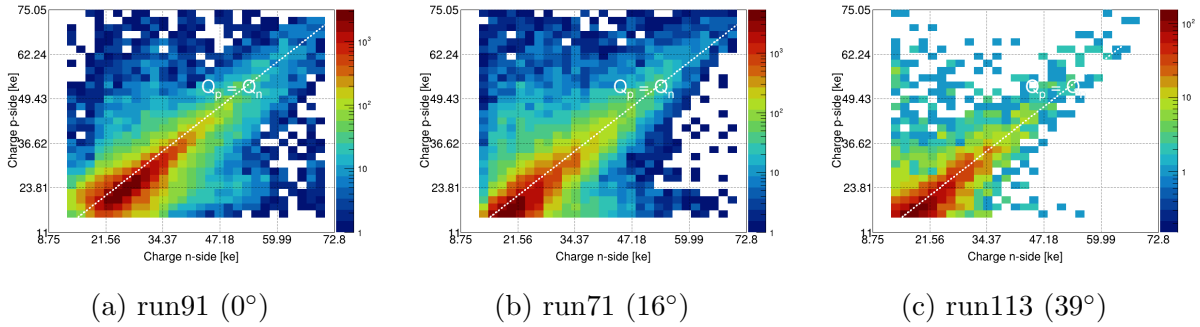


Figure 5.14: Signal amplitude correlation between n- and p-side for single-strip size clusters. Data measured with module E16-108-PB in different testing configurations. See Figure 5.3.

extremely inclined tracks, charge sharing across many strips can lead to individual strips collecting charges below the detection threshold, potentially resulting in missed hits.

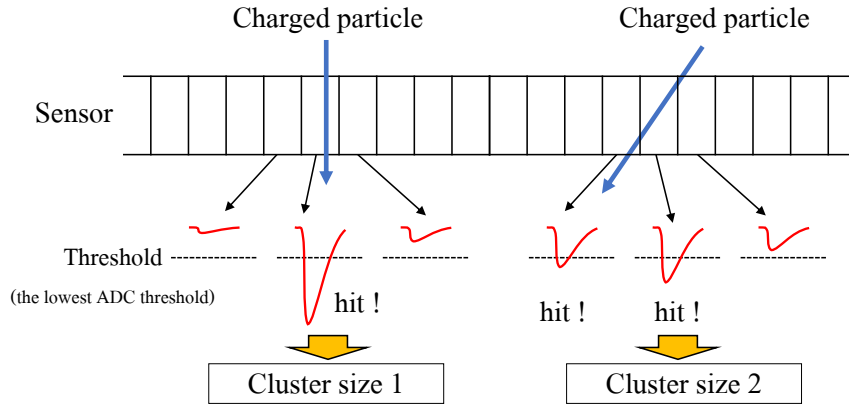


Figure 5.15: Representation of cluster size and signal amplitude for straight and inclined incident particles.

Figure 5.16 presents the average cluster size for both n- and p-side of all modules as a function of the incident angles of the particle beam. As anticipated, the size of the cluster generally increases with the angle of incidence, since a track traverses more strips, enhancing charge sharing across neighboring channels.

The module E16-108-PB was operated in all three configurations. In this case, the cluster sizes for both sides are nearly identical at 0° and 16° , with only a minor discrepancy observed at 0° . This small difference can be attributed to a slight variation in operational threshold levels between the two sides during that particular measurement. At 16° , however, thresholds were applied equally to both sides, resulting in a similar mean cluster size. In the case of 39° , a significant divergence in the size of the cluster is observed between the n- and p-side. This unexpected asymmetry is not yet fully understood.

Module E16-104-PA, when operated at a 40° inclination, shows a consistent cluster size on both the n- and p-side. The values are also comparable to the p-side response of module E16-108-PB at 39° , suggesting that the larger cluster size observed on the n-side of E16-108-PB at 39° may be overestimated.

In the case of module E16-107-PA at 62° , the expected increase in cluster size is not observed, which may seem counterintuitive given the high angle of incidence. At such angles, charge sharing should be significantly enhanced and a larger number of strips are expected to be activated. However, this anticipated effect is counterbalanced by two factors: firstly, the signal amplitude per strip is reduced; and secondly, a relatively high threshold was applied during the measurement. The combination of these two effects suppressed the formation of larger clusters, resulting in a very little increase or even a reduction in the average cluster size.

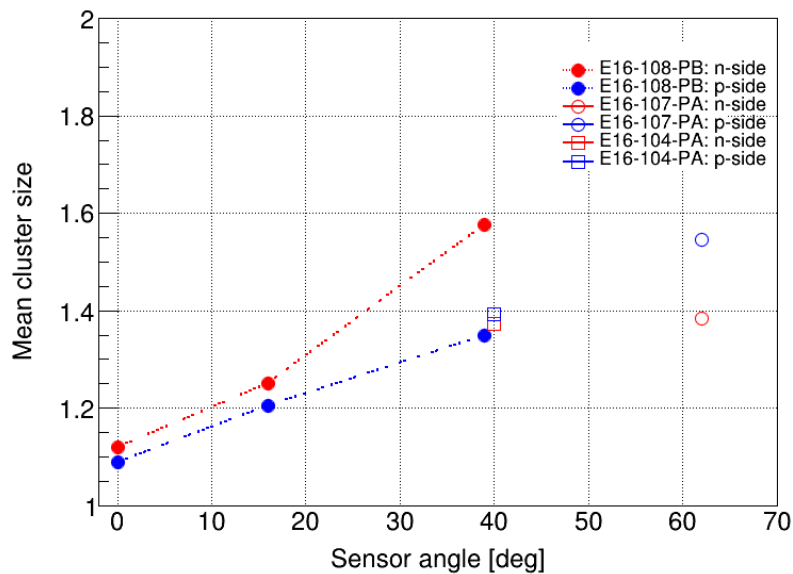


Figure 5.16: Average cluster size for n- and p-side of three E16-STs modules under different degrees of inclination. Lines are drawn to guide the eye.

5.3.3 Detection efficiency

The detection efficiency was calculated as the ratio of sensor hits recorded in coincidence with a scintillator hit and the total number of scintillator signals, shown in Equation 5.3. A sensor hit is defined or accepted as for a given scintillator coincidence signal exists at least one sensor response. The coincidence sensor hits were selected according to two criterias: sensor hits and scintillator hits are close in time (for the analysis a time window of 100 ns were used), and also geometrical constraints according to the scintillator acceptance $10 \times 10 \text{ mm}^2$.

$$Efficiency = \frac{\text{Number of hits in coincidence with scintillator signals}}{\text{Number of scintillator signals}} \quad (5.3)$$

Figure 5.17 shows the residuals of the hits position in the sensor and scintillators for the X- and Y-coordinates in the case of Run91 (no inclined tracks hitting the sensor). The red bands represent the geometrical acceptance determined by the scintillators. To estimate the detection efficiency, the geometrical limits are extracted from the area under the peak. This limits are in agreement with 1 cm^2 acceptance area of the scintillators. The residual distributions corresponding to the other detector configurations are presented in the Appendix F.

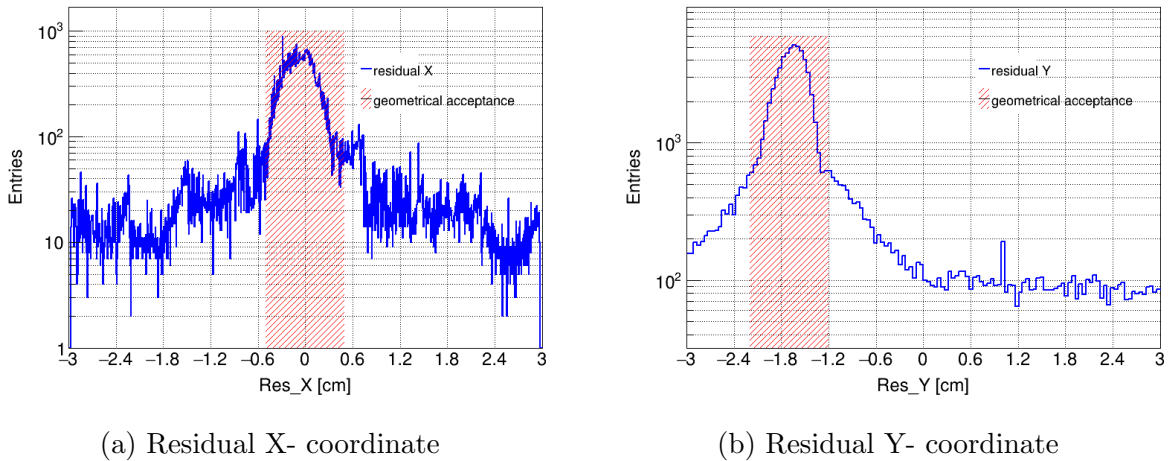


Figure 5.17: Residuals for X- and Y-coordinates in the configuration of 0° of inclination angle for module E16-108-PB. The geometrical acceptance refers to the area covered by the scintillators.

Figure 5.18 shows the hitmap recorded by module E16-108-PB for the 0° track inclination configuration. The outer pad presents the complete hitmap, displaying all detected hits within the active area of the sensor. The inner pad shows those hits in time coincidence with the scintillators, and within the geometrical acceptance region, depicted by the white square. These selected hits represent the subset used in the detection efficiency calculation.

The detection efficiencies values, calculated for all tested configurations, are summarized in Table 5.2. As expected, the highest efficiency (approximately 90%) is observed for geometry with 0° track inclination. This is consistent with a minimum charge sharing effect. As consequence of this, a minimum of hits fall below the detection threshold resulting in higher efficiency values compared to the other configurations.

For inclined geometries, the detection efficiency drops significantly. This decline is mainly due to the combination of increased charge sharing and the relatively high operational threshold. These cause a larger fraction of the signal to fall below the detection threshold, reducing the number of registered hits. However, these observed values are in accordance with the simulations performed using Garfield++ and presented in the Master thesis of Rento Yamada [74].

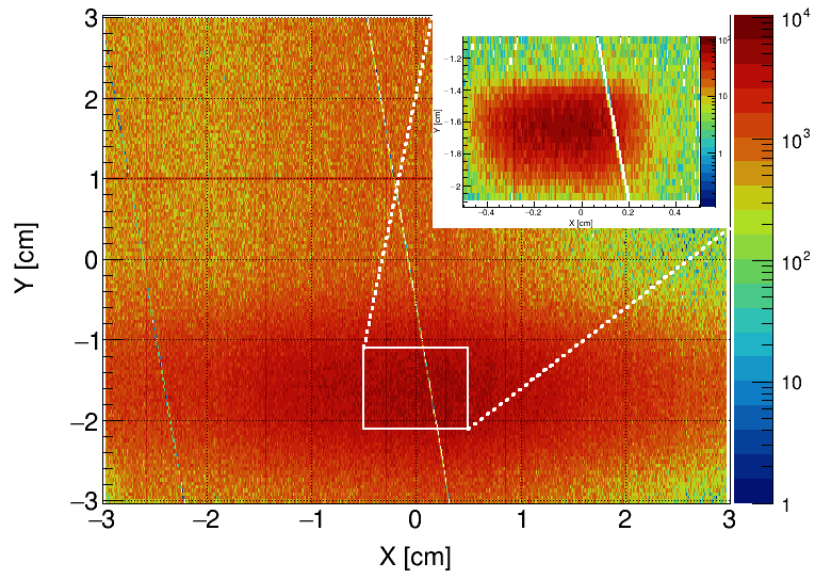


Figure 5.18: Hitmap and coincidence hits for module E16-108-PB under conditions of 0° of inclination angle and a time window of $\Delta t = \pm 100$ ns.

Table 5.2: Detection efficiency of all the modules in the different setup configurations. The errors are calculated using a binomial distribution.

Module ID	Incident beam angle (deg)				
	0	16	39	40	62
E16-104-PA	///	///	///	$11.29^{+0.16\%}_{-0.16\%}$	///
E16-107-PA	///	///	///	///	$23.47^{+0.22\%}_{-0.22\%}$
E16-108-PB	$89.85^{+0.11\%}_{-0.11\%}$	$49.65^{+0.11\%}_{-0.11\%}$	$13.88^{+0.18\%}_{-0.18\%}$	///	///

The uncertainties on the detection efficiencies were calculated assuming a binomial distribution, as the process can be modeled as a sequence of independent trials, each with a binary outcome: either a hit is detected (success) or not (failure). The statistical error on efficiency ε is given in Equation 5.4:

$$\sigma_\varepsilon = \sqrt{\frac{\varepsilon(1-\varepsilon)}{N}} \quad (5.4)$$

Where $\varepsilon = \frac{n_{\text{hits}}}{N}$ is the detection efficiency, n_{hits} is the number of detected hits, and N is the total number of scintillator coincidences.

5.3.4 Track reconstruction

The tracking procedure plays an important role in the performance evaluation of the detector system. It enables to determine spatial resolution, hit reconstruction efficiency, and overall alignment accuracy. In this part, the evaluation of the spatial resolution is

described. This includes 3D hit reconstruction with the setup corresponding to Run113 (the three modules in a telescope configuration) and track-to-hit residual analysis.

To reconstruct the particle trajectory in 3D space, a straight line is fitted through the set of hit positions registered by three sensor planes, using a Principal Component Analysis (PCA) method described in Appendix G. The main steps involved in the tracking algorithm are described below:

- **Set of hits:** For each event, a set of hits in coincidence with scintillators is selected from different sensor planes within a defined time window:

$$\vec{r}_1 = (x_1, y_1, z_1) \quad \text{from Sensor 1 (S}_1\text{)}$$

$$\vec{r}_2 = (x_2, y_2, z_2) \quad \text{from Sensor 2 (S}_2\text{)}$$

$$\vec{r}_3 = (x_3, y_3, z_3) \quad \text{from Sensor 3 (S}_3\text{)}$$

- **Time window:** Only hits occurring within a time window (100 ns) are considered for the combinatorial of them.
- **Combination of sensors:** All valid combinations of the two outer sensors are used to reconstruct the tracks.
- **3D line fit:** A straight line is fitted through the two sets of hit positions (S₁ & S₃) to reconstruct the trajectory particle in the 3D space. The fit is performed using the PCA method, which identifies the direction of maximum variance among the hit points. By centering the data and computing the eigenvectors of the covariance matrix, the primary eigenvector corresponds to the best-fit line direction.
- **Line-plane intersection:** The fitted track is intersected with the sensor plane under study to determine the expected hit position. See Appendix G.1 for more details.
- **Residuals:** The residuals are defined as the difference between the predicted and measured hit positions. They are used to evaluate the spatial resolution:

$$\text{Res}_x = x_p - x_{\text{hit}}$$

$$\text{Res}_y = y_p - y_{\text{hit}}$$

- **R²-coefficient:** It quantify how well the fitted line explains the variance of the data points around it. See Appendix G.2.

Figure 5.19 illustrates the steps mentioned before and the geometry used. Including the initial set of recorded hits from three different sensors, the fitted 3D trajectory, and the extrapolated intersection point on a reference sensor plane for the residual calculation.

Spatial resolution

To visualize and analyze the spatial arrangement of the detector modules and the corresponding particle trajectories, a 3D reconstruction of the experimental setup was

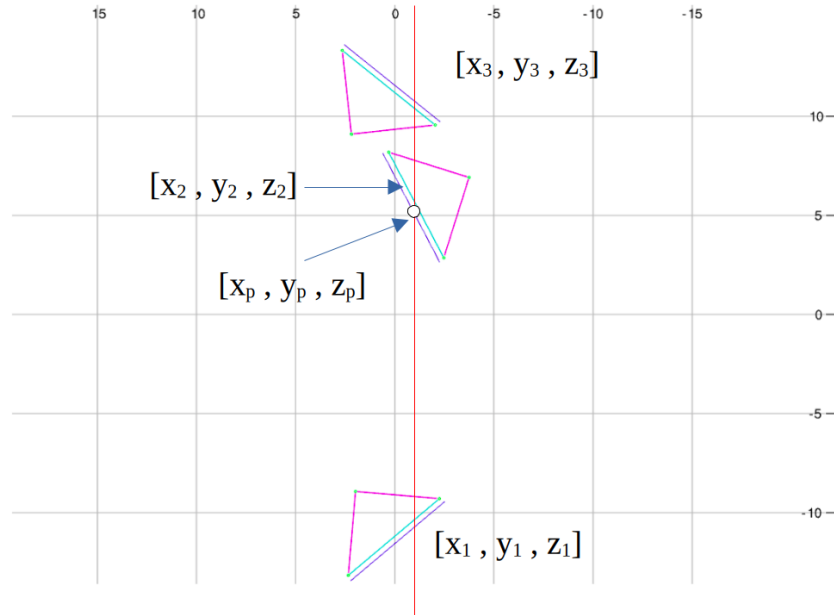


Figure 5.19: Visualization of the tracking method and geometry (run113). The recorded hits on three sensor planes, the fitted 3D trajectory, and the extrapolated intersection on the test sensor used for residual calculation are shown.

performed, see Figure 5.20a. This reconstruction is based on the reconstructed hit positions using the tracking method described for the multiple detector planes and without the geometrical acceptance conditions derivative from the scintillators. The reconstruction is illustrated in Cartesian coordinates (X, Y, Z) , where the Z -axis represents the beam direction. This visualization serves as a confirmation that we are able to reproduce the complexity of the setup configuration such as the X, Y, Z positions of each module and their corresponding inclination angles.

The spatial resolution is a fundamental parameter in detector systems, especially for those designed to track charged particles. It quantifies the capability of the detector to reconstruct positions with high accuracy, which enables precise determination of particle trajectories, which is essential for momentum determination. Figure 5.20a shows a few representative reconstructed tracks, which illustrate the performance of the tracking algorithm. The difference between the reconstructed hit positions and the track projections allows for the calculation of residuals. Also, in Figure 5.20b the corresponding XY reconstructed hitmap is illustrated.

Figure 5.21 presents the resulting residual distributions in the X - and Y - coordinates for module E16-107-PA, which corresponds to the middle sensor inclined at an angle of 62° . The residuals are in the orders of decimal of millimeters and the intense red region in the center of the distribution indicates the mean values.

The residuals are illustrated in more detail in Figure 5.22, projected on the X - and Y -axis, respectively. The distributions are fitted with the sum of two Gaussian functions, one corresponding to clusters of 1-strip size and the second for larger clusters, identified with red and blue lines, respectively. The assumption that the two Gaussian functions are due to the clusters of 1-strip or larger size is supported by the cluster distributions of the modules in each side, see Figure 5.23, where there is a ratio of 3:1 for 1-strip and

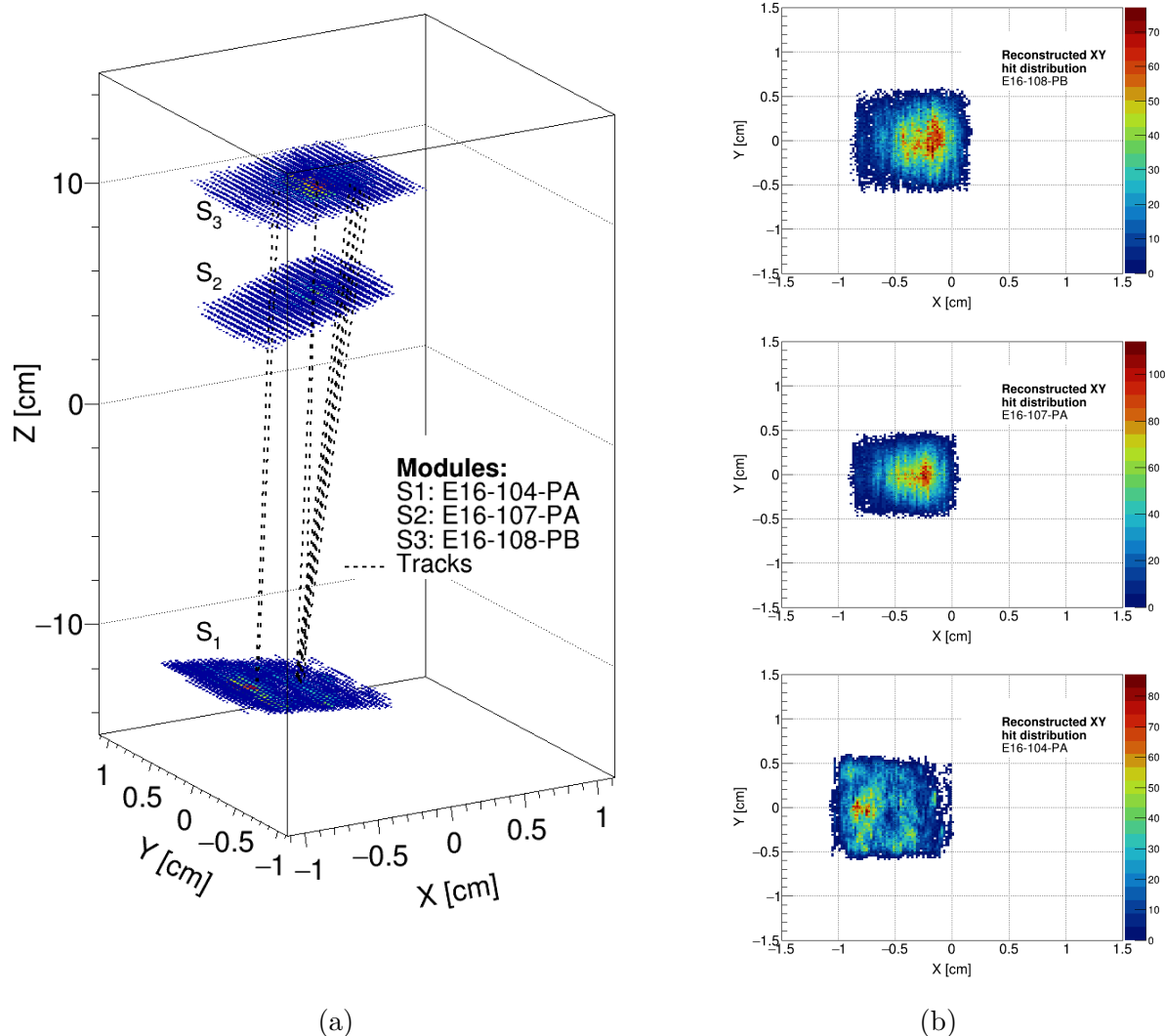


Figure 5.20: a) Visualization of reconstructed particle tracks crossing the three modules. b) The corresponding XY hit distributions of each module.

≥ 2 -strip clusters, slightly less for the area under the Gaussian fit (2:1).

Figure 5.22a shows the distribution for the X-coordinate. It is almost centered, with a mean value of $\mu_x = 0 \mu\text{m}$ and $\mu_x = 26 \mu\text{m}$ for the two different clusters size, and a standard deviation of $\sigma_x = 187 \mu\text{m}$ and $\sigma_x = 32 \mu\text{m}$, respectively. Similarly, the residual distribution in the Y-coordinate is presented in Figure 5.22b, where the means and standard deviation are $\mu_y = 1 \mu\text{m}$ and $\mu_y = 0 \mu\text{m}$, and $\sigma_y = 215 \mu\text{m}$ and $\sigma_y = 52 \mu\text{m}$, respectively.

These μ_x and μ_y indicate that the systematic offset in the X- and Y- directions are minimal. It is important to note that these σ_x and σ_y do not represent the intrinsic resolution of the sensor alone. Instead, they reflect the total uncertainty in the measurement, which includes contributions from detector resolution, multiple scattering, track incidence

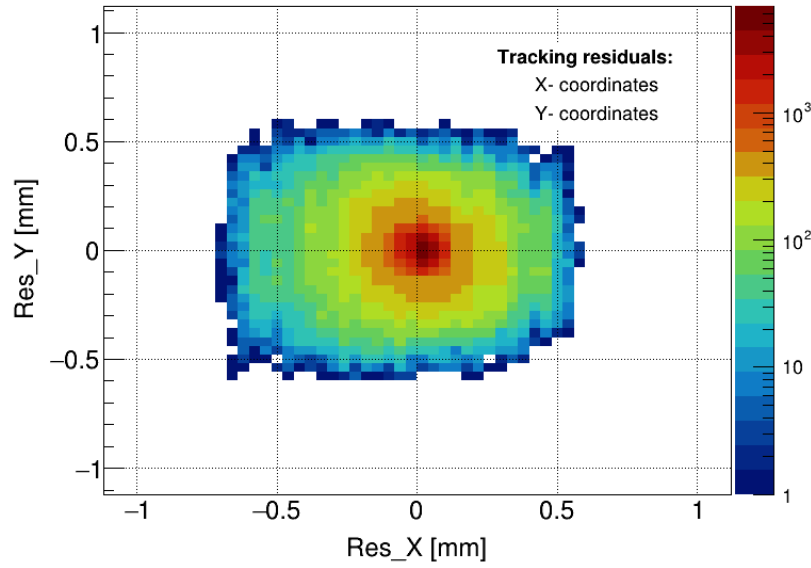
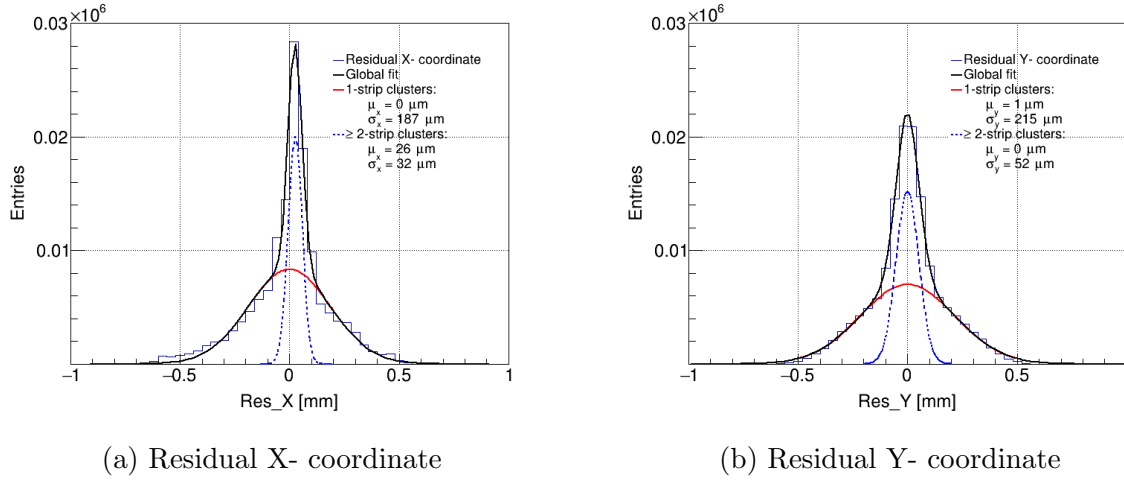


Figure 5.21: Residuals distribution of X- and Y-coordinate for module E16-107-PA (62° inclination angle). The values are in units of mm.



(a) Residual X- coordinate

(b) Residual Y- coordinate

Figure 5.22: Residuals projection for X- and Y-coordinates in the configuration of 62° of inclination angle for module E16-107-PA.

angles, and misalignment and it is shown in Equation 5.5:

$$\sigma_{sensor}^2 = \sigma_{residual}^2 - \sigma_{track}^2 - \sigma_{MS}^2 - \sigma_{rotation}^2 + \dots \quad (5.5)$$

If the contributions of multiple scattering and the rotation of the sensors is considered negligible with respect to the rest in a first approximation, the upper limit of the spatial resolution is calculated as $\sigma_{sensor}^2 \approx \sigma_{residual}^2 - \sigma_{track}^2$, where $\sigma_{track}^2 \approx \frac{3}{2}\sigma_{sensor}^2$, resulting in Equation 5.6:

$$\sigma_{sensor} \approx \frac{\sigma_{residual}}{1.58} \quad (5.6)$$

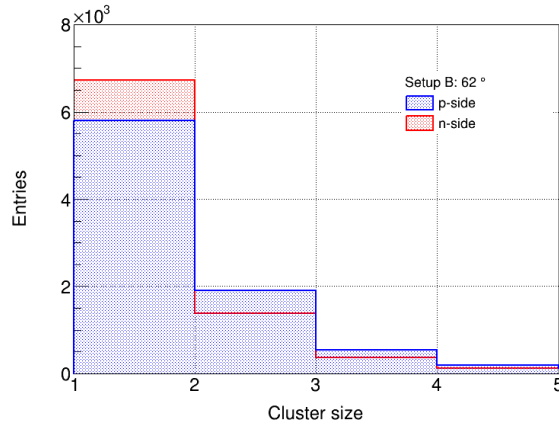


Figure 5.23: Cluster size distribution for n- and p-side of module E16-107-PA in setup configuration with a 62° sensor tilted.

The results of the spatial resolution for X- and Y-coordinate are summarized in Table 5.3. The values are reported with distinction of cluster size, in particular for 1-strip and ≥ 2 -strip clusters.

Table 5.3: Upper limit for spatial resolution of module E16-107-PA. The values are given for X- and Y-coordinate and make distinction in resolution for 1-strip or ≥ 2 -strip clusters. The reported values are in units of μm .

Module ID	σ_x (μm)		σ_y (μm)	
	1-strip	≥ 2 -strip	1-strip	≥ 2 -strip
E16-107-PA	118	20	136	33

5.4 Commissioning run at J-PARC

The commissioning run (Run-0e), was carried out using beam intensities of 1×10^9 , 5×10^9 , and 1×10^{10} pps. During this period, data was collected for various purposes, including detector performance evaluation, calibration, and physics data acquisition using the physics trigger. For the evaluation of the E16-STS system, the data was acquired at a beam intensity of 1×10^9 pps, in the absence of a magnetic field. Run-0e constituted the first time data acquisition was performed using the E16-STS modules with the online trigger system fully operational.

This section aims to summarize the work conducted by our colleagues from the E16 collaboration in Japan, particularly drawing on the materials presented in the Master's thesis of Rento Yamada [74].

5.4.1 Results

Online trigger selection

Figure 5.24 shows the distribution of the timing difference between the TDC signals from the E16-STS system and the GBTx-EMU trigger after applying the online trigger selection. A distinct peak around -95 ticks indicates that the online trigger selection was successfully implemented. More details are given in the thesis of Rento Yamada [74].

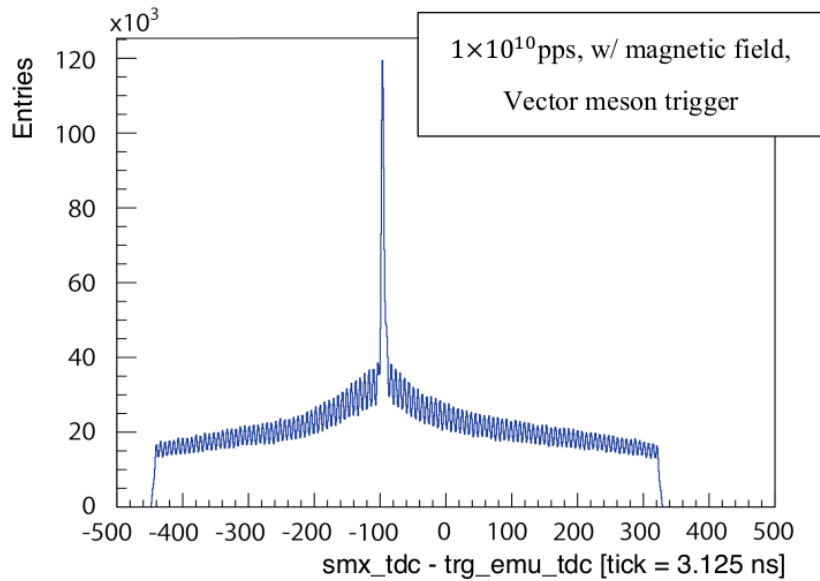


Figure 5.24: Time difference distribution between detector hits and trigger signals, performed under a beam intensity of 1×10^{10} pps, in a presence of a magnetic field and using a vector meson trigger [74].

Spatial resolution

Figure 5.25 shows the residual distribution for one of the E16-STS modules (specifically, the n-side of module E16-106-PB). The residual is defined as the difference between the intersection point of a track reconstructed using three GTR layers and the corresponding hit position recorded in the E16-STS module.

To validate the measured residual width of $144 \mu\text{m}$, a Monte Carlo simulation was performed, as described in [74]. The simulation included the geometry of a single E16-STS layer and three GTR layers, assuming a position resolution of $\sigma = 120 \mu\text{m}$ for each GTR layer. A straight line fit was applied to the three simulated GTR hit positions, and the residuals were calculated with respect to the E16-STS hit. The resulting residual width was $\sigma = 140 \mu\text{m}$, which is in good agreement with the experimental value. This agreement, obtained under the assumption of a $\sigma = 120 \mu\text{m}$ position resolution for the GTR, suggests that the spatial resolution of the E16-STS modules is consistent with expectations and is projected to meet the requirements for E16 and CBM experiments.

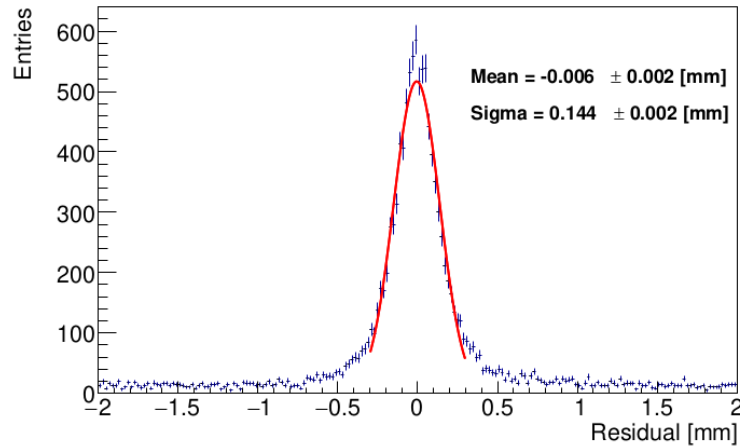


Figure 5.25: Residual in X-coordinate combined of E16-STS and three layers of GTR. A $\sigma = 144 \mu\text{m}$ with the assumption of $\sigma = 120 \mu\text{m}$ position resolution for the GTR, suggest a consistent with the expectation position resolution for the E16-STS modules. [74]

Energy loss for PID

The performance of the E16-STS modules was studied under magnetic field conditions and a beam intensity of 1×10^9 pps. Figure 5.26 presents the distribution of the charge deposited (using the charge calibration) in the E16-STS modules as a function of the reconstructed track momentum. The reconstruction of the track was performed using one layer of E16-STS in combination with three layers of the GTR.

The MPVs of energy loss for different particles (π , K , p , and d) are shown, where clear separation bands are observed for pions and protons. These results indicate that, while the main purpose of the E16-STS and STS modules is to track, they can also provide complementary particle identification information. This feature becomes particularly relevant for the full STS system, which will incorporate eight tracking layers.

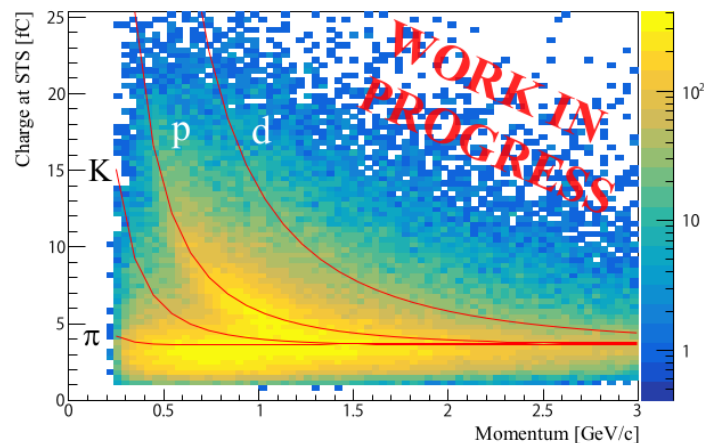


Figure 5.26: Energy loss distribution versus track momentum. The tracks were reconstructed using four tracking layers: one E16-STS and three GTR [74].

5.5 Summary

The performance of the E16-STS chamber was evaluated under beam conditions demonstrating that the system met its design specifications, representing an important milestone for both the E16 and CBM projects. In total, three modules of the chamber were tested using an electron beam of 3 GeV/c. The modules were studied in two different configurations. In the first configuration, a single module was evaluated at two different angles (0° and 16°), allowing the measurement of the time resolution, charge distribution, SNR, cluster size, and detection efficiency. In the second configuration, the three modules were placed at angles of 40° , 62° , and 39° , forming three tracking layers to allow the evaluation of position resolution.

Although the high threshold settings prevent fully firm assessments, the performance results can be summarized as follows:

- **Time resolution:** For large signal amplitudes, a time resolution of 3.2 ns was achieved. For signal amplitudes of approximately 2.7 fC, the measured time resolution was approximately 5 ns, satisfying the requirements for the E16 and CBM experiments.
- **Charge distribution and signal-to-noise ratio:** The collected charge on the n- and p-sides was $22212 e \pm 182 e$ and $19803 e \pm 243 e$, respectively. These values are up to 13% for n-side and 22% for p-side below the expected charge deposited in 320 μm of silicon by MIPs. The corresponding SNR values were 27.8 ± 2.2 (n-side) and 28.5 ± 1.5 (p-side), which are considered sufficient to ensure successful operation of the STS modules in both experiments.
- **Cluster size:** An increase in the average cluster size as a function of the incident angle was observed. The average values are in the range of 1.2-1.6. However, the variation was not as large as expected for such inclination angle because of the high signal threshold.
- **Detection efficiency:** For a normal incidence angle (0°), a detection efficiency of $89.85\% \pm 0.11\%$ was achieved. For other inclination configurations, the efficiency decreased significantly as a result of increased charge sharing while maintaining high threshold settings.
- **Position resolution:** Using the three modules configurations, the position resolution was evaluated through a PCA-based tracking reconstruction method. The residuals between the expected and measured hit positions were analyzed, resulting in upper limits for the position resolution of $\sigma_x = 118 \mu\text{m}$ and $\sigma_y = 136 \mu\text{m}$ for 1-strip clusters. For larger strip clusters (≥ 2 strips), the estimated resolutions improved to $\sigma_x = 20 \mu\text{m}$ and $\sigma_y = 33 \mu\text{m}$.

Finally, a summary of the results obtained during the commissioning run (Run-0e) was presented. In addition to the evaluation of the data acquisition system and the assessment of the spatial resolution, a major achievement was the first successful operation of the STS modules, together with the rest of the E16 setup, under magnetic field conditions. The energy-loss measurements revealed a clear separation between pions and protons

in the charge-momentum distribution. These findings demonstrate that, beyond precise tracking, the E16-STS modules also offer valuable particle identification capabilities, an important feature for the full eight-layer STS system planned for CBM experiment.

Chapter 6

Conclusions and Outlooks

This work presented a comprehensive study on the development, optimization, and validation of the calibration and characterization procedures for the SMX ASIC in modules of the E16-STS system, providing a critical contribution to the preparation and commissioning of the CBM-STS detector. The work addressed the full scope of the module life cycle: from the design and algorithmic level of calibration, through large-scale production testing and performance qualification, to the experimental validation under beam conditions.

The first major part of this work focused on improving the calibration algorithm of the SMX ASIC. The traditional ADC calibration method, while precise, was dramatically affected by the time-consuming of the coarse-scan stage, limiting its applicability for large-scale module testing. To overcome this constraint, a calibration procedure based on SAR algorithm was implemented. This approach replaced the exhaustive scan with a binary search mechanism, allowing rapid convergence toward the optimal threshold value. The SAR method achieved calibration precision equivalent to the standard approach, with DNL and INL values remaining below 0.4 LSB, while reducing the calibration time by 30%. Once the SAR calibration method proved to be a valid alternative to the STANDARD one, further optimization studies were carried out to refine the algorithm parameters, specifically the number of iterations, search width, and fine-range. The configuration of 10 iterations, 14 LSB search width, and 12 LSB fine-scan range was identified as the most efficient compromise between speed and precision. This configuration allows to reduce the calibration time from the 30% previously achieved to a significant 60%.

The implementation of a broadcasting mechanism represented another step forward in the pursue of reducing the calibration time. The method allows to calibrate multiple ASICs, modules and even ladders almost simultaneously. As part of this work, the broadcasting method based on the SAR algorithm was implemented for an entire module. An additional 50% reduction in the calibration time compared to the already established SAR method was achieved.

For operational purposes, to establish the correlation between the amplitude and timing is essential. In this context, a detailed analysis of the transfer functions of the ADC and FAST discriminators was performed, establishing a linear relationship between the DAC settings ($VRef_T$ and $Thr2_glb$) and the corresponding amplitude and timing thresholds, respectively. This study confirmed a slope ratio of approximately two between the ADC and FAST paths, consistent for both n- and p-side. The ADC slopes values for n- and

p-side resulted in 822 e/LSB and 718 e/LSB, respectively, while for the FAST the values were 397 e/LSB and 361 e/LSB. These results allow the creation of an operational table that correlates the thresholds, the DAC settings, and provides a better understanding of the two signal threshold system used in our FEE.

The feasibility of using one common global *Thr2_glb* setting to calibrate the FAST discriminator in an entire module was evaluated in a CRT-01-PB module. It demonstrates successfully that most of ASICs in a module can achieve between 95-100% calibration ratio with a common window of 22-26 LSB of the *Thr2_glb* register setting. It was not possible to identify a common *Thr2_glb* value to calibrate the Z-strips channels in module CRT-01-PB.

As a large-scale validation of the optimized calibration procedure, ten pre-series modules were fully calibrated using the SAR algorithm. The analysis of the resulting trim matrices revealed only a small fraction of outliers. The n- and p-sides exhibited 81 (0.03%) and 258 (0.08%) uncalibrated discriminators respectively, representing a minor proportion of the total. The p-side required smaller trimming corrections, with a maximum adjustment of 20 LSB to achieve 95% calibrated discriminators, compared to 28 LSB for the n-side.

The second part of the thesis extended these developments to the functional assessment and validation of complete detector modules. Fifteen modules including one prototype, ten pre-series, and four replacement units were systematically characterized. The test campaign followed a standardized four step procedure comprising module current-voltage (IV) evaluation, ASIC calibration, electronic performance characterization, and data acquisition using a radioactive source.

The IV were measured up to 150 V, and they confirmed stable sensor behavior. The calibration results verified consistent and reproducible performance across modules, with well-defined ADC gains, threshold levels, and limited channel-to-channel spread. The measured ENC values were found around 700 e and 900 e for the different modules and sides, and within approximately 20% of the parametrization expectations. Additionally, the broken channels across the modules were identified. In overall, only one of the fourteen modules (10 pre-series + 4 replacements) exceeded the production target of 31 broken channels, in this case by one broken channel, which represents 1.5% of the total.

The radioactive $^{90}\text{Sr}/\text{Y}$ source tests allowed the mapping of individual channel responses, served as a complementary method to identify broken channels and validated the already identified broken channels. Also, time correlation analysis between Digis inside clusters were performed with the maximum correlation peak well-centered around $\Delta t = 0$ ns. The spectra distributions were also evaluated and a reconstructed 2D hitmap in agreement with the location of the source during the data acquisition tests.

The valuable insights gained throughout this work led to the development of a comprehensive module testing protocol, which has now been integrated into the standardized quality assurance framework for the evaluation of the final STS modules. This protocol is currently used in the ongoing series-production phase of the STS construction, during which more than 550 modules have already been successfully characterized.

The final part of the thesis focused on the experimental validation of detector performance in a beamline. A dedicated beam campaign using a 3 GeV/c electron beam was conducted in the PF-AR facility in Japan. The E16-STC chamber, consisting of ten modules, was tested. In total three of the ten modules were evaluated in various geometrical

configurations.

The performance results can be highlighted as follows:

- a time resolution of 3.2 ns was achieved for large signal amplitudes, and approximately 5 ns for signals around 2.7 fC, fulfilling the timing requirements for both E16 and CBM experiments;
- the measured charge collected for n- and p-side was of $22212 e \pm 182 e$ and $19803 e \pm 243 e$, respectively. These measured values are up to 13% and 22%, for n- and p-side, below of the expected value for MIPs in 320 μm of silicon;
- the corresponding SNR values were 27.8 ± 2.2 for n-side and 28.5 ± 1.5 for p-side;
- the measured detection efficiency reached $89.85\% \pm 0.11\%$ at normal incidence;
- position reconstruction, based on a PCA-based tracking algorithm, yielded spatial resolutions of $\sigma_x = 118 \mu\text{m}$ and $\sigma_y = 136 \mu\text{m}$ for single-strip clusters, improving to $\sigma_x = 20 \mu\text{m}$ and $\sigma_y = 33 \mu\text{m}$ for multi-strip clusters.

Furthermore, during the commissioning run (Run-0e), the first successful operation of the CBM-STs modules under magnetic field conditions was achieved. The clear pion–proton separation via energy-loss measurements, demonstrated beyond precise tracking, capabilities for particle identification.

Looking forward, future efforts will concentrate on the large-scale integration of the STS system, with special emphasis on implementing the broadcasting calibration approach for simultaneous operation of multiple modules and ladders. Additionally, further studies will revisit the behavior of detection efficiency and cluster size at large incidence angles to achieve a more comprehensive understanding of the detector performance under the influence of the magnetic field.

Appendix A

The SAR method algorithm

A.1 The SAR method visual example

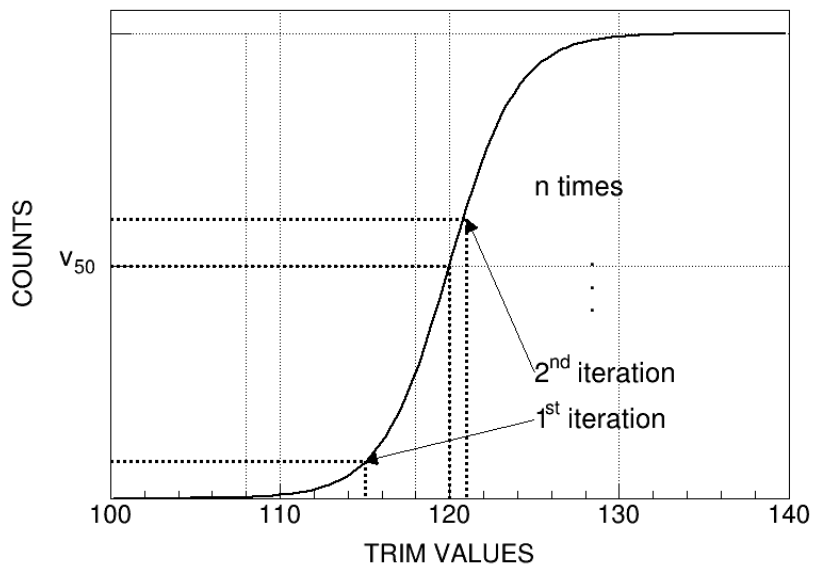


Figure A.1: Exemplary graph illustrating how the SAR method was implemented in the SMX calibration procedure to determine the trim value corresponding to the (V_{50}) threshold. The method refines the trim setting iteratively around the discriminator threshold through a binary search process.

A.2 The SAR main method code

```
1 for ch in range(ch_min, ch_max):
2     cnt[ch][d] = self.read(ch, count) & 0xff
3
4     if cnt[ch][d] > loop_max / 2.:
5         trim_before[ch][d] = trim_before[ch][d] - int(width / n)
6         trim_final[ch][d] = trim_before[ch][d]
7         self.write(ch, disc, trim_before[ch][d])
8
9     elif cnt[ch][d] < loop_max / 2.:
10        trim_before[ch][d] = trim_before[ch][d] + int(width / n)
11        trim_final[ch][d] = trim_before[ch][d]
12        self.write(ch, disc, trim_before[ch][d])
13
14    else:
15        self.write(ch, disc, trim_before[ch][d])
16        trim_final[ch][d] = trim_before[ch][d]
```

Listing A.1: SAR trim adjustment loop for each channel

Appendix B

The prototype FEB-C

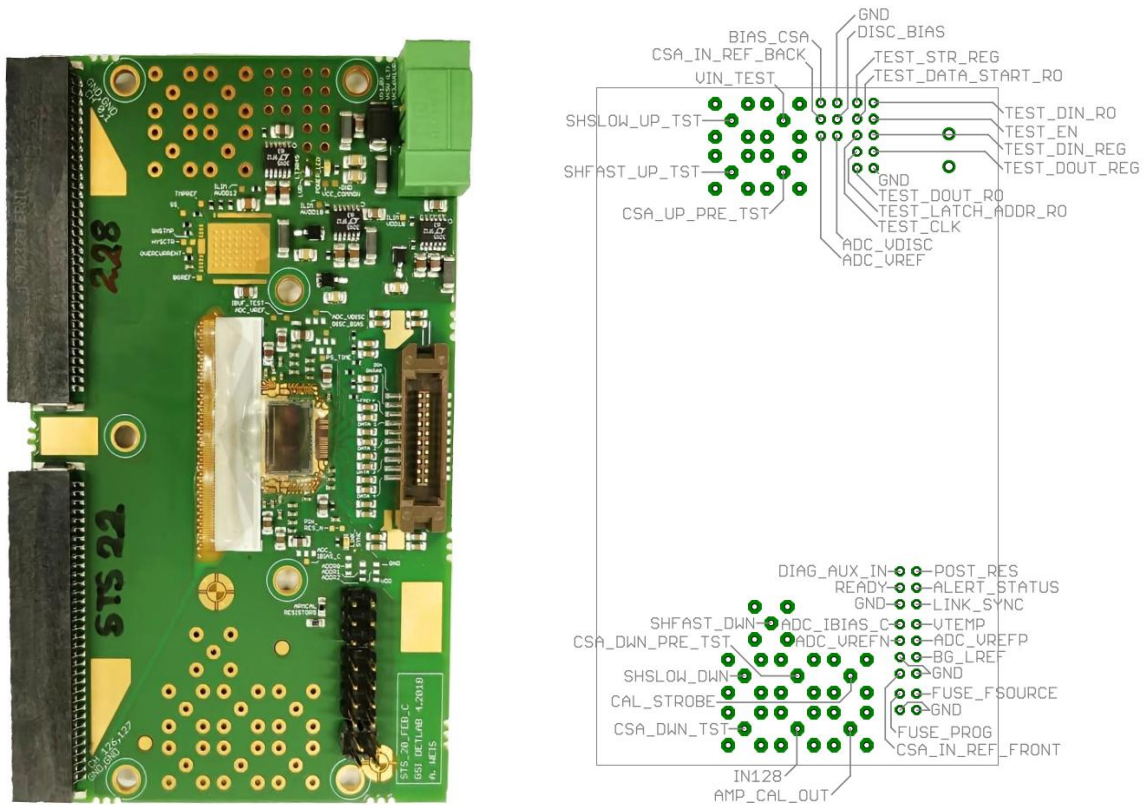


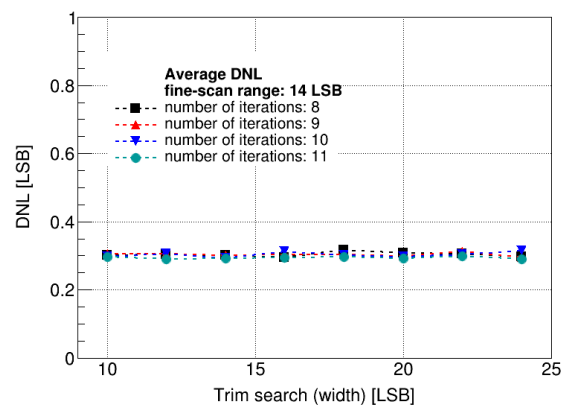
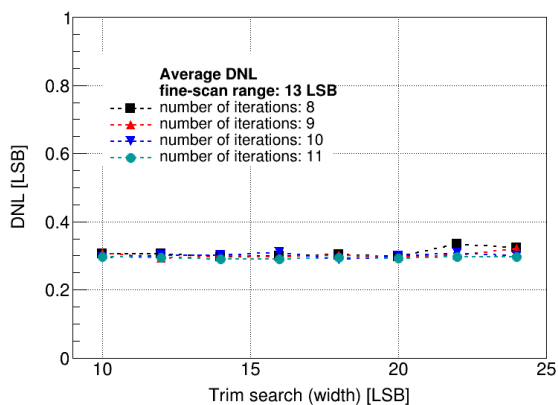
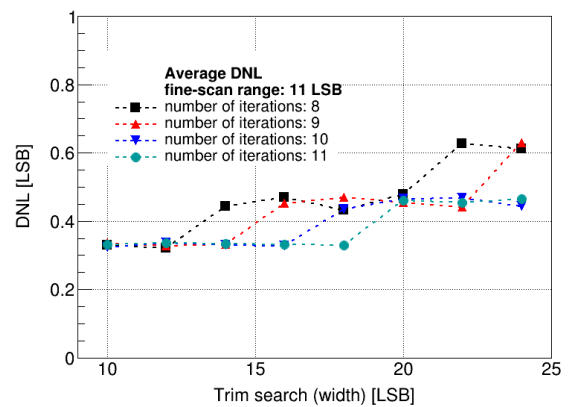
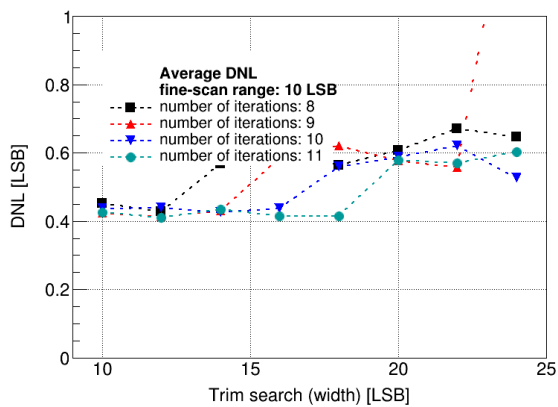
Figure B.1: Photo and schematics of the prototype FEB-C. The FEB-C carries the SMX2.2 ASIC.

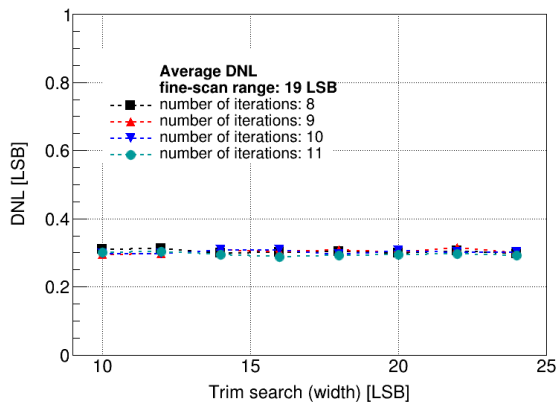
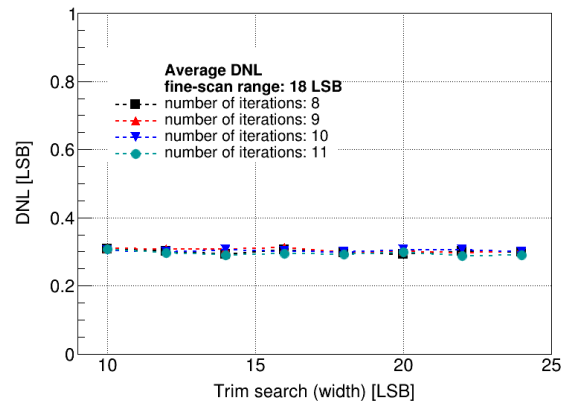
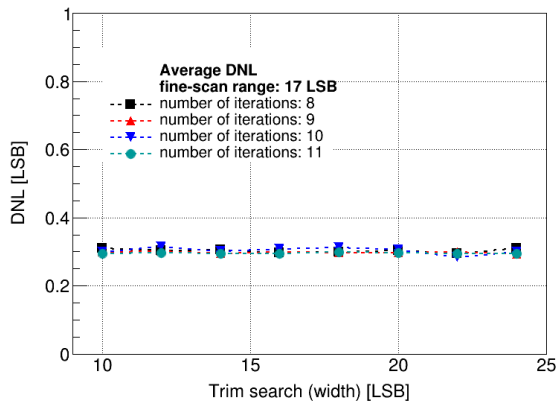
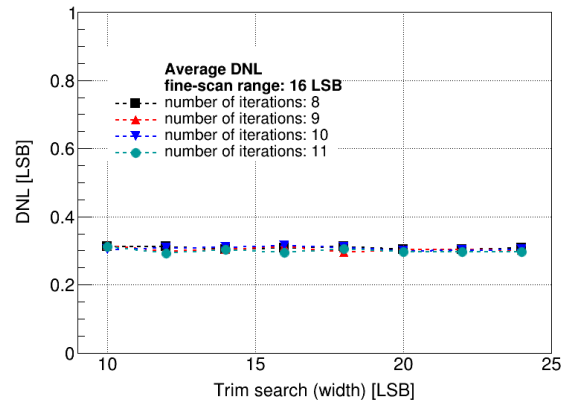
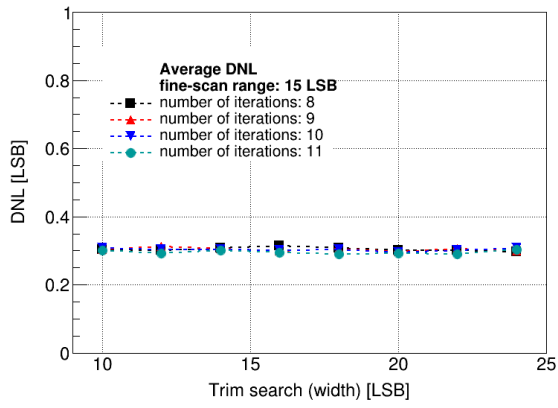
Appendix C

The SAR method quality parameters

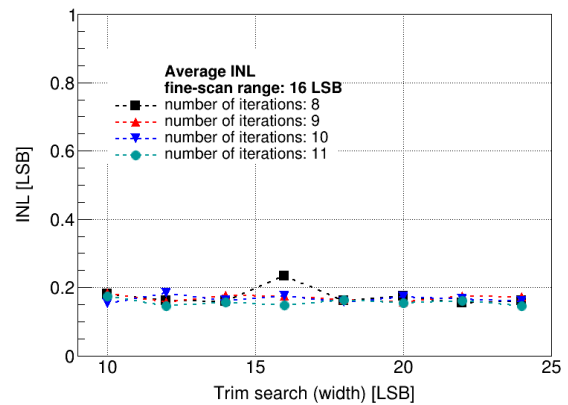
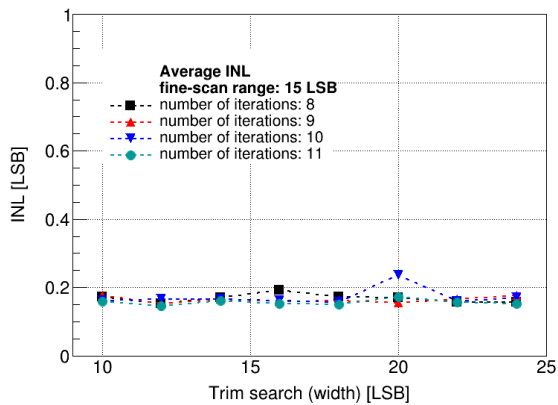
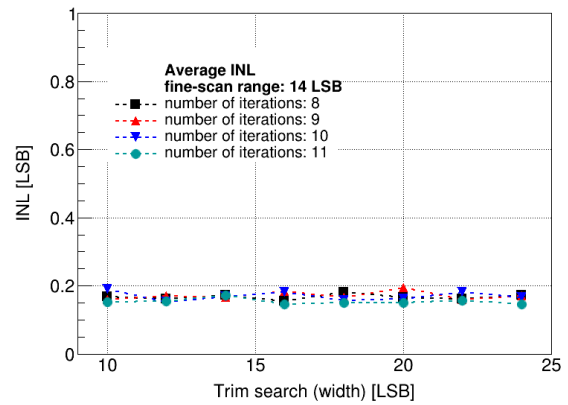
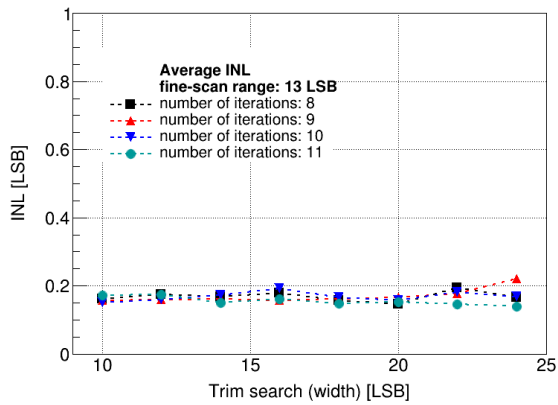
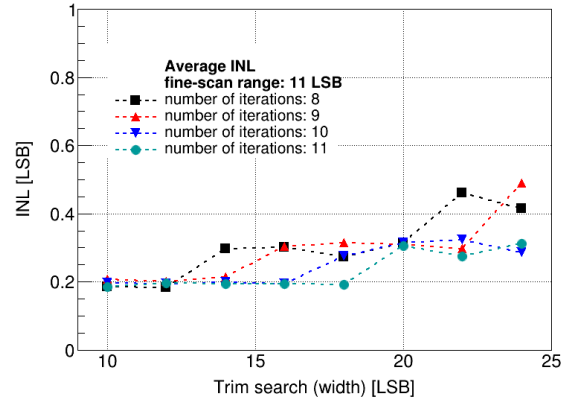
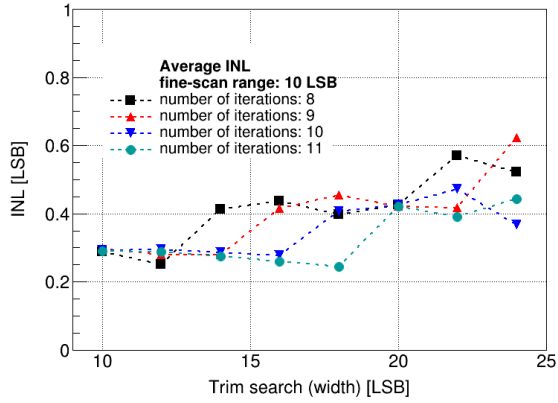
DNL, INL and standard deviation of the linear residual for different fine-scan range from 10-19 LSB, excluding the fine-scan range = 12 LSB.

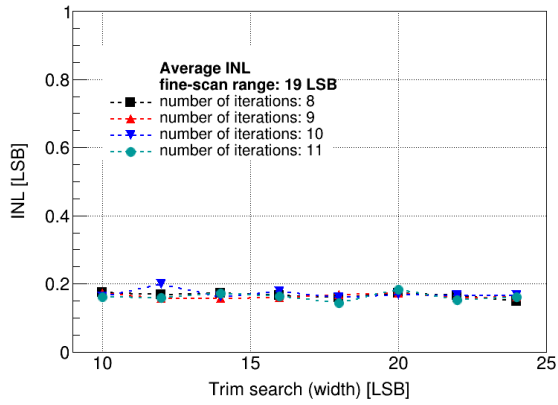
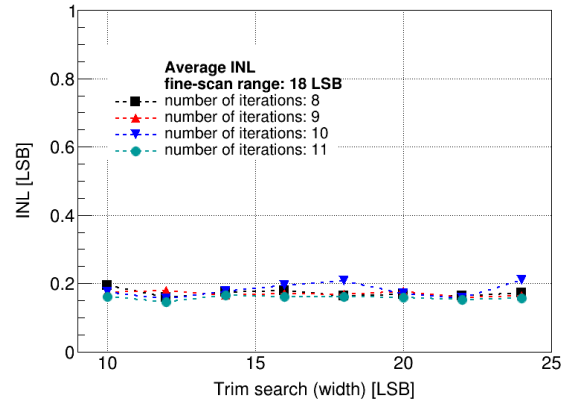
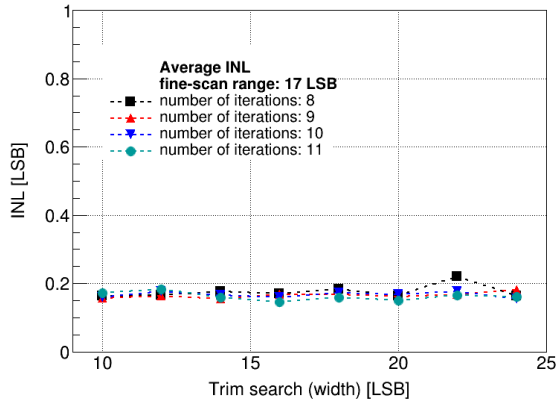
C.1 Differential Non-Linearity



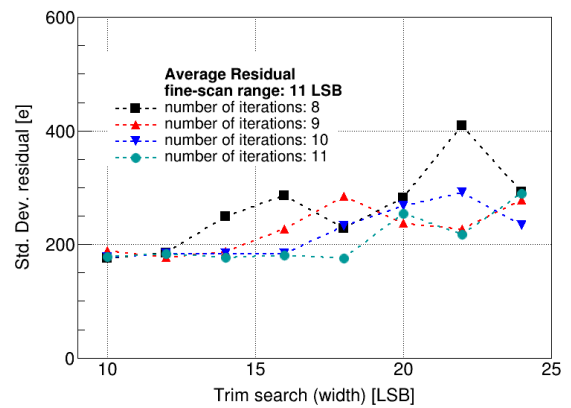
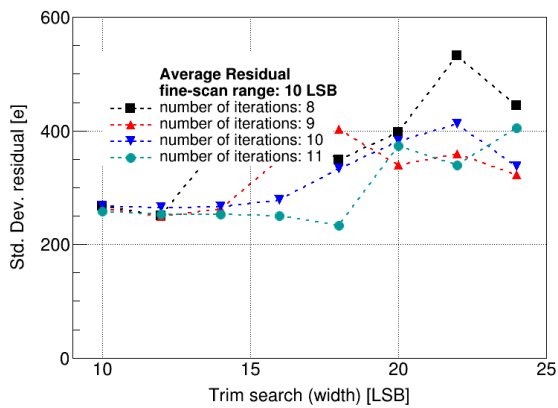


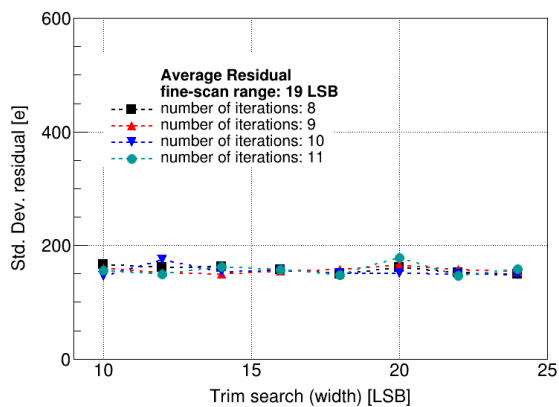
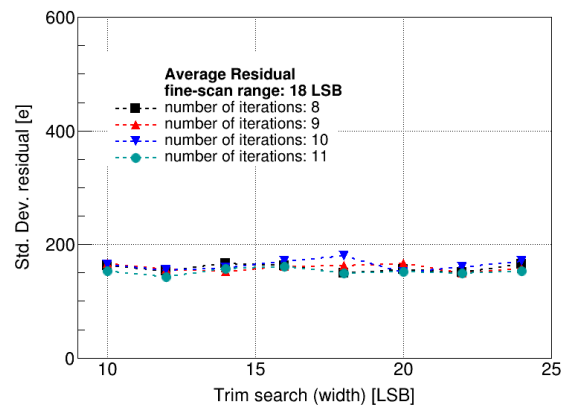
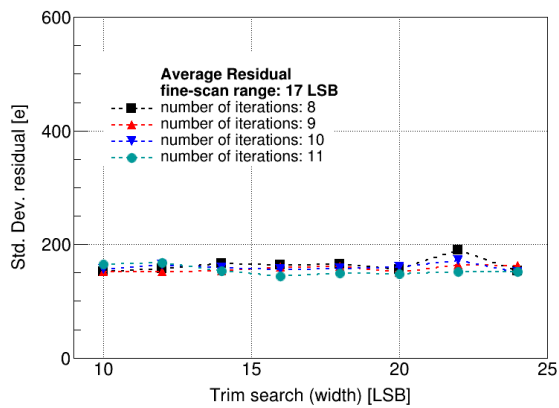
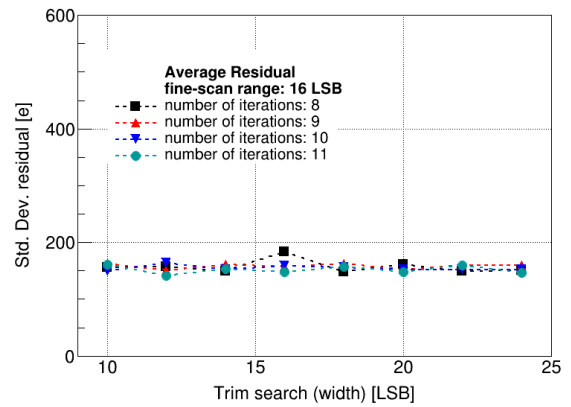
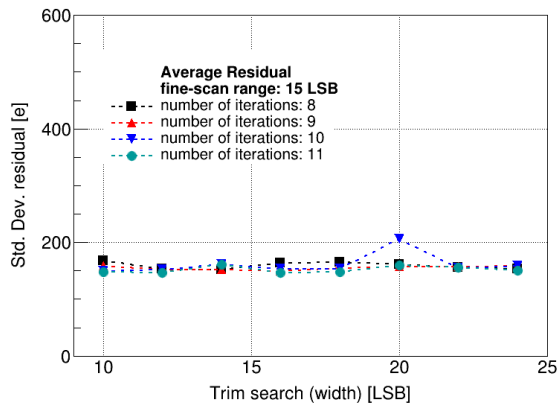
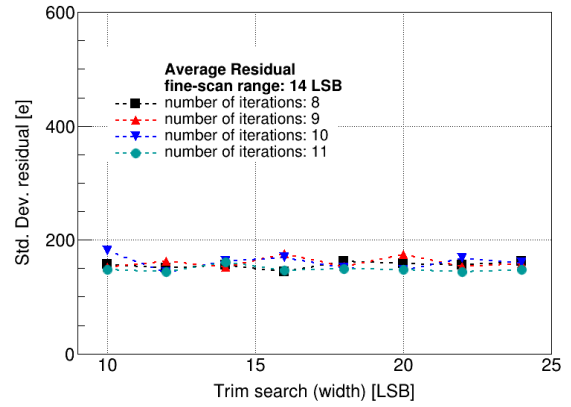
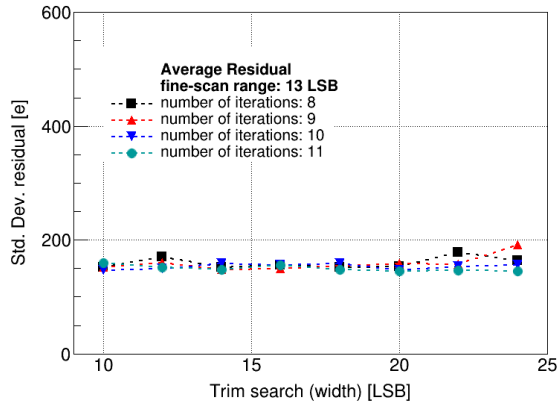
C.2 Integral Non-Linearity





C.3 Standard Deviation Linear Residual





Appendix D

Broadcasting commands and implementation in the SAR method

```
1 Class broadcast_master():
2
3     def __init__(self, hctsp_master, ack_monitor):
4         self.pulse_reg = (130,11)           # Pulse register
5         self.reset_counter_reg = (192,2)    # ADC counter reset
6                                             # register
7         self.group_reg = (130,5)           # Group selection
8                                             # register
9         self.pulse_amp_reg = (130,4)       # Pulse amplitude
10                                                # register
11         self.vrefp_reg = (130,9)           # VRef_P register
12         self.vrefn_reg = (130,8)           # VRef_N register
13         self.thr2glb_reg = (130,7)         # Thr2_glb register
14         self.vreft_reg = (130,18)         # VRef_T register
15
16         self.hctsp_master = hctsp_master
17         self.ack_monitor = ack_monitor
18         self.cmd_slot = self.hctsp_master.software_command_slot
19
20     # Generic command builder
21     def make_cmd(self, reg, data):
22         return hctsp.Command(
23             0xff,
24             0xffff,
25             2,
26             [hctsp.WRADDR, hctsp.WRDATA],
27             (reg[1] << 8) | reg[0],
28             data,
29             0xf
30         )
```

```

31
32
33 # === Test Pulse Control ===
34 def testpulse(self, on=True):
35     data = 0x80 if on else 0x00
36     cmd = self.make_cmd(self.pulse_reg, data)
37     self.cmd_slot.issue(cmd)
38
39 def testpulse_seq(self, n_pulse):
40     for _ in range(n_pulse):
41         self.testpulse(True)
42         self.testpulse(False)
43
44 # === ADC Counter Reset ===
45 def reset_adc_counter(self, on=True):
46     data = 0x20 if on else 0x00
47     cmd = self.make_cmd(self.reset_counter_reg, data)
48     self.cmd_slot.issue(cmd)
49
50 def reset_adc_counter_seq(self):
51     self.reset_adc_counter(True)
52     self.reset_adc_counter(False)
53
54 # === Group Selection & Pulse Injection ===
55 def group_select(self, group_id):
56     cmd = self.make_cmd(self.group_reg, group_id)
57     self.cmd_slot.issue(cmd)
58
59 def gen_pulses_all_groups_seq(self, n_pulse, grp):
60     for gid in grp:
61         self.group_select(gid)
62         self.testpulse_seq(n_pulse)
63
64 # === Pulse Amplitude ===
65 def pulse_amplitude(self, data):
66     cmd = self.make_cmd(self.pulse_amp_reg, data)

```

Listing D.1: Broadcasting commands

```

1 print("-----Calibrating_ADC-----")
2     step = int((amp_cal_max-amp_cal_min)/31)
3     for d in range(0,31):
4         disc = 61 - 2*d
5         count = 61 - 2*d - 1
6         print("Calibration_Pulse_Amplitude_set_to:{}".format(
7             amp_cal_min+d*step))
8         self.bcast.pulse_amplitude(amp_cal_min+d*step)
9         for n in range(1,it_coarse):
10            self.bcast.reset_adc_counter_seq()
11            self.bcast.gen_pulses_all_groups_seq(npulses,grp)
12            for ch in range(0,128):
13                for i_pol, smx_list in enumerate([smx_l_nside,
14                                                    smx_l_pside]):
15                    for i, smx in enumerate(smx_list):
16                        cnt[i_pol][i][ch] = smx.read(ch, count)
17                        & 0xfff
18                        cnt_value = cnt[i_pol][i][ch]
19                        if (cnt_value > npulses/2.):
20                            trim_before[i_pol][i][ch][d] =
21                                trim_before[i_pol][i][ch][d] -
22                                int(width_coarse/n)
23                        elif (cnt_value < npulses/2.):
24                            trim_before[i_pol][i][ch][d] =
25                                trim_before[i_pol][i][ch][d] +
26                                int(width_coarse/n)
27                        smx.write(ch,disc,trim_before[i_pol][i]
28                                [ch][d])
29
30            for itr in range(0,it_fine+1):
31                print("fine_disc_{}_itr_{}/{}".format(d,itr,it_fine))
32                for ch in range(0,128):
33                    for i_pol, smx_list in enumerate([smx_l_nside,
34                                                        smx_l_pside]):
35                        for i, smx in enumerate(smx_list):
36                            smx.write(ch,disc,trim_before[i_pol][i]
37                                    [ch][d] - 5
38                                    + itr)
39
40            self.bcast.reset_adc_counter_seq()
41            self.bcast.gen_pulses_all_groups_seq(npulses,grp)
42
43            for ch in range(0,128):
44                for i_pol, smx_list in enumerate([smx_l_nside,
45                                                    smx_l_pside]):
46                    for i, smx in enumerate(smx_list):
47                        fcnt[i_pol][i][ch][itr] = smx.read(ch,
48                            count) & 0xfff

```

Listing D.2: SAR calibration implementing the broadcasting approach

Appendix E

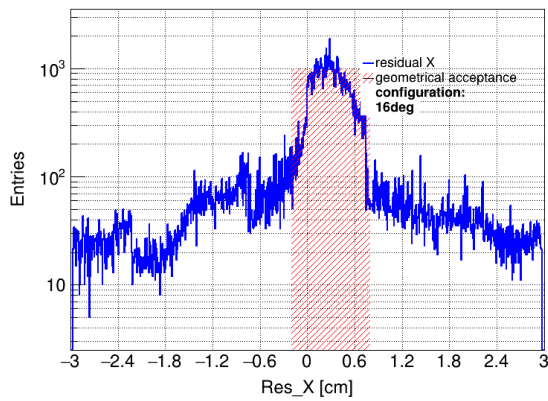
FAST discriminator trimming range

```
1 for (int thr = thr_min; thr < thr_max; thr++) {
2     for (int ch = ch_min; ch < ch_max; ch++) {
3         if (thr >= thr_trim[asic][36][ch] ||
4             thr <= thr_trim[asic][57][ch]) {
5             calibrated[thr] += 1;
6         } else {
7             ncalibrated[thr] += 1;
8         }
9     }
10    ratio_calibrated[thr] = calibrated[thr] / 128;
11 }
```

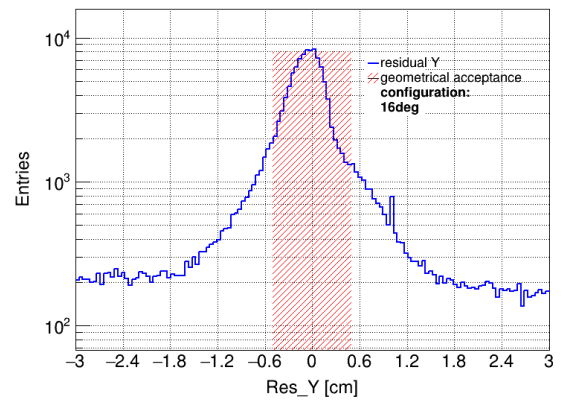
Listing E.1: Calibrated or uncalibrated FAST discriminator logic

Appendix F

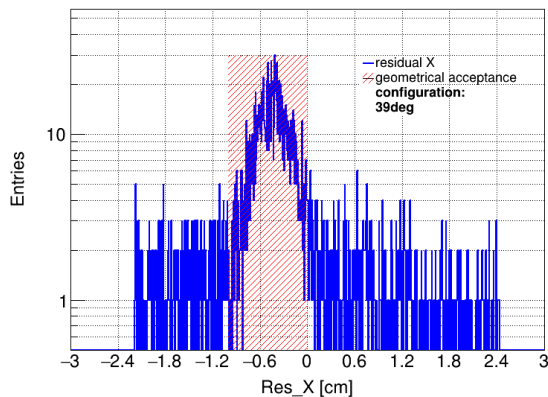
X- and Y-coordinate residuals under inclined tracks



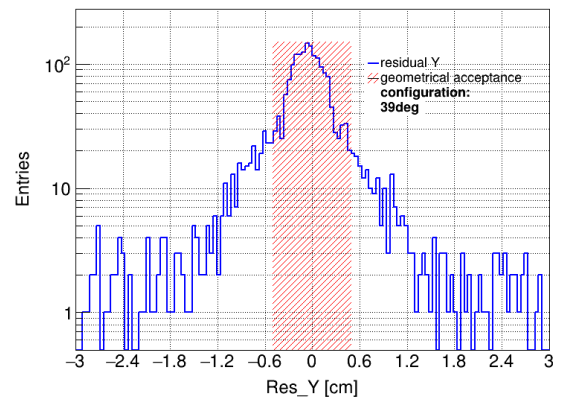
(a) Residual X- coordinate



(b) Residual Y- coordinate



(c) Residual X- coordinate



(d) Residual Y- coordinate

Figure F.1: Residuals for X- and Y-coordinates in the configuration of 16° and 39° of inclination angle for module E16-108-PB. The geometrical acceptance refers to the area covered by the scintillators.

Appendix G

Principal Component Analysis (PCA)

To reconstruct the particle trajectory in 3D space, a straight line is fitted through the set of hit positions registered by three sensor planes. This is achieved using the **PCA** method, which finds the line that best represents the spatial distribution of the hit points by minimizing the orthogonal distances from each point to the line.

Given a set of N hit positions $\mathbf{r}_i = (x_i, y_i, z_i)$, the centroid is first computed:

$$\bar{\mathbf{r}} = \frac{1}{N} \sum_{i=1}^N \mathbf{r}_i \quad (\text{G.1})$$

Then, the covariance matrix of the distribution is calculated:

$$C = \frac{1}{N} \sum_{i=1}^N (\mathbf{r}_i - \bar{\mathbf{r}})(\mathbf{r}_i - \bar{\mathbf{r}})^\top \quad (\text{G.2})$$

The principal axis of the hit distribution is given by the eigenvector \mathbf{d} corresponding to the largest eigenvalue of the covariance matrix C . This direction vector \mathbf{d} defines the best fit line in 3D space.

The equation of the reconstructed track line is then:

$$\mathbf{r}(t) = \bar{\mathbf{r}} + t \cdot \mathbf{d}, \quad t \in \mathbf{R} \quad (\text{G.3})$$

G.1 Intersection point line-plane

The extrapolation of the 3D track to the sensor plane is achieved by computing the intersection point between the fitted track (a straight line) and the sensor plane.

Let the track be represented in parametric form as:

$$\vec{r}(t) = \vec{r}_0 + t \cdot \vec{d} \quad (\text{G.4})$$

where \vec{r}_0 is a point on the track (e.g., the centroid of the fitted hits), \vec{d} is the direction vector of the track (typically the first principal component from PCA), and t is a scalar parameter.

The sensor plane is defined by a known point \vec{p}_0 on the plane and a normal vector \vec{n} . The intersection point \vec{p} is obtained by solving:

$$(\vec{p}_0 - \vec{r}_0) \cdot \vec{n} = t \cdot (\vec{d} \cdot \vec{n}) \quad (\text{G.5})$$

which yields:

$$t = \frac{(\vec{p}_0 - \vec{r}_0) \cdot \vec{n}}{\vec{d} \cdot \vec{n}} \quad (\text{G.6})$$

and thus the intersection point is:

$$\vec{p} = \vec{r}_0 + t \cdot \vec{d} \quad (\text{G.7})$$

This extrapolated point $\vec{p} = (x_p, y_p, z_p)$ represents the predicted impact position on the sensor.

G.2 Coefficient of determination for a 3D line fit

Given a point cloud $\{\mathbf{x}_i\}$ and the fitted principal-axis line from PCA, the coefficient of determination is defined as:

$$R^2 = 1 - \frac{\sum_i d_i^2}{\sum_i \|\mathbf{x}_i - \bar{\mathbf{x}}\|^2}, \quad (\text{G.8})$$

where

- $\bar{\mathbf{x}}$ is the mean position vector,
- d_i is the perpendicular distance from point \mathbf{x}_i to the fitted line,
- the denominator represents the total variance of the point cloud.

Values close to 1 indicate that the points lie tightly along a single linear direction, while values near 0 correspond to a weakly defined line.

List of Acronyms

A

ADC	Analog-to-Digital Converter.
AFE	Analog Front-End.
APPA	Atomic, Plasma Physics and Applications.
ASIC	Application-Specific Integrate Circuit.

C

C-ROB	Common Readout Board.
CBM	Compressed Baryonic Matter.
CERN	European Organization for Nuclear Research.
CLAS	CEBAF Large Acceptance Spectrometer.
CPU	Central Processing Unit.
CRI	Common Readout Interface.
CSA	Charge Sensitive Amplifier.

D

DAC	Digital-to-Analog Converter.
DAQ	Data Acquisition.
DCS	Detector Control System.
DIS	Deep Inelastic Scattering.
DMA	Direct Memory Access.
DNL	Differential Non-Linearity.
DPB	Data Processing Board.
DSSD	Double-Sided Silicon Strip Detector.

E

ENC	Equivalent Noise Charge.
EoS	Equation of State.

F

FAIR	Facility for Antiproton and Ion Research.
FCC	Flat Flexible Cable.
FEB	Front-End Board.
FEE	Front-End Electronics.
FLES	First Level Event Selector.
FMC	FPGA Mezzanine Card.
FSD	Forward Spectator Detector.

G

GBT-FPGA	Gigabit Transceiver-Field Programmable Gate Arrays.
GBT-SCA	Gigabit Transceiver-Slow Control Adapter.
GBTx	Gigabit Transceiver.
GBTx-EMU	GBTx-EMULATOR.
GEM	Gas Electron Multiplier.
GPU	Graphics Processing Unit.
GSI	GSI Helmholtzzentrum für Schwerionenforschung.
GTR	GEM Tracker.

H

HADES	High Acceptance Di-electron Spectrometer.
HBD	Hadron Blind Detector.
HV	High Voltage.

I

INL	Integral Non-Linearity.
IV	Current-Voltage.

J

J-PARC	Japan Proton Accelerator Research Complex.
JINR	Joint Institute for Nuclear Research.

K

KEK	High Energy Accelerator Research Organization.
-----	--

L

LDO	Low Drop-Out Voltage Regulator.
LG	Lead Glass Calorimeter.
LHC	Large Hadron Collider.
LSB	Least Significant Bit.
LV	Low Voltage.
LVDS	Low Voltage Differential Signaling.

M

MAPMTs	Multi-Anode Photo-Multipliers.
MAPS	Monolithic Active Pixel Sensors.
MIP	Minimum Ionizing Particle.
MPV	Most Probable Value.
MRPC	Multi-gap Resistive Plate Chambers.
MSB	Most Significant Bit.
MUCH	Muon Chambers System.
MVD	Micro Vertex Detector.
MWPC	Multi-Wire Proportional Chamber.

N

NA61	North Area 61.
NAR	No Analog Response.
NICA	Nuclotron-based Ion Collider fAcility.
NuSTAR	NUclear STructure, Astrophysics and Reactions.

P

PANDA	antiProton ANnihilation at DArmstadt.
PCA	Principal Component Analysis.
PF	Photon Factory.
PF-AR	Photon Factory Advanced Ring.
PHENIX	Pionering High Energy Nuclear Interaction eXperiment.
POB	Power Board.
PSC	Polarity Selection Circuit.
PSD	Projectile Spectator Detector.

Q

QA	Quality Assurance.
QCD	Quantum Chromodynamics.
QGP	Quark-Gluon Plasma.

R

RHIC	Relativistic Heavy Ion Collider.
RICH	Ring Imaging Cherenkov detector.
ROB	Readout Board.
RPC	Resistive Plate Chambers.

S

SAR	Successive Approximation Method.
SIS	Schwerionensynchrotron.
SNR	Signal-to-Noise Ratio.
SPS	Super Proton Synchrotron.
SSD	Silicon Strip Detector.
SSSD	Single-Sided Silicon Strip Detector.
STAR	Solenoidal Tracker at RHIC.
STS	Silicon Tracking System.

T

TAB	Tape-Automated Bonds.
TDC	Time-to-Digital Converter.
TFC	Timing and Fast Control System.
TOF	Time of Flight.
TPC	Time Projection Chamber.
TRD	Transition Radiation Detector.

U

UNILAC	UNiversal Linear ACelerator.
UT-3	Universal Trigger Board 3.

V

VUV

Vacuum-Ultraviolet.

Extended Abstract

One of the fundamental goals of modern physics is to understand how the universe and its constituents emerged and interact. The development of quantum field theories and experimental tools such as particles accelerators has enable the exploration of matter across an extraordinary range of scales, from quarks and gluons (10^{-15} m) to the structure of the cosmos (10^{26} m). Within this framework, the Standard Model describes the electromagnetic, weak, and strong interactions among elementary particles. The theory of the strong interaction, Quantum Chromodynamics (QCD), plays a central role in determining the properties of nuclear matter and the origin of the most of the visible mass in the universe.

QCD is non-Abelian gauge theory based on the local $SU(3)_{color}$ symmetry, whose elementary degrees of freedom are quarks and gluons. Two essential features characterize QCD: **asymptotic freedom**, which allows perturbative calculation at high energies, and **confinement**, which binds quarks and gluons inside color-neutral hadrons at low energies. Furthermore, the spontaneous breaking of chiral symmetry in the QCD vacuum generates the effective masses of light quarks. Under extreme conditions of temperature and/or baryon density, the chiral condensate is expected to melt, leading to the restoration of chiral symmetry and the formation of the new states of matter such as the Quark-Gluon Plasma (QGP) or dense baryonic matter.

The phase structure of QCD can be represented in the plane of temperature (T) and baryon chemical potential (μ_B). At high T and low μ_B , as realized in the early universe, a smooth crossover transition between hadronic and partonic matter occurs and has been explored at Relativistic Heavy Ion Collider (RHIC) and Large Hadron Collider (LHC) energies. In contrast, at high μ_B and moderate T , theory predicts a first-order phase transition and a possible critical endpoint, which remain unconfirmed experimentally. These regions are relevant for the cores of neutron stars and can be studied through relativistic heavy-ion collisions at intermediate energies.

While astrophysical observations, such as gravitational waves from binary neutron star mergers constrain the equation of state of dense matter, laboratory experiments allow controlled exploration of the QCD phase diagram. In this context, the Compressed Baryonic Matter (CBM) experiment, one of the key scientific pillars of the Facility for Antiproton and Ion Research (FAIR) and currently under construction in Darmstadt, will probe nuclear matter at high net-baryon densities and moderate temperatures, with unprecedented interaction rates up to 10 MHz. Its physics program aims to identify signatures of the QCD phase transition, critical phenomena, and chiral symmetry restoration through observable such as collective flow, event-by-event fluctuations, strangeness production, hypernuclei, charm, and dilepton spectra.

Complementary to CBM, the E16 experiment at the Japan Proton Accelerator Research Complex (J-PARC) focuses on investigating in-medium modifications of vector mesons in pA collisions, aiming to detect partial restoration of chiral symmetry in cold, dense nuclear matter via dilepton decays. Together, these experiments provide access to different regions of the QCD phase diagram: E16 addresses dense, low-temperature matter, while CBM explores dense and hot conditions created in heavy-ion collisions. The combined results will help to understand the origin of hadrons masses, the nature of confinement, and the QCD Equation of State (EoS) under extreme conditions.

Previous experimental effort have provided essential, though not yet conclusive information on in-medium behavior of hadrons. Measurements at the European Organization for Nuclear Research (CERN) Super Proton Synchrotron (SPS) (NA45/CERES) and High Energy Accelerator Research Organization (KEK) (E325) have shown excess dilepton production in the invariant-mass region below the ρ -meson, suggesting modifications of the vector meson spectral functions in nuclear matter. These observations are consistent with a broadening of the ρ -meson width rather than a simple mass shift, indicating a possible partial chiral symmetry restoration. However, the limited statistics and restricted kinematics coverage of earlier experiments make difficult a quantitative comparison with theoretical models.

In order to solve these limitations, the E16 experiment has been designed to improve upon the sensitivity achieved by the KEK E325 experiment by two orders of magnitude in statistics and mass resolution. Its setup features a high-intensity 30 GeV proton beam incident on nuclear targets, a large acceptance spectrometer with a dipole magnet, and a tracking system based on Silicon Strip Detector (SSD) and Gas Electron Multiplier (GEM) trackers. The first physics run demonstrated the feasibility of high-rate operation and precise dilepton reconstruction but also revealed limitations in spatial resolution and occupancy in the innermost region near the target. To overcome these constraints and fully exploit the available beam intensity, an upgrade of the innermost tracking layer has been proposed, replacing the original SSD modules with a lightweight, high-rate Silicon Tracking System (STS) derived from the CBM-STs design. This upgrade will enhance vertex reconstruction, improve the mass resolution of dilepton pairs, and ensure stable operation under high multiplicity and radiation load. This upgrade will not only extend the physics reach of E16 but also provide a valuable testbed for the CBM tracking system under realistic experimental conditions.

The CBM experiment is designed as a fixed-target setup optimized for measuring rare probes with high precision and statistical significance. It operates at interaction rates up to 10 MHz, which imposes demanding requirements on all subsystems, from sensors to data acquisition. To meet its requirements and fully exploit its physical potential in the high-rate regime, the experiment is equipped with fast, self-triggering, radiation-tolerant detectors employing free-streaming readout electronics.

At the heart of this detection concept lies the STS. It is responsible for reconstructing charged particle trajectories and determining their momenta with high accuracy. The STS is built from 876 double-sided silicon microstrip sensors arranged in eight tracking stations, covering a polar angle between 2.5° and 25° , and positioned within a 1 T m dipole magnetic field. The high occupancy environment, the large number of channels (more than 1.7 millions), and the timing demands make the Front-End Electronics (FEE) one of the most critical components of the detector.

Each STS module serves as an independent functional unit, combining a double-sided, double-metal silicon microstrip sensor with lightweight microcables and two Front-End Board (FEB), that carry out eight custom-developed SMX Application-Specific Integrate Circuits (ASICs) each one. These ASICs are low-power, self-triggering chips providing both charge and timing information with 128 channels. They digitize the analog signals from the silicon strips through a 5-bit flash Analog-to-Digital Converter (ADC) and a 14-bit Time-to-Digital Converter (TDC) for timing measurement. The calibration, stability, and precision of the SMX ASICs are crucial for ensuring consistent detector performance, both in laboratory and beam environments. Therefore, an accurate and efficient calibration strategy is fundamental not only for single-module characterization but also for the large-scale production testing of the full detector.

The present work reports the development, optimization, and validation of the calibration and characterization procedures for the SMX ASICs and their integration in the E16-STs system. The work was carried out within the framework of the E16 experiment at the J-PARC, which share similar physics program and a serve as a technology demonstrator for CBM. The E16 experiment investigates the in-medium modifications of vector mesons via their di-electron decay channels in pA collisions. Its tracking system is based on STS modules identical in concept to those planned for CBM, making it an ideal platform for evaluating detector performance and calibration strategies under realistic experimental conditions.

This thesis comprises the entire module life cycle, from the algorithmic level of ASIC calibration to large-scale testing, qualification, and experimental verification in beam conditions. The first major part of the work focuses on improving the calibration algorithm of the SMX ASIC. The standard ADC calibration procedure, while accurate, required a coarse-scan stage that significantly extended calibration time. Such a time intensive method is unsuitable for large-scale module characterization, where hundreds of modules and thousands of ASICs must be calibrated efficiently.

To overcome this limitation, a new calibration procedure based on a Successive Approximation Method (SAR) algorithm was developed and implemented. Unlike the STANDARD method, which performs an exhaustive search across the entire threshold range, the SAR approach uses an iterative binary search to rapidly converge to the correct discriminator threshold. This method reduces the number of calibration steps, resulting in a substantial gain in speed. The SAR calibration demonstrated equivalent accuracy to the STANDARD method, with Differential Non-Linearity (DNL) and Integral Non-Linearity (INL) remaining below 0.4 LSB. Importantly, it achieved a 30% reduction in calibration time during initial tests, validating its feasibility as a replacement for the STANDARD procedure.

Following this proof of concept, a detailed optimization of the SAR algorithm parameters was carried out. The number of iterations, search width, and fine-range parameters were systematically tuned to achieve the optimal balance between calibration precision and processing time. The configuration of 10 iterations, a search width of 14 LSB, and a fine range of 12 LSB was identified as the most efficient setup, achieving up to 60% reduction in total calibration time compared to the STANDARD approach, while maintaining identical accuracy.

Building upon these results, the calibration procedure was extended with a broadcasting mechanism, allowing the simultaneous calibration of multiple ASICs. This paral-

lization represents a crucial step toward series-production scalability. The broadcasting calibration achieved an additional 50% reduction in total time relative to the already optimized SAR approach, confirming its suitability for large-scale deployment in the final STS production line.

A detailed study of the ADC and FAST discriminator transfer functions was performed to establish the relationship between Digital-to-Analog Converter (DAC) settings and effective thresholds. The results revealed linear dependencies with well-defined slopes, confirming the expected electronic behavior. The measured conversion slopes were 822 e/LSB and 718 e/LSB for the ADC path on the n- and p-side, respectively, and 397 e/LSB and 361 e/LSB for the FAST path. These results provided a quantitative basis for correlating amplitude and timing thresholds and for defining global operational parameters. These results enabled the creation of an operational table linking DAC settings to physical thresholds, thereby simplifying the configuration and tuning of the detector during operation. Furthermore, a global FAST discriminator threshold (Thr_{2glb}) was evaluated, and an optimal range between 22 LSB and 26 LSB was identified where all channels could be successfully calibrated, excluding the Z-strips.

To validate the procedure on a large scale, ten pre-series modules (80 ASICs per side) were calibrated using the optimized SAR method. The resulting trim matrices were analyzed to quantify the number of corrected and uncalibrated discriminators, as well as deviations from the default configuration. The results confirmed uniform calibration behavior across all channels, with only a small number of outliers (81 discriminators on the n-side and 258 on the p-side). The p-side required smaller trimming corrections, up to 20 LSB to reach 95% of calibrated discriminators, compared to 28 LSB for the n-side. These findings confirmed both the precision and reproducibility of the SAR-based calibration, validating its integration into the series-production framework of the STS.

The functional and electrical characterization of complete E16-STs modules was also performed. Over two years, fifteen modules: comprising one prototype, ten pre-series, and four replacement units were systematically evaluated following a standardized four-step testing protocol. This included sensor Current-Voltage (IV) characterization, ASIC calibration, evaluation of Equivalent Noise Charge (ENC), and data acquisition using a $^{90}\text{Sr}/\text{Y}$ radioactive source.

The IV measurements verified stable sensor performance up to 150 V in reverse mode. The ASIC calibration data demonstrated well-defined ADC gains and uniform threshold distributions. The ENC values were measured between 700 e and 900 e for the different sides and modules, aligning within 20% of analytical expectations. Broken channels were systematically identified, with all modules fulfilling the production target of 31 broken channels, except one that exceeded the limit by one channel.

Tests using the radioactive source enabled the evaluation of signal response, providing additional verification of broken channels. Time correlation analyses between signals within clusters confirmed synchronization, with the correlation peak centered around $\Delta t = 0$ ns. Furthermore, a reconstructed hitmaps showed excellent agreement with the physical positioning of the source during measurements.

The knowledge and experience gained through these studies led to the development of a module testing and QA protocol. This procedure is now implemented as part of the standardized Quality Assurance (QA) workflow for the final STS series production. It includes automatic calibration, noise and gain assessment, and functional channel verifi-

cation. The protocol has been successfully applied in the ongoing production campaign, during which more than 550 modules have already been characterized and validated.

A performance validation of the detector modules under realistic beam conditions was conducted in a dedicated beam campaign at the Photon Factory Advanced Ring (PF-AR) in Tsukuba, Japan, using a 3 GeV/c electron beam. The E16-STS chamber, composed of ten modules, was tested in multiple geometrical configurations to evaluate timing, charge collection, cluster size, detection efficiency, and spatial resolution.

The results demonstrated that the E16-STS modules meet and in some aspects exceed the design performance goals. A time resolution of 3.2 ns was achieved for large signal amplitudes, and approximately 5 ns for signals around 2.7 fC, fulfilling the timing requirements of both the E16 and CBM experiments. The measured charge collection was 22 ke on the n-side and 20 ke on the p-side, these values are up to 13% and 22%, for n- and p-side, below of the expected energy deposition of Minimum Ionizing Particle (MIP) in 320 μm of silicon, due to the large thresholds employed in the run. The resulting SNR were 27.8 ± 2.2 (n-side) and 28.5 ± 1.5 (p-side). The average cluster size ranged from 1.2 to 1.6 depending on the incident angle, and the detection efficiency reached $89.85\% \pm 0.11\%$ for normal incidence.

Position reconstruction was performed using a Principal Component Analysis (PCA)-based tracking algorithm. The residual distributions between expected and measured hit positions yielded spatial resolutions of $\sigma_x = 118 \mu\text{m}$ and $\sigma_y = 136 \mu\text{m}$ for single-strip clusters, improving to $\sigma_x = 20 \mu\text{m}$ and $\sigma_y = 33 \mu\text{m}$ for multi-strip clusters.

A significant milestone was reached during the J-PARC commissioning run (Run-0e), where the CBM-STS modules achieved their first successful operation under magnetic field conditions. The energy-loss measurements demonstrated a clear separation between pions and protons. This result confirmed not only the accurate tracking performance of the system but also its capability for particle identification, an essential feature for the future eight-layer STS system at FAIR.

Zusammenfassung

Eines der grundlegenden Ziele der modernen Physik besteht darin, zu verstehen, wie das Universum und seine Bestandteile entstanden sind und miteinander wechselwirken. Die Entwicklung der Quantenfeldtheorien und experimenteller Werkzeuge wie Teilchenbeschleuniger hat die Erforschung der Materie über einen außergewöhnlich großen Skalenbereich ermöglicht, von Quarks und Gluonen (10^{-15} m) bis zur Struktur des Kosmos (10^{26} m). In diesem Rahmen beschreibt das Standardmodell die elektromagnetischen, schwachen und starken Wechselwirkungen zwischen den Elementarteilchen. Die Theorie der starken Wechselwirkung, “Quantum Chromodynamics (QCD)”, spielt eine zentrale Rolle bei der Bestimmung der Eigenschaften der Kernmaterie und des Ursprungs des größten Teils der sichtbaren Masse im Universum.

QCD ist eine nicht-Abelsche Eichtheorie, die auf der lokalen $SU(3)_{color}$ Symmetrie basiert, deren elementare Freiheitsgrade Quarks und Gluonen sind. Zwei wesentliche Eigenschaften kennzeichnen die QCD: **asymptotische Freiheit**, die störungstheoretische Berechnungen bei hohen Energien erlaubt, und **Confinement**, das Quarks und Gluonen bei niedrigen Energien in farbneutralen Hadronen bindet. Darüber hinaus erzeugt die spontane Brechung der chiralen Symmetrie im QCD Vakuum die effektiven Massen der leichten Quarks. Unter extremen Bedingungen von Temperatur und/oder Baryonendichte wird erwartet, dass das chirale Kondensat schmilzt, was zur Wiederherstellung der chiralen Symmetrie und zur Bildung neuer Materiezustände wie des “Quark-Gluon Plasma (QGP)” oder dichter baryonischer Materie führt.

Die Phasenstruktur der QCD kann in der Ebene von Temperatur (T) und baryochemischem Potential (μ_B) dargestellt werden. Bei hohen T und niedrigen μ_B , wie sie im frühen Universum vorherrschten, tritt ein glatter Crossover Übergang zwischen hadronischer und partonischer Materie auf, der bei “Relativistic Heavy Ion Collider (RHIC)” und “Large Hadron Collider (LHC)” Energien untersucht wurde. Im Gegensatz dazu sagt die Theorie bei hohen μ_B und moderaten T einen Phasenübergang erster Ordnung und einen möglichen kritischen Endpunkt voraus, die experimentell bisher nicht bestätigt wurden. Diese Bereiche sind z.B. für das Verständnis von Neutronensternen relevant und können durch relativistische Schwerionenkollisionen bei mittleren Energien untersucht werden.

Während astrophysikalische Beobachtungen wie Gravitationswellen von binären Neutronensternverschmelzungen die Zustandsgleichung dichter Materie einschränken, ermöglichen Laborexperimente eine kontrollierte Erforschung des QCD Phasendiagramms. In diesem Zusammenhang wird das “Compressed Baryonic Matter (CBM)” Experiment, eine der zentralen wissenschaftlichen Säulen von “Facility for Antiproton and Ion Research (FAIR)” und derzeit im Aufbau in Darmstadt, Kernmaterie bei hohen Nettobaryonendichten und moderaten Temperaturen mit hohen Wechselwirkungsraten von bis zu 10 MHz untersuchen. Sein Physikprogramm zielt darauf ab, Signaturen des QCD

Phasenübergangs, kritische Phänomene und die Wiederherstellung der chiralen Symmetrie durch beobachtbare Größen wie kollektiven Fluss, Ereignis für Ereignis Fluktuationen, Strangenessproduktion, Hyperkerne, Charm und Dileptonenspektren zu identifizieren.

Ergänzend zu CBM untersucht das E16 Experiment am “Japan Proton Accelerator Research Complex (J-PARC)” in-medium Modifikationen von Vektormesonen in pA Kollisionen, mit dem Ziel, eine partielle Wiederherstellung der chiralen Symmetrie in kalter, dichter Kernmaterie über Dileptonenzerfälle nachzuweisen. Zusammen ermöglichen diese Experimente den Zugang zu verschiedenen Bereichen des QCD Phasendiagramms: E16 adressiert dichte, kalte Materie, während CBM dichte und heiße Bedingungen erforscht, wie sie in Schwerionenkollisionen entstehen. Die kombinierten Ergebnisse werden helfen, den Ursprung der Hadronenmassen, die Natur des Confinements und die QCD “Equation of State (EoS)” unter extremen Bedingungen zu verstehen.

Frühere experimentelle Anstrengungen haben wesentliche, wenn auch noch nicht abschließende Informationen über das Verhalten von Hadronen im Medium geliefert. Messungen am “European Organization for Nuclear Research (CERN) Super Proton Synchrotron (SPS)” (NA45/CERES) und am “High Energy Accelerator Research Organization (KEK)” (E325) zeigten eine erhöhte Dileptonenproduktion im invarianten Massenbereich unterhalb des ρ -Mesons, was auf Modifikationen der Spektralfunktionen von Vektormesonen in Kernmaterie hindeutet. Diese Beobachtungen sind mit einer Verbreiterung der ρ -Meson Breite, statt einer einfachen Massenverschiebung, vereinbar und deuten auf eine teilweise Wiederherstellung der chiralen Symmetrie hin. Die begrenzte Statistik und der eingeschränkte kinematische Bereich früherer Experimente erschweren jedoch einen quantitativen Vergleich mit theoretischen Modellen.

Um diese Einschränkungen zu überwinden, wurde das E16 Experiment entwickelt, um die Empfindlichkeit des KEK E325 Experiments in Statistik und Massenauflösung um zwei Größenordnungen zu verbessern. Das Experiment verwendet einen hochintensiven 30 GeV Protonenstrahl, diverse Kernziele sowie ein Spektrometer mit großem Akzeptanzbereich, mit einem Dipolmagneten sowie einem Trackingsystem, das auf “Silicon Strip Detector (SSD)” und “Gas Electron Multiplier (GEM)” Trackern basiert. Erste Experimente mit Strahl demonstrierten die Machbarkeit des Hochratenbetriebs und die präzise Dileptonenrekonstruktion, offenbarte jedoch auch Einschränkungen in der Ortsauflösung und Sensorbelegung im innersten Bereich nahe dem Target. Um diese zu überwinden und die verfügbare Strahlintensität voll auszuschöpfen, wurde ein Upgrade der innersten Tracking Lage vorgeschlagen, bei dem die ursprünglichen SSD Module durch ein leichtes, hochratenfähiges “Silicon Tracking System (STS)” ersetzt werden, das vom CBM-STS Design abgeleitet ist. Dieses Upgrade verbessert die Vertexrekonstruktion sowie die Massenauflösung der Dileptonpaare und gewährleistet einen stabilen Betrieb bei hoher Multiplizität und Strahlenbelastung. Es erweitert nicht nur das physikalische Spektrum von E16, sondern dient auch als wertvolle Testplattform für das CBM Trackingsystem unter realistischen experimentellen Bedingungen.

Das CBM Experiment ist als Fixed-Target Aufbau konzipiert und für präzise Messungen seltener Sonden mit hoher statistischer Signifikanz optimiert. Es arbeitet bei Wechselwirkungsraten bis zu 10 MHz, was hohe Anforderungen an alle Subsysteme, von den Sensoren bis zur Datenerfassung, stellt. Um diesen Anforderungen zu genügen und das physikalische Potenzial im Hochratenbetrieb voll auszuschöpfen, ist das Experiment mit schnellen, selbsttriggernden, strahlungstoleranten Detektoren mit kontinuierlicher Date-

nauslese ausgestattet.

Das Herzstück dieses Detektionskonzepts bildet das STS. Es ist verantwortlich für die Rekonstruktion geladener Teilchenspuren und die präzise Bestimmung ihrer Impulse. Das STS besteht aus 876 doppelseitigen Silizium-Mikrostreifensensoren, die in acht Tracking Stationen angeordnet sind, einen Polarwinkel zwischen 2.5° und 25° abdecken und in einem 1 Tm Dipolfeld positioniert sind. Die hohe Belegungsrate, die große Kanalanzahl (mehr als 1.7 Millionen) und die Anforderungen an die Zeitauflösung machen die “Front-End Electronics (FEE)” zu einer der kritischsten Komponenten des Detektors.

Jedes STS Modul ist eine unabhängige Funktionseinheit, die einen doppelseitigen, doppelt metallisierten Silizium-Mikrostreifensensor mit leichten Mikrokabeln und zwei “Front-End Board (FEB)” kombiniert, die jeweils acht speziell entwickelte SMX “Application-Specific Integrate Circuits (ASICs)” tragen. Diese ASICs sind selbsttriggernde Chips mit optimierter Leistungsaufnahme, die sowohl Ladungs als auch Zeitinformationen für 128 Kanäle bereitstellen. Sie digitalisieren die analogen Signale der Siliziumstreifen über einen 5-Bit Flash “Analog-to-Digital Converter (ADC)” und einen 14-Bit “Time-to-Digital Converter (TDC)” zur Zeitmessung. Die Kalibrierung, Stabilität und Präzision der SMX ASICs sind entscheidend für die konsistente Detektorleistung, sowohl im Labor als auch im Strahlbetrieb. Daher ist eine präzise und effiziente Kalibrierstrategie nicht nur für die Einzelmodulcharakterisierung, sondern auch für die Serien Produktionstests des gesamten Detektors von grundlegender Bedeutung.

Diese Dissertation umfasst den gesamten Lebenszyklus des Moduls, von der algorithmischen Ebene der ASIC Kalibrierung bis hin zu großangelegten Tests, Qualifikationen und experimentellen Überprüfungen unter Strahlbedingungen. Der erste Hauptteil der Arbeit konzentriert sich auf die Verbesserung des Kalibrierungsalgorithmus des SMX ASIC. Das Standardverfahren zur ADC Kalibrierung ist zwar präzise, erforderte jedoch eine Grobabtastungsphase, die Kalibrierungszeit erheblich verlängerte. Ein dergleichen zeitaufwändiges Verfahren ist für die großflächige Charakterisierung von Modulen ungeeignet, bei der Hunderte von Modulen und Tausende von ASICs effizient kalibriert werden müssen.

Um diese Einschränkung zu überwinden, wurde ein neues Kalibrierungsverfahren auf Basis eines “Successive Approximation Method (SAR)” Algorithmus entwickelt und implementiert. Im Gegensatz zur STANDARD Methode, die eine vollständige Suche über den gesamten Schwellenwertbereich durchführt, nutzt der SAR Ansatz eine iterative binäre Suche, um schnell zum korrekten Diskriminatorschwellenwert zu konvergieren. Dieses Verfahren reduziert die Anzahl der Kalibrierungsschritte und führt somit zu einer erheblichen Beschleunigung. Die SAR-Kalibrierung zeigte eine gleichwertige Genauigkeit zur STANDARD Methode, wobei “Differential Non-Linearity (DNL)” und “Integral Non-Linearity (INL)” unter 0.4 LSB blieben. Besonders hervorzuheben ist, dass sie in ersten Tests eine Reduzierung der Kalibrierungszeit um 30% erreichte, was ihre Eignung als Ersatz für das STANDARD Verfahren bestätigt.

Aufbauend auf diesem Proof of Concept wurde eine detaillierte Optimierung der Parameter des SAR Algorithmus durchgeführt. Die Anzahl der Iterationen, die Suchbreite und die Feinstufenparameter wurden systematisch abgestimmt, um das optimale Gleichgewicht zwischen Kalibrierungspräzision und Verarbeitungszeit zu erreichen. Die Konfiguration mit 10 Iterationen, einer Suchbreite von 14 LSB und einem Feinstufenbereich von 12 LSB erwies sich als die effizienteste Einstellung. Damit konnte die gesamte Kalib-

rierungszeit im Vergleich zur STANDARD Methode bei gleichbleibender Genauigkeit um bis zu 60% reduziert werden.

Auf diesen Ergebnissen aufbauend wurde das Kalibrierungsverfahren um einen Broadcast Mechanismus erweitert, der die gleichzeitige Kalibrierung mehrerer ASICs ermöglicht. Diese Parallelisierung stellt einen entscheidenden Schritt in Richtung Serienproduktionsfähigkeit dar. Die Broadcast Kalibrierung erzielte eine zusätzliche Reduktion der Gesamtzeit um 50% gegenüber dem bereits optimierten SAR Verfahren und bestätigt damit ihre Eignung für den großflächigen Einsatz in der finalen STS Produktionslinie.

Eine detaillierte Untersuchung der Übertragungsfunktionen des ADC und des FAST Diskriminators wurde durchgeführt, um die Beziehung zwischen den “Digital-to-Analog Converter (DAC)” Einstellungen und den effektiven Schwellenwerten zu bestimmen. Die Ergebnisse zeigten lineare Abhängigkeiten mit klar definierten Steigungen, was das erwartete elektronische Verhalten bestätigte. Für den ADC-Pfad wurden Steigungen von 822 e/LSB auf der n-Seite und 718 e/LSB auf der p-Seite gemessen. Für den FAST-Pfad ergaben sich entsprechend 397 e/LSB bzw. 361 e/LSB. Diese Resultate lieferten eine quantitative Grundlage zur Korrelation von Amplituden und Zeitschwellen und zur Definition globaler Betriebsparameter. Auf dieser Basis konnte eine Tabelle erstellt werden, die DAC Einstellungen mit physikalischen Schwellenwerten verknüpft und so die Konfiguration und Feinabstimmung des Detektors im Betrieb vereinfacht. Darüber hinaus wurde ein globaler FAST-Diskriminatorschwellenwert (*Thr2_glb*) evaluiert, wobei ein optimaler Bereich zwischen 22 LSB und 26 LSB identifiziert wurde, in dem alle Kanäle erfolgreich kalibriert werden konnten, mit Ausnahme der Z-Strips.

Zur Validierung des Verfahrens wurden zehn Vorserienmodule (mit zusammen 80 ASICs pro Seite) mit der optimierten SAR Methode kalibriert. Die resultierenden Trim Matrizen wurden analysiert, um die Anzahl der korrigierten und nicht kalibrierten Diskriminatoren sowie Abweichungen von der Standardkonfiguration zu quantifizieren. Die Ergebnisse bestätigten ein gleichmäßiges Kalibrierungsverhalten über alle Kanäle, mit nur wenigen Ausreißern (81 Diskriminatoren auf der n-Seite und 258 auf der p-Seite). Die p-Seite erforderte geringere Trimmkorrekturen, bis zu 20 LSB, um 95% der Diskriminatoren zu kalibrieren, im Vergleich zu 28 LSB auf der n-Seite. Diese Befunde bestätigten sowohl die Präzision als auch die Reproduzierbarkeit der SAR basierten Kalibrierung und untermauerten ihre Integration in den Serienproduktionsrahmen des STS.

Darüber hinaus wurde die funktionale und elektrische Charakterisierung kompletter E16-STs Module durchgeführt. Über einen Zeitraum von zwei Jahren wurden fünfzehn Module, bestehend aus einem Prototyp, zehn Vorserien und vier Ersatzmodulen, systematisch anhand eines standardisierten Vierstufen Testprotokolls untersucht. Dieses umfasste die “Current-Voltage (IV)” Charakterisierung der Sensoren, die ASIC Kalibrierung, die Bewertung des “Equivalent Noise Charge (ENC)” sowie Datennahme unter Verwendung einer $^{90}\text{Sr}/\text{Y}$ radioaktiven Quelle.

Die IV Messungen bestätigten eine stabile Sensorleistung bis zu 150 V im Sperrbetrieb. Die Kalibrierdaten der ASIC zeigten klar definierte ADC Verstärkungen und gleichmäßige Schwellenwertverteilungen. Die ENC Werte lagen zwischen 700 e und 900 e für die verschiedenen Seiten und Module und stimmten innerhalb von 20% mit den analytischen Erwartungen überein. Defekte Kanäle wurden systematisch identifiziert; alle Module erfüllten das Produktionsziel von maximal 31 defekten Kanälen, mit Ausnahme eines Moduls, das dieses Limit um einen Kanal überschritt.

Tests mit einer radioaktiven Quelle ermöglichten die Bewertung der Signalantwort und lieferten eine zusätzliche Überprüfung der defekten Kanäle. Zeitkorrelationsanalysen zwischen Signalen innerhalb von Clustern bestätigten die Synchronisation, wobei das Korrelationsmaximum bei $\Delta t = 0$ ns lag. Darüber hinaus zeigten rekonstruierte Hitmaps eine hervorragende Übereinstimmung mit der physikalischen Positionierung der Quelle während der Messungen.

Das im Rahmen dieser Studien gewonnene Wissen und die gesammelten Erfahrungen führten zur Entwicklung eines Modultest und “Quality Assurance (QA)” Protokolls. Dieses Verfahren ist nun als Teil des standardisierten QA Workflows für die finale STS Serienproduktion implementiert. Es umfasst automatische Kalibrierung, Rausch und Verstärkungsbewertung sowie die Funktionsprüfung der Kanäle. Das Protokoll wird erfolgreich in der laufenden Produktionskampagne angewendet, in deren Verlauf bereits mehr als 550 Module charakterisiert und validiert wurden.

Eine Leistungsvalidierung der Detektormodule unter realistischen Strahlbedingungen wurde in einer speziellen Strahlkampagne am “Photon Factory Advanced Ring (PF-AR)” in Tsukuba, Japan, mit einem 3 GeV/c Elektronenstrahl durchgeführt. Der E16-STs Aufbau, bestehend aus zehn Modulen, wurde in mehreren geometrischen Konfigurationen getestet, um Zeitauflösung, Ladungssammlung, Clustergröße, Detektionseffizienz und Ortsauflösung zu bewerten.

Die Ergebnisse zeigten, dass die E16-STs Module die vorgesehenen Leistungsziele erfüllen und in einigen Aspekten sogar übertreffen. Für große Signalamplituden wurde eine Zeitauflösung von 3.2 ns erreicht, und etwa 5 ns für Signale um 2.7 fC, womit die Zeitauflösungsanforderungen sowohl des E16 als auch des CBM Experiments erfüllt werden. Die gemessene gesammelte Ladung betrug 22 ke auf der n-Seite und 20 ke auf der p-Seite, Diese Werte liegen für die n- und p-Seite um bis zu 13% bzw. 22% unter der erwarteten Energieabgabe von “Minimum Ionizing Particle (MIP)” in 320 m Silizium, was auf die hohen Schwellenwerte zurückzuführen ist, die verwendet wurden. Die resultierenden “Signal-to-Noise Ratio (SNR)” Werte betrugen 27.8 ± 2.2 (n-Seite) und 28.5 ± 1.5 (p-Seite). Die durchschnittliche Clustergröße lag, abhängig vom Einfallswinkel, zwischen 1.2 und 1.6, und die Detektionseffizienz erreichte $89.85\% \pm 0.11\%$ bei senkrechtem Einfall.

Die Positionsrekonstruktion wurde mithilfe eines auf “Principal Component Analysis (PCA)” basierenden Tracking Algorithmus durchgeführt. Die Residualverteilungen zwischen erwarteten und gemessenen Trefferpositionen ergaben Ortsauflösungen von $\sigma_x = 118 \mu\text{m}$ und $\sigma_y = 136 \mu\text{m}$ für Einzelstreifen Cluster, die sich auf $\sigma_x = 20 \mu\text{m}$ und $\sigma_y = 33 \mu\text{m}$ für Mehrstreifen Cluster verbesserten.

Ein bedeutender Meilenstein wurde während des J-PARC Inbetriebnahmelaufs (Run-0e) erreicht, bei dem die CBM-STs Module erfolgreich erstmals unter Magnetfeldbedingungen betrieben wurden. Die Energieverlustmessungen zeigten eine klare Trennung zwischen Pionen und Protonen. Dieses Ergebnis bestätigte nicht nur die präzise Tracking Leistung des Systems, sondern auch seine Fähigkeit zur Teilchenidentifikation, ein wesentliches Merkmal für das zukünftige achtlagige STs System bei FAIR.

References

- [1] J. Steinheimer et al. Examination of directed flow as a signal for a phase transition in relativistic nuclear collisions. *Physic Review*, C89, 2014.
- [2] S. Borsànyi et al. Is there still any T_c mystery in lattice QCD? Results with physical masses in the continuum limit III. *Journal of High Energy Physics*, 2010. DOI: 10.1007/JHEP09(2010)073.
- [3] S. Borsànyi et al. Full result for the QCD equation of state with 2+1 flavors. *Physics Letters B*, 2014. <https://www.sciencedirect.com/science/article/pii/S0370269314000197>.
- [4] S. Ejiri et al. End point of the first-order phase transition of QCD in the heavy quark region by reweighting from quenched QCD. 101, 2020.
- [5] M. A. Stephanov. QCD phase diagram and the critical point. *International Journal of Modern Physics A*, 2005. DOI: 10.1142/S0217751X05027965.
- [6] K. Fukushima and T. Hatsuda. The phase diagram of dense QCD. *Reports on Progress in Physics*, 2010. DOI: 10.1088/0034-4885/74/1/014001.
- [7] P. B. Demorest et al. A two-solar-mass neutron star measured using Shapiro delay. *Nature*, 467, 2010.
- [8] G. Baym, T. Hatsuda, and T. Takatsuka. From hadrons to quarks in neutron stars: A review. *Reports on Progress in Physics*, 81, 2018.
- [9] D. Logoteta and I. Bombaci. Constraints on Microscopic and Phenomenological Equations of State of Dense Matter from GW170817. *Universe*, 5, 2019.
- [10] E. Pian et al. Spectroscopic identification of r-process nucleosynthesis in a double neutron star merger. *Nature*, 551, 2017.
- [11] X. Forteza, P. Acdelsalhin, and L. Gualtieri. Impact of high-order tidal terms on binary neutron-star waveforms. *Physical Review D*, 98, 2018.
- [12] B. Friman et al. The CBM physics book: Compressed baryonic matter in laboratory experiments. *Lectures Notes Physics*, 814:1–980, 2011.
- [13] H. Heiselberg and M. Hjorth-Jensen. Phases of dense matter in neutron stars. *Physics Report*, 328:237–327, 2000.

- [14] A. Kalweit. Highlights from the ALICE experiment. *Nuclear Physics A*, 982, 2019.
- [15] Y. Zhenyu. Highlights from the STAR experiment. *Nuclear Physics A*, 982, 2019.
- [16] J. Grosse-Oetringhaus. The Future of High-Energy Heavy-Ion Facilities. *Nuclear Physics A*, 982, 2019.
- [17] T. Galatyuk. Future facilities for high μ_B physics. *Nuclear Physics A. XXVII International Conference on Ultrarelativistic Nucleus-Nucleus Collisions: Quark Matter*, 982:163–169, 2019. <https://www.sciencedirect.com/science/article/pii/S0375947418304172>.
- [18] BM@N Collaboration. BM@N-conceptual Design Report 2012. 2012. <http://bmnshift.jinr.ru/wiki/lib/exe/fetch.php?media=bmncdr.pdf>.
- [19] CBM-Compressed Baryonic Matter experiment. <http://www.fair-center.eu/for-users/experiments/nuclear-matter-physics/cbm/introduction.html>.
- [20] FAIR-Baseline Technical Report 2006. <http://www.fair-center.eu/fileadmin/fair/publicationsFAIR/FAIRBTR1.pdf>.
- [21] W. Henning. FAIR-An International Accelerator Facility for Research with Ions *AIP Conference Proceedings*, 773(1):3–5, 2005. DOI: 10.1063/1.1949487.
- [22] M. M. Aggarwal and the STAR Collaboration. An Experimental Exploration of the QCD Phase Diagram: The Search for the Critical Point and the Onset of Deconfinement. *ArXiv e-prints*, 2010.
- [23] T. Ablyazimov et al. Challenges in QCD matter physics -The scientific programme of the Compressed Baryonic Matter experiment at FAIR. *European Physical Journal*, A53, 2017.
- [24] I. C. Arsene et al. Dynamical phase trajectories for relativistic nuclear collisions. *Physical Review C*, 75, 2007.
- [25] J. Chen, J. Deng, and L. Labun. Baryon susceptibilities, non-Gaussian moments, and the QCD critical point. *Physical Review D*, 92, 2015.
- [26] W. Reisdorf et al. Systematics of central heavy ion collisions in the 1 AGeV regime. *Nuclear Physics A*, 848, 2010.
- [27] B. Tomásic and E. E. Kolomeitsev. Complete strangeness measurements in heavy-ion collisions. *The European Physical Journal A*, 52, 2016.
- [28] T. Matsui and H. Satz. J/ψ Suppression by Quark-Gluon Plasma Formation. *Physics Letter*, B178, 1986.
- [29] C. Djalali. Properties of light mesons in the nuclear medium. *Strong interaction in the nuclear medium: new trends*, 2009. https://heberge.lp2ib.in2p3.fr/heberge/EcoleJoliotCurie/coursannee/transparents/Lecture1_Djalali_EJC09.pdf.

- [30] R. Muto et al. Evidence for In Medium Modification of the ϕ Meson at Normal Nuclear Density. *Physics Review Letter*, 2007. <https://link.aps.org/doi/10.1103/PhysRevLett.98.042501>.
- [31] A. Malakhov and A. Shabunov. Technical Design Report for the CBM Superconducting Dipole Magnet. 2013. <http://repository.gsi.de/record/109025>.
- [32] M. Koziel et al. The prototype of the Micro Vertex Detector of the CBM Experiment. *Nuclear Instruments and Methods in Physics Research Section A: Accelerators, Spectrometers, Detectors and Associated Equipment*, 732, 2013.
- [33] J. Adamczewski-Musch et al. The CBM RICH detector. *Journal of Instrumentation*, 11, 2016.
- [34] S. Chattopadhyay et al. *Technical Design Report for the CBM: Muon Chambers (MuCh)*, 11, 2015. <http://repository.gsi.de/record/161297>.
- [35] N. Herrmann et al. *Technical Design Report for the CBM Time-of-Flight System (TOF)*, 2014.
- [36] D. Dvorak. Forward Spectator Detector for CBM. *EPJ Featured Poster, Quark Matter*, 2025.
- [37] I. Kisel, I. Kulakov, and M. Zyzak. Standalone First Level Event Selection Package for the CBM Experiment. *IEEE Transactions on Nuclear Science*, 60, 2013.
- [38] S. Yokkaichi et al. Addendum to the J-PARC E16 Technical Design Report for Run-1 approval. *Technical report, J-PARC*, 2022.
- [39] T. N. Murakami. Development and construction of GEM tracker system for the J-PARC E16 experiment. 2020. https://indico2.riken.jp/event/3353/contributions/14087/attachments/9222/11966/Murakami_master.pdf.
- [40] Y. Giomataris and G. Charpak. A hadron-blind detector. *Nuclear Instruments and Methods in Physics Research Section A: Accelerators, Spectrometers, Detectors and Associated Equipment*, 310, 1991.
- [41] S. Nakasuga. https://indico2.riken.jp/event/3676/contributions/15905/attachments/10038/14158/master_nakasuga_final.pdf, 2021.
- [42] I. Panasenko. Development of electrical quality assurance procedures and methods for the silicon tracking system of the CBM experiment. *Ph.D thesis*, 2023. DOI: 10.15496/publikation-80578.
- [43] W. R. Leo. Techniques for Nuclear and Particle Physics Experiments: A How-to Approach. *Springer-Verlag*, 1987.
- [44] V. Friese, C. Sturm, and A. Toia. *CBM Progress Report 2015*, 2016. <http://repository.gsi.de/record/186952>.
- [45] D. S. Koczoń and P. A. Rost. Radiation tolerance of electronics for STS low-voltage power supply. 2016. <http://repository.gsi.de/record/186952>.

- [46] J. Heuser et al. *Technical Design Report for the CBM Silicon Tracking System (STS)*, 2013. <http://repository.gsi.de/record/54798>.
- [47] J. Lehnert et al. GBT based readout in the CBM experiment. *Journal of Instrumentation*, 12, 2017.
- [48] J. Lehnert, W. Muller, and C. Schmidt. The GBT-based readout concept for the Silicon Tracking System of the CBM experiment. *Proceedings of IEEE-SPIE Joint Symposium Wilga 2015*, 2015.
- [49] O. M. Rodriguez. Characterization and commissioning of the front-end electronics for the Silicon Tracking System of the CBM experiment. *PhD thesis, Johann Wolfgang Goethe-Universität in Frankfurt am Main*, 2023.
- [50] K. Kasinski et al. STS/MUCH-XYTERv2 Manual v1.30. 2014.
- [51] K. Kasinski et al. Characterization of the STS/MUCH-XYTER2, a 128-channel time and amplitude measurement IC for gas and silicon microstrip sensors. *Nuclear Instruments and Methods in Physics Research, A*, 908:225–235, 2018.
- [52] R. K. Kasinski and K. R. Szczygiel. Front-end electronics consideration for Silicon Tracking System and Muon Chambers. *Journal of Instrumentation*, 2016.
- [53] K. Kasinski et al. A protocol for hit and control synchronous transfer for the front-end electronics at the CBM experiment. *Nuclear Instruments and Methods in Physics Research, A*, 865:66–73, 2016.
- [54] A. R. Rodriguez. The CBM Silicon Tracking System front-end electronics, from bare ASIC to detector characterization, commissioning and performance. *PhD thesis, Johann Wolfgang Goethe-Universität in Frankfurt am Main*, 2019.
- [55] F. Switakowski. AMC FMC carrier kintex (AFCK). <https://www.ohwr.org/projects/afck>.
- [56] C. Ghabrous Larrea et al. IPbus: a flexible Ethernet-based control system for xTCA hardware. *Journal of Instrumentation*, 10, 2015.
- [57] K. Aoki et al. JPARC E16-STs: its status and results of a test experiment at KEK PF-AR. *CBM Progress Report*, pages 40–42, 2023. DOI: 10.15120/GSI-2024-00765.
- [58] M. Teklishyn. Laboratory infrastructure arrangement. https://indico.gsi.de/event/16793/contributions/69596/subcontributions/2996/attachments/42809/59819/teklishyn_24FEB2023_sts_assembly_test_setups.pdf.
- [59] A. Rodriguez Rodriguez et al. Functional characterization of modules for the Silicon Tracking System of the CBM experiment. *Nuclear Instrumentation and Methods in Physics Research Section A: Accelerators, Spectrometers, Detectors and Associated Equipment*, 1058, 2024. DOI: 10.1016/j.nima.2025.170714.
- [60] I. Momot. Characterization and radiation hardness studies of the silicon microstrip sensors for the CBM experiment. *PhD thesis, Johann Wolfgang Goethe-Universität in Frankfurt am Main*, 2019.

- [61] <https://ni.com>.
- [62] <https://www.wiener-d.com/product/mpod-lv-module/>.
- [63] <https://iseg-hv.com/en/products/detail/EHS>.
- [64] <https://www.lauda.de/us/>.
- [65] W. Zubrzycka and K. Kasinski. Biasing potentials monitoring circuit for multi-channel radiation imaging ASIC in-system diagnostics. *Proc. 2017 MIXDES-24th International Conference "Mixed Design of Integrated Circuits and Systems"*, pages 234–239, 2017. DOI: 10.23919/MIXDES.2017.8005190.
- [66] L.M. Collazo. Laboratory infrastructure arrangement. https://indico.gsi.de/event/16428/contributions/70293/attachments/43001/60168/CBM_CM_STS_Collazo.pdf.
- [67] I. Keshelashvili. https://indico.gsi.de/event/15512/contributions/66156/attachments/41334/57454/i.keshelashvili_STS_Warsaw.pdf.
- [68] CbmRoot. <https://git.cbm.gsi.de/computing/cbmroot>.
- [69] V. Friese. The high-rate data challenge: computing for the CBM experiment. *Journal of Physics: Conference Series 898*, 2017. DOI: 10.1088/1742-6596/898/11/112003.
- [70] T. Miyajima et al. Operation and recent developments of the Photon Factory Advanced Ring. pages 2845–2847, 2005.
- [71] PF-AR test beamline at KEK. <https://itdc.kek.jp/en/testBeamLine/index.html>.
- [72] Y. Iwasaki et al. Level 1 trigger system for the Belle II experiment. *IEEE Trans. Nucl. Sci.*, 58:1807–1815, 2011.
- [73] S. Yokkaichi et al. Addendum-2 to the J-PARC E16 Technical Design Report. 2024.
- [74] Y. Rento. Development and Performance Evaluation of Silicon Strip Detector for Next Generation High Luminosity Heavy-Ion Collision Experiments. *Master thesis, Quark Physics Laboratory*, 2025.

Acknowledgements

This thesis would not exist without me, of course, but it would not exist without all of you either. And so:

My deepest gratitude goes to Alberica and Adrian for the opportunity they gave me, which today takes shape in this work. But also for the countless successive approximations of corrections, for their trust, their patience (surely not in a small amount), and the many hours of help. For guiding me and for defending me. And for caring for me so much.

I want to thank every colleague in the STS group, because every professional moment has, directly or indirectly, become part of this work. In particular, I want to thank Adrian, Osnan, Lady, Dario, David, Alberica, Jörg, Patryk, Maksym, Kshitij, Shaifali, and Mehul, with whom I have shared all kinds of moments (the bad ones and the even worse ones) throughout the life of this thesis. In addition, to Natalia: at one point you asked me whether your summer project would ever be useful, I can only say, read the thesis!

To the E16 collaboration. In particular to K. Ozawa and K. Aoki, for the opportunity to work together, for their hospitality and kindness during the long beamtime days. To Rento, my friend “Lento”, for the days we worked side by side and especially for your detailed emails, no matter the time of the day I bothered you. But also for the meals with chopsticks, in which you were a true master to me. As for the English, believe me, you could not guess who was doing worse.

I want to thank all the teachers who have been part of my development and who encouraged me to follow this path.

To the Cuban Gang + 3, for being there when I was at my limits, in every sense. For the company, that is something I need, and I need very much: Adrian, we’ve already cried together more than once, so there’s not much more to say, oh yes, someday we will have freedom. Osnan, for the best explanation ever given in the best equipped laboratory ever seen, about the greatest experiment ever built. Captain Alejandro Casco, you still have a lot of work to do on your Spanish. Tobias, my brother in beers, thank you so much for your unconditional support. David, my grill apprentice. Evgenia, thank you for your kindness and patience with this group of Cubans. Lady, still waiting to see your legendary Spider-Man pasta again, and as always, Dairon is watching you from above. Katia, “boniato otra vez”. Dario, who’s the real proof that one isn’t sick in Cuba, one is just simply allergic to communism. Claire, thank you for the time we shared, so here’s a ‘le clavile’ for you. Patryk, my dear red friend and newest member of the gang, after many tests I would like to ask you, is the coffee in Poland much much better than here?

To FN-13, for the great team we formed in the face of every obstacle during student time, and because we were never fast individual cars in a race, but rather a bus, slower yes, but one in which we were all together: Daniel, my brother, on Vía Blanca there’s a pothole that you can’t even imagine. Gabo, pipo, let me go to the board first at least

once. Migue, the eternal black sheep. Cesar, now you tell me, what do you need?. Raulo, best goalkeeper of the Minions team. Andy, did you see? In the end, there was a good guy from Havana. Jorgito, a pity you're a Barça fan. Jose Manuel, the "Caoba Roclan". Mariela, the very, very mulatta from Marianao. Dario, there aren't so many "guayabas" anymore, but we can still tell Guzmán there are tougher roots. Eliecer, another coffee my friend? Javier, the eternal free electron. And Katia, my catch.

To my Cuban crew, for their loyalty, and for their trust in me: Pedro, the doctor and no, not the salsa one. Tase, the true "wherever you all are, that's where I'm going". My cousins Marcote (the *compotón*) and Carlitos (the skinny one). "El Viejo", he's and old that's it. "El Carli", the one who's not Carlitos the skinny one or Carlitos the ugly one. Armando, who took "8 Apellidos Vascos" way too seriously. Marcos, what a wild horse you are. Victor, you won't find a more stingy "prieto" than him. "El Chino", whose biggest Chinese trait is his height. "El Ruso", Jacobo what a night you gave us. "Reglanos", there're still plenty of ñangas parties left to throw. There's so much to tell to all of you, but for now I'll just say: get your livers ready, because there's plenty of *plancha'o* and Marc Gasol to drink.

To Malkys, for her infinite love, and for being the mother of the person I happily call my wife.

A more than special thank you to my family, to whom I will be eternally indebted, for so many life lessons, for their love, and for their struggles, which were carried out not only for themselves but for me. To my parents, Iris and Paquitín. To my grandparents Mima, Pipo, and my Chinese grandma Eolia. To my many uncles and aunts, in particular my aunt Alina. To my cousins, especially Gretel, Jessica, Raidel, Marcote, and Carlitos.

And to my wife Katia, who has given me a boundless love and who has fought by my side, not only through the good times, but far more through the difficult ones.

Many thanks also to all those who are not explicitly mentioned in the text, but who have undoubtedly made the journey to this point less difficult.

Dairon Rodríguez Garcés

Johann Wolfgang Goethe-Universität in Frankfurt am Main
GSI Helmholtzzentrum für Schwerionenforschung GmbH
Planckstraße 1, 64291, Darmstadt, Germany
Phone: +49-176-8920-2168
E-mail: d.rodriguezgarces@gsi.de
Born: October 27th, 1994, La Habana, Cuba



Education

- **May. 2021–Today:** PhD student, Institut für Kernphysik Goethe-Universität Frankfurt am Main, Germany.
Thesis: *The Silicon Tracking System of the E16 experiment at J-PARC: Characterization, Beam commissioning, and implications for the CBM series production*
Supervisor: Prof. Dr. Alberica Toia and Dr. Adrian Rodríguez Rodríguez.
- **Sept. 2013–Jul. 2018:** Degree in Physics: Bachelor in Science in Nuclear Physics. Higher Institute of Technologies and Applied Sciences (InSTEC), Habana, Cuba.
Thesis: *Characterization by photoelectronic spectroscopy of X-rays (XPS) of Carbon nanostructures obtained by underwater arc discharge of graphite electrodes.*
Supervisor: Dr. Daniel Codorniu Pujals.

Professional experience

- **May. 2021–Today:** PhD student at the Silicon Tracking System (STS) group of the Compressed Baryonic Matter (CBM) experiment at GSI, Darmstadt, Germany.
- **Sept. 2018–Apr. 2021:** Junior Professor for the Nuclear Physics Department of the Faculty of Science and Nuclear Technologies, Higher Institute of Technologies and Applied Science (InSTEC), La Habana, Cuba.

Conference participation

- XXXI International Conference on Ultra-Relativistic Nucleus-Nucleus Collisions (Quark-Matter), 2025, Frankfurt, Germany.
- DPG Annual Spring Meeting, 2025, Köln, Germany.
- 12th Beam Telescopes and Test Beams Workshop, 2024, Edinburgh, Scotland.
- DPG Annual Spring Meeting, 2024, Gießen, Germany.
- DPG Annual Spring Meeting, 2023, Dresden, Germany.
- XXIX International Conference on Ultra-Relativistic Nucleus-Nucleus Collisions (Quark-Matter), 2022, Krakow, Poland.
- DPG Annual Spring Meeting, 2022, Mainz, Germany.

Training schools

- Beamtime at the PF-AR facility at KEK, November 13rd – 22nd, 2023, Tsukuba Campus, Japan.
- HGS-HIRe Power Week on Silicon Pixel Detectors, November 6th – 10th, 2023, Castle Rauschholzhausen, Germany.
- EURIZON Detector School, July 17th – 28th, 2023, Wuppertal, Germany.
- HGS-HIRe Basic Course I: Making an Impact as an Effective Researcher.

Publications

- *Performance of the prototype Silicon Tracking System of the CBM experiment tested with heavy-ion beams at SIS18*. A. Agarwal et al. Nuclear Inst. and Methods in Physics Research, A (2025), DOI:10.48550/arXiv.2505.20517.
- *Minimal material, maximum coverage: Silicon Tracking System for high-occupancy conditions*. M. Teklishyn et al. Nuclear Inst. and Methods in Physics Research, A 1080 (2025), DOI: 10.1016/j.nima.2025.170714.
- *Addendum-2 to the J-PARC E16 Technical Design Report*. S. Yokkaichi et al. November (2024).
- *From 3D to 5D tracking: SMX ASIC-based double-sided micro-strip detectors for comprehensive space, time, and energy measurements* M. Teklishyn et al. Journal of Instrumentation, 19 (2024), DOI: 10.1088/1748-0221/19/07/C07002.
- *Functional characterization of modules for the Silicon Tracking System of the CBM experiment*. A. Rodríguez Rodríguez et al. Nuclear Inst. and Methods in Physics Research, A 1058 (2024), DOI: 10.1016/j.nima.2023.168813.
- *XPS of Carbon nanostructures obtained by underwater arc discharge of graphite electrodes*. D. Codorniu Pujals et al. Nucleus N°64 (2018), 15-18.

Personal and technical skills

- **Language:** Spanish (native), English (advanced)
- **Programming and software:** C/C++, Python, L^AT_EX, Microsoft Office package
- **Data analysis and simulation tools:** ROOT, GEANT4

Awards

- Giersch Excellence Award 2023 for the scientific work in the first two years of PhD studies. Stiftung Giersch and HGS-HIRe for FAIR, October 2023.

